warwick.ac.uk/lib-publications

Quantifying the touch feel perception:

Tribological Aspects

by

Hui Niu

Thesis

Submitted to the University of Warwick

in partial fulfilment of the requirements

for admission to the degree of

Doctor of Philosophy

School of Engineering,

University of Warwick

Jun 2017

THE UNIVERSITY OF

WARWICK

Supervisor

Dr. Xianping Liu
  School of Engineering, *University of Warwick*, U.K.

Examiners

Dr. Marc Masen (external)
  Faculty of Engineering, Department of Mechanical Engineering, *Imperial College London*, U.K.

Dr. Ken Mao (internal)
  School of Engineering, *University of Warwick*, U.K.

Contents

List of Figures

ix

xii

List of Tables

xvi

Acknowledgements

This thesis is dedicated to my Family, Friends and especially my Father, who always lives within my heart, who teaches his princess that, wherever there is a dream, pursuit it with courage!

My sincerest gratitude goes to Professor Xianping Liu, for being more than great mentors me as a good friend. This endeavour would not have been possible without the technical guidance and emotional support by my supervisor, especially when I become a mother. In addition to the important technical advice and directions, thank you very much for your selfless support and encouragement during times of difficulty, both inside and outside of work. Many thanks go to quite a few people in the School of Engineering, especially to lab technician Mr. Dave Robinson and Mr. Martin Davis. Their kindness was heartfelt and their technical support was invaluable for experiment ideas and design. I would also like to thank Professor Derek Chetwynd and Professor Yanling Tian for their general support and references. Many thanks for Dr. Lei Wang and Dr. Yuan Xue, who offered me a lot of helpful advice.

A big thanks to my big family for their endless encouragement and selfless devotion to my well-being and happiness. I am very grateful to God for bringing me the best gift of my life—my lovely little son Rui. He is our angel who brings unending love and joy to everyone in my family. He carries on with him my thoughts of my father and the love to whom, is now fully devoted to Rui. Thanks to my mother and my uncle, whom I admire as the kindest people in the world; who would at times of difficulty sacrifice everything to offer me assistance, care, spoiling and love. Thanks to my mother-in-law and father-in-law for their generous help with looking after my son, despite having to travel from afar. I would also like to thank

my friends from the community, in no particular order: Zhongnan Wang, Dan Zhou, Zhengyu Zhou and family, Yuqing Zheng, Han Zhao, Xinyao Zhu, Zedong Hu, Yan Zhang, Modupe and Xiaojing Lin.

I am also very grateful for the financial support from the China Scholarship Council and numerous opportunities from the University of Warwick.

Last but not least,the author would like to express her deepest gratitude to my loving husband Roland Hin Kwan Wong, who love me the most second only to my mother; who would stay by my side no matter rich or poor, happy or sad, and is a perfect match as my soulmate.

List of publications arising from this research

- Hui Niu, Xianping Liu, Quantifying touch-feel perception on some treated thermoplastic materials, 3rd International Conference on BioTribology, London, September 11st-14th, 2016;

- Hui Niu, Xianping Liu and Hin Kwan Wong. Friction measurement apparatus for touch-feel perception studies; 3M International Confenernce, Changchun, China, October 5th-9th, 2015;

- Hui Niu, Xianping Liu and Hin Kwan Wong. Quantifying touch-feel perception: Tribological Aspects on a new artificial finger design. The international conference on Multiscale Materials Modelling 2014, San Fancisco Bay Area, USA, October 6-10,2014;

- Hui Niu, Quantifying touch-feel perception, Surface Science Symposium, June 3rd, University of Warwick, Coventry, UK;

Declarations

This thesis was submitted to the University of Warwick in partial fulfilment of the requirements for the Doctor of Philosophy. The work presented here is my own, except where specifically stated otherwise. The work was performed both in the School of Engineering at the University of Warwick under the supervision of Dr. Xianping Liu.

Abstract

Kansei or affective engineering is the discipline of designing products to be psychophysically more appealing to the human mind and senses. Touch-feel perception of the materials used in consumer products ranging from portable electronics, furniture to automotive interiors plays an important role in the attractiveness of a product. Touch-feel perception is a qualitative measure and is an extrinsic property of the material. To better assist designers and material scientists to optimise aspects of a material for touch-feel perception, it is important to find a link between the qualitative touch-feel attributes with quantitative intrinsic properties of the materials. There is ongoing research in trying to decipher the links between touch-feel perception expressed through semantic psychophysical descriptor words, to physical parameters of the material sample such as the surface topographical, mechanical and tribological attributes. The objective of this work is to fill the current knowledge gap between micro-surface physical properties and customer's perceptual response to surface tactile sensory information as well as their affective preference through theory, correlation models and experimentation.

A conceptual framework of surface tactile evaluation system can be divided into three parts: measurement of the surface physical characteristics, sensory evaluation and correlation analysis. To this end, the thesis documents the development of a friction measurement apparatus including an artificial finger to estimate the friction of a material against human skin in an accurate and repeatable manner. Secondly, correlation analyses were performed on the skin-against-material friction and the tribological factors, including the material surface parameters (e.g. roughness) and physical characteristics (e.g. hardness) of various metal and thermoplastic materials. Finally, the human touch-feel perception was assessed through a questionnaire and the results were modelled to obtain a link between the tribological factors and touch-feel perception.

Generally, human beings feel a surface by stroking or sliding one's finger, which experiences friction. It is challenging to objectively describe the friction experienced by a human finger with respect to surfaces being stroked, as different surfaces and different working conditions can all influence the results. In order to understand the interaction between different surfaces and the friction experienced by a human finger, one has to minimise the variation due to human fingertips and

touch conditions across experiments, such as fingertip humidity, temperature and elastic properties. To achieve this, a friction measurement apparatus incorporating an artificial fingertip has been developed. The artificial fingertip is made of multi-layered materials to mimic the structure, shape, softness and friction properties of a real human fingertip. The friction test apparatus consists of the artificial fingertip, a linear flexure mechanism and a reciprocal linear stage. It is capable of measuring the contact force and friction force simultaneously to give an estimate of the friction coefficient of the material-under-test. Twelve aluminium samples and five steel samples of different surface finishes were tested under different contact forces and stroking speeds. Comparisons were made between the friction results measured in vivo by a human fingertip and those by the artificial fingertip. The results have shown that for the material samples investigated, measurements from the artificial finger achieved a high correlation with results from real human fingers ($r^2 = 0.8 \sim 0.98$) for surface ground steel and milled aluminium. Therefore the artificial finger can be used to mimic the friction characteristics of a real human fingertip and more importantly to measure the skin-against-material friction accurately and in a repeatable way.

In addition, in order to better understand the contact mechanism between the artificial finger and the surface, a suitable theoretical model which incorporates how the contact force relates to the contact area is essential. To enable the modelling of the contact mechanism, the Young's modulus of the artificial fingertip has to be identified, as it is an essential input parameter for all contact theory models as well as FEM. The artificial finger was measured by using micro- and nano-indentation with Berkovich/spherical-tipped indenters. The contact area measurement was conducted by loading a custom-built glass plate on the artificial fingertip and observing the contact area under an optical microscope. Hertz theory was used to model the fingertip and predictions were compared against finite element analysis. The results support the fact that the Hertz contact theory is valid for modelling the contact mechanism of the artificial finger. Thermoplastic elastomers (TPE) and copolymers of elastomer are commonly used in manufacturing car interiors to give the surface a less harsh and more pleasing feel. Ongoing research has been trying to decipher the links between touch-feel perception expressed through semantic psychophysical descriptor words, to physical parameters of the material sample such as the surface topographical, mechanical and tribological properties. A series of five patterned and five coated TPE surfaces provided by an automotive manufacturer were characterized-topographical parameters of the samples by a surface profiler and mechanical/tribological parameters by a nanoindenter. The friction characteristics of these specimens were measured by the friction test apparatus and the artificial finger. The results showed that the artificial finger is representative of a human finger in its friction-sensing capability.

In the second part of the thesis, the relationship between the skin-against-material friction coefficient and the surface topography parameters Rq and Sm were deduced according to Hertz contact theory. The theory gives good agreement with experimental results. In addition, the relationship between the friction coefficient and the other mechanical parameters such as the Young's modulus, skewness, kurtosis, surface slope were investigated through correlation analysis. Finally, 54 people of

different age and gender were asked to rank the specimens in terms of 5 pairs of psychophysical descriptors, such as 'rough/smooth', 'cold/warm', 'slippery/sticky', 'soft/hard' and 'like/dislike'. A rank-ordered logit model was deployed to correlate the human touch feel perception rankings and the thermoplastic samples, and the results were compared with correlation methods used in previous work. The results indicated the specific parameters which are correlated with human touch-feel perception and also their relative contributions.The results form a good guideline for material scientists and designers to, for example, build more touch-desirable car interior materials and consumer packaging.

Introduction

TActile perception is a fast developing subject that attracted great attention. Customer-oriented affective design, which takes account of their feelings and preferences are of great importance for the commercial success. This interest is driven by a range of factors: the development of a sense of touch in robotics, haptic perception for virtual reality and remote sensing, as well as the desire to improve the tactile aesthetics in "touch intensive" consumer products such as phones, touch-pads, paper, fabrics and conditioners [1].

People make a judgement about whether they like a touch sensation or not for products selection. It is crucial for industries such as automotive, textile, cosmetics and telecommunication to identify a way of quantifying the touch feel perception and introducing it as a key design factor [2]. In today's markets, consumers regularly take functionality, usability and safety for granted and look for an emotional connection with a product, especially in the automotive industry where the customer will spend a large amount of time inside their vehicle.

1.1   Background

Nowadays customer-oriented affective design is becoming increasingly important in consumer product development. Unlike vision or sound, touch-feel perception can only be considered during skin contact or when stroking the surface of an object, and designing a better-perceived surface material is often left to trial-and-error. If the relationship between surface characteristics and touch-feel perception is understood, better surfaces can be designed to satisfy the customers' needs. It is also an important factor in affective and hedonistic touch, and in associated emotional attributes such

as pleasantness and comfort [3]. Hence, there has been growing interest in quantifying and modelling touch friction perception recently [4–12].

Skin friction has a direct effect on touch-feel perception. It is influenced by many factors such as skin moisture, age and temperature [13]. Because an artificial finger is more or less immune to skin moisture, ageing and temperature effects, an artificial finger can measure surface properties with much higher repeatability. However, to be able to sense touch in a similar way to that of a human finger, the artificial finger should be designed such that it is anthropomorphic, i.e. to have physical properties resembling a human finger. An artificial finger with touch sensing capability offers several applications, for example, telepresence can be enhanced with robot hands transmitting touch-feel information remotely to the haptic actuators at operator's end. A robot that is more human-like would need to understand what make something 'nice' to touch—it has been found that a target surface that is less rough than a fingertip is more pleasant to touch or stroke [14]. Artificial fingers can also be used to validate advanced haptic devices and models such as that of [15] and [16] in an automated manner. Previous research involving quantifying the perception of touch feeling had been conducted, for example, on car interior components using the tribological probe microscope (TPM) [17–19]. The TPM however, could not replicate the same measurement conditions a human finger experiences, e.g. the stroking motion, and did not have the same mechanical properties of a human fingertip.

Moreover, we can design better touch-desirable components or materials if the correlation between human touch-feel and the physical properties of the contact surfaces can be understood. Commercially, products are increasingly focused on ergonomics and there is increasing demand for surface materials with desirable touch-feel properties [20]. Correlation and regression analyses were carried out on materials used in confectionery packaging to identify the relationships between the people's touch feel responses and the physical measurements of thirty-seven tactile textures; the results showed that touch perception is often associated with more than one physical property [7]. The artificial finger friction sensing capability is correlated against typical surface topography parameters to see which parameters are linked to friction coefficients for various materials. These parameters are then correlated against subjective touch-feel perception on two of the fundamental (lowest-level, see Nagano, Okamoto and Yamada [21]) psychophysical semantic touch-feel descriptors: 'rough/smooth' and 'slippery/sticky'.

'Soft-touch' polymer surfaces should offer desirable features of warm and velvet-like feel, high scratch resistance and aesthetically pleasing features such as

contrasting surfaces, reducing sheen, and enhancing colour depth [22]. As far as car interior surfaces are concerned, the market requires an innovative design of functionality, aesthetics and ergonomics. Specifically, a proper tactile design of polymer surface finishing is essential to achieve such design in terms of cost, safety, comfort and attractiveness [23]. As an cost-effective routine, paint finishes and coating of soft polymers such as thermoplastic elastomers (TPE) and copolymers of elastomer are commonly used in manufacturing car interiors to give the surfaces a less harsh and more pleasing feel. Over-moulding of TPE is also widely applied in manufacturing control knobs and switches to achieve so-called 'soft-touch' feel.

However, to guide the tactile design of 'soft-touch' polymer surface, the database of their physical properties and perceived tactile sceneries should be established and then the potential links could be explored. The physical softness of a material is often measured by Vickers hardness and stiffness (elastic modulus). But the sensorial 'softness' or 'soft-touch' is a combination of sensations derived from the contact interaction with a surface. Inevitably, such interactions are influenced by both skin features and a range of surface properties such as topography, hardness and friction resistance. In contrast, the sensation of 'soft-touch' is subjectively evaluated or quantified by a procedure of psychophysical test.
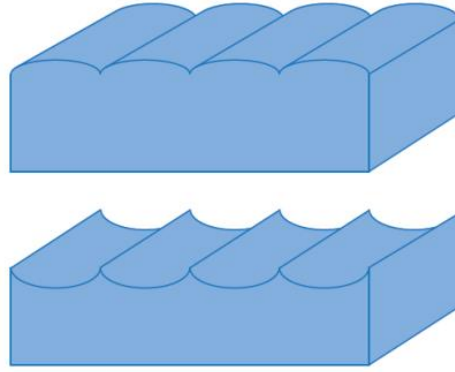
©2011 Bruker Corporation, reprinted with permission from Cohen et al. [24, Fig. 2]

Figure 1.1: Surface textures can vary widely while their R_{a} values are similar when using stylus profilometers

Traditionally, surface texture is measured with a stylus, also known as contact profilometer. While stylus profilometers are indeed useful, the resulting surface parameters are of 2D nature—measured by striding a line over the surface. The measured 2D parameters are conventionally denoted by the letter R, such as R_{a}, R_{z} and R_{pm}. They typically prove too vague in characterising the nature of the surface.

For example, a surface with mostly sharp spikes, deep pits, or general isotropy may all yield the same average roughness value (see Fig. 1.1). Parameters relating to the maximum and minimum profile height ar highly sensitive to the location and length of the measurement site. Moreover, the stylus tool itself can contribute error to the measurement—Shaft alignment of the stylus is critical, as its orientation with respect to the shaft will affect the measured roughness. Even if the stylus scan begins with the stylus translating parallel to the shaft, the tip can sometimes get caught in a groove and bumped off-axis. Also, with soft materials deformation may occur and this affects the accuracy of the results.

International Standards Organization [25] developed a set of comprehensive 3D surface parameters, called S-parameters, for quantitative 3D metrology [26, 27]. Material surfaces can be measured and characterised by instruments such as surface profilometers or microscopes. Apart from 2D/3D raw data of the surface profile, software of the profilometers often output statistics of the profiles called surface topography parameters. They are denoted by capital S for statistics related to 3D profiles, opposed to the conventional capital R for 2D profiles. This thesis uses the following common parameters: Average roughness S_a, root mean square roughness S_q, maximum valley depth S_v and mean spacing between peaks S_m are parameters that provide hybrid roughness and spatial information of 3D surfaces. Skewness S_{sk} is a measure of the asymmetry of the amplitude density curve and Kurtosis S_{ku} is the measure of the peakiness of the amplitude density curve; they are, respectively, the third moments and fourth moment of the surface topography. Root mean square surface slope S_{dq} and arithmetic mean slope R_{da} quantify the gradient of the surface topography.

Because friction measurement is performed by physical contact, it is essential to study the relationship between the measured surface friction coefficient and the physical property parameters of the material. Although there is ongoing research on this subject, there are still many unanswered questions. Previous studies showed the friction coefficient is related to several surface topography parameters. However, the association depends on many environmental factors and initial conditions. For example, when one of the contact surfaces is a compliant material, such as an elastic material or skin, an increased surface roughness will result in a larger separation between the mean planes of contact surfaces, causing a reduction in the adhesion amount. Therefore a reduced friction will be shown with an increase of surface roughness when friction is dominated by adhesion [28]. In addition, other lateral geometry such as wavelength or the spacing between the individual asperities also plays an important role in friction [29]. The friction behaviour of human skin in

contact with well-defined regular patterned surface shows that the determining parameter is the ratio of the asperity size to the inter-asperity distance [30]. However, until now there is no clear picture on how the surface topography of a material can affect human fingertip friction.

1.2 The objective and the outline of the thesis

1.2.1 The objective of the thesis

The mechanoreceptors in the skin are more sensitive to dynamical stimuli such as stroking the finger on a surface [31]. As such, friction mechanisms directly influence the stimuli on the mechanoreceptors. It follows that an important part of touch-feel perception is to quantify the friction coefficient experimented by a human finger. To address this a friction measurement apparatus was developed. The idea is for such an apparatus to be useful in the industry to simulate and quantify the friction interaction between a human fingertip and a material sample to aid affective engineering design.

This thesis introduces an artificial finger specifically developed to have properties close to that of a human finger, both structurally and the way it strokes and applies a load to the surface. The objective is to enable the artificial finer to experience friction in a similar way to that of a human finger, by linking human touch-feel perception to the different surface physical/topographical parameters.

1.2.2 Outlines of the thesis

The thesis is split into 7 chapters.

Chapter 2 presents a literature review following topics in the order of appearance in the thesis. It summarises the latest research work on artificial fingertips and friction measurement apparatuses for tribological studies, and in particular, their advantages and disadvantages. Furthermore, the relationships between surface property parameters and their friction coefficient highlighted by existing literature are examined. Correlation studies between touch-feel perception and surface properties in the literature are also discussed.

The first part of Chapter 3 gives a detailed illustration of the complete friction test apparatus design, which includes 1) a new multilayered artificial fingertip, mimicking structure and elasticity of a human fingertip; 2) a linear stage system that simulates the reciprocating movements of a human finger; 3) a flexure system previously designed and used by our research group. Then, calibration of the system was carried out to make sure the apparatus produce valid and accurate measurements.

In the second part of the chapter, 12 aluminium samples and 5 steel samples were measured by the friction test apparatus under different normal forces and different stroking speeds. The influence of normal loads and sliding speeds on the friction measurement results were investigated. Comparisons were made with the human fingertip measurement results and an old silicone rubber roller design previously used in the research group.

To aid understanding of the experiment results, the theoretical contact mechanism between the artificial fingertip and the contacted samples should be investigated. Chapter 4 gives a formal definition of human skin friction coefficient, and the various contact theory models in the literature were discussed, including 1) The classic Hertz contact model for solid contact between two elastic bodies; 2) The Johnson-Kendall-Roberts (JKR) model for a contact with adhesion mechanisms 3) Greenwood-William model for a contact between a sphere and a rough surface with Gaussian-distributed asperities; 4) Kotwal-Bhushan contact theory which relaxes the Gaussian assumption. The value of Young's modulus of the artificial fingertip plays a key role in the theoretical modelling analysis, therefore different indentation methods were applied to measure its value. The resulting Young's modulus was applied a FEM analysis of the artificial fingertip. An experiment on the contact mechanism of the artificial fingertip was carried out, using a specially designed instrument simulating a contact with a controlled load. The contact area and deformation depth were measured using a Bruker 3D microscope. The results suggested that the contact could be suitably modelled using the Hertz contact theory.

Touch-feel perception of materials in car interiors is a topic of great interest to car manufacturers. Chapter 5 presents a study of five coated thermoplastic samples and ten patterned thermoplastic samples that are commonly used in the manufacturing of car interiors. Surface topography, materials mechanical properties and their friction coefficient were measured using different instruments. Comparisons were made with results from the tribological probe microscope (TPM) [17–19].

Chapter 6 documents correlation analyses performed using data obtained from Chapter 5. Fifty-seven people of different age and gender were asked to rank the TPE samples using the 5 pairs of psychophysical descriptors. Then, Spearman's rank method was used to identify which material property parameters were correlated with measured friction coefficients. The various relationships between surface friction measurements with various parameters that were found to be possibly correlated, including 1) S_a, S_m; 2) Young's modulus; 3) R_{sk}, R_{ku}; and 4) R_{da} were analysed in more detail both theoretically and experimentally.

After studying the links between surface topography parameters, material

mechanical properties and surface friction coefficients, Chapter 7 looks at the relationships between friction coefficients measured by a human/artificial finger and the physical parameters. Firstly, theoretical modelling using the Hertz and Greenwood-William contact theory is presented. Secondly, experiment was performed where 54 people of different gender and age were asked to touch the material samples and rank them using 5 different psychophysical descriptor pairs, namely 1) 'rough/smooth', 2) 'soft/hard', 3) 'cool/warm', 4) 'slippery/sticky' and 5) 'like/dislike' [32]. Several correlation methods already applied in previous work were summarised and their strength and weakness were discussed. The rank-ordered logit modelling technique was used to develop a model for the correlation between the touch-feel perception and the material surface topographical parameters, mechanical properties and friction coefficients.

1.3 Contributions

The thesis introduces a new anthropomorphic artificial finger that has properties close to that of a human finger, both structurally and mechanically. The artificial finger is integrated with a linear stage mechanism to form parts of a friction measurement apparatus. The linear stage allows the artificial finger to simulate the way human finger strokes and applies a load onto a surface. The friction measurement apparatus avoids the uncertainty of human finger-based in-vivo testing due to natural variations between subjects such as skin temperature, humidity and loading forces.

Finite element method (FEM) has been carried out to analyse the contact mechanism of the artificial finger. The contact mechanism was also looked at using theory-based models from the literature. A compact contact area measurement device was developed in order to validate the model and theory experimentally.

Based on the theoretical modelling results and friction measurement results, further relationships between friction coefficients and surface physical property parameters have been investigated according to Hertz contact theory. The results provide a guideline for better surfaces design in industries. Thermoplastic materials have been widely applied in car interiors. While people have a degree of personal taste regarding the materials in a car interior, if the physical property parameters such as surface topography, surface hardness and surface friction characteristics can be determined accurately, their identified correlations with human touch perception can nevertheless give a quantifiable direction for the designers to pursuit from.

In this case, the physical characteristics of 5 coated and 5 patterned TPE samples have been measured, including 3D surface topography, surface mechanical

properties by nano-indentation and surface friction by the newly developed friction test rig. In addition, correlations between these physical characteristics with the touch-feel perception obtained from a survey were sought.

Fifty-four candidates with different age and different sex touched the samples for the psychological part experiments. They were asked to rank the feeling on the measured samples in terms of 6 dimensions, namely rough/smooth, soft/hard, sticky/slippery, cold/warm, like/dislike and 'soft-feel'. Based on several correlation methods, rank ordered logit modelling has been chosen to correlate the touch-feel perception rankings with physical properties of TPE materials. The results have potential to guide industrial materials design.

Literature Review

T̲he objective of this thesis is to investigate the relationship between human touch feel perception and different materials, so this chapter reviews the literature following the research cue. Normally human touch-feel perception is evoked by stroking fingers over a surface, which is largely affected by friction. Because of this, human skin friction mechanism is reviewed first in this chapter. Secondly, an overview of the history of the artificial finger is presented. Thirdly, the literature on the relationship between surface friction and their physical parameters such as surface topography, surface mechanical properties were reviewed according to the contact theory based on different surface textures. Lastly, correlation studies in the literature on touch-feel perception and materials physical property including their friction characteristics are summarised.

2.1 Human skin friction mechanism

As described in [33], the sensory evaluation is defined as "a scientific discipline used to evoke, measure, analyse and interpret reactions to those characteristics of food and other materials as they are perceived by the sensation of sight, smell, taste, touch and hearing." Tactile evaluation specifically refers to perception through touch, which can only be considered when human skin in contact or stroking over the surface of an object. To be more specifically, tactile perception is realised by stroking, tapping or pinching the surface with a tip of a finger, which illustrated in Fig. 2.1 of [32].

Touch evaluation is a complex process involving the physical and psychological domains, and can be separated into three parts in the order of: 1) the physical interaction level, 2) neuron sensory level and 3) the psychological evaluation level.
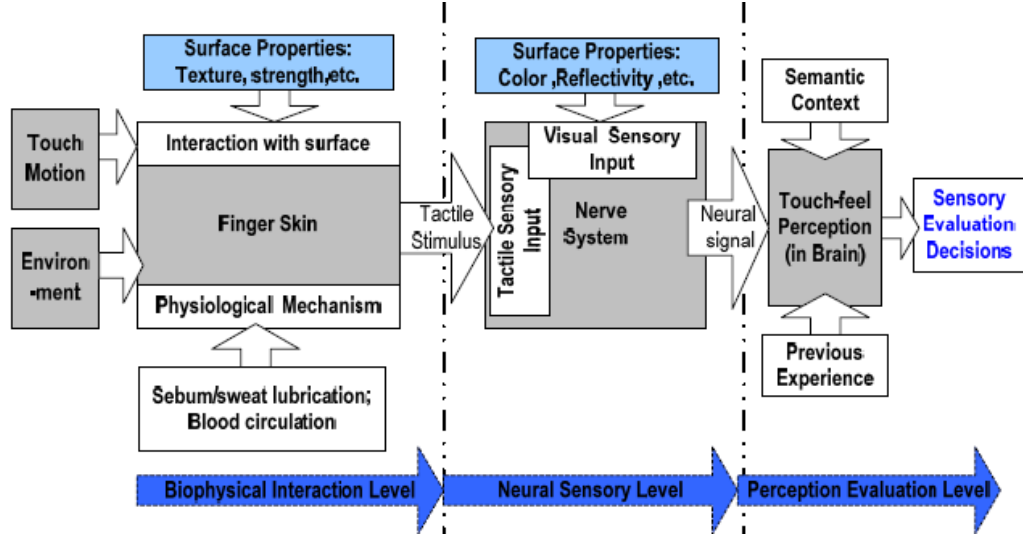
Figure 2.1: The tactile perception process with finger touching

In the physical interaction level, a human finger interacts with the sample surface by reciprocating stroking or sliding motion. It established the physical interfacial interaction between the finger skin epidermis layer and the surface. This interaction is determined by the strain/stress or thermal state of the dermis layer of the skin, changes of which are picked up as tactile stimuli by numerous mechanic-receptors or thermo-receptors at the neural sensory level [34]. At the final psychological evaluation level, the psychological judgements are made by the tactile stimuli transferred. By combining and comparing to the memory of a previous experience, the affective judgement is expressed [35].

Tribology is defined as the 'science and technology of interacting surfaces in relative motion' [36]. The sliding friction of human finger to the contacted surface is highly complex due to deformation of the finger under pressure and lateral movement [1, 13, 37]. In addition, the surface topography, the frictional force between finger and surface and the mechanical vibration introduced by sliding will also affect the friction results [9, 38, 39]. A schematic of fingertip subsurface structure is shown in [40]. The blood circulation, sebum/sweat lubrication both have effects on the sliding friction results [41]. The human touch perception related to surfaces roughness, softness and warmth which would influence the strain, strain rate and temperature receptors [34]. In this case, a new artificial finger design becomes a trend for touch feel perception research.

The fingertip has three main components: it has firstly the bone structure,

which combines rigidity with light weight. It connects with the muscles in the forearm by ligaments fixed on the bone. Secondly, collagen fibres link the skin with the bone tip. The collagen fibres in the subcutaneous tissues constitute the intermediate layer of the fingertip. Large deformation occurs in this composite material during sliding. The last medium is the human skin, which is the cover of the human fingertip. It is crucial to understand the friction properties of human skin. The touch-feel perception can be displayed in Fig. 2.2.
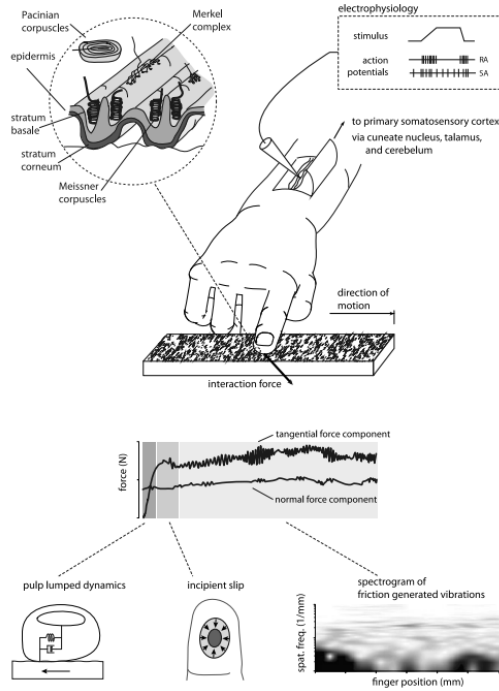
Reproduced with permission from Wiertlewski [42].

Figure 2.2: Mechanism of tactile evaluation. Mechanoreceptors location (top left), afferent responses (top right), and mechanical interaction during tactual exploration (bottom).

In order to understand the human finger friction characteristics, first of all it is important to understand and characterise skin friction. Egawa et al. [43] evaluated the friction properties of human skin under different moisture and viscosity. The KES-SE friction tester—a commercial device for surface friction coefficient measurement—was used. An arm holder was added to the device to measure the skin friction coefficient of a human forearm. Measurements were taken along the surface of the contact probe; from which the averaged value was taken as the friction coefficient and the mean deviation was computed. The moisture content in the

stratum corneum was measured with a CM825 Corneometer, the transepidermal water loss with a Tewameter TM210, the viscoelastic properties of the skin with a Cutometer SEM575 and the skin surface pattern by observing the negative replica made with silicon rubber. The results showed that friction coefficient of the skin was not influenced by load but by skin moisture. The mean deviation was influenced by the pattern and the viscosity of the skin. On the contrary, Koudine et al. [44] argued that for skin, Amontons' Law stipulating the invariance of friction coefficient with load does not hold. The experiment results also showed that friction coefficient depends on the load applied to the finger pad.
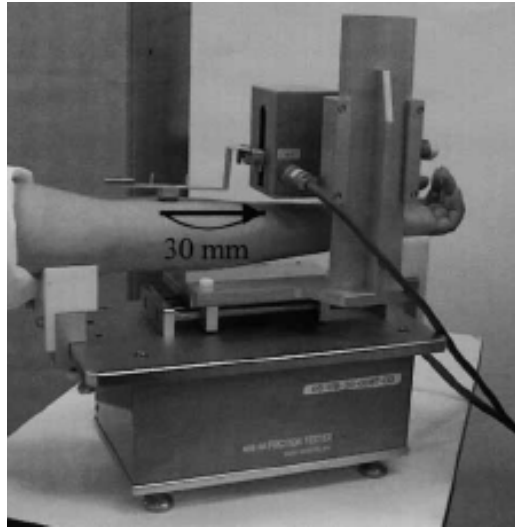
©2002 John Wiley and Sons, reprinted with permission.

Figure 2.3: The view of arm skin friction measuring unit of Egawa et al. [43]

Tang et al. [45] conducted tests on forearm skin with the UMT Series Micro-Tribometer, shown in Fig. 2.4, to assess the influence of sliding speed and the normal load of the measurement probe on the skin friction measurement. The probe was a polypropylene sphere of $10\,\text{mm}$ in diameter attached to a suspension system. The forearm was kept immobile while the probe was pressed onto the skin with a normal load maintained constant by a servo feedback loop. As the normal load was increased from $0.1\,\text{N}$ to $0.9\,\text{N}$, the probe was moved linearly for $12\,\text{mm}$ at a constant speed of $1\,\text{mm}\,\text{s}^{-1}$. Then, the sliding speed was increased from $0.5\,\text{mm}\,\text{s}^{-1}$ to $4\,\text{mm}\,\text{s}^{-1}$ and the probe moved on the right forearm skin linearly for $12\,\text{mm}$ at a constant normal load of $0.2\,\text{N}$. The friction coefficient and the friction force between skin and probe were measured with a load cell, and the normal displacement was also recorded. When the normal load increases, the normal displacement and friction coefficient of skin increase. The friction of the rigid probe sliding on the viscoelastic

skin surface is determined by adhesion, probably due to the molecular bonding of surface atoms in both contacting surfaces as well as the deformation during the mutual mechanical interaction of the asperities of the rigid probe surface into the soft skin surface. Meanwhile, sliding speed also influences the friction behaviour of human skin. When the sliding speed increases, friction coefficient increases and the "stick-slip" phenomenon becomes more pronounced. As the sliding speed increases, hysteric friction increases with more energy lost in elastic hysteresis [45], i.e. the energy dissipated due to material internal friction.
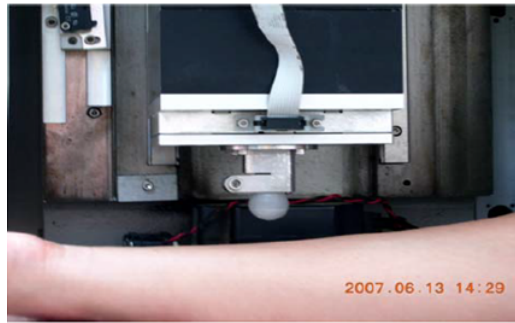
©2008 Elsevier, reprinted with permission.

Figure 2.4: Measurement of skin frictional properties by Tang et al. [45]

In[46], how the epidermal hydration affects the friction between human skin and textiles was investigated. Eleven males and eleven females rubbed their forearm against textile samples on a force plate using defined normal loads and friction measurements. The results showed there is a highly positive linear correlation between skin moisture and friction coefficient. No correlation was observed between moisture and elasticity, nor between elasticity and friction.

Another study on the effect of hydration on friction coefficient involved a method for measuring the friction coefficient between non-woven materials and the curved surface of the volar forearm. The measurement was tested on normal (dry) and over-hydrated volar forearms of five female volunteers [47, 48]. Straight and curved friction experiments had been carried out. The instruments are shown in Fig. 2.5. For the three non-woven polymer fibre material tested, the friction coefficient results varied in the ranges of about 0.3 to 0.5 when the skin of the participant's forearm was dry and 0.9 to 1.3 when the skin was wet.

A key to understanding human finger friction mechanism is to investigate the mechanical responses of a fingertip under a linear load. The vibrotactile sensation and tactile performance are believed to be strongly influenced by the non-linear and time-dependent properties of soft tissue [49]. Wu et al. [49]'s paper developed
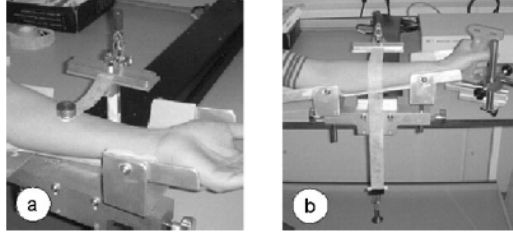
©2008 SAGE Publications, reprinted with permission.

Figure 2.5: Configurations for (a) straight and (b) curved friction experiments in Cottenden et al. [47]

a structural model of the fingertip incorporating its anatomical structure and the nonlinear and time-dependent properties of soft tissue. It proposed that surface deflection most occurs in the soft tissue of human fingertips. Researchers also think stratum corneum contributes a friction adhesion component which influences the overall skin friction behaviour. By realising in vivo tribological test with a tribometer (indentation and friction), the results showed principally an increase of the adhesion force between the probe and skin surface and a decrease of the lateral stiffness in absence of the stratum corneum [50] (removed in vivo by successive tape-stripping).
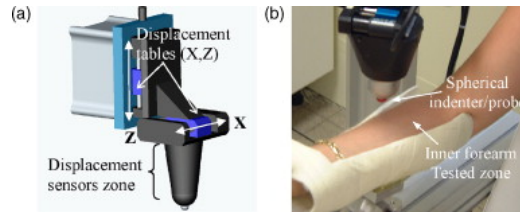
©2007 Elsevier, reprinted with permission.

Figure 2.6: Skin tribometer developed in Pailler-Mattei et al. [50]

However, in-vivo friction measurements are very much influenced by the environment and test conditions. The friction coefficient changes between subjects and with factors such as age and skin temperature [13]. For instrumentation and experiment design, there is a need to look into the literature to identify these confounding factors.

2.2 Artificial finger

Artificial finger specifically designed to be anthropomorphic in order to emulate human friction sensing capability or touch-feel is a relatively new field. The earliest design of artificial finger using elastic material began with Hanafusa and Asada [51];

the use of elastic materials was to enhance the gripping power of robotic hands or be compatible with various tactile sensors, rather than to emulate human friction sensing [52–54]. An early attempt for to develop an anthropomorphic artificial fingertip is shown in Fig.2.7 [55, 56]. The artificial finger was comprised of cover, filler and bone parts. The cover part was made of silicone rubber with a thickness of 1 mm; the filler part contained silicone rubber and silicone gel, and the bone was made of aluminium. The stiffness values of the artificial fingertip in unloading and loading condition have been analysed. The friction results show lower friction coefficients and larger normal forces compared to those of a human finger. The analysis and measurement of the softness of finger joint provided important guidelines for the future design of artificial fingers.
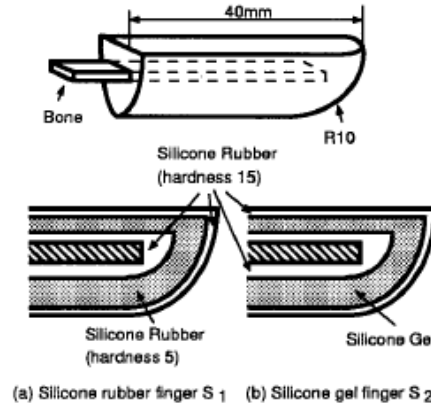
©1999 IEEE

Figure 2.7: The multilayered artificial fingertip designed by Han and Kawamura [55]

Wettels et al. [57] developed a tactile sensor array mimicking the mechanical properties and distributed touch receptors of human skin. The sensor array was not intended for friction characterisation, but was developed to be integrated into a robot in order to produce patterns of grip force that mimic those described in psychophysical experiments on human subjects. Later, Wettels, Fishel and Loeb [58] built an artificial finger called BioTac with a skin layer encapsulating a fluid filled rigid core. Changes in the impedance of the fluid due to deformation are picked up by impedance electrodes. The fluid also acts as a conduit for acoustic waves produced during sliding movement, which is then picked up by a built-in pressure sensor. The artificial finger was capable of measuring forces in multiple axes and hence allows friction coefficient measurement. It could also measure micro-vibrations patterns when stroking over a textured surface, as well as estimate the temperature
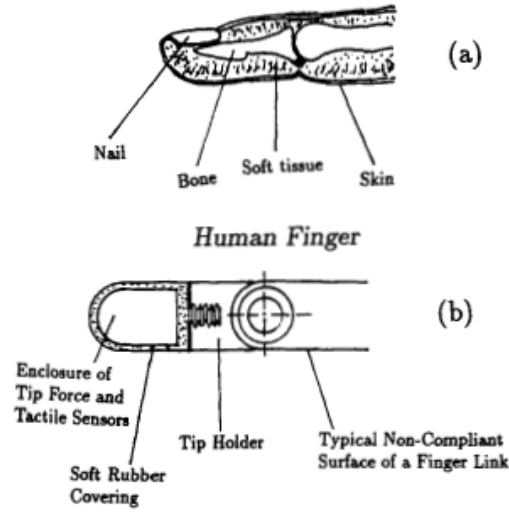
Figure 2.8: The comparison between a human finger and a robotic finger

of an object with a built-in thermistor.

An artificial fingertip with a viscoelastic core, skin with fingerprint surface has been constructed in Shao, Childs and Henson [5] and is shown in Fig. 2.9. Its objective was to mimic the structure, the shape, softness and friction properties of human fingertips. Their pure silicone artificial fingertip had different friction characteristics compared to a real fingertip—the pure silicone used was softer and deformed more under friction. However, when the softness of the artificial fingertip was made closer to real human fingertips, the frictional properties also became more similar to human fingertips. Based on [5], a multi-layered artificial finger construction with the softness of the fingertip as close to that of a human is desirable. The softness can be characterised by the surface mechanical parameters such as Young's modulus and Vickers hardness. To facilitate choosing the right material, these parameters should be known. Young's moduli of various part of human fingers (including plate, bone, soft tissue, epidermis and dermis) are provided in Shao et al. [59].

A multilayered 2D finite element (FE) fingertip model was created using the commercial software Abaqus by Shao et al. [59]. The results show that fingertip's epidermal ridges have little effect on stress distribution within the fingertip in static loading but significantly increase oscillations when sliding over a textured surface. In the case of sliding contacts, the existence or absence of epidermal ridges strongly affects the models' behaviours. FE modelling was able to give insights as to how microstructures on the skin may aid tactile perception.

Based on the above analyses, there are a few key aspects in the design of

Figure 2.9: The pure silicone artificial fingertip used in Shao, Childs and Henson [5]

artificial finger to better replicate the human finger friction characteristics. Firstly, the shape, size and the structure should resemble a human finger. Secondly, the 'softness' characterised by Young's modulus and Vickers hardness is important—the artificial fingertip should have a multilayer composite structure and suitable materials should be chosen with similar Young's modulus and hardness of each layer. To this end, a new artificial fingertip has been designed and documented in this thesis, details of which are shown in Chapter 3.

If the developed artificial fingertip can represent the real human fingertip friction, accurate friction coefficients can be obtained to link the touch feel perception. The next step is to understand the contact mechanism between the fingertip and the touched surface. In addition, better friction measurement instruments are reviewed.

2.3 Friction theory and measurement

A static elastic model of a hemispherical soft fingertip undergoing large contact deformation has been established in [60]. An elastic potential energy function based on virtual springs inside a hemispherical soft fingertip for the finger deformation has been formulated. The equations are functions of two variables: the maximum

displacement of the hemispherical fingertip and the orientation angle of a contact planar object. The elastic potential energy has a local minimum in the model.

In [61], it has been shown that for 'tactile friction', the friction coefficient cannot be considered a property of the skin alone, but depends on the whole system; it required a full understanding of the contact mechanics and the behaviour of human skin.

The friction force during contact between human skin and a counter surface is a combination of forces due to both adhesion and deformation [62–64].

$$F_{\text{f,adh}} = \pi * \tau_0 * (\frac{3R}{4E^*})^{2/3} * N^{2/3} \tag{2.1}$$

$$F_{\text{f,def}} = 0.17 * \beta_{\text{ve}} * (\frac{1}{R^2 * E^*})^{1/3} * N^{4/3} \tag{2.2}$$

$$\mu = \frac{F_{\text{f}}}{N} \tag{2.3}$$

where $F_{\text{f,i}}$ represents the respective friction forces, τ_0 is the shear strength of the interface, R is the reduced radius of the two contact bodies, β_{ve} is the visco-elastic hysteresis loss fraction, N is the applied normal load and E^* is the reduced Young's modulus. In the skin contact case, E^* depends solely on the properties of the skin.

By combining the equations above, the adhesion friction coefficient reduces with the increasing normal load N, while the deformation friction coefficient increases with increasing load [44]. More details are summarised in Chapter4.

$$\mu \propto C_{\text{adh}} * N^{-1/3} + C_{\text{def}} * N^{1/3} \tag{2.4}$$

Once an artificial finger has been designed, the next task is to measure the friction between the artificial fingertip and contacted surfaces. Generally speaking, the load force applied by people when they feel a surface is not larger than 2 newton [3, 65]. Because of this, a sensitive and accurate setup to measure the frictional force and the normal force is required. The friction measurement apparatus can either be custom-built or uses commercially available bespoke solutions; this section reviews a few of the setup used in the literature.

In Skedung et al. [11], friction was measured with a device shown in Fig. 2.10 that consists of a three-component piezoelectric force sensor (Kistler 9251A) with a charge amplifier (Kistler 5038A3). When moving the finger over the surface, the normal force and friction forces were recorded; the resultant tangential force or the friction force was divided by the normal force to obtain the friction coefficients using Amontons' laws of friction. The force transducer was fixed between two parallel steel plates and the paper samples were mounted on the top plate with double

sided adhesive tape. However, only paper samples were tested. A new measurement apparatus suitable for other material samples such as those used in car interiors is essential for the aim of this thesis.
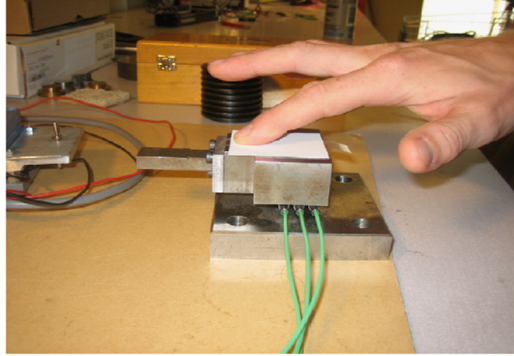
Figure 2.10: Finger friction measurement on printing paper from Skedung et al. [11]

Another paper describes the design, construction, and use of a multi-sensory measurement system for tactile sensation that can be used to evaluate the feel of different packaging materials [6]. This paper has demonstrated a new approach to quantifying touch perception of different surfaces using a multi-sensory measurement system. The experiments were conducted by sliding or pressing an artificial fingertip with embedded sensors against the surfaces of different samples which were fixed on a force table. The roughness, friction coefficients, compliance, and rate of change in the temperature were obtained. Forty volunteers were asked to touch and rate the samples by filling in questionnaires about how they felt. A multi-regression analysis was performed to examine the relationship and strong correlations were found between subject's feelings and the physical measurements. Although the types of samples may have limited the application, the results show very promising correlations between tactile perception and the measured surface parameters.

[66] detailed a set-up based on a balanced loading arm supported on a variable velocity stage, where a human finger pad would rub against a small selection of solid materials with a range of sliding velocities (from $1\,\mathrm{mm\,s^{-1}}$ to $100\,\mathrm{mm\,s^{-1}}$) at a fixed normal load ($0.2\,\mathrm{N}$). The measurement apparatus is shown in Fig. 2.11. The frictional force was measured using a strain-gauged double cantilever transducer. The friction coefficients measured were in the range from 0.2 for filter paper to 4 for smooth glass.

A friction measurement apparatus design had been proposed in [61]. The apparatus uses strain-gauged flexure element technology. Measurement of the vertical force was made using three strain-gauged flexure couples. The schematic diagram is
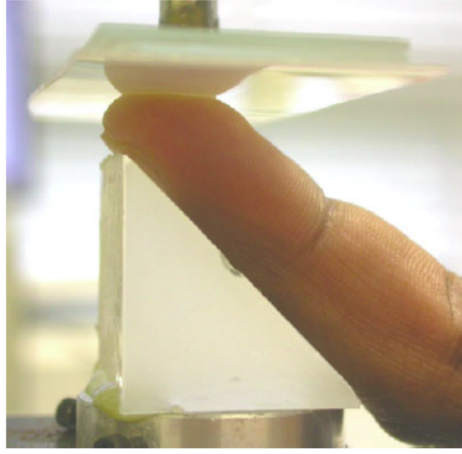
Figure 2.11: The orientation of the index finger and the counter-surface in the tribological experiments

shown in Fig. 2.12. The normal load was applied in experiments between about $2\,\text{N}$ to $20\,\text{N}$. It was found that human finger resulted in higher friction coefficient than using a rubber probe or a steel probe.
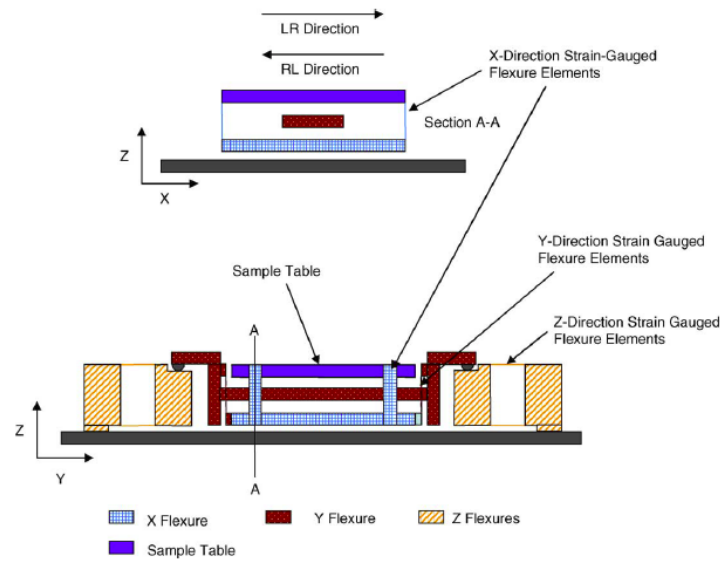
©2005 Elsevier, reprinted with permission.

Figure 2.12: Schematic diagram of soft metrology friction test system in [61]

Another approach is using a commercial load cell to measure the friction such as [9]. The ATI force transducer measures the forces with six degrees of freedom. The normal force(z-direction) and the two forces in the tangential or xy-plane were

measured. The resolution of the force measurements is 25 mN in the normal direction and 12.5 mN in the tangential direction.

2.4 Relationship analysis between friction and surface physical parameters

Since the objective of the thesis is to link the human touch-feel perception and the various surface physical parameters of the material, and that friction is the most direct property a human finger experiences, the relationship between friction and surface physical parameters need to be identified.

Surface topographical parameter R_a gives an overall summary of height variations, however, it does not give any information on waviness and it is insensitive to small height changes. R_q gives more information about height variations, but it still does not give a satisfactory description of the surface roughness. R_{sk} is the skewness and is sensitive to deep valleys and high peaks. Zero skewness reflects in symmetrical height distribution; positive skewness occur when a surface has high peaks or filled valleys; negative skewness describes surfaces with deep scratches or lack of peaks. R_{ku} is the kurtosis which measures the sharpness of both peaks and valley. R_{ku} is less than 3 when surfaces have relatively smooth peaks and valleys, while R_{ku} is more than 3 for surfaces with relatively sharp peaks and narrow valleys [67].

Skin friction appears to dependent on several factors such as age, anatomical site and skin hydration. In addition, the choice of the probe and the test apparatus will also influence the measurement. Differences in probe material, geometry and smoothness affect friction coefficient measurements. An increase in skin hydration, either through water or moisturiser application, increases its friction coefficient; whereas a decrease in skin hydration, either through clinical dermatitis or through alcohol addition, decrease the coefficient [3, 43, 44, 46, 47, 66]. Differences are present between anatomical sites. Conflicting results are found regarding age and no differences are apparent as a result of gender or race [68].

In van Kuilenburg et al. [10], four different surface structures of metal and polymer were made with picosecond laser pulses. The four different surface textures were composed of two different radii and two different spacings. Sliding friction was measured in-vivo against the human skin. van Kuilenburg et al. [10] found that the friction coefficient decreased strongly with the increase of the normal loads. In addition, the adhesion friction is the dominant friction mechanism.

2.4. Relationship analysis between friction and surface physical parameters

Four types of surface textured (produced on `080 M40 (E80)` steel plates) have been dry grinned against dry emery paper in Menezesa, Kishorea and Kailasb [69]. The correlation between friction and surface topography parameters has been analysed in lubricated conditions. The results are shown in the Fig. 2.13. It was calculated using the variance method as it was suggested that the variation method was substantially more accurate than the other methods. It had been observed that for a given kind of surface texture, the coefficient of friction did not vary with R_a. However, the mean slope of the profile, δ_a was found to explain the friction variations best. The coefficient of friction depends on δ_a values irrespective of surface textures. The coefficient of friction primarily depends on the mean slope of the profile. The slope of the asperities can be used to predict boundary friction. It was concluded that friction coefficient decreases as the asperity slope of the harder surface decreases [70]. The lower value of δ_a causes lower stresses and corresponding ploughing component of friction results in a mild shear failure and lower material transfer. The theoretical analyses of the influence of surface roughness on the adhesion of elastic solids suggest that the introduction of roughness should reduce the adhesion to an extent governed by an adhesion parameter [71].

The friction coefficient in dry conditions depends on the real area of contact and the shear strength of the materials due to adhesion and two-three body deformation [3]. The real contact area depends on the surface topography and elastic modulus for elastic contact, and on the hardness for plastic contact. In the presence of a liquid film, the measured value of the friction coefficient is different from the dry friction due to the meniscus contribution. The coefficients of friction during two-body deformation depends on the average slope of the rough surface. The average slope is scale dependent due to the scale dependence of the standard deviation of the surface heights and the correlation length. As a result, the two-body deformation component of the coefficient of friction increases with decreasing scale. The contact area for particles decreases with decreasing scale because, for smaller average contact sizes, the probability particles with a certain size distribution to be trapped at the contact decreases [72].

For random surfaces, the low value of the slope will lead to lower stresses and corresponding ploughing component of friction results in a mild shear failure and lower material transfer [70].

In most cases, the influence of surface physical parameters such as R_a, R_q and E to the friction coefficient can be calculated according to Hertz contact theory (elastic). In most contact models, surface height distribution is assumed to follow a Gaussian distribution. However, most engineering surfaces are frequently non-

(a) dry condition

(b) lubricated conditions

Figure 2.13: Correlation coefficient between coefficient of friction and roughness parameters under (a)dry and (b)lubricated conditions. White and black bars represent positive and negative correlations, respectively

gaussian with the degree of non-gaussianity dependent upon materials and surface finishing process used. A positive skewness value and a kurtosis value of at least 3 or greater substantially lowers the real area of contact, meniscus force, and sensitivity of film thickness to static friction [73].

Compared with the Gaussian distribution ($R_{sk} = 3, R_{ku} = 0$), surfaces with a higher R_{ku} value and a positive R_{sk} value should be result in a lower static friction coefficient demonstrated in the dry contact model of Michalski and Pawlus [74]. At high R_{ku} values, the static friction coefficient will decrease with the reduced load, while higher R_{sk} values would result in an increased static friction coefficient [75]. [76] found an increased contact area, static friction coefficient decreased by a factor of about 6 when R_{ku} increased from 2 to 10. The maximum pressure, the area and load rotations increase when R_{ku} increases [77]. In dry sliding, surface with a positive R_{sk} should show good adhesion resistance. Positive R_{sk} values lead to a greater real contact area and large numbers of peaks in the contact, with tangential and adhesion forces more similar to a Gaussian distribution. On the contrary, a negative R_{sk} leads to lower values and larger deviations from the Gaussian distribution [78].

2.5 Correlation study between touch-feel perception and surface properties

As Katz [79] pointed out, "In touching, one brings object properties to life, creating through one's muscular activity such qualities as roughness and smoothness, and hardness and softness", and "Eye movements do not create colour the way finger movements create touch". The movement of the fingertip across a surface plays an

important part in the perception of surface roughness/smoothness, high/low friction and to a lesser extent, surface hardness.[79]. Finally, Katz concluded that the 'feel' of a surface is a summation of the perception through the fingertips of the warmth/coolness, roughness/smoothness, hardness/softness and slipperiness/stickness of the surface. The theory and initial investigations are detailed in [80].

Tactile information may be transferred by compressing, stretching, vibrating, changing the temperature of the skin surface [81]. The tactile sensation can be an important cue to any user-interface and as methods of producing tactile simulation mature, the tactile technology has become more widespread [82, 83].

There are growing interests in the automotive industries application for quantifying the touch feel perception studies. Better car interior materials can be made to meet the personal preferences of the customers. In the previous work of our group, ten specimens with materials ranging from natural wood, leather to engineered plastics and metal were selected for investigation. It is aimed to understand what properties matter and to what extent the different factors weight the human perception. A group of untrained people were asked to rank the sample surfaces in terms of smooth/rough, soft/hard, slippery/grippy, warm-cold and like/dislike. In addition, surface topography, friction, Young's modulus and hardness of the samples were measured by an instrument called the tribological probe microscope (TPM), which through point-by-point scanning [2]. Cross correlation between function had been established. The results showed that the human touch perception may be influenced by the nano-micro surface structure [2, 84].

Toyota Motor has been described a study in the subjective assessment of seven paint finishes on smooth ABS panels in Kawazu et al. [85]. The assessed samples include 5 soft-feel finishes with intentionally different tactile properties, 2 with conventional 'hard' finishes, and 8 without paint finishes. They proposed a hypothetical equation for soft-feel (S_0) by giving weights a, b, c, d to each of the four sensory modes of: 'Moist/Dry','Smooth/Rough','Warm/Cool' and 'Soft/Hard', as in

$$S_0 = a(\text{Moist/Dry}) + b(\text{Smooth/Rough}) + c(\text{Warm/Cool}) + d(\text{Soft/Hard}) \quad (2.5)$$

Multivariate and multiple regression analysis of the results using the 'soft-feel' score as the object variable and the four other sensory factors as the explanatory variables gave partial regression coefficients of

$$S_0 = 0.13(\text{Moist/Dry}) + 0.03(\text{Smooth/Rough}) + 0.11(\text{Warm/Cool}) + 0.68(\text{Soft/Hard}) \tag{2.6}$$

The results showed that for soft-feel paints, 'Soft/Hard' and 'Moist/Dry' are the

dominant perceptions while 'Smooth/Rough' perception was not significant. The 'Warm/Cool' dimension was significant with warm materials perceived as being soft.

In a touch-feel perception study by Skedung et al. [11], 25 undergraduates students including 10 females and 15 males were asked to touch and rate several different coated paper and uncoated paper samples. They are allowed to arbitrarily create their own scoring scale from the first sample. For example, if the second sample was perceived to be twice as coarse as the first sample, then its assigned score should be doubled. The aim was to investigate if and how perceived coarseness is linked to physical roughness and friction. The experiment results showed that both the roughness parameter and the finger friction can be related to perceived coarseness, where group data show that perceived coarseness increase with increasing roughness. The research showed clearly that smoother papers have higher finger friction than rougher papers [11].

Correlation and regression analyses were carried out to investigate the relationships between subject's responses and the physical measurement in Chen et al. [7]. Thirty-seven tactile textures including 22 cardboards, 9 flexible materials and 6 laminate boards were tested. The author performed 4 physical measurements on surface roughness, compliance, friction and the rate of cooling of an artificial finger when samples were touched. On the other hand, 18 participants (12 males and 6 females, aged 20 to 60) completed questionnaires to rank the material samples against six word pairs: warm-cold, slippery-sticky, smooth-rough, hard-soft, bumpy-flat and wet-dry. The pairs of words were separated on a twenty point scale from -10 to 10. The results show that touch-feel perception is often associated with more than one physical property, and the strength and form of the combined contribution can be represented by a regression model.

Barnes et al. [14] performed multivariate statistical analysis of self-report data to measure how roughness affects a person's feeling when the person believes the material sample (glass) was intended to be used in cosmetics packaging. The conclusion from principal component and cluster analyses was that when the surface is less rough than a fingertip, it generates desirable feelings. On the other hand, when the surface is rougher than a fingertip, it generates undesirable ones.

In Elkharraz et al. [86], Twenty-four tactile plagues were manufactured and the textural features of the plaques' topographies were extracted using the most common statistical analysis techniques used in machine vision. One hundred and seven participants were asked to touch and rate the plagues against a set of 20 adjectives in a psychological experiment. And the words were presented on a seven-point bi-polar scale. Then partial least squares regression based on genetic algorithm

(PLSRGA) and wrapper methodology were used to find out the most important computational textural features. The results identify a subset of features that appear to have the most important effect on human touch feeling. These results will be used to synthesise plaques with the required human touch feeling features.

In Childs and Benson [13], Several people stroked their fingers over 16 different patterned polyester sheets. The patterns were arrays of bumps or pockets with different pitch and percentage coverage of ink. They were asked to report their feelings in terms of 15 pre-chosen word pairs, ranging from psycho-physical smooth-coarse to the more impressionable or affective artificial-natural and happy-sad. Sliding friction was measured about the samples. The apparent contact area between a fingertip and a flat surface had been measured through the paper sheet ink as a function of load. The area was circular. At loads up to $2\,\mathrm{N}$, the contact diameter increased with load to the power of 0.2. Analysis of the self-report experimental data has shown that almost 80% of the variance of feelings that people had on touching the printed surfaces could be described within a two-dimensional semantic space. The results showed that the human touch-feel perception depends on a surface's roughness and also on the sliding friction coefficient.

Thirty-seven material samples were reported in Chen et al. [8] with their physical parameters such as samples roughness, compliance, sliding friction and thermal contact properties measured. Psychophysical and affective judgements were requested from subjects, such as how pleasurable, exciting, indulgent, the samples felt to touch. The relationship between the Psychophysical and affective judgement and the physical measurement was explored by using principle component analysis and Pearson correlation analysis. However, further work was needed on how to quantify some aspects of surface properties, particularly of roughness and sliding friction.

2.6   Summary

This chapter summarised the literature on various topics according to the whole thesis cue. For human skin friction, the typical touch-feel process and several human skin friction measurement and simulation studies have been introduced. For artificial fingertip design and friction measurement, several types of research have been carried out with respect to size and material properties. With guidance from literature, a multilayered artificial finger has been developed in this thesis.

If the links between friction coefficients, surface physical parameters and touch-feel perception can be identified, designer and material scientists would be

able to easily design products that satisfies customer's touch-feel requirement. At the moment in literature, the relationships are not obvious and are very system-dependent.

Instrument Design

T HIS chapter describes an investigation into a new design of friction test apparatus with an artificial fingertip. In order to mimic a human finger stroking on surfaces, a special friction apparatus consisting of an artificial fingertip, a linear flexure mechanism and a reciprocal stage was developed. The apparatus measures normal forces and friction forces simultaneously. The detailed design, as well as the calibration of the friction test rig, are discussed. Experiments were carried out to measure surface friction coefficients of aluminium and steel with different roughness, under different contact forces and different stroking speeds. Comparison between human finger friction and artificial finger friction are made. The friction measurement results demonstrate that the designed artificial finger can be used to represent the real human fingertip for friction tests.

3.1   Introduction

Touch-feel perception has been investigated in cosmetic and clinical studies. It has been found that a target surface that is less rough than a fingertip is more pleasant to touch or stroke [14], but it is unclear what other factors are involved. Commercially, products are increasingly focused on ergonomics and there is increasing demand for surface materials with desirable touch-feel properties [20]. Touch-feel perception is influenced by human skin friction, which in turn is influenced by many factors such as skin moisture, age, temperature, anatomical site [13]. Hence, it is not a surprise that development of an artificial fingertip that mimics a human's fingertip in quantifying touch-feel perception has been very challenging [87]. To objectively quantify touch-feel perception, therefore it is important to build artificial finger measurement devices

with structural and mechanical properties resembling real human fingers. The aim of the present study is to construct an artificial fingertip mimicking the structure, the shape, softness and friction properties of human fingertips for studies of tactile measurements and to aid product design.

Previous research involving quantifying perception of touch feeling had been conducted, for example, on car interior components using the tribological probe microscope (TPM) [17–19]. The TPM however, cannot replicate the same measurement conditions a human finger experiences, e.g. the stroking motion, and does not have the same mechanical properties of a human fingertip. To this end, this thesis combines idea from four areas of research, introduced in the following paragraph, to develop an anthropomorphic artificial finger and fingertip assembly.

Shimoga and Goldenberg [88] reported a multiple layer artificial fingertip model which has an external elastic cover and gel for the filler material. Phillips, Johansson and Johnson [89] proposed 'continuum' fingertip virtual models where the skin and subcutaneous tissues were represented by homogeneous, isotropic, and incompressible elastic media. The continuum fingertip models predict the stress and strain distributions within the tissues, and thus the response profiles of the receptors within the skin tissue. Derler, Schrade and Gerhardt [12] introduced a polyurethane coated polyamide fleece with a surface structure similar to that of human skin. Its properties are most similar with human skin under dry conditions. Shao et al. [59] developed two-dimensional finite element (FE) models of fingertips, which included the most important anatomical structures: soft tissue, nail, and bone. The skin was considered as hyper elastic and viscous, and the subcutaneous tissue was modelled using a sponge-like media. Guided by Young's modulus analysis and FE modelling of human fingertips, materials for artificial fingertip can be chosen to have a comparable stiffness to human fingertips [5, 6].

The artificial finger and fingertip assembly were mounted on an improved version of the friction test rig previously used by our research group [4, 32]. To test the apparatus, twelve aluminium samples and five steel samples were tested and comparison was made between the friction profile of human fingertip measured in-vivo and that of the artificial fingertip. Further, the new artificial fingertip was compared to a silicone cover previously used by the group [32].

3.2   Design of friction test rig

The apparatus consists of two major parts: an artificial finger and a friction test rig which are described in detailed in the following sections.

First, in order to better illustrate the subcomponents of the friction apparatus, the parts were drawn using SOLIDWORKS computer aided design (CAD) software, shown in Fig. 3.1 and Fig. 3.2. In the figures, different components are displayed in different colour. Refer to Appendix A.1 for the complete set of drawings for the design.
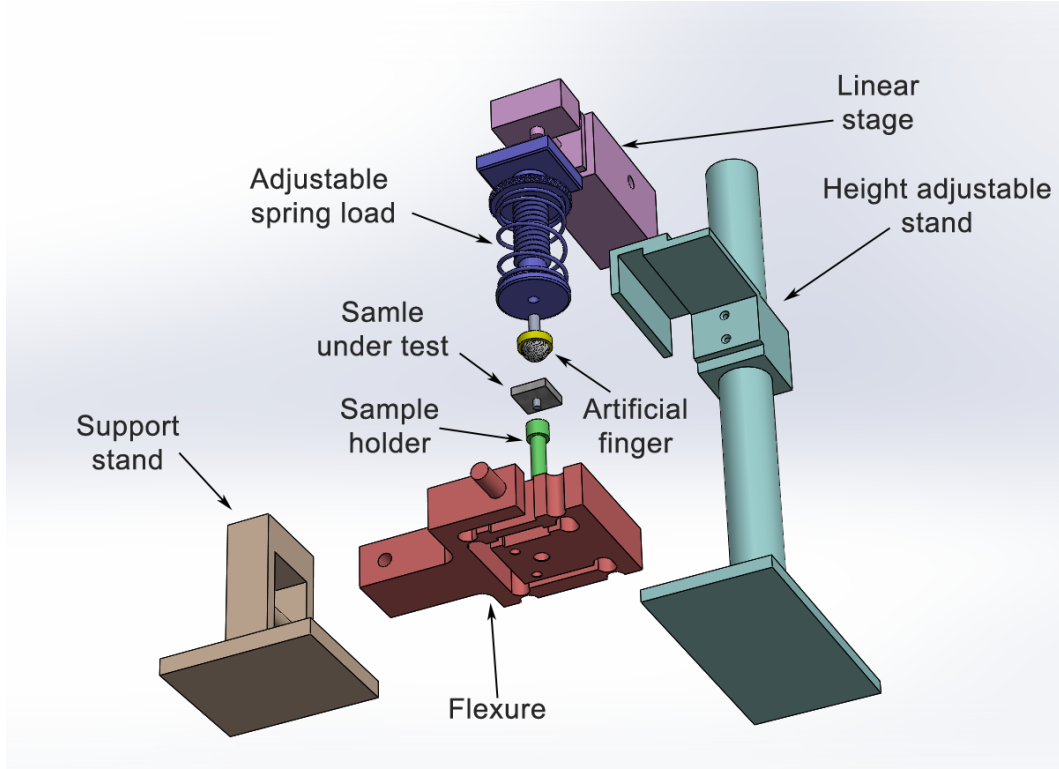
Figure 3.1: Exploded view of the whole apparatus in SolidWorks from below

3.2.1 Construction of the multilayer artificial fingertip

Table 3.1: Mechanical properties of the fingertip model in Shao et al. [59]

Part	Young's modulus (MPa)	Poisson's ratio
Bone	17000	0.3
Soft tissue	0.024	0.4
Epidermis	0.08	0.48
Dermis	0.05	0.48
Nail	170	0.3

30
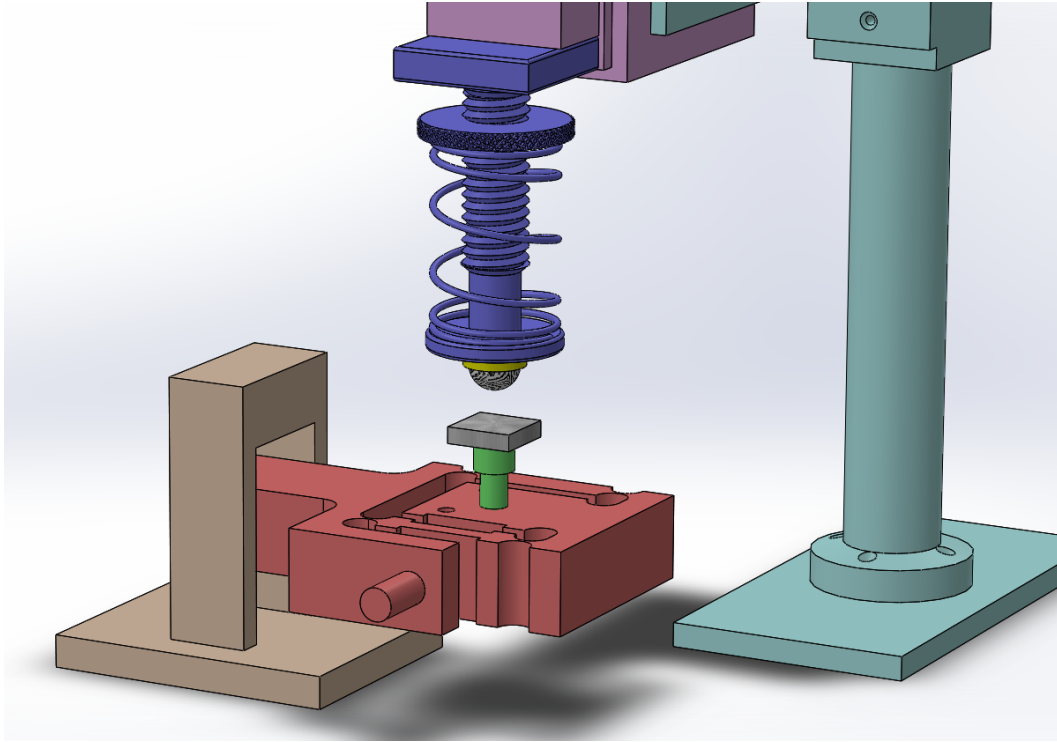
Figure 3.2: Unexploded view of the apparatus in SolidWorks
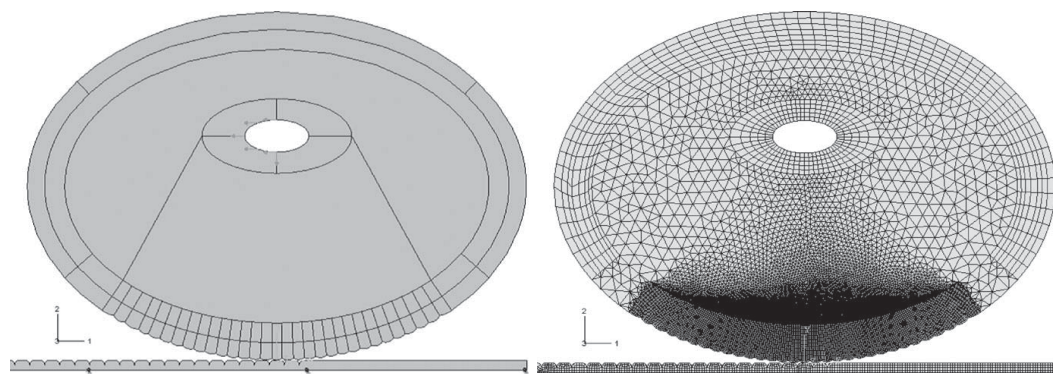
(a) Structure view   (b) Mesh view

©2009 Elsevier, reprinted with permission from Shao et al. [59]

Figure 3.3: FE model of the fingertip

31

The basic structure of human skin consists of the epidermis as the surface layer, beneath which there is the dermis, followed by the subcutaneous and the bone. As shown in Fig. 3.3, Shao et al. [59] developed a finite element model of a human fingertip, and Table 3.1 shows the mechanical properties of each part used in their model. These values were used as a guideline to select the materials to make the artificial finger introduced in this work.

The artificial fingertip has a multilayered construction comprising of the cover layer, the filler layer and an internal bone support structure. The fingertip has a diameter of 15 mm, typical size of a human index finger [90]. To mimic the stiffness (Young's modulus) of the epidermis of a human fingertip, the cover layer was made from 1 mm thick silicone rubber *RTV139* (hardness: Shore A 23-33 cured with *catalyst 148*); the thickness is comparable to that of the epidermis of an index finger at 250 µm [91]. Similarly, mimicking the dermis layer of a human fingertip, the filler part was made from 3 mm thick silicone rubber *RTV 135* (hardness: Shore A 13-17, cured with *catalyst 135*). Lastly, the internal bone structure was made of aluminium with a thickness of 2.5 mm and was slotted into a supporting base. The details are shown in Fig. 3.4.

Figure 3.4: The multi-layer artificial fingertip (a) side view (b) top view with a diameter of 15 mm

3.2.2 Fingerprint imprint on the artificial finger

A fingerprint sample was taken from a technician with his consent by imprinting it onto wax. The surface parameters of the fingertip of the technician were measured in vivo using a Taylor Hobson *Form Talysurf* surface profilometer, along the longitudinal

axis of the finger. The results are listed on Table 3.2, from which one can see the mean spacing successive ridge and valley were approximately $S_{\mathrm{m}} = 0.5\,\mathrm{mm}$. The wax was pressed onto the cover layer of the artificial fingertip during the curing stage in order to transfer the fingerprint pattern. The realistic surface contour of the resulting artificial fingerprint serves to replicate the friction characteristics of a real human fingertip.

Table 3.2: Fingerprint surface topographical and mechanical parameters measured by Form Talysurf surface profilmeter

The fingertip surface	R_{a}(µm)	R_{q}(µm)	R_{sk}	R_{ku}	S_{m}(µm)	S_{dq}
Topography	44.824	49.822	-0.1	1.6	488.295	47.26
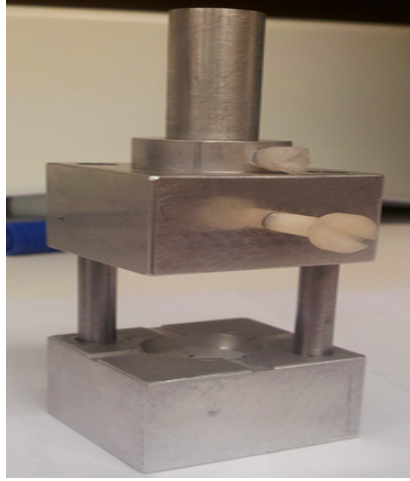
Figure 3.5: The press used to imprint the fingerprint on the artificial fingertip

3.2.3 Friction test rig

The friction test rig is shown in Fig. 3.6, which consists of the artificial finger support structure fixed to a linear stage. The height of the whole structure is adjustable to accommodate a large range of thickness of the material samples. The flexible design of the friction test rig has several advantages over previous designs [4, 32]: firstly, the adjustable spring load provides a continuous fine tuning mechanism for application of a constant normal force; secondly, the simplicity of the single moving part design means minimal calibration is required; and finally, the linear stage provides a repeatable and programmable reciprocating motion.
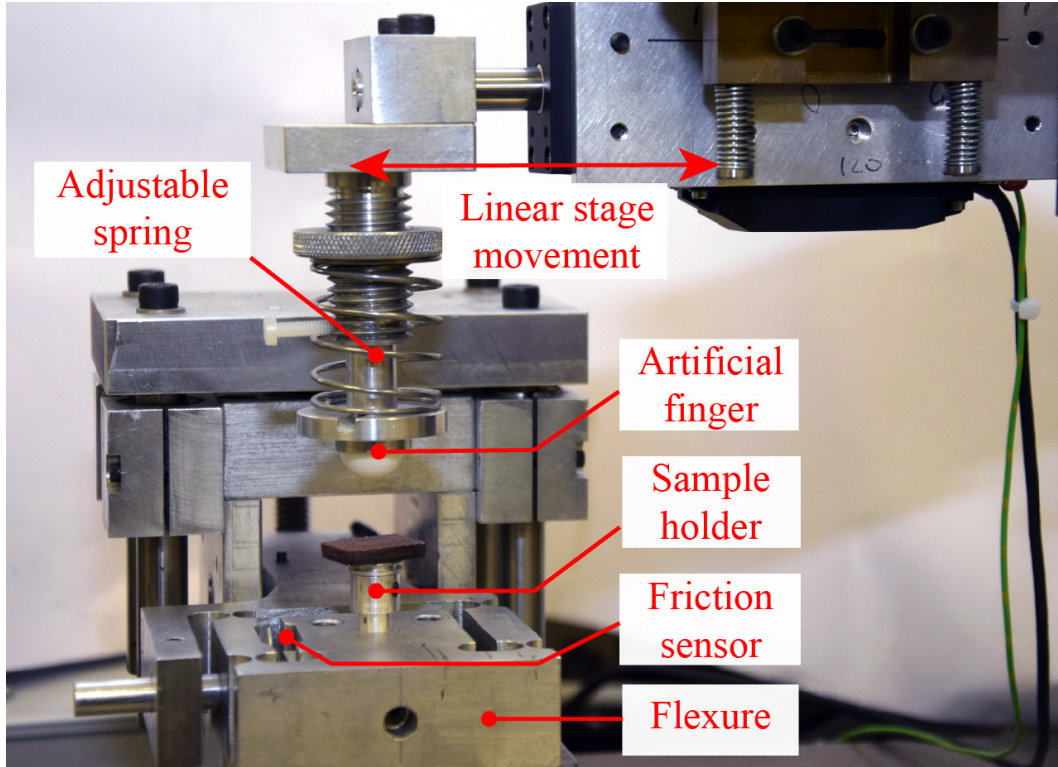
Figure 3.6: Photo of the friction test apparatus with labelled parts

Linear stage mechanism

To simulate the reciprocating human fingertip movement, a programmable linear stage was utilised, comprising of a Physik Instrumente *PI M-272.2c* ultrasonic piezomotor driven by a *C-867.OE* motion controller. This linear stage improved upon the roller mechanism reported previously [4]. It moves the artificial finger back and forth can provide a stroking velocity up to a maximum of $150\,\mathrm{mm\,s^{-1}}$. It was programmed in LabVIEW software running on a computer, which interfaces directly with the *C-867.OE* motion controller. Once programmed, the linear stage generates accurate ($\pm 0.9\,\mathrm{\mu m}$) and consistent reciprocating motion (bidirectional repeatability $< 3\,\mathrm{\mu m}$) [92].

Damped artificial finger support structure with adjustable spring

The artificial finger support structure has an adjustable spring which can be used to finely control the constant loading force exerted by the artificial fingertip on the material sample. The structure also contains a damper arrangement which will help to dampen down any vertical vibrations during operation of the linear stage.

Flexure and sample holder
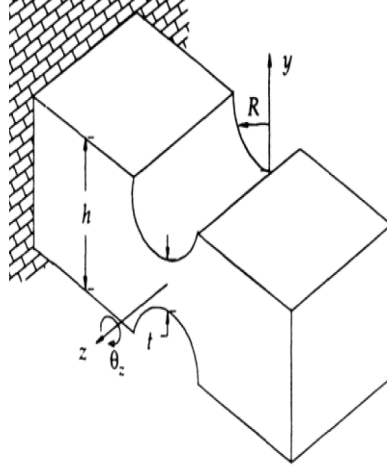
Figure 3.7: The notch hinge structure

A notch type flexure [93, see Fig. 3.7] incorporating a capacitive sensor was used to measure the friction force. The notch acts as an elastic rotary bearing [94], allowing deflection tangentially. It works on the basis of the mechanical principle that a force applied to an elastic element produces a measurable deflection [95]. The advantages of flexure are 1) it gives a linear output relationship between the applied force and the measured deflection, and 2) it is insensitive to forces which are not aligned with the principal axis of the sensing elements. 3) displacement output is easy to measure with high accuracy, despite being small in magnitude. The force for a given deflection is dependent upon the elastic modulus of the flexure, and the effective stiffness of a flexure system is reduced by the presence of externally applied loads, hence it is important to verify the contact force working range to make sure the flexure does not over-deform as to affect the effective stiffness. The calculation is shown in Appendix A.2 [96–98].

The flexure used in the friction test apparatus may be considered as a simple linear spring mechanism. The parameters for each notch is defined as $t = 1\,\text{mm}$, $R = 5\,\text{mm}$, $b = 25\,\text{mm}$, $h = 11\,\text{mm}$ and $L = 15\,\text{mm}$, with respect to Fig. 3.7.

For flexure hinge design, compliance is the most important parameter, and it can be calculated based on the bending theory of Euler-Bernoulli beam. A simple linear spring has four notches. The accuracy of the spring flexure is primarily dependent upon the accuracy of the centre of the holes, with the materials removed from the rest of the original blank being of little influence.

| (a) sample holder | (b) Load cell | (c) Capacitive Sensor |

Figure 3.8: Capacitive sensor, load cell and the sample holder

3.3 Calibration and testing of the friction measurement apparatus

3.3.1 Calibration of the flexure

To calibrate the flexure mechanism for friction measurement, the stiffness of the load region should be measured. The flexure was mounted vertically and precision weights were placed on the top of the flexure. Its displacement was measured by a Taylor Hobson *Form Talysurf* surface profilometer. The results are shown in A.2.2. The stiffness of the flexure was measured to be $33.5\,\mathrm{kN\,m^{-1}}$.

The mass of the 'moving part' of the flexure (the blue region shown in Fig. 3.9a) is estimated by SolidWorks to be $227.42\,\mathrm{g}$, with a volume of $87\,450\,\mathrm{cm^3}$. Fig. 3.9a shows the deflection of the flexure under a load in the direction of the purple arrows using FEA analysis; the blue region experiences the most deflection, about $0.56\,\mathrm{mm}$ under a load of $10\,\mathrm{N}$. FEA modal analysis was also performed and the natural frequency of the flexure was found to be $61.08\,\mathrm{Hz}$.

3.3.2 Calibration of the capacitive sensor and the load cell

In the design of friction test apparatus, a load cell (*XLF212R Miniature*, Measurement Specialities Inc.) was fixed under the flexure (see Fig. 3.8b). Then, a sample holder was fixed above it (see Fig. 3.8a) to measure the normal forces pressed to the samples. The load cell has a temperature compensation module integrated into the output cable. Unlike sensors with flat forces application surfaces, the XLF212R incorporates a spherical load button, which results in more precise point loading application

(a) FEA analysis of the flexure   (b) Stiffness calibration of the flexure

Figure 3.9: FEA analysis and experimental calibration of the flexure

and measurement accuracy. Likewise, the sample holder also has a steel ball at the contact point to make sure normal forces would be focused on this point.

The load cell has a range of 10 N, but was calibrated up to 2 N including the weight of the sample holder by putting standard weights from 0 g to 150 g on the sample holder. This range covers the normal force that human fingers exert and coincides with suggestions in skin tribology studies of about 0 N to 1.5 N. As shown in Fig. 3.10a, the output of load cell gives a sensitivity of $1.371\,\mathrm{V\,N^{-1}}$, with an amplification of 100 in the conditioning circuit.

The capacitive sensor, shown in Fig. 3.8c, is used for friction force measurement by sensing the deformation of the flexure. A suitable distance between two pieces of the capacitive sensor is very important because high sensitivity and high accuracy are essential for reliable friction coefficient measurement. The sensor was calibrated using standard weights. The flexure was vertically placed and the weights were set on top of one arm, while the output of the capacitive sensor was monitored. It is shown in Fig. 3.10b. The capacitive sensor output voltage is proportional to the normal force with a sensitivity of about $0.9276\,\mathrm{V\,N^{-1}}$, with the root mean square of noise equivalent to 1.2 mN.

3.3.3 Testing the friction measurement apparatus

Different stroking speeds and distances can be set up in the PI measurement software. The load cell and the capacitive sensor configurations were controlled by a LabVIEW-based software system which operated on the PC installed with a data acquisition card, as shown in Fig. 3.11. The software interface was designed to display the real-time measurements of the normal force and the friction force based on the

(a) Load Cell
(b) Capacitive Sensor
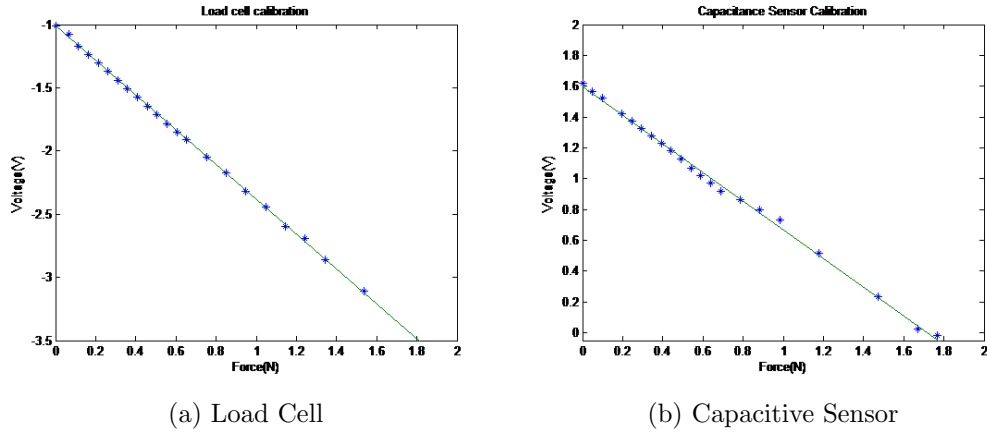
Figure 3.10: Calibration of the load cell and the capacitive sensor
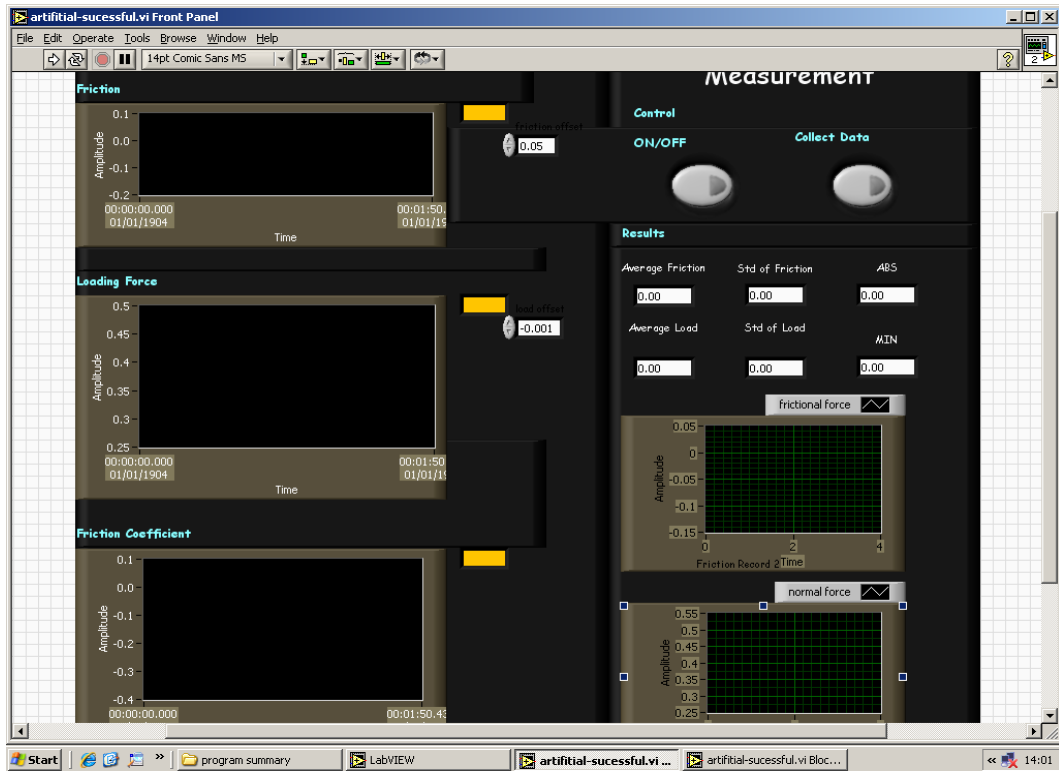
Figure 3.11: Software panel

acquisition from outputs of the sensors and its own calibration coefficients, which is detailed in appendix. The operation software system can be described as follows:

a) Setting: The sampling rate can be set manually. Also the stroking speed and stroking distance can be set manually in different measurement conditions. Because the natural frequency of the flexure is 61.08 Hz, the sampling fre-

38

quency should be at least the same or higher as twice of the natural frequency according to sampling theory. 1000 Hz was selected during the whole friction measurement.

b) Real-time Display: Including real-time graphs of friction force, normal force and the dynamic friction coefficient (the ratio of real time friction to normal force); the offset of both can be adjusted in the control box of the LabVIEW Software.

c) Recording & Data Processing: When 'Collect Data' button is clicked, the recording process starts with Direct Memory Allocation(DMA) mode triggered, while the real-time display screen would stop. Then the time average friction force and normal force as well as friction coefficient, would be displayed in the indicators of the red framed box, as shown in Fig. 3.11.

Signal to noise analysis

Signal-to-noise ratio (SNR) analysis was performed during calibration of the instruments. SNR is defined as the ratio of signal power to the noise power, often expressed in decibels. A ratio higher than 1:1 (greater than 0 dB) indicates more power in information than noise.

$$SNR = \frac{P_{\text{signal}}}{P_{\text{noise}}} = \left(\frac{A_{\text{signal}}}{A_{\text{noise}}}\right)^2 \tag{3.1}$$
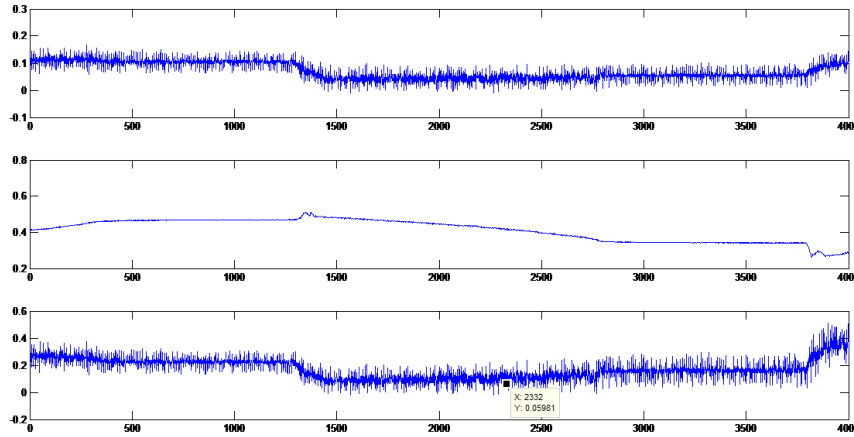
Figure 3.12: One of the measurement taken during SNR analysis

The aluminium sample AM5 was arbitrarily chosen to experimentally measure the SNR of the friction measurement rig. The sampling frequency of DAQ acquisition card was 1000 Hz. The measurement record was chosen to be 40 seconds. The output signals of both load cell (for normal force) and capacitive sensor (for friction force) during static and sliding working conditions were measured: Firstly, the background noise level was measured while the apparatus was idling. Secondly, a contact force and a stroking motion were applied to the AM5 sample (e.g. see Fig. 3.12). Using (3.1), both SNRs of friction force and normal force were determined.
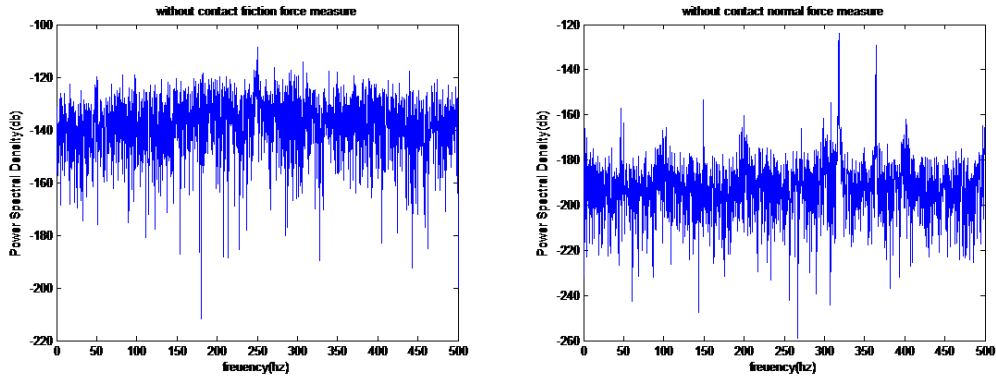
(a) Noise PSD (under no force) on the capacitance sensor (friction force sensor)

(b) Noise PSD (under no load) on the load cell (normal force sensor)

Figure 3.13: Power spectral density (PSD) of sensor outputs when there is no operation
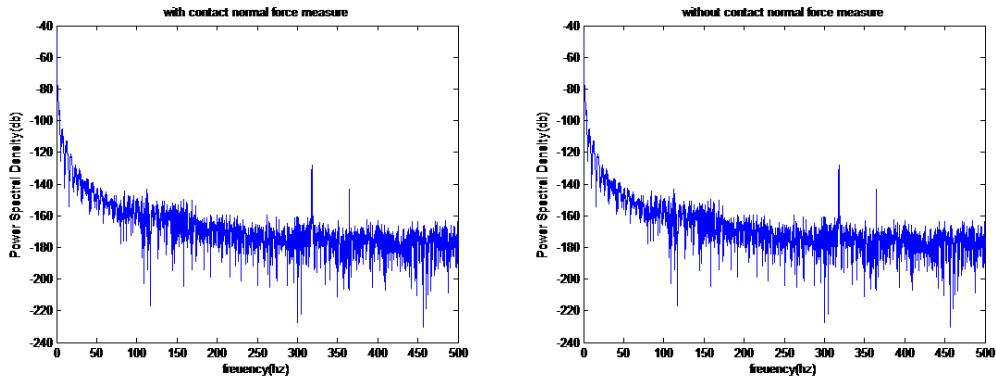
(a) PSD of the signal on the capacitance sensor (friction force sensor)

(b) PSD of the signal on the load cell (normal force sensor))

Figure 3.14: Power spectral density (PSD) of sensor outputs during measurement under normal load and friction

While the friction force measurement in Fig. 3.12 appear noisy at first glance—to the contrary, those are high-frequency signal components due to the surface roughness of the sample being measured. The SNR is considered by comparing the power of the signal during measurement versus the power of the background noise when the sensors were subjected to no inputs. As shown in Fig. 3.13, without physical contact, the average power spectral density (PSD) of the capacitance sensor signal was about -195 dB and the average PSD of the capacitance sensor signal was about -140 dB. In contrast, the average PSD of the output signals were shown in Fig. 3.14 when the normal force was 0.5 N. By averaging over the spectrum, the load cell had an SNR of about 32 dB and the capacitive sensor had an SNR of about 18 dB. However, because the friction test apparatus is a low frequency device, the higher frequencies can be filtered out and only frequencies from 0 Hz to 10 Hz were considered for SNR calculation. The load cell had an SNR of about 49.7 dB and the capacitive sensor had an SNR of about 33.3 dB.

Static friction measurement was also performed and the instruments had a very low bias ($< 4\%$). In order to set the optimal working conditions for friction measurements, different contact forces, different stroking distances and different stroking speeds were tried. The contact force was applied from 0.35 N to 2.5 N, the stroking distance was tried from 2 mm to 12 mm, and stroking speed was tried from $0.5\,\mathrm{mm\,s^{-1}}$ to $10\,\mathrm{mm\,s^{-1}}$. When the contact force is too low, the stroking distance is too long/short, or the stroking speed is too high/low, the uncertainty of the friction measurement would be high because of the sensitivity of the sensors or mechanical instability. Because of this, the range of the contact force was chosen to be from 0.5 N to 1.5 N, the stroking distance at 6 mm (± 3 mm from the central point) and the stroking speed was set from $2\,\mathrm{mm\,s^{-1}}$ to $8\,\mathrm{mm\,s^{-1}}$. The contact forces are still within the reasonable range expected on a human finger on a touch-feel perception task, which is between 0.2 N to 0.8 N [99]. The current setup is unable to match the range of sliding speed observed with a human finger by Tanaka et al. [99] of between 50 mm to 130 mm. However, the size of the sample used in this thesis is much smaller (¡25% the size) compared to the reference, and therefore it is safe to assume that the participants would have stroked the sample at a slower pace.

Stick-slip Analysis

Stick-slip can be described as surfaces alternating between sticking to each other and sliding over each other, with a corresponding change in the force of friction. Typically, the static friction coefficient (a heuristic number) between two surfaces is larger than the kinetic friction coefficient. If an applied force is large enough to

overcome the static friction, then reduction of the friction to the kinetic friction can cause a sudden jump in the velocity of the movement.

The stick-slip effect should be into consideration in friction test apparatus design, because the presence of stick-slip effect will introduce large errors to the friction measurement and that the reciprocating movement of the linear stage increases the likelihood of the effect happening—the phenomenon occurs easiest at the end points of sliding motion when the linear stage changes direction.

Here, the linear stage sliding speed was set to $2\,\mathrm{mm\,s^{-1}}$, the sliding distance was set to $3\,\mathrm{mm}$ and the normal force was set to $0.5\,\mathrm{N}$, 4000 points were sampled. As shown in Fig. 3.15, there was a disturbance on the normal force measurement when the linear stage changed its direction. However, there was no corresponding obvious effect on the friction force and the friction coefficient measurement, whereas one would expect visible jumps on both ends if the stick-slip effect was significant. The non-negative friction force reading after direction change on the figure is due to bias before calibration settings were applied.
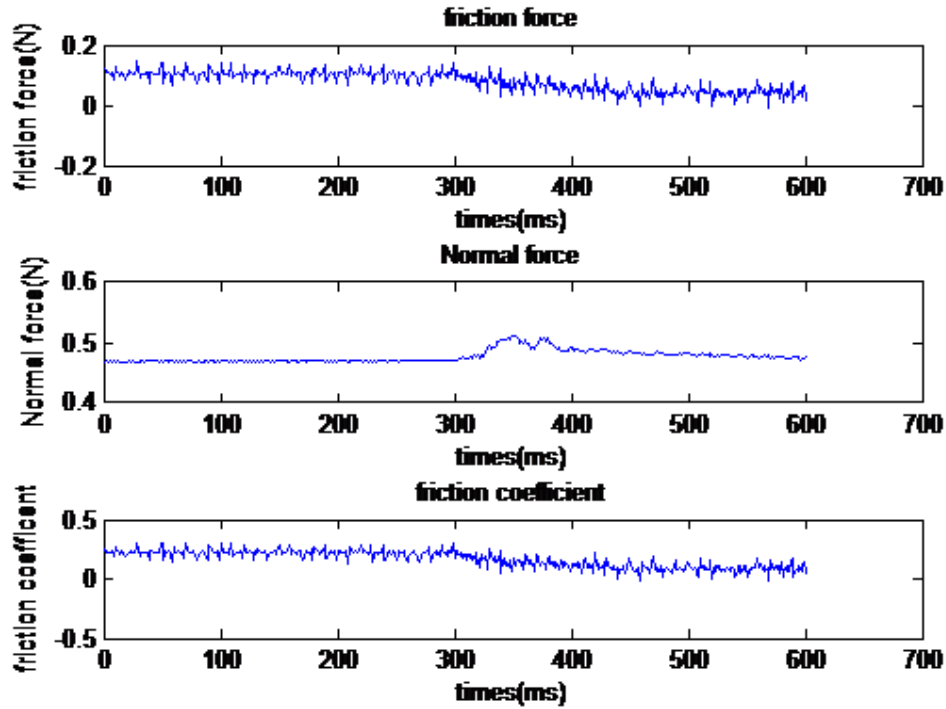
Figure 3.15: Stick-slip effect check during friction measurement

Bias Characterisation, optimal normal force and movement range

One of the objectives of calibration is to make sure there is no significant bias in the friction coefficient measurement. Another objective is to find the optical normal force and the travelling distance for accurate friction measurement. Here, one of milled aluminium samples, AM4, was used to test for bias and to choose the optimal normal force and measurement range. Its size is $20\,\text{mm} \times 15\,\text{mm}$. The central point of the sample was at $-11.5\,\text{mm}$ in the linear stage axis. Normal forces of $0.5\,\text{N}$, $1.0\,\text{N}$, $1.5\,\text{N}$ and $2.0\,\text{N}$ were applied. Bias measurement was performed by setting linear stage speed to zero. The procedure was performed at different points of the AM4 sample from $0\,\text{mm}$ to $17\,\text{mm}$, measured from one of the edges.
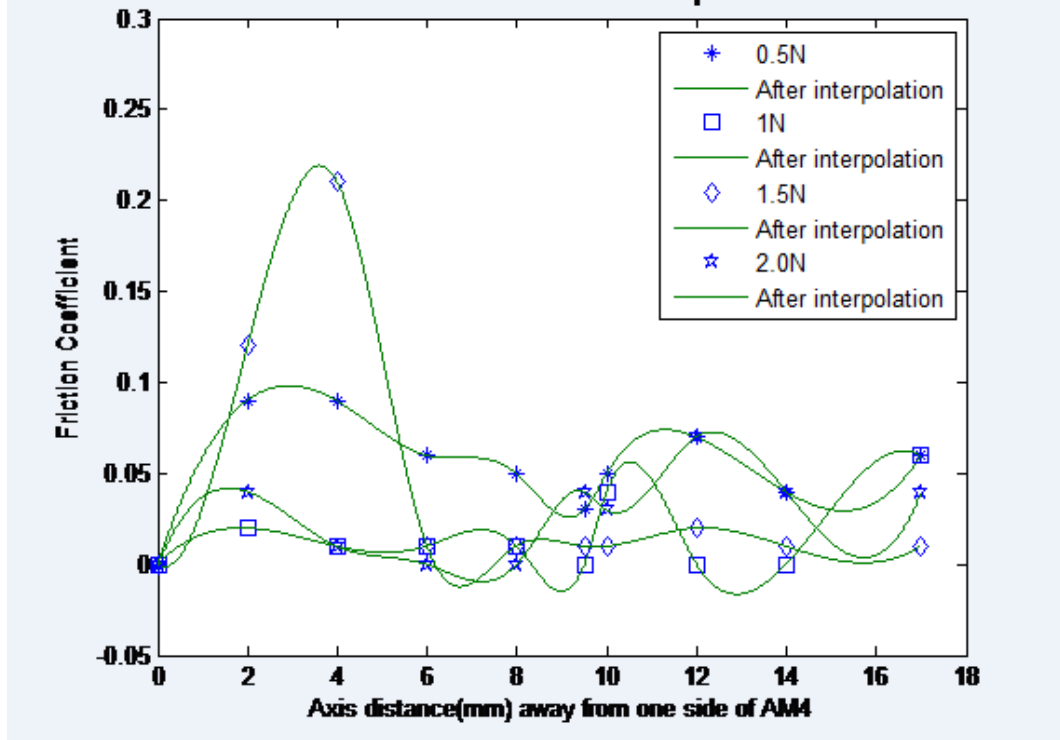
Figure 3.16: Bias measurement of $AM0.4$

As shown in Fig. 3.16, the friction coefficient was stable between 0 to 0.05 when the normal forces were $0.5\,\text{N}$, $1.0\,\text{N}$ and $2.0\,\text{N}$. This low level of bias can safely be ignored. The friction coefficient jumped above 0.2 at $4\,\text{mm}$ when the normal force was $1.5\,\text{N}$ in the linear stage axis, which is $7.5\,\text{mm}$ away from the central point of the sample. Because the normal stroking force of human fingertip is at about $0.5\,\text{N}$ [99], $0.5\,\text{N}$ and $1.0\,\text{N}$ were chosen as default settings for future friction measurement. Also, $\pm 5\,\text{mm}$ was chosen as the largest travelling distance away from the central

point, corresponding to 6.5–17.5 mm on Fig. 3.16.

3.4   Friction measurement of metal samples

In order to minimise the influence due to different materials and further understand the surface topography effect on touch friction, a set of samples made of aluminium milled/turned and ground steel were first selected for the investigation. The friction coefficient measurement experiment is separated into two parts; the first part concerns with different contact forces and the second part concerns with different linear sliding speeds. As shown in Tables 3.3 and 3.5,the aluminium and steel samples have roughness ranging from about 0.1 µm to 25 µm, and spacing parameter S_m ranging from approximately 20 µm to 600 µm .

3.4.1   Topography measurements
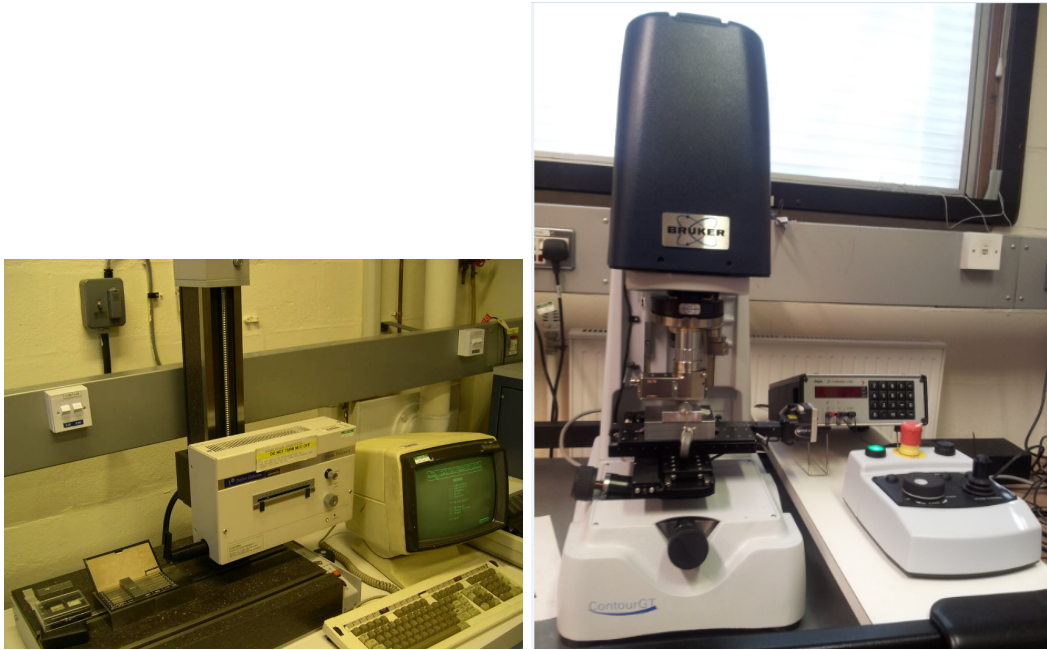
(a) Taylor Hobson Form Talysurf 2D stylus surface profilometer

(b) Bruker Corporation ContourGT-K 3D optical microscope

Figure 3.17: 2D and 3D surface metrology instrument

In order to compare the differences between traditional 2D contact stylus and 3D optical profilometers, and to measure the topography of the surfaces more accurately, the Taylor Hobson *Form Talysurf* and Bruker Corporation *ContourGT-*

K were used to measure the above samples shown in Fig. 3.17. All of the 3D measurement images were shown in Appendix A.4.
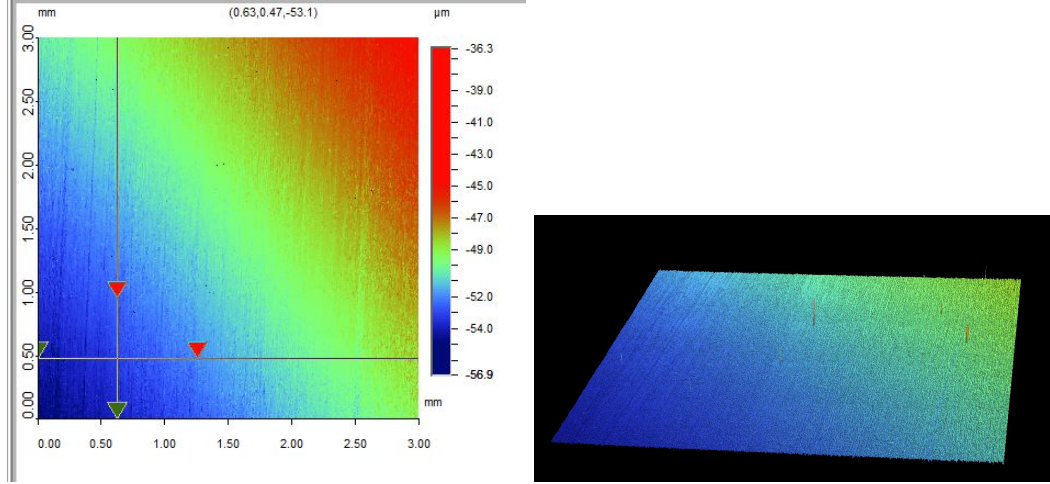
Figure 3.18: The Bruker scanning results of one of the steels samples (ID S2)
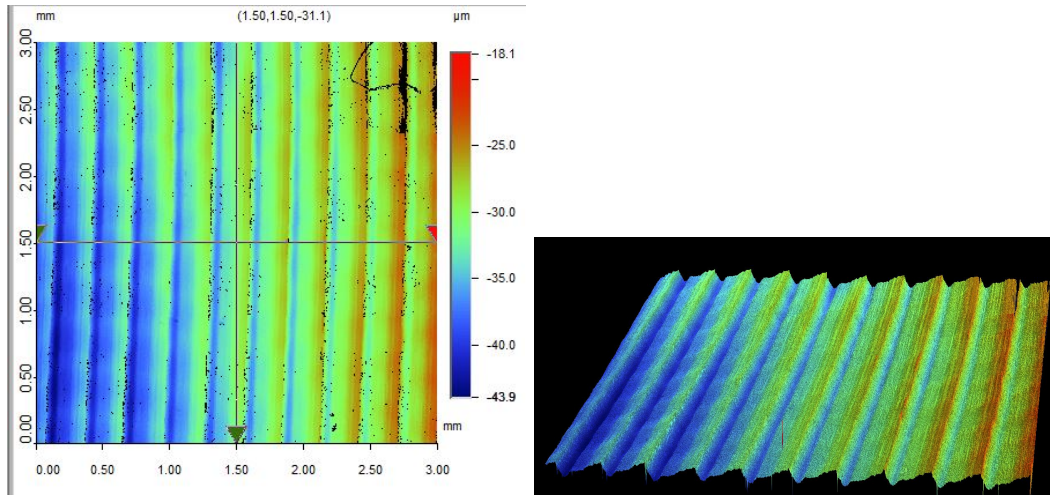
Figure 3.19: The Bruker scanning results of one of the milled aluminium samples (ID AM3)

Because the contact radius under the range of normal forces during frictional measurement is no more than 3 mm (see Section 4.4), the stitching setup in the Bruker was set to be 3 mm × 3 mm. Fig. 3.18 and Fig. 3.19 show the detailed topography in both 2D plan view (left) and 3D view (right), measured from the centre of the sample. The red colour indicates regions of high surface height, while the blue colour indicates regions of low surface height. Each sample was measured 5 times and results were averaged.

The summary bar plots of measurements using 2D and 3D methods for various materials are shown in Figures 3.20, 3.21 and 3.22. The blue bars the Bruker ContourGT-K measurement results while the red bars are the Taylor Hobson Form Talysurf measurement results. Compared with the conventional 2D roughness parameters of R_a, R_q from the Form Taysurf, the 3D S_a, S_q results from ContourGT-K are numerically greater. The 3D measurements include extra spatial information over a large area through stitching and can be expected to be more accurate than 2D measurements where the directionality may affect the results in some materials.
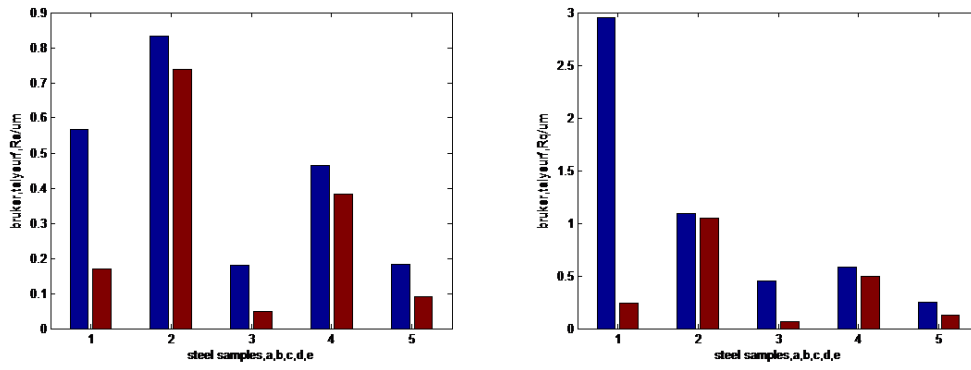
Figure 3.20: Roughness measurements of steel obtained using ContourGT-K (blue) and Form Talysurf (red)
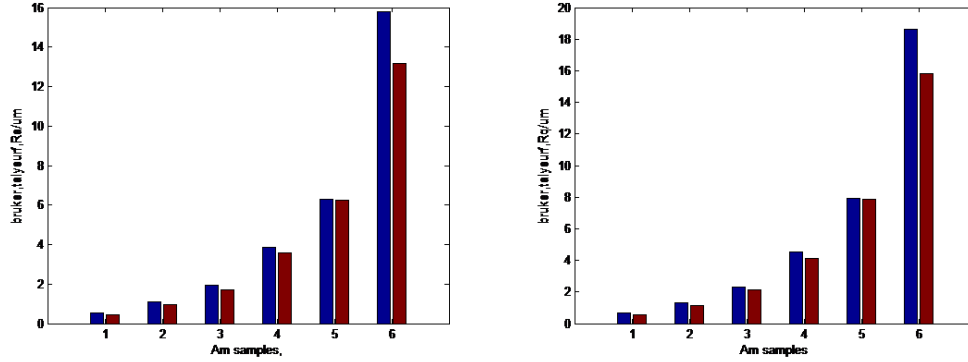
Figure 3.21: Roughness measurements of milled aluminium obtained using ContourGT-K (blue) and Form Talysurf (red)

The inferred surface roughness parameters are shown in Tables 3.3 and 3.4 for the aluminium samples and 3.5 and 3.6 for the steel samples. While R parameters represent the data measured by the Taylor Hobson Form Talysurf, the S parameters represent the data measured by the Bruker Contour GT-K. In this thesis, unless
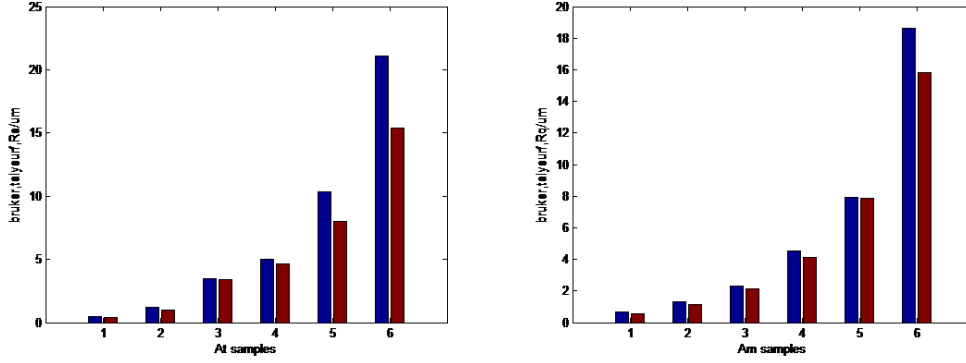
Figure 3.22: Roughness measurements of turned aluminium obtained using ContourGT-K (blue) and Form Talysurf (red)

otherwise specified, topography parameters data reported without symbols are 3D parameters from the Bruker Contour GT-K.

Table 3.3: Surface texture parameters of the Aluminium samples measured by Bruker

	Sample	$S_a(\mu m)$	$S_q(\mu m)$	S_{sk}	S_{ku}	$S_m(\mu m)$
Milled	AM1	0.531	0.698	−0.899	4.208	51.797
	AM2	1.083	1.317	−0.811	2.854	130.745
	AM3	1.935	2.328	−0.075	2.223	253.498
	AM4	3.868	4.552	0.120	1.785	283.379
	AM5	6.310	7.931	1.073	3.744	365.373
	AM6	15.768	18.651	0.970	3.252	530.893
Turned	AT1	0.485	0.622	0.338	5.120	30.342
	AT2	1.184	2.711	0.500	2.100	86.657
	AT3	3.507	4.619	1.240	3.713	214.751
	AT4	4.997	6.122	1.218	5.733	346.076
	AT5	10.367	11.104	0.323	1.383	508.793
	AT6	21.121	23.133	0.334	1.492	602.454

3.4.2 Friction measurement results and analysis

The sliding (stroking) speed of the linear stage, as well as the contact force applied by the spring, can be varied to accommodate the investigation. The mean friction coefficient is obtained by averaging the absolute values of friction coefficient derived from the reciprocating motion in both directions. The sampling rate of $100\,\mathrm{Hz}$ was used and each measurement took about $40\,\mathrm{s}$. Every set of measurement was repeated five times and results were averaged.

Table 3.4: Surface texture parameters of the Aluminium samples measured by Taylor Hobson

	Sample	R_a(μm)	R_q(μm)	R_{sk}	R_{ku}	S_m(μm)
Milled	AM1	0.424	0.550	−0.845	4.235	40.836
	AM2	0.911	1.122	0.268	2.674	67.507
	AM3	1.702	2.158	0.268	3.622	140.656
	AM4	3.507	4.174	0.381	2.327	191.311
	AM5	6.564	7.619	0.423	2.028	277.230
	AM6	13.823	16.080	0.436	1.956	413.422
Turned	AT1	0.411	0.513	−0.059	2.838	45.750
	AT2	0.720	0.879	0.655	2.612	70.241
	AT3	3.259	3.890	−0.038	1.937	118.056
	AT4	4.867	5.525	0.117	1.733	184.615
	AT5	7.294	8.287	0.034	1.685	238.177
	AT6	15.142	17.079	−0.686	1.970	390.947

Table 3.5: Surface texture parameters of the steel samples measured by Bruker

Sample	S_a (μm)	S_q (μm)	S_{sk}	S_{ku}	S_m (μm)
S1	0.179	0.451	−0.800	4.500	21.884
S2	0.184	0.254	0.267	8.700	25.441
S3	0.464	0.586	−0.243	7.300	23.776
S4	0.834	1.092	−0.908	7.780	32.504
S5	2.567	2.948	−1.900	16.700	35.078

Table 3.6: Surface texture parameters of the steel samples measured by Taylor Hobson

Sample	R_a(μm)	R_q (μm)	R_{ku}	R_{sk}	S_m (μm)
S1	0.061	0.101	0.225	5.398	6.558
S2	0.110	0.183	0.225	5.398	6.914
S3	0.220	0.312	−1.228	7.179	8.162
S4	0.430	0.532	−0.619	3.996	9.740
S5	0.790	0.824	0.249	2.829	14.363

For human finger measurements, 10 subjects were recruited to stroke on six different milled aluminium samples and turned aluminium samples, 6 subjects for the five ground steel samples (see Table 3.3 and Table 3.5). Before the experiment, participants were asked to wash their hand with soap and dried with a towel. Material samples were cleaned with isopropyl alcohol. The subjects were then asked to 1) stroke the material surface using his/her index finger back and forth, at an angle of about 60 degrees 2) maintain a normal force as specified by the test (0.5 N) with feedback from a computer monitor 3) maintain a natural stroking speed. The stroking direction was perpendicular relative to the axis of the surface texture (along the x-axis as seen in Figures 3.18 and 3.19). The results were labelled 'human finger' in the subsequent figures. The average human fingertip stroking speed is about $8 \, \mathrm{mm \, s^{-1}}$ and the average contact force is approximately 0.5 N [32].

For the artificial fingertip friction experiment in this paper, the contact loading forces of 0.5 N, 1 N, 1.5 N and 2 N and the sliding speeds of $0.5 \, \mathrm{mm \, s^{-1}}$, $2 \, \mathrm{mm \, s^{-1}}$, $5 \, \mathrm{mm \, s^{-1}}$, $8 \, \mathrm{mm \, s^{-1}}$ and $10 \, \mathrm{mm \, s^{-1}}$ were investigated. It was later found that some of the extreme values were outside the linear range of the capacitive sensor and excess vibration on the sample holder was observed. Because of this, results are only reported for the sliding speed settings of $0.5 \, \mathrm{mm \, s^{-1}}$, $2 \, \mathrm{mm \, s^{-1}}$, $5 \, \mathrm{mm \, s^{-1}}$ and $8 \, \mathrm{mm \, s^{-1}}$ and contact force settings of 0.5 N and 1 N.
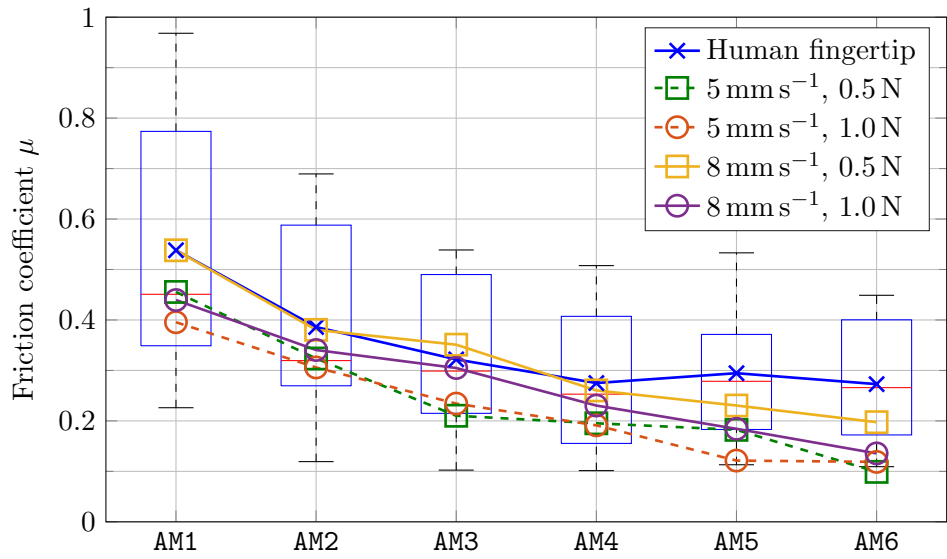
(a) Aluminium (milled) samples
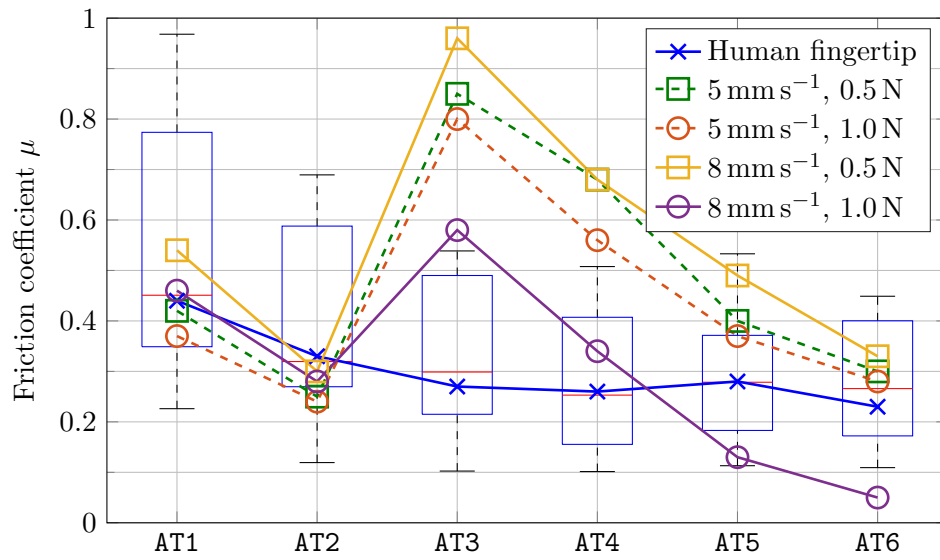
(b) Aluminium (turned) samples
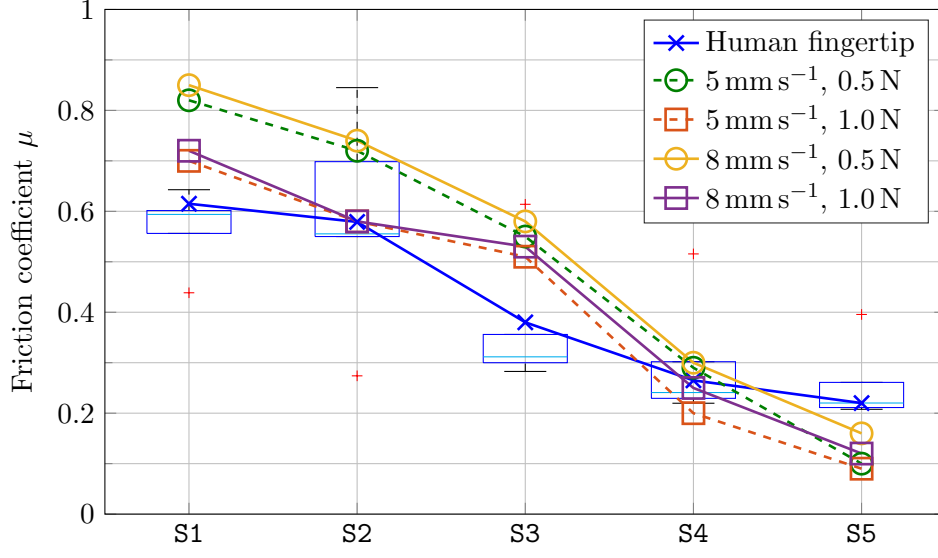
(c) Steel samples

Figure 3.23: Friction coefficient measurements comparing human fingertip and artificial fingertips applied on (a and b) aluminium and (c) steel samples at various stroking speed and loading forces. Boxplot applicable to human fingertip measurements of 10 adult subjects for aluminium samples and 6 subjects for steel samples — dotted black whiskers: data range, blue boxes: 25% – 75% quartiles, horizontal cyan lines: median, blue crosses: mean, small red plus signs: outliers.

Comparison with human fingertip friction

In order to assess if the artificial fingertip was close to human fingertip in terms of friction properties, Fig. 3.23 was plotted. It contains the results of friction coefficient measurement obtained from human fingertips (boxplot with blue crosses marking the means) and that from the artificial fingertip on aluminium and steel samples. Overall the results show that the artificial finger is relatively close to human finger in terms of the friction measurement characteristics for these samples, compared to previous attempts by our group [32]. The results are better matched with milled aluminium samples (root mean squared error (RMSE) $\sim 0.043 - 0.13$) compared to steel samples (RMSE $\sim 0.12 - 0.19$), with the outlier S3 contributing to most error. Considering the results on the milled aluminium samples in Fig. 3.23a, it can be seen that for the smoother samples AM1–6 (lower S_a and S_q values, see Table 3.3), the lowest root mean square error (RMSE = 0.043) was obtained with the artificial finger at a sliding speed of $8\,\mathrm{mm\,s^{-1}}$ and a normal force of $0.5\,\mathrm{N}$.

As shown in Fig. 3.23b, the friction measurement results for the turned aluminium samples are less satisfactory. It may be due to the fact that the surfaces of the aluminium turned samples are not strictly flat, but slightly curved because of different machining technology. For AT1 and AT2, the artificial finger friction measurements are quite close to the mean human finger measurement results under all conditions. The $8\,\mathrm{mm\,s^{-1}}$ condition results seems to better compared with the $5\,\mathrm{mm\,s^{-1}}$. For the remaining 4 samples, it is difficult to identify their friction coefficients. The artificial fingertip occurs the same trends, which is different from the human fingertip measurement results. However, the $8\,\mathrm{mm\,s^{-1}}$ and $1\,\mathrm{N}$ results are the most similar to human fingertip friction results.

For the steel samples in Fig. 3.23c, the trend is different; a sliding speed of $5\,\mathrm{mm\,s^{-1}}$ and a normal force of $1.0\,\mathrm{N}$ seem to result in the lowest error between the artificial finger measurements and the human finger measurements for the smoother samples S1–S3 (RMSE = 0.135). For these samples, it will be seen later that $2\,\mathrm{mm\,s^{-1}}$ achieve even better matching with the human finger measurements. The faster sliding speed of $8\,\mathrm{mm\,s^{-1}}$ was slightly closer to human finger for samples S4 and S5 (RMSE = 0.060). At higher roughness ($S_{\mathrm{a}} > 6\,\mathrm{\mu m}$), AM5 and AM6 results suggest that higher sliding speeds and/or lower normal forces may match better with human finger measurements. The influences of normal force and sliding speed will be discussed in more detail later in Sections 3.4.5 and 3.4.6. It is interesting to note that the outliers marked by crosses for S1 and S2 are results from the same participant and similarly the outliers for S3–S5 are results from the same participant.

The variation of human results for the steel samples is indicated by the averaged standard deviation across the samples of 0.11. This is lower than the value for milled aluminium of 0.16 and that turned aluminium of 0.15. A hypothesis is that the steel surface topography is irregular and random as shown in Appendix A.4.1, compared to that of aluminium samples which have regular patterns as shown in Appendix A.4.1.

To study the overall correlation between human finger friction results with the artificial finger results, sliding speeds as low as $0.5\,\mathrm{mm\,s^{-1}}$ were tried on steel samples and $2\,\mathrm{mm\,s^{-1}}$ on the aluminium samples. The coefficient of determination, commonly known as the r^2 value, are computed on the friction coefficient measurement results for each material and for each condition. The r^2 values are shown in Table 3.7. The closer the r^2 value is to one, the higher the correlation is between the artificial finger and human finger friction results. However, this measure is heavily influenced by outliers and no obvious trend can be observed. Therefore, the RMSE values are also tabulated in Table3.8.

Table 3.7: Coefficient of determination r^2 between artificial finger and human finger friction measurements

Configuration		Material		
Sliding speed ($mm\,s^{-1}$)	Normal force (N)	Aluminium (milled)	Aluminium (turned)	Steel (ground)
0.5	0.5	0.8755		
0.5	1	0.7448		
1	0.5	0.6787		
1	1	0.6385		
2	0.5	0.9141	0.0306	0.9721
2	1	0.8787	0.1832	0.9102
5	0.5	0.9023	0.8494	0.9250
5	1	0.8209	0.0705	0.8566
8	0.5	0.4679	0.0176	0.9183
8	1	0.8067	0.1648	0.8251

Table 3.8: Root mean squared errors between artificial finger and human finger friction measurements

Configuration		Material		
Sliding speed ($mm\,s^{-1}$)	Normal force (N)	Aluminium (milled)	Aluminium (turned)	Steel (ground)
0.5	0.5	0.2681		
0.5	1	0.2820		
1	0.5	0.2211		
1	1	0.2127		
2	0.5	0.1027	0.2357	0.2315
2	1	0.1281	0.2991	0.2387
5	0.5	0.1583	0.1104	0.1098
5	1	0.1329	0.2554	0.1259
8	0.5	0.1822	0.3443	0.0426
8	1	0.1179	0.1658	0.0867

The trend is clearer with RMSE. There is a clear trend of decreasing error when the sliding speed is increased for the materials except for the turned aluminium. This is expected as the typical speed at which human stroke one's finger during touch sensing is usually greater than $50\,\mathrm{mm\,s^{-1}}$ [99]. The trend is less clear with respect to which contact force offers lower error. The settings of $8\,\mathrm{mm\,s^{-1}}$ and $1\,\mathrm{N}$ offers the best performance in this set of experiment.

Comparison with previous roller-on-block friction rig

Previously a friction apparatus with a flexure mechanism was built for the in-situ measurement of friction properties; both contact force and frictional force can be measured simultaneously [4]. The apparatus provided a direct measurement of the friction when the human finger stroked on the test specimen. However, the friction measurement results varied significantly across human subjects. In order to mimic a human finger, a roller-on-block friction test configuration was developed by using steel, brass and rubber materials [32]. The results were not satisfactory; for example, the steel and brass were too hard and thus the measurement results were not representative of that from human fingertips. The rubber roller was however too soft to resemble human fingertip. The rubber, lacking a solid core, deformed during measurement.

To see if the new multilayer artificial finger design is better than the previously used rubber roller rig, the same five steel samples listed in Table 3.5 were tested on the current friction test rig using linear stage sliding speeds of $0.5\,\mathrm{mm\,s^{-1}}$, $1\,\mathrm{mm\,s^{-1}}$, $2\,\mathrm{mm\,s^{-1}}$ and $5\,\mathrm{mm\,s^{-1}}$, matching the roller rotation speeds used in Yue [32]. For a contact force of $0.5\,\mathrm{N}$, the previous measurements of friction coefficients ranged from 1.2 to 1.7. The high friction coefficients were due to the soft pure silicone rubber used as the tip material. In comparison, the multilayered artificial fingertip in this paper resulted in friction coefficients ranging from 0.1 to 0.9. The friction measurement results from the roller apparatus also had significantly lower correlation ($r^2 < 0.5$) compared to the new apparatus ($r^2 = 0.5 \sim 0.91$).

3.4.3 Influence of material roughness

Figure 3.25 shows that increasing roughness of the material results in lower measured friction coefficient regardless of sliding speed. Although only R_{q} is shown here, similar observations can be made with R_{a} and indeed the S parameters from Tables 3.3 and 3.5. A similar trend can also be seen with a lower contact force of $0.5\,\mathrm{N}$.
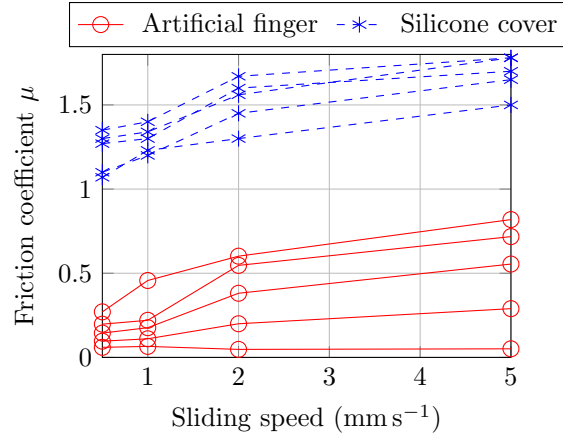
Figure 3.24: Comparison of friction coefficients against sliding speed of steel samples measured using the artificial finger and the roller rig with silicone cover
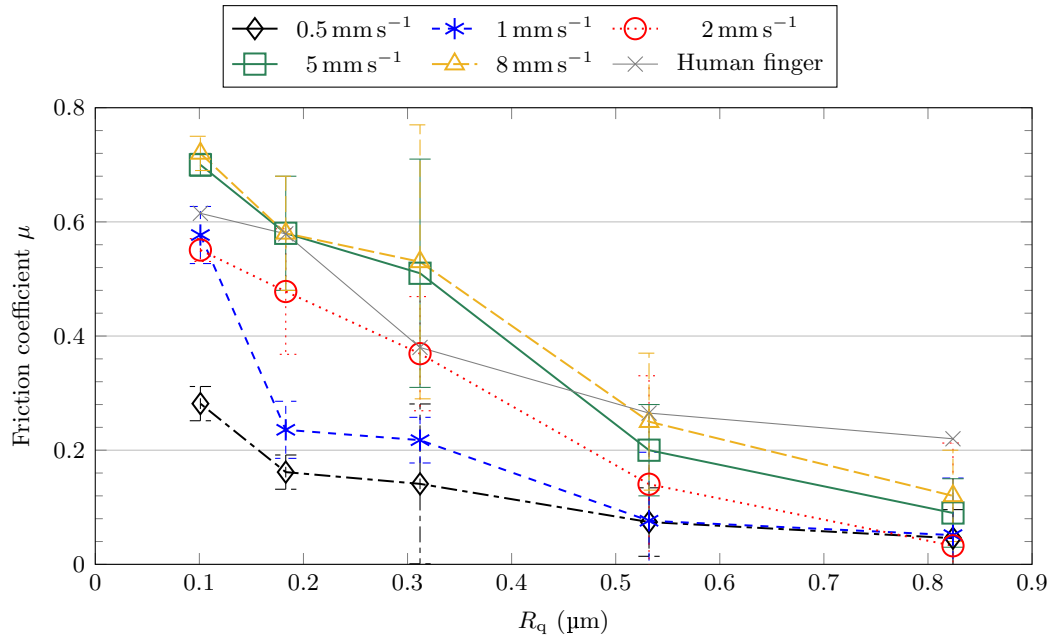
Figure 3.25: Friction coefficients of the ground steel samples against R_q at different sliding speeds with fixed contact force OF 1 N

With aluminium samples, apart from `AT1` and `AT2`, Figures 3.23a and 3.23b also support the idea that increasing roughness parameter result in lowered measured friction coefficient, as the sample IDs are also ordered in increasing R_a and R_q (see Table 3.4).

The trend seen here agrees with theory which will be discussed at the end of Section 4.2.4.

3.4.4 Influence of the fingerprint

To better replicate the friction characteristics of a human fingertip, a real human fingerprint pattern was imprinted on the surface of the artificial fingertip. In order to assess the effect of this addition, we compared the steel samples friction with and without a fingerprint as follows. The linear stage sliding speeds were set to $2\,\mathrm{mm\,s^{-1}}$ and $5\,\mathrm{mm\,s^{-1}}$, and the normal forces applied were $0.5\,\mathrm{N}$ and $1\,\mathrm{N}$.

As shown in Fig. 3.26, the curves with diamond markers are the friction measurement results without fingerprint, where the surface of the artificial fingertip was smooth and hemispherical. The curves with circle markers are the friction measurement results with a fingerprint; it can be seen that the friction coefficients increase when the fingerprint was present. This increase may have been caused by higher pressure induced deformation due to fingerprint edges decreasing the apparent contact area. The deformation may also cause adhesive friction mechanisms, described by the Greenwood-Williamson (GW) theory (Section 4.2.4) [100]. The results with fingerprint track the human fingertip trajectory through the samples better, and hence the inclusion of the fingerprint is beneficial in mimicking human finger friction properties.

3.4.5 Influence of normal force

The friction coefficient is the ratio of the friction force to the normal load which, according to Amontons' first Law, is constant regardless the applied normal force for well-behaved materials. However, adhesion friction is the dominant friction mechanism and the viscoelastic nature of human skin leads to nonlinear deformation. This results in a strong dependence of the measured coefficient of friction on the applied normal load caused by normal adhesion. At high loads and high roughness, the frictional force contains a deformation component which should not be ignored [9].

Putting this in context with human skin studies, Naylor [101] showed that the friction coefficient was a constant for a range of normal forces from $2\,\mathrm{N}$ to $7\,\mathrm{N}$.

(a) 0.5 N

(b) 1 N
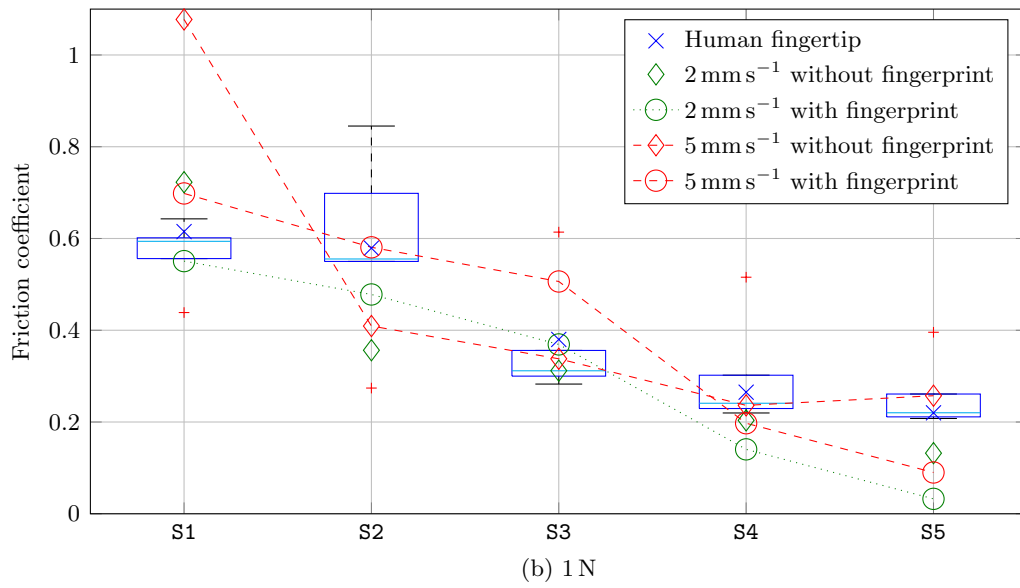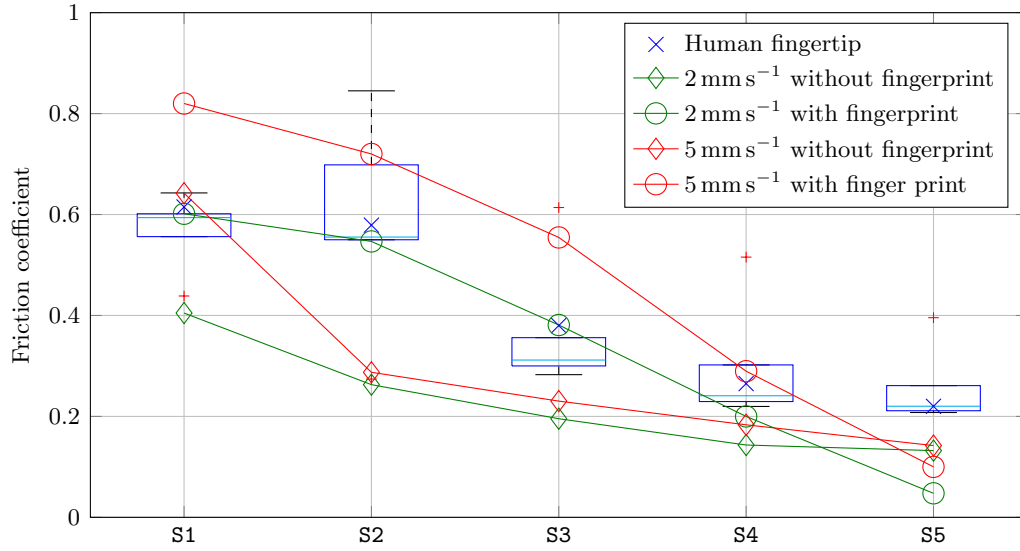
Figure 3.26: The influence of fingerprint texture on the artificial fingertip friction; In-vivo friction of 6 adult subjects—dotted black whiskers: data range, blue boxes: 25% – 75% quartiles, horizontal cyan lines: median, blue crosses: mean.

Table 3.9: Friction coefficients of aluminium samples

Sample		Friction coefficient μ								
		Finger stroke		Sliding speed at contact force = 0.5 N				Sliding speed at contact force = 1 N			
				$2\,\mathrm{mm\,s^{-1}}$		$5\,\mathrm{mm\,s^{-1}}$		$2\,\mathrm{mm\,s^{-1}}$		$5\,\mathrm{mm\,s^{-1}}$	
		Mean	Std.	Mean	Std.	Mean	Std.	Mean	Std.	Mean	Std.
Milled	AM1	0.54	0.27	0.39	0.06	0.46	0.07	0.20	0.10	0.40	0.15
	AM2	0.39	0.19	0.14	0.10	0.32	0.11	0.13	0.15	0.31	0.09
	AM3	0.32	0.15	0.09	0.06	0.21	0.10	0.12	0.09	0.23	0.17
	AM4	0.28	0.15	0.06	0.05	0.20	0.10	0.09	0.06	0.19	0.08
	AM5	0.30	0.14	0.03	0.05	0.18	0.07	0.08	0.09	0.12	0.14
	AM6	0.27	0.12	0.01	0.03	0.10	0.04	0.05	0.05	0.12	0.06
RMSE				0.08		0.07		0.13		0.08	
Turned	AT1	0.44	0.24	0.35	0.11	0.42	0.17	0.32	0.16	0.37	0.22
	AT2	0.33	0.17	0.14	0.08	0.25	0.13	0.18	0.17	0.24	0.16
	AT3	0.27	0.15	0.73	0.24	0.86	0.23	0.80	0.20	0.80	0.17
	AT4	0.26	0.13	0.53	0.23	0.68	0.15	0.62	0.17	0.56	0.15
	AT5	0.28	0.15	0.29	0.19	0.40	0.20	0.57	0.09	0.37	0.15
	AT6	0.23	0.11	0.18	0.10	0.30	0.17	0.30	0.11	0.28	0.19
RMSE				0.19		0.44		0.29		0.51	

(a) Milled, sliding speed = $5\,\mathrm{mm\,s^{-1}}$ (b) Milled, sliding speed = $8\,\mathrm{mm\,s^{-1}}$
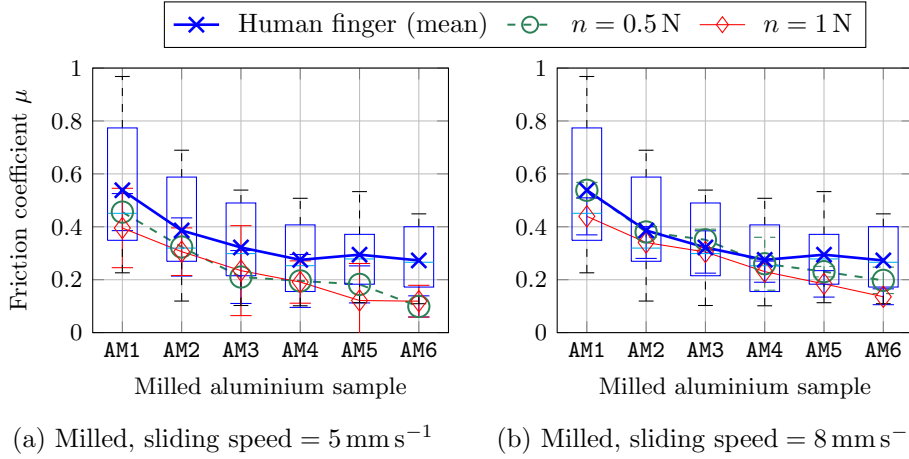
Figure 3.27: Friction coefficients of the milled aluminium samples at different contact forces with fixed sliding speeds of (a) $5\,\mathrm{mm\,s^{-1}}$ and (b) $8\,\mathrm{mm\,s^{-1}}$; Boxplots only applicable to human fingertip measurements of 10 adult subjects—dotted black whiskers: data range, blue boxes: 25% – 75% quartiles, horizontal cyan lines: median, blue crosses: mean.

Table 3.10: Friction coefficients of steel samples

Sample	Friction coefficient μ									
	Sliding speed at contact force = 0.5 N									
	Finger stroke		$0.5\,\mathrm{mm\,s^{-1}}$		$1\,\mathrm{mm\,s^{-1}}$		$2\,\mathrm{mm\,s^{-1}}$		$5\,\mathrm{mm\,s^{-1}}$	
	Mean	Std.	Mean	Std.	Mean	Std.	Mean	Std.	Mean	Std.
S1	0.62	0.13	0.27	0.02	0.46	0.02	0.60	0.02	0.82	0.02
S2	0.58	0.07	0.20	0.02	0.22	0.03	0.55	0.06	0.72	0.11
S3	0.38	0.07	0.14	0.07	0.18	0.12	0.38	0.24	0.55	0.23
S4	0.27	0.11	0.10	0.03	0.11	0.04	0.20	0.21	0.29	0.19
S5	0.17	0.19	0.06	0.03	0.07	0.05	0.05	0.10	0.10	0.12
RMSE			0.25		0.19		0.09		0.19	
	Sliding speed at contact force = 1 N									
	Finger stroke		$0.5\,\mathrm{mm\,s^{-1}}$		$1\,\mathrm{mm\,s^{-1}}$		$2\,\mathrm{mm\,s^{-1}}$		$5\,\mathrm{mm\,s^{-1}}$	
	Mean	Std.	Mean	Std.	Mean	Std.	Mean	Std.	Mean	Std.
S1	0.62	0.13	0.28	0.03	0.58	0.05	0.55	0.02	0.70	0.03
S2	0.58	0.07	0.16	0.03	0.24	0.05	0.48	0.10	0.58	0.10
S3	0.38	0.07	0.14	0.14	0.22	0.04	0.37	0.20	0.51	0.34
S4	0.27	0.11	0.07	0.06	0.08	0.16	0.14	0.28	0.20	0.28
S5	0.17	0.19	0.05	0.05	0.05	0.11	0.03	0.19	0.09	0.28
RMSE			0.26		0.18		0.11		0.13	

(a) Turned, sliding speed = $5\,\mathrm{mm\,s^{-1}}$ (b) Turned, sliding speed = $8\,\mathrm{mm\,s^{-1}}$
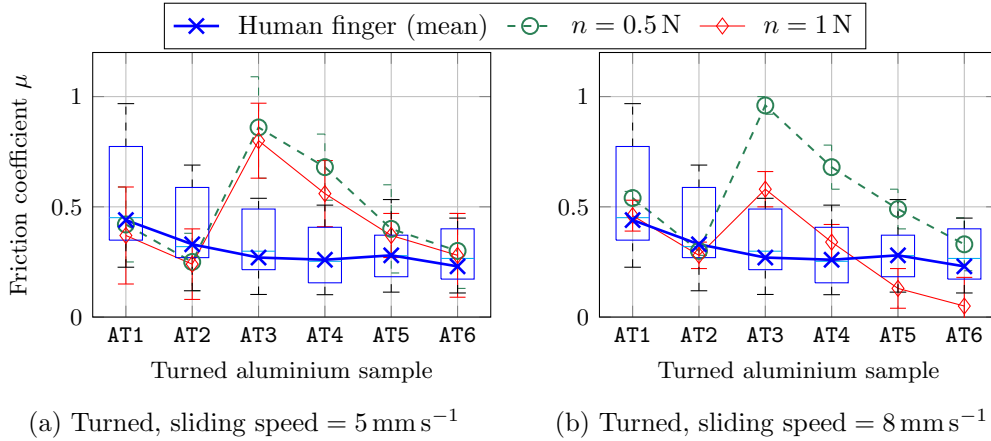
Figure 3.28: Friction coefficients of the turned aluminium samples at different contact forces with fixed sliding speeds of (a) $5\,\mathrm{mm\,s^{-1}}$ and (b) $8\,\mathrm{mm\,s^{-1}}$; Boxplots only applicable to human fingertip measurements of 10 adult subjects—dotted black whiskers: data range, blue boxes: 25% – 75% quartiles, horizontal cyan lines: median, blue crosses: mean.

(a) Sliding speed $= 5\,\mathrm{mm\,s^{-1}}$ (b) Sliding speed $= 8\,\mathrm{mm\,s^{-1}}$
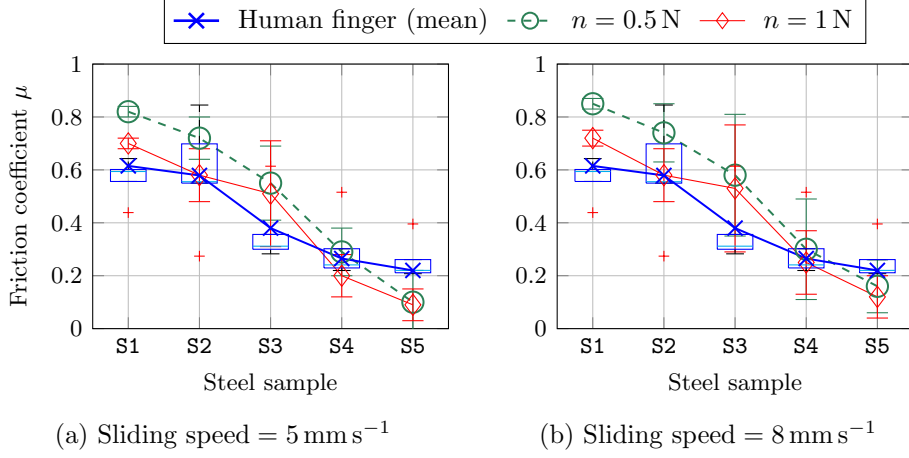
Figure 3.29: Friction coefficients of the ground steel samples at different contact forces with fixed sliding speeds of (a) $5\,\mathrm{mm\,s^{-1}}$ and (b) $8\,\mathrm{mm\,s^{-1}}$; Boxplots only applicable to human fingertip measurements of 6 adult subjects—dotted black whiskers: data range, blue boxes: $25\% - 75\%$ quartiles, horizontal cyan lines: median, blue crosses: mean.

When the normal load was increased from $0.25\,\mathrm{N}$ to $1.8\,\mathrm{N}$, the friction coefficient decreased [102]. For normal loading forces in the range of $0.05\,\mathrm{N}$ to $0.8\,\mathrm{N}$, it has been established that the friction coefficient is inversely proportional to the normal force raised to the power of one-third [44, 103], such that $\mu \propto N^{-\frac{1}{3}}$. This is in agreement with Hertz contact theory [104]. However, there are some reports claiming that for some materials, the contact area during sliding is proportional to the normal force rather than to its cubic root [105, 106]. For such materials, the friction coefficient is proportional to the normal forces.

With respect to Figs. 3.27, 3.28 and 3.29, one can observe that the friction coefficient generally decreases as the normal force increases. This is verified for the steel samples with an extended ranged of normal forces applied, from $0.25\,\mathrm{N}$ to $1.5\,\mathrm{N}$, but only 0.5 and $1\,\mathrm{N}$ results are shown in Fig. 3.29. The trend is similar for milled aluminium samples in Fig. 3.27, although the difference between the normal forces is less pronounced. Note that the roughness range of the steel sample tested was narrower from $S_\mathrm{a} = 0.179\,\mathrm{\mu m}$ to $2.567\,\mathrm{\mu m}$, compared to the aluminium samples with a roughness range from $0.485\,\mathrm{\mu m}$ to $21.121\,\mathrm{\mu m}$. It can be seen that for the rougher samples AM4–6 (S_a above $4\,\mathrm{\mu m}$), the friction coefficient remains fairly constant when roughness increases. For the rougher turned aluminium samples AT3–6, there is a significant discrepancy of the friction coefficient measurement under the different normal forces. This may be due to the fact that the adhesion friction is the dominant friction mechanism. The strong dependence of the measured coefficient of friction

on the applied normal load is expected to be caused by normal adhesion. At high loads and high roughness, the friction force contains a deformation component which should not be ignored [9].

Overall, for the normal forces investigated, the influence on the friction measurement is relatively small and the error bounds overlap, except for the very smooth samples (S1 and S2), and the rougher turned aluminium (AT3–6).

3.4.6 Influence of stroking/sliding speed
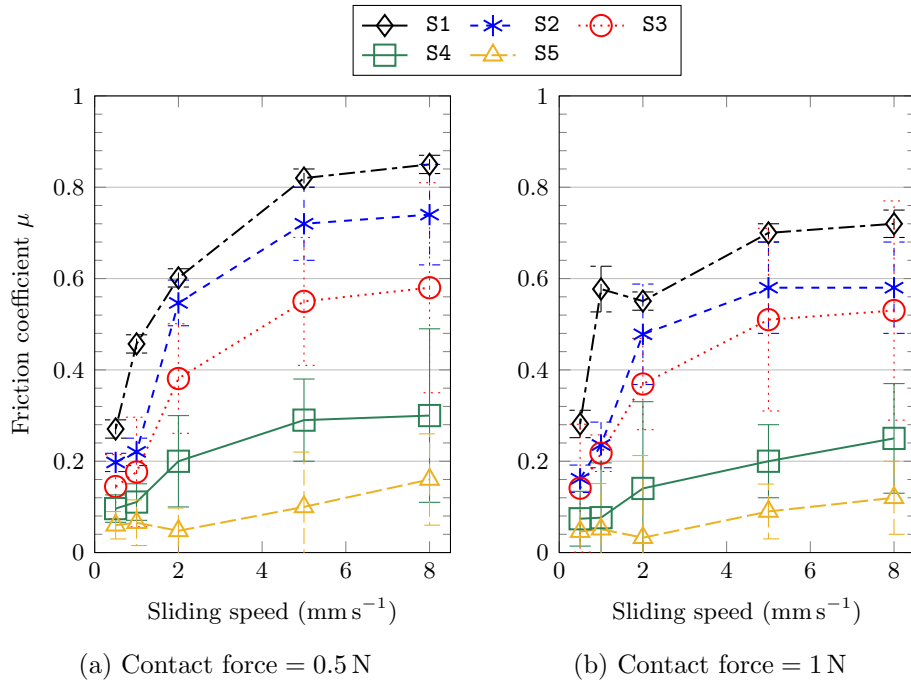
Figure 3.30: Friction coefficients of the ground steel samples at different sliding speeds with fixed contact forces of (a) 0.5 N and (b) 1 N

Comparing the sub-figures in Fig. 3.27 and Fig. 3.29, friction coefficients seem to increase when the sliding speed of the linear stage was increased from $5\,\mathrm{mm\,s^{-1}}$ to $8\,\mathrm{mm\,s^{-1}}$, except for turned aluminium AM3–AM6. To verify this, the experiment was repeated with steel samples only but with an extended range of sliding speeds of $0.5\,\mathrm{mm\,s^{-1}}$, $1\,\mathrm{mm\,s^{-1}}$, $2\,\mathrm{mm\,s^{-1}}$, $5\,\mathrm{mm\,s^{-1}}$ and $8\,\mathrm{mm\,s^{-1}}$; the result of which is shown in Fig. 3.30. The trend of increasing friction coefficient with sliding speed is consistent with the different contact forces of $0.5\,\mathrm{N}$ and $1\,\mathrm{N}$ for smooth surfaces.

To explain the trend, consider that the sliding motion of the artificial fingertip against the material sample causes a cyclic deformation of viscoelastic silicone rubber of the artificial finger. Energy is dissipated through internal damping when through

the deformation and relaxation cycle [106–108]. When the sliding speed is low, the loss through the hysteric component of the friction mechanism is small. However, as the sliding speed increases, the deformation rate increases and the recovery is slow to recoup the elastic energy. The hysteric friction increases as more energy is lost in elastic hysteresis [45]. Recently, numerical simulations and analytical solutions based on Persson's theory (Section 4.2.6) show the increase in friction with sliding speed [109].

3.5 Conclusion

Touch friction is complicated and it can be affected by many factors such as surface material, surface properties, skin conditions and test conditions. An artificial finger can potentially eliminate much of the variability of real human fingers and also allow a much more automated iterative design process for touch-feel optimised materials.

Expanding on the work performed in the research group on the friction aspect of touch-feel perception, an anthropomorphic artificial finger had been developed. The artificial finger is multilayered, including a bone support and two layers of silicone rubber. The rubber that makes up the cover layer was chosen to mimic the stiffness and the thickness of the epidermis, whereas the rubber that makes up the inner filler layer was chosen to mimic the stiffness of the dermis. The artificial finger was mounted on an improved friction measurement rig that is capable of measuring normal forces and friction forces simultaneously, with a load cell and a capacitive sensor, respectively. Measurements were taken on a set of aluminium and steel specimens with different roughness. The results of the artificial finger on the new friction test rig show a much-improved correlation between real human finger, with coefficients of determination (r^2) between 0.5 to 0.91 compared to that of an older roller-on-block rig ($r^2 < 0.5$) [32].

The friction coefficient measurement obtained through the artificial finger is very similar to that from a real human fingertip, as evidence from Section 3.4.2 shows. Overall the setting of $5\,\mathrm{mm\,s^{-1}}$ sliding speed and $0.5\,\mathrm{N}$ normal force achieved the highest r^2 correlation with human finger results, while the setting of $8\,\mathrm{mm\,s^{-1}}$ and $1\,\mathrm{N}$ resulted in the lowest root mean squared errors (RMSE), followed by $5\,\mathrm{mm\,s^{-1}}$ and $0.5\,\mathrm{N}$. A trend can be observed with the RMSE that it seems to decrease with increasing sliding speed. This is reasonable as human finger typically stroke a sample during touch-feel at more than $50\,\mathrm{mm\,s^{-1}}$ [99]. Normal force applied seemed to have no effect on the RMSE, more contact forces should be tested to investigate this further.

The results in Section 3.4 show that, even with the same material, different experiment conditions produces different friction results. Section 3.4.3 shows that rougher surfaces tend to have lower friction coefficients for the materials tested. Section 3.4.4 looked at the effect of the presence of a fingerprint on friction measurements and found that the fingerprint increases friction except for the roughest steel samples tested (S4 and S5). Ridges on the fingerprint increases the apparent contact area leading for a given pressure or loading force (see Section 4.5.2), and therefore increases friction.

Analyses were performed in Section 3.4.5 on the relationship between surface friction coefficients and the contact forces. It is concluded that as the contact forces increase, the friction coefficients decrease. Section 3.4.6 investigates the relationship between surface friction coefficients and the linear stage sliding speeds. When the linear stage sliding speeds increases, the obtained friction coefficients increase.

Future work is required on looking at natural variability of different human fingertips and how to best design an artificial finger that can emulate these differences in a controlled manner. Increasing the capability of the apparatus to operate at higher sliding speed may improve the matching with human fingers.

Measurement and Theoretical Analysis of Contact Area

C HAPTER 3 introduced a multi-layered artificial fingertip design mimicking the structure, shape, stiffness and the friction properties of real fingertips in order to facilitate human touch-feeling studies. Experiment results confirmed that the friction properties of the artificial fingertip are close to that of a real human fingertip. In order to understand the contact mechanism, a suitable theoretical model of the friction mechanism, in particular, how the normal force and contact area relates to the friction perceived by people is essential in understanding touch-feel perception.

4.1 Introduction

There is a growing interest in quantifying and modelling touch-feel perception over the past decade in order to understand customers' needs in product design [4–12]. Touch-feel perception can only be evaluated when a person performs skin contact or strokes over the surface of an object. Designing a surface material for desirable touch-perception is often left to trial-and-error and hence a time-consuming process. From Chapter 3, an artificial fingertip can replace a human fingertip for friction characterisation with much higher repeatability (precision), controllability and lower turn-around time. Identifying the relationship between the friction measurement and touch-feel perception is not enough—a designer can only design a material against material properties quantified by surface topographical parameters and mechanical parameters. Hence, it is essential to first identify the links between the friction

characteristics and the material properties—this is to study the contact mechanism (see Section 1.1)

For 'hard-on-hard' surface contact such as steel-on-steel, it is generally accepted that there is only negligible association between surface roughness and friction force [110, 111]. The real contact area is the summation of the localised spots inside the contact where actual micro-scale contact occurs; the real contact area is much smaller than the apparent contact area. However, when one of the contact surfaces is a compliant material that is not overly soft, such as rubber or skin, an increased surface roughness will result in a larger separation between the mean planes of contact surfaces, causing a reduction in the adhesion amount. Therefore an increase in surface roughness manifests as reduced friction when friction is dominated by adhesion [28, 112]. In addition, lateral geometrical parameters such as the wavelength or the spacing between the individual asperities also play an important role in friction [29]. Experiments on the friction characteristics of human skin in contact with well-defined regular patterned surface show that the determining parameter is the ratio of the asperity size to the inter-asperity distance [30]. Persson [105] showed that surface roughness that results from frozen capillary waves can have a large influence on the contact between solids. Still, there is no clear picture on how surface topography and mechanical parameters affects the friction perceived by a human fingertip.

This chapter investigates the possible contact mechanism between the artificial fingertip and hard surfaces. The developed artificial fingertip can be used to simulate the human fingertip under different working conditions (see Chapter 3). The contact areas when the artificial fingertip presses against the test samples under different contact forces have been measured using an optical profiler (Bruker ContourGT-K 3D optical microscope). Finite element modelling (FEM) has also been carried out to model the contact mechanism between the artificial fingertip and the hard surface using the software Abaqus.

4.2 Contact Mechanics theories

4.2.1 Human skin friction coefficient

The *coefficient of friction* (CoF), also known as the 'friction coefficient' and conventionally denoted by Greek letter μ, is a dimensionless value which describes the ratio of the friction force between two bodies and the force pressing them together. Generally, the CoF depends on the applied materials. For example, the CoF is low for contact between ice and steel, while a contact between rubber and pavement results in a relatively high CoF. Most dry materials in combination have CoF values from

0.3 to 0.6, while rubber in contact with other surfaces can yield friction coefficients from 1 to 2 [105]. For most material interactions, CoF is less than 1, but this may not be true for soft materials such as rubber which can be substantially larger than 1. A value above 1 merely implies that the force required to slide an object along the surface is greater than the normal force on the object such as silicone rubber or acrylic rubber-coated surfaces.

(a) Partial contact.   (b) Full contact.
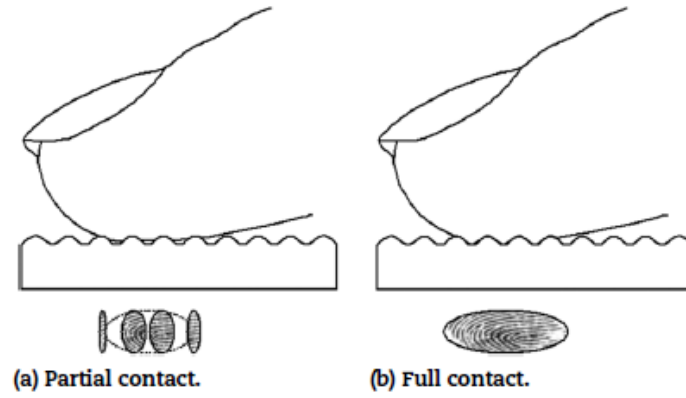
©2011 Elsevier, reprinted with permission from Masen [9].

Figure 4.1: Partial contact and full contact depends on the surface micro-geometry and loading conditions

While it is often stated that μ is a 'material property', it is better categorised as a 'system property' [9]. Unlike true material properties(such as conductivity, hardness, yield strength), μ for any two materials depends on system variables like temperature, velocity, atmosphere and also what are now popularly described as age and dealing times, as well as on geometric properties of the interface between materials. In this thesis, the friction coefficient is simplified as the friction between the multi-layered artificial fingertip and metal (hard) or thermoplastic (soft) materials. Fig.4.1 simulates the contact between human skin and different surfaces. The height and spacing of the surface texture both affect the friction coefficient. When the asperities are too high or positioned too close to each other, the valleys will not be filled and only partial contact occurs [9]. In addition, human skin shows similar viscoelastic material properties as a soft elastomer; the human fingertip deforms during sliding friction.

In dry conditions, when the viscosity component of friction can be ignored, friction of the interface involves two mechanisms

$$F_{\text{total}} = F_{\text{adh}} + F_{\text{def}} \tag{4.1}$$

where F_{adh} is the adhesive force and F_{def} is the deformation force. The relationship between the adhesive and deformation components in the friction force are given in Wolfram [62] and Johnson [104] as

$$F_{\text{adh}} = \tau_0 \pi \left(\frac{3R}{4E^*} \right)^{2/3} F_{\text{N}}^{2/3} \tag{4.2}$$

$$F_{\text{def}} = 0.17 \beta_{\text{ve}} \pi \left(\frac{1}{R^2 E^*} \right)^{2/3} F_{\text{N}}^{4/3} \tag{4.3}$$

where τ_0 is the shear strength of the interface, R the reduced radius of the two bodies in contact, β_{ve} is the viscoelastic hysteresis loss fraction, and F_{N} is the applied normal force. E^* is the reduced Young's modulus, which in the case of contact between skin and a rigid counter body depends solely on the properties of the skin. During the skin friction process, it is considered that adhesion is the main mechanism, where the deformation friction is believed to be unimportant [37, 46], i.e. the adhesion friction coefficient dominates. The deduction of its equation will be given in Chapter6.

The adhesion friction analysis uses Hertz contact theory, which considers elastic bodies contact. However, Hertz contact theory is not suitable for analysing all contact mechanisms, especially when the surface is discontinuous, conforming or non-smooth. The area of real contact influences a large number of physical properties such the contact resistivity, heat transfer, adhesion and friction.

In order to better understand the contact mechanism between rough surfaces and soft materials and to choose an accurate theoretical model framework for our experiments, various contact mechanism theories including the Hertz model, the Johnson-Kendall-Roberts (JKR) model, the Greenwood-Williamson (GW) model and the Persson model are discussed and compared with each other in the following subsections.

4.2.2 Hertz contact model

The Hertz contact theory treats each contacting surface as elastic half-spaces, being perfectly smooth and approximated by elastic spheres with radii R_1 and R_2. In most cases, when the average distance between nearby contact regions is large enough, the elastic couplings between the asperity contact regions are neglected. Hertz made several assumptions: 1) the strains are small and within the elastic limits 2) the contacting surfaces are elastic half-spaces 3) Surfaces are continuous and non-conforming (implying that the area of contact a should be much smaller than the dimension of the half-spaces R), and 4) the surface at points of contact are

frictionless. The normal force must be weak such that the real contact area is small compared to the nominal contact area [28, 113, 114]

The deformation area can be determined by the normal force (F_N) pressed on the bodies. Minimising the elastic deformation energy, the radius of the circular contact area (a_0) is calculated as

$$a_0 = \left(\frac{3F_N R}{4E^*}\right)^{1/3}, \tag{4.4}$$

where

$$\frac{1}{R} = \frac{1}{R_1} + \frac{1}{R_2}, \tag{4.5}$$

$$\frac{1}{E^*} = \frac{1 - \nu_1^2}{E_1} + \frac{1 - \nu_2^2}{E_2}, \tag{4.6}$$

R_1, R_2 are the curvature radii of the two solids, E_1, E_2 are the Young's moduli of the elastic solids and ν_1, ν_2 are the corresponding Poisson's ratios. In addition, the deformation distance s when the two solids penetrate is calculated by

$$s = \left(\frac{R_1 + R_2}{R_1 R_2}\right)^{1/3} \left(\frac{3F_N(1 - \nu^2)}{4E^*}\right)^{2/3} \tag{4.7}$$

For the contact between a sphere and a flat surface whose R is approximately infinite, the contact area can be obtained using (4.4) and (4.7):

$$A = \pi a_0^2 = \pi R s = \pi \left(\frac{3F_N R}{4E^*}\right)^{2/3} \tag{4.8}$$

and the normal force is

$$F_N = \frac{4E^*}{3(1 - \nu^2)} s^{3/2} R^{1/2}. \tag{4.9}$$

The pressure distribution in the contact area depends only on the distance from the centre of the circular contact area:

$$\sigma(a) = \sigma_0 \left[1 - \left(\frac{a}{a_0}\right)^2\right]^{0.5}, \tag{4.10}$$

where $\sigma_0 = F_N/\pi a_0^2$ is the average pressure in the contact.

While one of the assumptions of the theory was that the contact surfaces are smooth such that there is full contact throughout the nominal elliptical area of contact, in reality, all surfaces are rough to some degree and intimate contact only takes places at the crests of the contact surface asperities. Statistical theories of surface contact suggest that the roughness influence is governed primarily by a single

non-dimensional parameter α [115], defined by:

$$\alpha \equiv \frac{\sigma R}{a_0^2} \tag{4.11}$$

where σ is the combined roughness of the two surfaces, R is the radius of the sphere and a_0 is the contact radius for the smooth surfaces given by Hertz contact theory. Experimental and theoretical examinations showed that if the value of α is less than 0.05, errors in the application of Hertz Contact theory are not likely to exceed about 7 percent due to the influence of surfaces roughness. But when α is larger than 0.05, the influence of surface roughness is not negligible and should be considered.

4.2.3 Johnson-Kendall-Roberts (JKR) contact model

The Johnson-Kendall-Roberts (JKR) theory is a generalisation of the Hertz contact model by allowing tensive adhesive forces *inside* the area of contact [116]; this is opposed to the Derjaguin-Muller-Toporov (DMT) model of elastic contact where it considers additional attractive interactions *outside* the area of contact. The contact area calculation relies on elastic material properties and the interfacial interaction strength. Contacts can be formed during the unloading cycle and in the negative loading (pulling) regime. However, the JKR solution is restricted to elastic sphere-to-sphere contact [104]. When the normal force is low, the contact area between the two elastic bodies is larger than that predicted by the Hertz model and tends towards a constant finite value as the normal force is reduced to zero. In addition, the contact area closely follows the Hertz theory when the normal force is high. The JKR theory may be applied to tips with a large curvature radius (most applicable to macroscopic bodies) and small stiffness. This kind of system is termed strongly adhesive.

The adhesion force between two rigid spheres can be described as [100]

$$F_{\text{adh}} = -2\pi R \Delta\gamma \tag{4.12}$$

$$\Delta\gamma = \gamma_1 + \gamma_2 - \gamma_{12} \tag{4.13}$$

where $\Delta\gamma$ is called the 'work of adhesion' per unit area, R is the combined curvature radius of the two bodies, as shown in Eq. (4.5). This corresponds to both the Bradley model and DMT model of adhesion. The elastic adhesion model in JKR provides

$$F_{\text{adh}} = -\frac{3}{2}\pi R \Delta\gamma \tag{4.14}$$

which considers adhesion over the contact area, and an elastic response of the spheres. Based on this model, the contact area A can be easily deduced from its contact
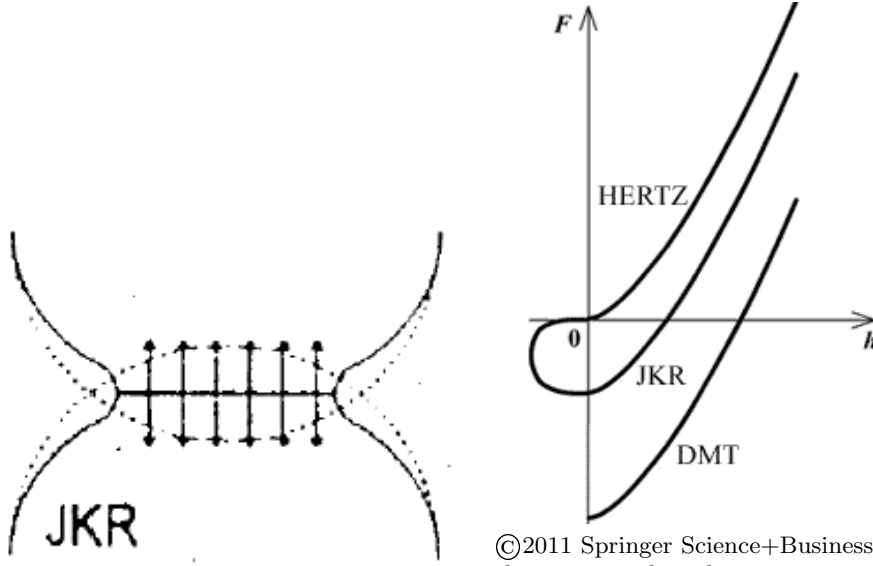
©1987 Cambridge University Press, reprinted with permission from Johnson [104]

(a) JKR: fully elastic model considering adhesion in the contact zone

©2011 Springer Science+Business Media, reprinted with permission from Fischer-Cripps [117]

(b) Plot of the forces and the penetration depth of the JKR, Hertz and DMT model

radius, i.e,

$$a_0 = \left[\frac{3R}{4E^*} \left(F_N + 3\pi R\Delta\gamma + \sqrt[2]{6\pi R\Delta\gamma + (3\pi R\Delta\gamma)^2} \right) \right]^{1/3}. \qquad (4.15)$$

The displacement is given by

$$s = \frac{a_0{}^2}{R} - \frac{2}{3}\sqrt{\frac{6\pi\Delta\gamma}{E^*}}. \qquad (4.16)$$

The JKR expression result in contact radius approaches that of the Hertz contact theory for vanishing work of adhesion ($\triangle\gamma$). The difference of the two models becomes significant when the normal force F_N is small [104].

Tabor [118] showed that the discrepancy between the DMT (eq. (4.13)) and JKR (eq. (4.14)) models can be resolved by a unified theory parametrised by the Tabor parameter, defined as

$$\mu_0 = -\frac{R^{1/3}\Delta\gamma^{2/3}}{\sigma E^{*2/3}} \qquad (4.17)$$

where E and R are the combined Young's modulus and curvature radius as shown in Eq. (4.5), and σ is the characteristic atom-atom distance. This coefficient determines whether or not the sphere maybe treated as rigid. μ expresses the relative importance of the adhesive interaction versus the elastic deformation. The JKR theory is more appropriate for to large, compliant spheres when μ_0 is large, e.g. > 5, which is

typical for soft organic materials.

4.2.4 Greenwood-Williamson contact theory

Greenwood and colleagues [28, 119] proposed the Greenwood-Williamson (GW) theory, which is to extend Hertz contact theory by considering one of the contact surfaces as being rough. The GW theory assumes [120]:

1. the rough surface is isotropic;

2. asperities are spherical near their summits;

3. all asperity summits have the same radius of curvature and their heights vary stochastically around an average value;

4. there is no interaction between neighbouring asperities; and

5. there is no bulk deformation.

The contact occurs at a number of discrete micro contacts. The total force is the sum of all of the equal "summit" forces, which can be still calculated using Hertzian contact theory. Therefore, the total contact area is the sum of the individual "micro" contact areas. The asperity summits can be approximated as spherical bumps with an equal radius of curvature R and with a Gaussian height distribution, as follows:

$$P_{\mathrm{h}} = \frac{1}{(2\pi)^{1/2} h^*} \exp\left(-\frac{h^2}{2h^{*2}}\right) \tag{4.18}$$

where h^* is the root mean square of the height distribution of the summits, given by

$$h^* = \sqrt{\overline{h^2}}. \tag{4.19}$$

Because summits are considered instead of the asperities, h^* is related but not equivalent to the roughness parameter.

The separation distance between surfaces is defined as h_0, the contact will occur when the asperity $h > h_0$, and $h - h_0$ is defined as the 'penetration depth'. For a single contact, according to the Hertz contact theory, the radius of contact area is obtained as $\Delta a = R(h - h_0)$. Therefore, the contact area of a single asperity is

$$\Delta A = \pi a^2 = \pi R(h - h_0), \tag{4.20}$$

and the normal force on a single asperity is

$$\Delta F_{\mathrm{N}} = \frac{4}{3} E^* R^{1/2} (h - h_0)^{3/2}. \tag{4.21}$$

71

The total number of contacts, the total contact area, and the total normal force F_N are found through integration over all the asperities in contact, meaning that the integration must be performed over all height values from h_0 to infinity, resulting in

$$n = \int_a^b n_0 P_h \, \mathrm{d}h; \tag{4.22}$$

$$A = \int_a^b n_0 P_h \pi R(h - h_0) \, \mathrm{d}h; \tag{4.23}$$

$$F_N = \int_a^b n_0 P_h \pi \frac{4}{3} E^* R^{1/2} (h - h_0)^{3/2} \, \mathrm{d}h. \tag{4.24}$$

for the total numbers of contacts, total area and the total force, respectively. It can be seen as the bodies are pressed closer together (a decrease in h_0), their values increase exponentially due to the P_h term in the equations. The average contact area of an asperity can be calculated with

$$\langle \Delta A \rangle = \frac{A}{n} = \frac{\int_{h_0}^{\infty} n_0 P_h \pi R(h - h_0) \, \mathrm{d}h}{\int_{h_0}^{\infty} n_0 P_h \, \mathrm{d}h}. \tag{4.25}$$

By inserting the dimensionless variable $\xi = h/h^*$, and defining $\xi_0 = h_0/h^*$, one obtains:

$$\langle \Delta A \rangle = \pi R h^* \left(\frac{\int_{\xi_0}^{\infty} \exp(-\xi^2/2)(\xi - \xi_0) \, \mathrm{d}\xi}{\int_{\xi_0}^{\infty} \exp(-\xi^2/2) \, \mathrm{d}\xi} \right). \tag{4.26}$$

The results in [104] shown that the 'typical' range of average normal forces which correspond to a real contact area of between 10^{-2} and 10^{-4} of the apparent contact area is achieved when $\xi_0 = 2.5$ to 3.5. The value of ξ_0 is not realistic, because in this case, the contact will only exist at very few contact points. The ratio $\langle \Delta A / \pi R h^* \rangle$ changes in this range only marginally around the value 0.3. A good approximation for the average area of an asperity is therefore,

$$\langle \Delta A \rangle \approx R h^*. \tag{4.27}$$

The average value of a microscopic contact area remains practically constant as the forces changes by several orders of magnitude. In addition, the ratio of the total contact area to the normal force remains constant when the ξ changes from 2.5 to

3.5 [104].

$$\frac{A}{F_{\mathrm{N}}} = \frac{\int_{h_0}^{\infty} n_0 P_{\mathrm{h}} \pi R(h - h_0)\,\mathrm{d}h}{\int_{h_0}^{\infty} n_0 P_{\mathrm{h}} \frac{4}{3} E^* R^{1/2}(h - h_0)^{3/2}\,\mathrm{d}h} \tag{4.28}$$

$$= \left(\frac{R}{h^*}\right)^{1/2} \frac{3\pi}{4E^*} \frac{\int_{\xi_0}^{\infty} \exp(-\xi^2/2)(\xi - \xi_0)}{\int_{\xi_0}^{\infty} \exp(-\xi^2/2)(\xi - \xi_0)^{3/2}}$$

The ratio $(\frac{A}{F_{\mathrm{N}}})/(\frac{R}{h^*})^{1/2}\frac{3\pi}{4E^*}$ changes only marginally around the value of 1.4. Hence, a good approximation for the ratio of the real contact area can be approximated as:

$$\frac{A}{F_{\mathrm{N}}} \approx \left(\frac{R}{h^*}\right)^{1/2} \frac{3.3}{E^*} \tag{4.29}$$

The equation shows that when the surface roughness h^* increases, the contact area decreases, and hence the friction coefficient decreases as well.

4.2.5 Kotwal-Bhushan contact theory for non-Gaussian surfaces

Gaussian distribution of peak heights is often assumed in contact analyses in order to determine the real contact area. However, this is generally not true [121]. Positive skewness is produced by certain milling and turning operations. A kurtosis greater than three can be produced using laser polishing. When the actual surface height distribution is non-Gaussian, the assumption can lead to errors. According to [122], a contact model applicable for non-Gaussian surfaces should fulfil two objectives: 1) Correct trends for the real contact area can be predicted; 2) An optimum skewness and kurtosis can be determined for the smallest real contact area. The probability density function of the non-Gaussian asperity heights can be generated in two ways, either by 1) direct 3D surface topography profiling by imaging, or by 2) measuring the mean, standard deviation, skewness and kurtosis parameters and then fitting distribution basis functions such as Pearson system of frequency curves in order to obtain a synthetic distribution matching those parameters [122]. Once the probability distribution function is known, the contact model can be built using GW modelling approach described in the previous section of 4.2.4.

It is convenient to use standardized variables and describe heights in terms of the equivalent standard deviation of the peak asperities, σ, of the two surfaces given by

$$\sigma = \sqrt{\sigma_1^2 + \sigma_2^2} \tag{4.30}$$

where σ_1 and σ_2 are the standard deviations of the peak asperities of the two contacted surfaces. This equation is valid if the random distributions are independent.

The surface density of asperities η is defined as

$$\eta = n_0/A_\mathrm{a} \tag{4.31}$$

where A_a is the nominal contact area, n_0 is the nominal contact number of asperity peaks. Incorporating into equations (4.22), (4.23) and (4.24) results in:

$$n = \eta A_\mathrm{a} F_0(h') \tag{4.32}$$

$$A = \pi \eta A_\mathrm{a} R \sigma F_1(h') \tag{4.33}$$

$$F_\mathrm{N} = \frac{4}{3} \eta E^* R^{0.5} \sigma^{1.5} F_{1.5}(h') \tag{4.34}$$

where h' is the standardized separation given by d/σ and

$$F_\mathrm{N}(h') = \int_{h'}^{\infty} (s - h)^n p^*(s)\, \mathrm{d}s \tag{4.35}$$

where $s = z/\sigma$, $p^*(s)$ is the standard height distribution, normalised such that its standard deviation equals unity.

Using the contact model described, the normalised load is $\frac{F_\mathrm{N}}{\eta A_\mathrm{a} E^* R^{0.5} \sigma^{1.5}}$, the normalised number of contacts is $\frac{n}{\eta A_\mathrm{a}}$, the normalised real area of contact is $\frac{A}{\pi \eta A_\mathrm{a} R \sigma}$. The normalised mean asperity contact area is the ratio of the normalised real area of contact to the normalised number of contacts. Finally, the normalised mean contact pressure is the ratio of the normalised load to the normalised real area of contact [73, 114].

4.2.6 Persson contact theory

Motivated by rubber friction, Persson and colleagues developed a contact theory suitable for randomly rough surfaces [106, 107, 123].

The Persson model is valid not only when the area of real contact is small compared to the nominal contact area but is particularly accurate when the squeezing force is so high that nearly complete contact occurs within the nominal contact area [125, 126]. Fig. 4.3 illustrates the contact between two solids at increasing magnification ζ. At low magnification ($\zeta = 1$) it looks as if complete contact occurs between the solids at many macro-asperity contact regions; but when the magnification is increased, roughness manifests in a smaller length scale, and only partial contact occurs at the asperities. In many cases, the local pressure at asperity contact regions at high magnification will become so high that the material yields plastically before reaching the atomic dimension. In these cases, the size of the real contact area will be determined mainly by the yield stress of the solid.
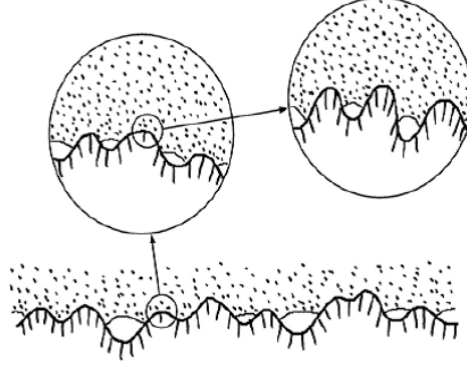
Figure 4.3: A rubber block (dotted area) in adhesive contact with a hard rough substrate (dashed area).

The magnification ζ refers to some (arbitrary) chosen reference length scale. This could be set to the lateral size L of the nominal contact area, in which case $\zeta = L/\lambda = q/q_{\mathrm{L}}$, where λ is the shortest wavelength roughness which can be resolved at magnification ζ. The roll-off wavelength $\lambda_0 = 2\pi/q_0$ is the reference length so that $\zeta = \lambda_0/\lambda = q/q_0$. Let us define the stress distribution at the magnification ζ:

$$P(\sigma, \zeta) = \langle \delta(\sigma - \sigma(x, \zeta)) \rangle \tag{4.36}$$

Here $\sigma(x, \zeta)$ is the stress at the interface calculated when only the surface roughness components with wave vector $q < \zeta q_{\mathrm{L}}$ is included. The angular brackets $\langle \rangle$ denotes the ensemble average, which is in most cases equivalent to the average over the surface area.

$$P(\sigma, \zeta) = \frac{1}{A_0} \int \mathrm{d}x^2 \delta(\sigma - \sigma(x, \zeta)) \tag{4.37}$$

Where A is the area of contact. If the integral in Eq. (4.37) would be over the whole surface area A_0 then $P(\sigma, \zeta)$ would have a delta function $[(A_0 - A)/A_0]\delta(\sigma)$ but this term is excluded with the definition Persson used. The area of real contact, projected on the xy-plane, can be obtained directly from the stress distribution, since from Eq. (4.37).

$$\frac{A(\zeta)}{A_0} = \int \mathrm{d}\sigma P(\sigma, \zeta) \tag{4.38}$$

we will often denote $A(\zeta)/A_0 = P(\zeta)$, L is the diameter of the nominal contact area between the solids and λ is the shortest surface roughness wavelength which can be detected at the resolution ζ.

Assuming complete contact one can show that $P(\sigma, \zeta)$ satisfied the diffusion-

like equation

$$\frac{\partial P}{\partial \zeta} = f(\zeta)\frac{\partial^2 P}{\partial \sigma^2}, \tag{4.39}$$

and

$$f(\zeta) = \frac{\pi}{4}\left(\frac{E}{1-\nu^2}\right)^2 q_{\mathrm{L}}q^3 C(q) \tag{4.40}$$

where $q_{\mathrm{L}} = 2\pi/L$ and $q = \zeta q_{\mathrm{L}}$. It is now assumed that Eq. (4.2.6) holds locally also when only partial contact occurs at the interface. The calculation of the stress distribution in the latter case involves solving Eq. (4.2.6) with appropriate boundary conditions.

If a rectangular elastic block is squeezed against the substrate with the (uniform) stress σ_0, then at the lowest magnification $\zeta = 1$ where the substrate appears flat, we have

$$P(\sigma, 1) = \zeta(\sigma - \sigma_0) \tag{4.41}$$

which forms an 'initial' condition. In addition, the two boundary conditions along the σ-axis are necessary in order to solve Eq. (4.2.6). For elastic contact, $P(\sigma, \zeta)$ must vanish as $\sigma \to \infty$. In the adsense of an adhesion interaction, the stress distribution must also vanish for $\sigma < 0$ since no tensile stress is possible without adhesion. Eq. (4.2.6) is easy to solve with the 'initial' condition Eq. (4.41) and the boundary condition $P(0, \zeta) = 0$. The area of (apparent) contact when the system is studied at the magnification ζ is given by

$$\frac{A(\zeta)}{A_0} = \frac{1}{\sqrt{\pi}}\int_0^{\sqrt{G}} e^{-x^2/4}dx = erf(1/2\sqrt{G}) \tag{4.42}$$

Where

$$G(\zeta) = \frac{\pi}{4}\left(\frac{E}{(1-\nu^2)\sigma 0}\right)\int_{q_{\mathrm{L}}}^{\zeta q_{\mathrm{L}}} q^3 C(q)dq \tag{4.43}$$

When the squeezing force $F_{\mathrm{N}} = \sigma_0 A_0$ is so small that $A \ll A_0$, the equation above reduce to $A = \alpha F_{\mathrm{N}}$ with α given by

$$\alpha = \kappa\frac{1-\nu^2}{E}\left(\int d^2q q^2 C(q)\right)^{-1/2} \tag{4.44}$$

where $\kappa = (8\pi)^{1/2}$.

The Persson contact theory can also predict that the contact area increases linearly with the squeezing force F_{N} as long as the contact area is small compared to the nominal contact area. It has been shown that the Persson contact theory is in good agreement with the numerical calculations [109]. The analytical model, in addition to providing deeper insight into the nature of the area of contact, can be

applied to surfaces with arbitrary surface roughness with only a small computational effort. The theory can also be applied to viscoelastic solids by treating the elastic modulus as a complex variable on frequency. The theory plays an important role in the theory of sliding friction for visco-elastic materials such as rubber [105–107].

4.3 Measuring the Young's modulus of the artificial fingertip
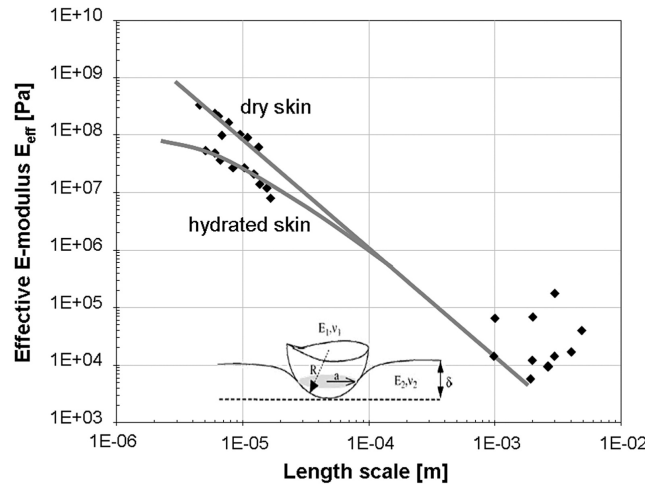
©2011 Elsevier, reprinted with permission from Masen [9]

Figure 4.4: Effective Young's modulus as a function of length scale for dry and hydrated skin

According to the various contact models, in order to calculate the contact area, the Young's modulus of human skin is an essential input parameter. It is also important for an artificial finger material to have similar Young's modulus to simulate the friction behaviour of human skin. Skin elasticity is a function of the Length scale of the contact [127, 128]. The effective elastic modulus of human skin decreases several orders of magnitude when the length scale increases Pailler-Mattei et al. [50], Tobin [129], Pailler-Mattei, Bec and Zahouani [130] and van Kuilenburg, Masen and van der Heide [131]. At an indentation depth of $10 \, \mu m$, the effective elastic modulus was shown to decrease from $0.15 \, MPa$ to $0.015 \, MPa$ when the radius of curvature of the indenter increases from $10 \, \mu m$ to $10 \, mm$ [131–133]. Fig. 4.4 illustrates how the effective Young's modulus depends on the length scales [9]. The appropriate value of E_{eff} to be used should be determined at the correct length scale and under representative conditions. In addition, the composition and properties of different skin layers will also affect the elasticity variation. The effective elastic modulus of

77

skin also depends on variables such as age, gender and environmental conditions (e.g. skin moisture).

The materials that made up the artificial fingertip are elastic and the inertial effect can be ignored. The hardness of silicone rubber used in this thesis are specified in the Shore hardness scales. The Shore-A scale (S_A) can be converted to Young's Modulus E (in MPa) using $\log_{10} E = (S_A \times 0.0235 - 0.6403)$ for $20 < S_A < 80$ [134]. This is only an approximation as the true value depends on the thickness of the material. For the artificial finger, the Young's moduli of the silicone cover layer, the silicone filler layer and the aluminium bone layer are, respectively, $0.9486\,\text{MPa}$, $0.7499\,\text{MPa}$ and $70\,\text{GPa}$. All of these values were supplied to the Abaqus FEM software.

Due to the multilayered nature of the finger, it is difficult to envision how each layer affects the Young's modulus of the artificial fingertip. In this case, the materials constituting each layer were separately subjected to micro-indentation. Then, the artificial fingertip was subjected to micro- and nano-indentation. Based on experience, the maximum deformation during friction contact is known to be less than about $0.6\,\text{mm}$, limited by the maximum applied contact force of $2\,\text{N}$. Because of this, the Young's modulus was measured when the deformation was smaller than $0.6\,\text{mm}$.

4.3.1 Theory of micro-indentation

The mechanical strength of the multilayered artificial finger is determined by the mechanical strength and the viscosity of the substrates and the curing catalysts from which each layer was made. Depth sensing micro-indentation has been widely used to characterise mechanical properties of various materials, in particular soft materials [135]. Micro-indentation has been well recognised for characterising the mechanical properties of solid materials due to its non-destructive approach. The rubber is often idealised as incompressible due to the structure of rubber containing cross-linked polymer chains with covalent bonding which makes rubber exhibit a high bulk modulus.

Although the Hertz contact theory and indentation methods are suitable for soft materials, some methodological consideration needs to be first addressed due to the assumptions of the theory (see Section 4.2.2) [136]. Several of the assumptions have been listed plus additions to the classical Hertz contact theory and these assumptions will be addressed with the practical application and restrictions.

A micro-indentation experiment involves specifying the continuous loading parameters and measuring the depth of indentation into the material. Analysis of the

measured force-displacement curves uses contact theory with mathematical principles regarding spherical and conical indentation to determine the Young's modulus.

In this thesis, the experiments were carried out by a Stevens CR Analyser. Observing the assumptions of the Hertz contact theory, the physical dimensions of the materials should be much larger than the dimensions of the contact surface, typically at least 10 times the radius of the indenter [137], such that the material is able to demonstrate continuous and non-conforming properties. This ensures the stresses that arise due to the contact dissipate at the opposite end of the body. The spherical indenter used in experimentation was designed with this consideration. The loads applied was static, which allows for seismic dissipation of energy (vibrations or sound waves) during the collision between the two objects to be neglected. Because the diameter of the artificial fingertip is 15 mm, the radius of sphere indenter chosen was 1 mm so that the deformation of the artificial fingertip surface is assumed to be small. This reduces geometric non-linearities that arise due to large deformations. For the individual analysis of the two layers (cover layer and filler layer), each of them was made from the same rubber type as the two layers in the artificial fingertip, with a square cross-section of 15 mm × 15 mm—a similar footprint as the artificial fingertip. The cover layer sample had a thickness of 2 mm and the filler sample had a thickness of 3 mm. Each set of measurement was repeated 5 times.

The micro-indentation theory is valid for small deformations caused by a non-adhesive elastic sphere against a flat surface. According to Hertz contact radius equation in (4.4), a spherical indenter with a specified radius R causes an indentation depth δ given by

$$\delta = \frac{a^2}{R} = \left[\frac{3F_{\mathrm{N}}}{4E^*\sqrt{R}} \right]^{2/3} \tag{4.45}$$

when the normal force F_{N} is applied. In addition, Eq. (4.4) and Eq. (4.45) are used to calculated the Young's modulus of the test material [138]. For the rubber materials, the Poisson's ratio is assumed to be 0.5.

The Stevens CR Analyser measures the depth of indentation when a H1KS-0088 force transducer applies a set loading. The silicon rubber from which the artificial fingertip cover was made had a Shore-A hardness of 23. The Shore hardness was the basis of selection as the Young's modulus was not provided from the distributor initially.

Fig. 4.5 shows the micro-indentation measurement results of the Young's modulus for the artificial fingertip using Stevens CR Analyser. The measured surface mechanical properties (hardness and Young's modulus) vary depending on the indentation depth and load due to the indentation size effect [139, 140]. Here,

(a) Under different displacements

(b) Under different normal forces
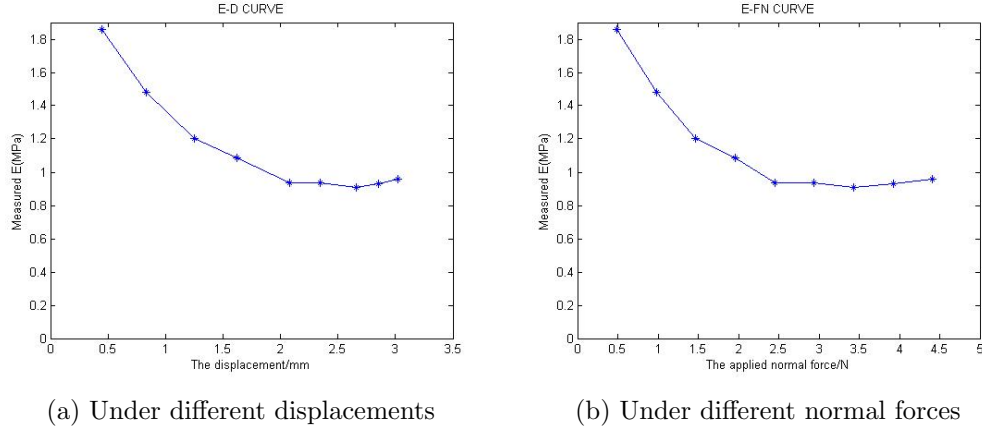
Figure 4.5: Measurement of the Young's modulus measurement of the artificial fingertip

Table 4.1: Young's modulus measurement results on the multilayer artificial finger and its constituent materials

Part	Cover	Filler	Bone (Aluminium)	Combined finger
Young's modulus (MPa)	1.25	0.742	70×10^3	0.945

we take an average of the Young's modulus by considering the asymptotic stiffness at high loads (when load > 2N), resulting in a stiffness value of 0.945 MPa. Similar characterisations were performed on the materials that made up the cover and filler parts of the artificial fingertip independently. The results are shown in table 4.1.

4.3.2 Nano-indentation

Theory

Nanoindentation is an indentation test in which the length scale of the penetration is measured in nanometres rather than micrometres or millimetres, the latter being common in conventional hardness tests. As with conventional micro-indentation, nanoindentation can also be used to calculate elastic modulus, strain-hardening exponent, fracture toughness (for brittle materials), and viscoelastic properties.

In indentation testing, the most common types of indenter is either blunt or sharp. The most common types of blunt indenter are the spherical and the spheroconical tips. The most common types of blunt indenters are the conical, the four-sided Vickers indenter and the three-sided Berkovich indenter. An important result for the Hertz contact equations occurs when the derivative of the force with respect to the depth is taken. This quantity, $\frac{dP}{dh}$, is the contact stiffness, where P
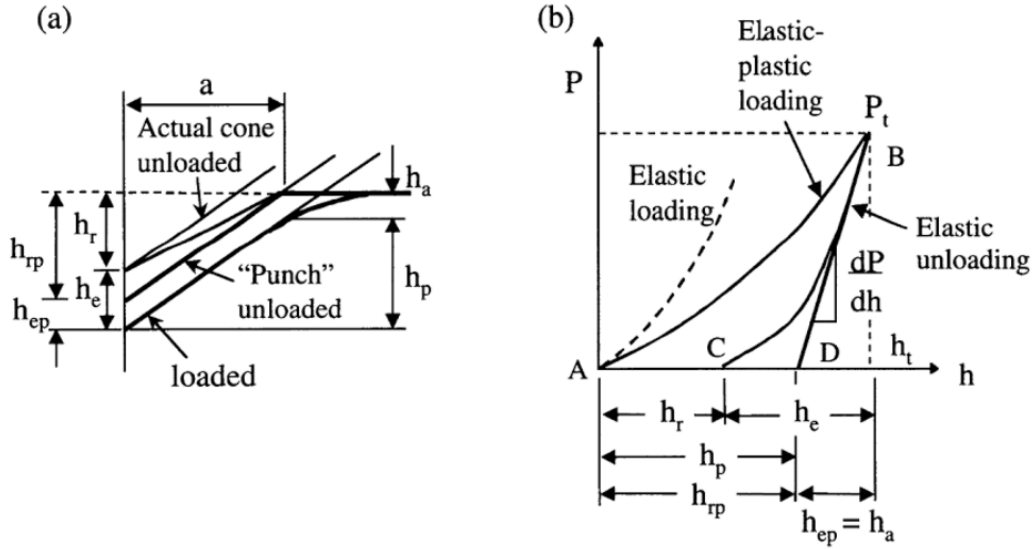
Figure 4.6: (a) The indenter and specimen surface at full load and unload for a conical tip (b) Load versus displacement for elastic-plastic loading followed by elastic unloading
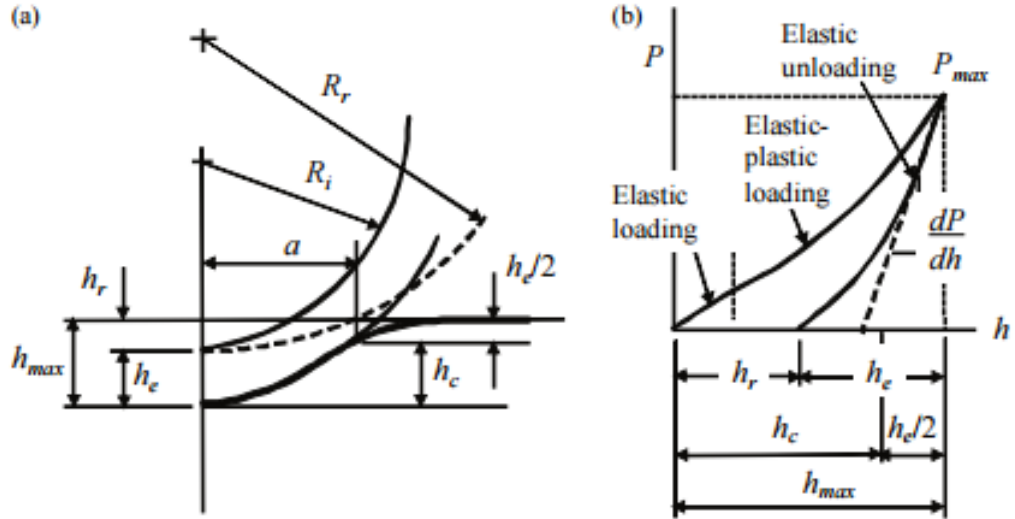
Figure 4.7: Geometry and compliance curve of loading for a spherical tip
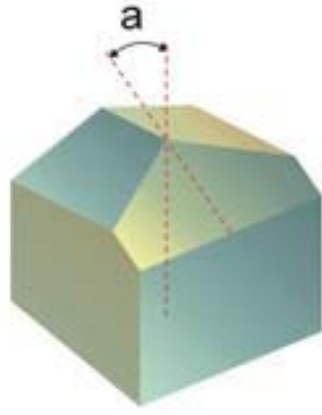
(a) The Berkovich indenter   (b) The sphere-conical indenter

Figure 4.8: The shape of indenters

is the normal force and h is the penetration depth. For example, in the case of a spherical indenter, Oliver and Pharr [141] gives

$$\frac{dP}{dh} = 2\sqrt{R\left(h - h_e\right)}E^* \tag{4.46}$$

where h_e is the elastic depth of penetration for unloading (see Fig. 4.6b); $R = \left(R_i^{-1} + R_r^{-1}\right)^{-1}$ and R_i is the radius of the spherical indenter and R_r is the curvature of the residual unloaded impression (see Fig. 4.7); E^* is the combined elastic modulus of the indenter and the specimen. The contact depth $h_c = 0.5\left(h_{max} + h_e\right)$. Note that Hertz contact analysis is only valid when the depth of penetration h is small relative to the radius of the sphere.

Similar method applies to other indenter shapes to determine the hardness and modulus [141]; who gave

$$\beta E^* = \frac{1}{2}\frac{dP}{dh}\frac{\sqrt{\pi}}{\sqrt{A}} \tag{4.47}$$

where A is the projected contact area and β is a correction term depending on the tip geometry and is close to unity. Eq. (4.47) forms the basis of analysis techniques in nano-indentation testing where the contact stiffness is evaluated at the beginning of the unloading response. Indentation tests on many materials result in both elastic and plastic deformation of the specimen material. In brittle materials, plastic deformation most commonly occurs with pointed indenter such as Vickers diamond pyramid.

The Berkovich indenter is shown in Fig. 4.8a [142]. It is generally used in small-scale indentation studies and has the advantage that the edges of the pyramid are more easily constructed to meet at a single point compared to a four-sided Vickers pyramid. Thus it can allow a more precise control over the indentation process. The face angle of the Berkovich indenter used in this thesis is 65.27°, which gives the same actual surface area to depth ratio as a Vickers indenter. The radius of the tip is smaller than 0.2 μm. The mean contact pressure is usually determined from a measure of the contact depth of penetration, h_c. Once h_c is found, then the projected area of contact is calculated and the hardness computed from $H = P/A$, i.e.:

$$A = 3\sqrt{3}h_c^2\tan\theta^2 \tag{4.48}$$

where $\theta = 65.27°$. It evaluates to

$$A = 24.494h_c^2 \tag{4.49}$$

and hence the mean contact pressure, or hardness, is

$$H = P/A = \frac{P}{24.5h_c^2} \tag{4.50}$$

Fig. 4.6 shows the schematic of the indenter and specimen surface after full loading and unloading of a conical indenter on the left and a load versus displacement curve for elastic-plastic loading followed by elastic unloading on the right. h_r is the depth of the residual impression, h_{max} is the depth from the original specimen surface at load P_{max}, h_e is the elastic displacement during unloading, and h_a is the distance from the edge of the contact to the specimen surface at full load. Upon elastic reloading, the tip of the indenter moves through a distance h_e, and the eventual point of contact with the specimen surface moves through a distance h_a.

Test procedures

A typical nanoindentation test cycle consists of an application of load followed by an unloading sequence, but there are many variations. The load may be applied continuously until the maximum load is reached, or as a series of small increments. At each load increment, a partial unloading may be programmed to provide a measurement of stiffness of the contact, which is important for measuring changes in the elastic modulus or the hardness with penetration depth. Contact stiffness may also be found by superimposing a small oscillatory motion onto the load signal.
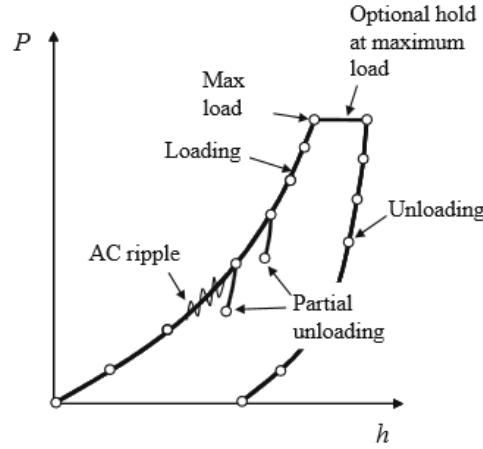
Figure 4.9: Various components of a nano-indentation test cycle

The indentation instrument may be set into either load or depth control. In load control, the user specifies the maximum test force (usually in mN) and the number of load increments or steps to use. The progression of load increments may be typically set to be a square root or linear progression. A square root progression attempts to provide equally spaced displacement readings. In a depth control mode, the user specifies a maximum depth of penetration. It should be noted that most nanoindentation instruments are inherently load-controlled devices, but true load and depth control is available if there is a feedback loop employed which can take a signal from either a force or displacement sensor. It is customary for a nanoindentation instrument to allow for a dwell or hold period at each load increment and at maximum load. The dwell settings at each load increment allow the instrument and specimen to stabilise before depth and load readings are taken. Hold period data at maximum load can be used to measure creep within the specimen. Hold measurements are carried out at the end of indentation to minimise any effects from creep within the specimen. The test cycle is shown in Fig. 4.9.

For the case of a Berkovich indenter, the loading curve can be found from the addition of h_c and h_a as shown in Fig. 4.6. For a load of P_{max},

$$h_c = \frac{P_{max}}{3\sqrt{3}H\tan\theta^2}. \tag{4.51}$$

The distance h_a is most easily determined from the intercept of the slope of the unloading curve at maximum load P_{max} with $P = 0$, as shown in Fig. 4.6. This is

given by

$$h_{\mathrm{a}} = \varepsilon \frac{\pi P_{\max} H}{2E^*} \qquad (4.52)$$

where ε is equal to 0.72, or, as is usually used for a Berkovich indenter, to 0.75. The total depth $h_{\max}$ is thus

$$h_{\max} = \sqrt{P_{\max}} \left[\frac{1}{\sqrt{3\sqrt{3}H\tan\theta^2}} + \varepsilon \frac{\sqrt{H\pi}}{2E^*} \right]. \qquad (4.53)$$

This equation is applicable at any load P given a depth of penetration h and so the subscripts 'max' can be discarded if desired [117].

4.3.3 Nano-indentation results with different indenters

The choice of the indenter tip is important and depends on upon the information one wishes to obtain from the indentation test. The representative strain in the specimen material, for example, depends solely on the effective cone angle of the indenter. The sharper the angle, the great the strain. According to Tabor, the representative strain for a conical indenter is given by $\varepsilon = 0.2\cot\alpha$ [143]. For a Berkovich and a Vickers indenter, this evaluates to about 8%. Sphere intenders offer a gradual elastic to elastic-plastic response. The representative strain varies as the load is applied is given by $\varepsilon = 0.2\frac{a}{R}$ [143]. A fully developed plastic zone will be obtained when measuring hardness using a spherical indenter. The spherical indentation strain will be smaller than that of the Berkovich tip. The changing strain throughout an indentation test with a spherical indenter enables the elastic and elastic-plastic properties of the specimen to be examined along with any strain-hardening characteristics.

Young's modulus measurement using a Berkovich tip
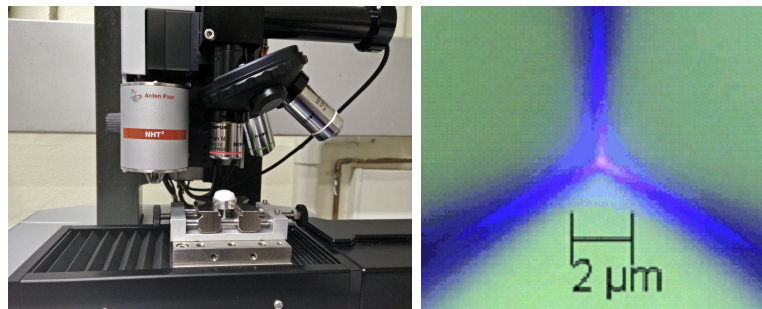
Figure 4.10: The nano-indentation setup and the Berkovich tip used

In order to better validate the true Young's modulus of the artificial fingertip, nanoindentation measurement of the artificial fingertip was carried out using the

Anton-Paar NHT[2] nano-indenter shown in Fig. 4.10. The instrument uses a camera with high resolution (0.25 µm pixels) in X-Y. The range of normal load supported is 1 mN to 500 mN. The load resolution is 20 nN and its depth resolution is 0.06 nm. The maximum penetration depth for this instrument is 200 µm. The Berkovich indenter, made of diamond, has a tip radius smaller than 0.2 µm. The artificial fingertip was measured under the tip by applying linear loading. In order to reduce the creep effect of the artificial fingertip, after reaching the maximum normal force, a pause of 15 seconds was applied to each measurement. The hardness and Young's modulus are calculated automatically by the software.
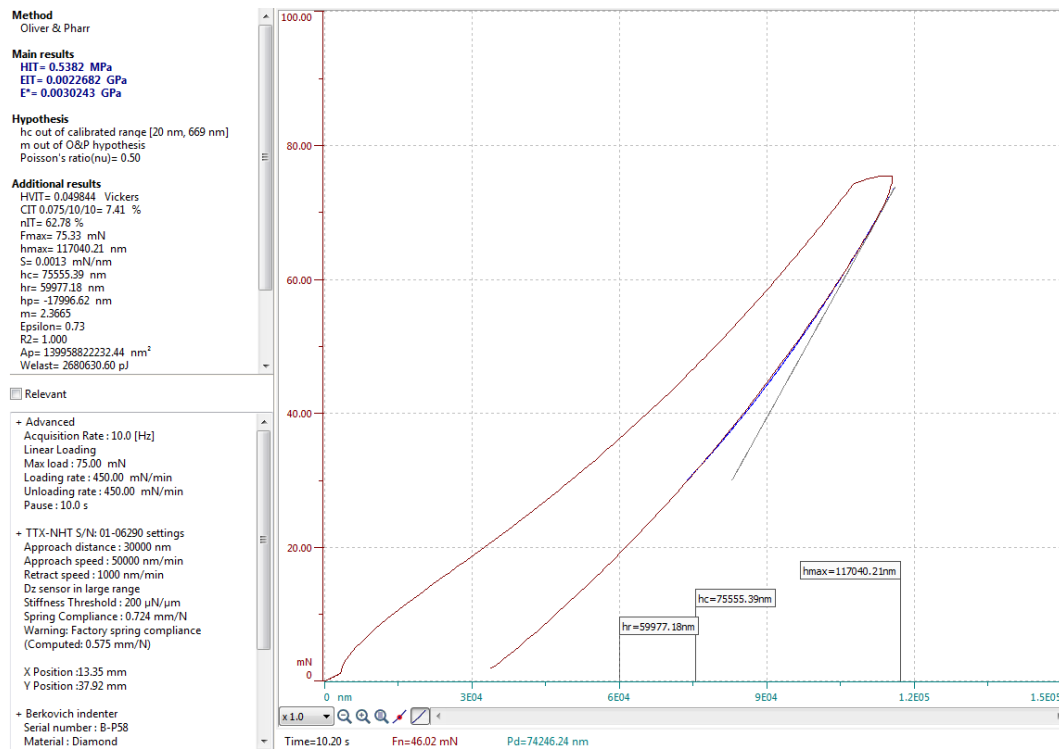
Figure 4.11: The Young's modulus measurement of the artificial fingertip ($P_{\max} = 75$ mN)

Fig. 4.11 shows the result from one nano-indentation experiment of the artificial fingertip. The maximum load was set to 75 mN. The loading rate was set to 450 mN min^{-1}. As shown in Fig. 4.12, the Young's modulus (the slope of the load curve) changes when the normal force changes. When the normal force was increased from 2 mN to 100 mN, the penetration depth increased from 25 µm to 160 µm. The Young's modulus was 2.2 MPa when the normal force was 70 mN. This is about 2 times higher than the micro-indentation estimate from 4.1. According to the contact radius measurements shown in Table 4.3, the penetration depth can

be calculated to be about 200 µm using the Hertz Contact theory. However, the maximum penetration depth of the nano-indenter is limited to 200 µm.
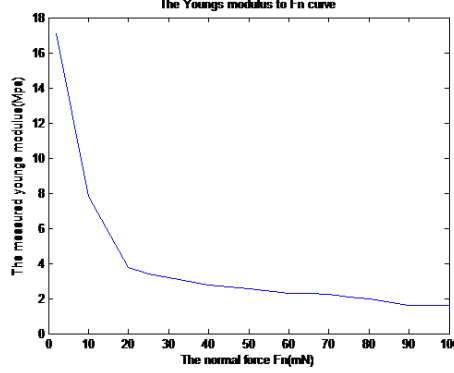
Figure 4.12: The Young's modulus measurement results by applying different maximum loads

Young's modulus measurement using a Sphero-conical tip

Spherical-capped indenters are increasingly popular because this type of indenter provides a smooth transition from elastic to elastic-plastic contact. Indenters can generally be classified into two categories: sharp or blunt. For soft materials, a sphero-conical tip is more suitable for preventing contact damage during indentation. Generally speaking, spherical-capped indenter is termed blunt. It is particularly suitable for measuring soft materials and for replicating contact damage in in-service conditions. Han, Sanei and Alisafaei [140], for example, shows that spherical intenders measure a stable Young's modulus value regardless of penetration depth for soft materials, whereas a Berkovich tip resulted in measured stiffness changing upon different penetration depths. The response of the sample materials follows that predicted by the expanding cavity model or the elastic constraint model, depending on the type of specimen and magnitude of the load.

For this case, the hardness and indentation depth are calculated following the equations.

$$h_{\max} = h_{\mathrm{c}} + h_{\mathrm{a}} \tag{4.54}$$

$$h_{\mathrm{c}} = h_{\max} - \frac{h_{\max}}{2} \tag{4.55}$$

$$H = \frac{P}{A} \tag{4.56}$$

where A is the area of contact given by πa^2 with the term a being the radius of the circle of contact at $P = P_{\max}$. Elastic modulus is determined from the slope of the unloading curve or by the Hertz equation directly.

Compared with the Berkovich tip, the sphero-conical tip is much larger, whose radius is 20 μm. Limited to the maximum penetration depth of 200 nm, the maximum load that could be applied to the sample was found by trial-and-error to be 30 mN. As shown in Fig. 4.13, green lines represent the nanoindentation results by the sphero-conical tip, and blue lines represent the results by the Berkovich tip. sphero-conical tip penetration depth is much larger than the Berkovich tip. However, limited by the accuracy of the instrument, the Young's modulus was measured as 4 MPa, which is not satisfactory.
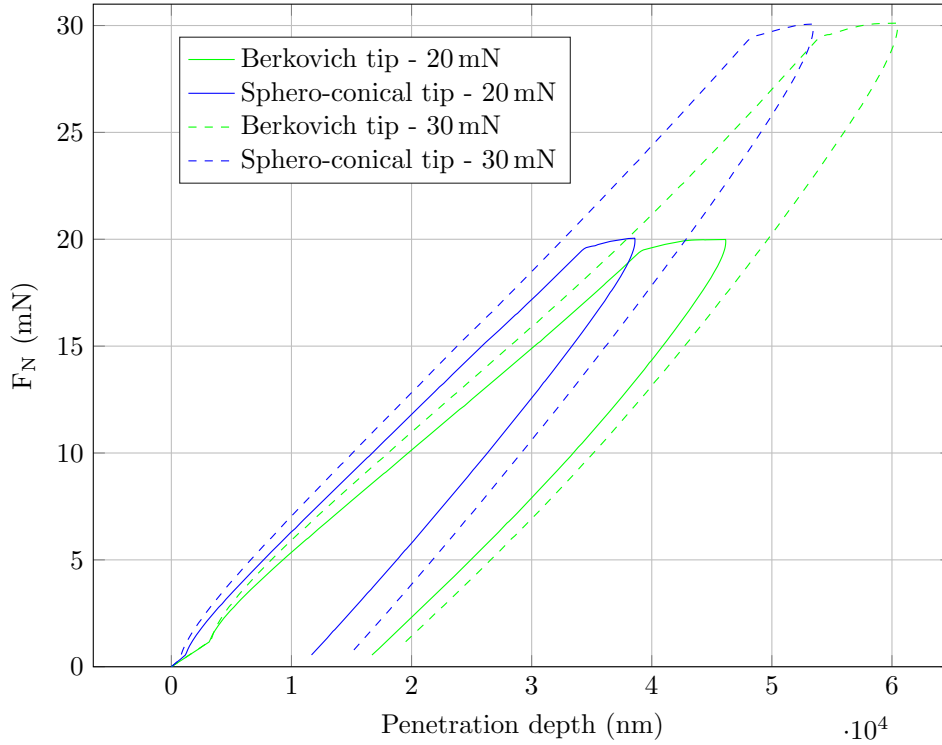
Figure 4.13: The indentation results for the artificial fingertip

4.4 Contact area measurement

4.4.1 Instrument Design

In order to better understand the contact mechanism between human fingertip friction and surfaces topography, a contact area measurement instrument, shown in
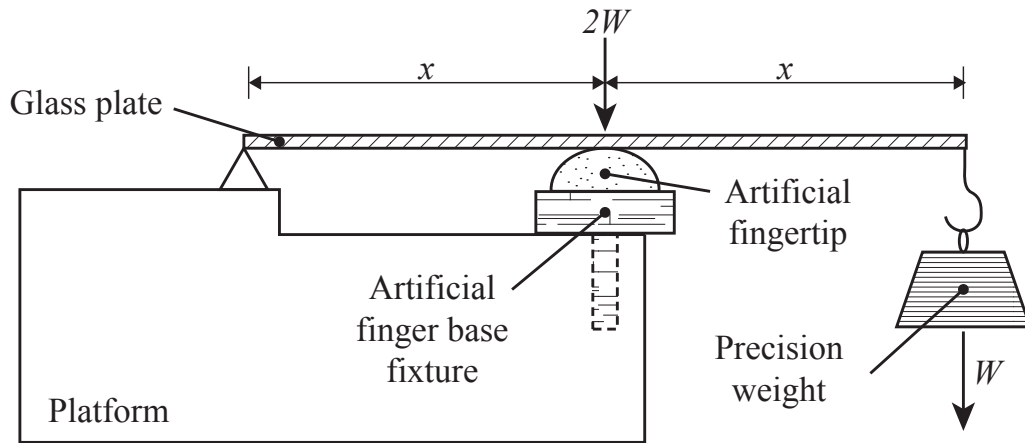
Figure 4.14: Schematic Diagram of the instrument
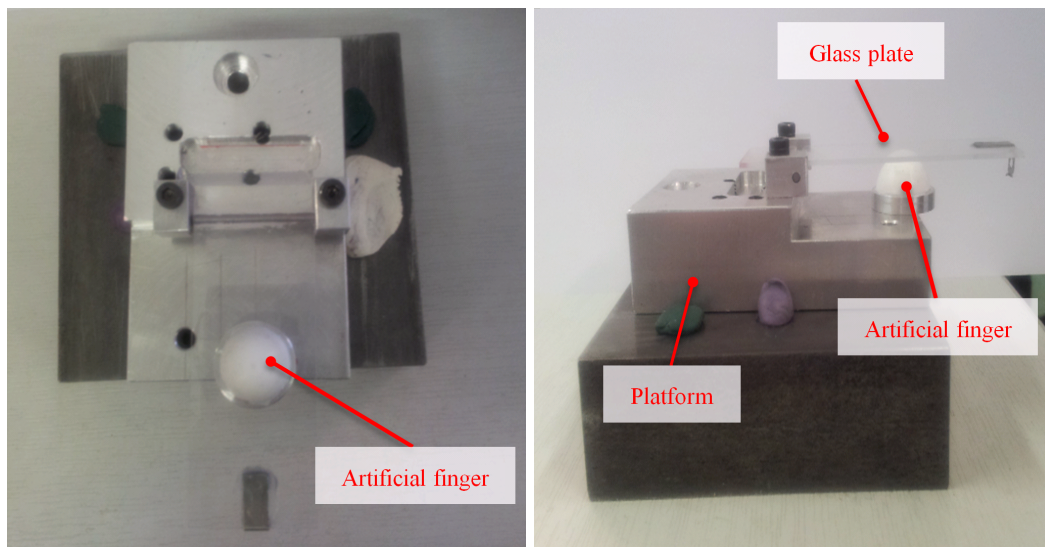
(a) Top view   (b) Side view

Figure 4.15: Contact measurement instrument

89

Fig. 4.15, was built. The schematic diagram of the instrument design is in Fig. 4.14.

Glass was chosen as the material for the plate because its Young's modulus is very similar to that of aluminium (about 70 GPa); more crucially, it is transparent— allowing an optical microscope, namely, the Bruker *ContourGT-K 3D* to be used to measure the contact area. According to Hertz contact theory, the choice of the material has a limited effect on the measurement as long as the material is highly rigid (i.e., its Young's modulus is high) and is flat (near infinite curvature radius), such that the effective contact radius and the effective combined Young's modulus only depends mostly on the fingertip [104]. The glass plate used was 1 mm thick and has a negligible weight of 0.2 g. The Bruker Through Transmissive Media (TTM) module shown in Fig.4.17 was used to compensate for interference fringes caused by the glass plate, by inserting another identical plate between the beam splitter and reference mirror.

4.4.2 Methodology

(a) Front view   (b) Side view
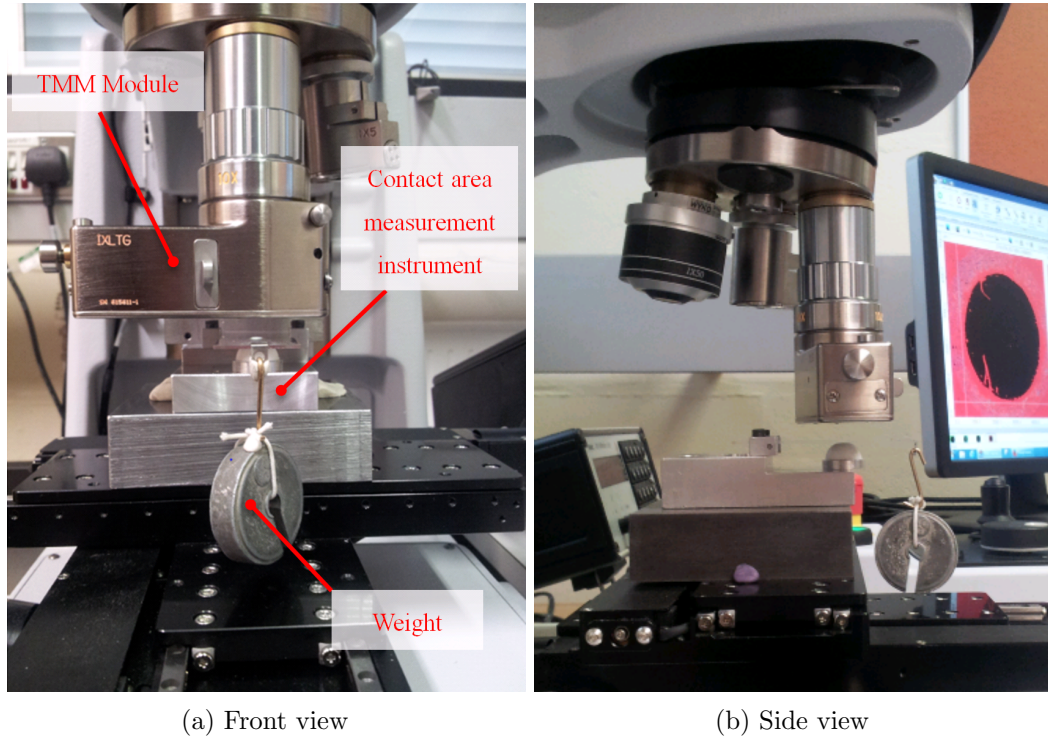
Figure 4.16: Contact measurement instrument

Contact areas were measured using the Bruker microscope with the TTM module mentioned. As shown in Fig. 4.16, the artificial finger was fixed on the
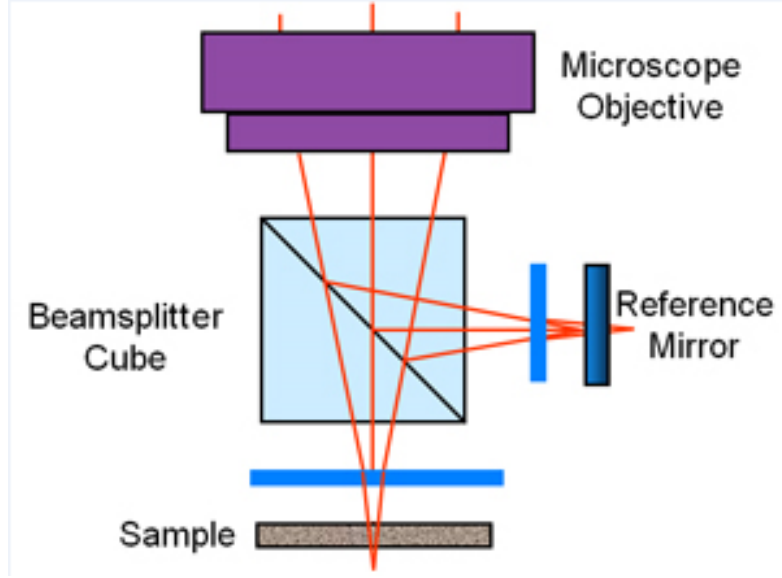
Figure 4.17: Schematic diagram of TTM module, reprinted from Bruker [144]

measurement instrument. The glass plate was fixed at one end and its centre rests freely on top of the artificial fingertip. Precision weights are suspended from the unfixed end of the plate to vary the normal force acting on the fingertip. According to the lever principle, the force acting on the artificial finger is half of the weight hanging on the unfixed side of the glass. The weights used were 20 g, 25 g, 50 g, 80 g, 100 g, 150 g and 200 g, resulting in corresponding normal forces of 0.392 N, 0.49 N, 0.98 N, 1.568 N, 1.96 N, 2.94 N and 3.92 N (to 3 significant figures).

4.5 Results and Analysis

4.5.1 Measurement Results

First of all, it is important to test the artificial fingertip's deformation under no load and under the weight of the glass plate (0.2 g, approximately 1.96 mN). Fig. 4.18a is the surface profile of the hemispherical fingertip measured without the glass plate nor the TTM module. Fig. 4.18b shows the results with the TTM module and glass plate. Here the black shadow represents the area of contact where the glass plate pressed against the artificial finger and covers the whole surface of the artificial fingertip. Comparing this to results shown later of the cases with loading applied, the shadow pattern under no load has negligible effects on the contact area measurement.

Fig. 4.19 shows the contact area measurement results obtained from the Bruker microscope when the weights were 50 g and 100 g. Part results for other
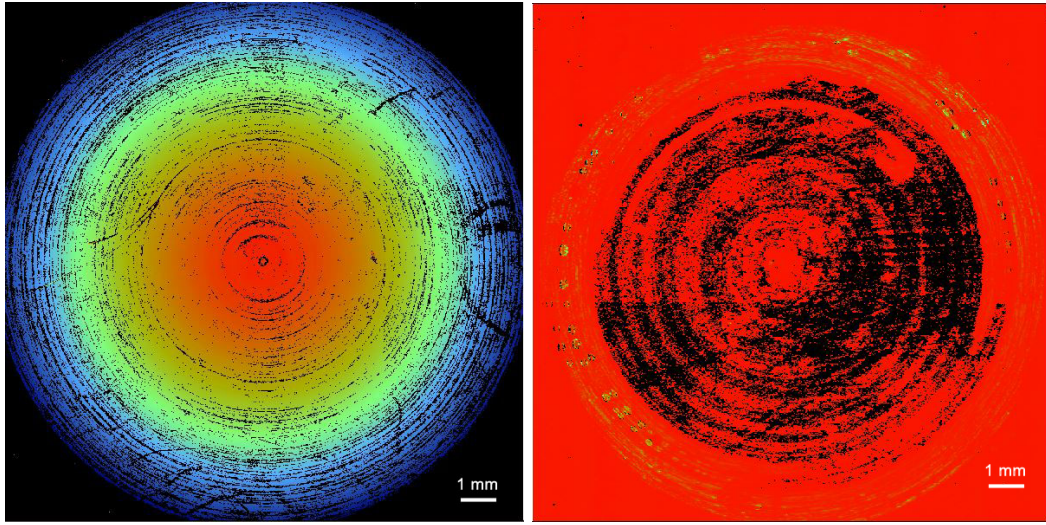
(a) The artificial fingertip image   (b) With TTM module and glass plate

Figure 4.18: Artificial finger surface metrology under the Bruker microscope

Table 4.2: Surface parameters of the artificial finger (units in µm)

R_a	R_p	R_q	R_t	R_v
0.246	0.445	0.484	15.568	15.123
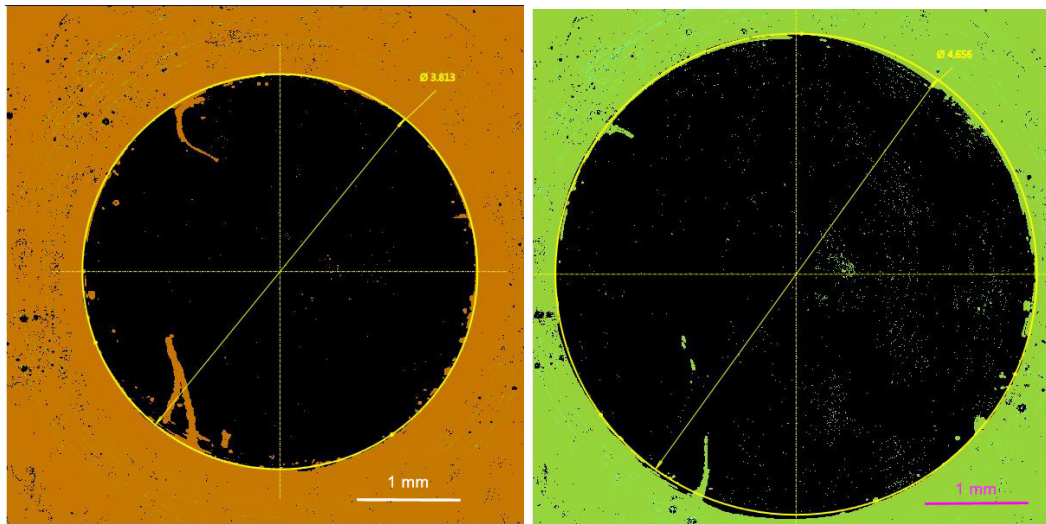
(a) Weight = 50 g   (b) Weight = 100 g

Figure 4.19: Contact area measurement results for 50 g and 100 g weights

weights are shown in Appendix A.3. For each weight, three points at the edge of the contact area guide the construction of a circle, and the contact radius is defined as the radius of the said circle. The radius of contact area increases with increasing weight (i.e. contact normal force). Based on the contact area measurement results, the next step is to analyse the contact mechanism between the surfaces.

Table 4.3: Contact radii and deformation depth under different weights (normal forces) (Experiment)

Weight (g)	Contact force (N)	Contact radius (mm)
20	0.39	1.350
25	0.49	1.492
50	0.98	1.906
80	1.57	2.045
100	1.96	2.302

4.5.2 Hertz contact theory, JKR contact theory and finite element modelling

According to the Hertz contact model, if an elastic body with curvature radius R indents a flat rigid surface (flat in the macroscopic sense that its curvature radius is infinite), it can be shown that the contact radius a is given by Eq. (4.4)

$$a_0 = \left(\frac{3F_\mathrm{N}R}{4E^*}\right)^{1/3} \tag{4.57}$$

where F_N, and E^* are respectively the normal force and Young's modulus of the elastic body. In addition to the relatively simple theory, a complex finite element model was also developed using the software Abaqus (see next section) to account for the structure and different layers of material used to construct the artificial fingertip. Since the artificial fingertip material is made of rubber—a relatively soft material— JKR model was also investigated to model the contact between the artificial fingertip and the glass plate.

The combined curvature radius of the artificial fingertip and the glass plate calculated according to Eq. (4.5) is $R = 0.0075\,\mathrm{m}$, $\Delta\gamma(\mathrm{rubber}) = 30\,\mathrm{mJ/m^2}$ and $E^* = 1.067\,\mathrm{MPa}$. Substituting these into Eq. (4.17), the Tabor coefficient is

$$\mu = \frac{(0.0075)^{1/3}(0.03)^{2/3}}{(\sigma \times 10^{-9})(1.067 \times 10^6)^{2/3}} = 5.3244 \times 10^3 \gg 5 \tag{4.58}$$

with $\sigma = 0.34$ nm. As $\mu > 5$, the contact model of the artificial fingertip should be analysed by JKR model [145]. Based on Eq. (4.15), the radii of contact area under different normal forces is given in 4.4.

Table 4.4: Contact radii under different normal forces (JKR simulation)

Weight (g)	Contact force (N)	Contact radius (mm)
20	0.39	1.314
25	0.49	1.391
50	0.98	1.687
80	1.57	1.943
100	1.96	2.082

In order to better understand the contact mechanism between the artificial fingertip and contacted surfaces, finite element models (FEM) were developed. As the artificial fingertip is composed of three different material layers (namely, the cover layer, the filler layer and the aluminium bone), the Abaqus CAE (Complete Abaqus Environment) FEM suite was used to model the component assembly, with the geometries and the material parameters of the three material layers accurately specified in the software. The Young's modulus settings for each layer was determined by the micro-indentation measurement results in Table 4.1. 20 000 elements were used in the FEM analysis; more mesh elements were used on the outside layer (cover layer) compared to the bone structure. The interface between the cover, filler layers and the bone have merged geometry (partitioned as different material but share mesh) to ensure displacement continuity at the interfaces. Boundary conditions were applied to fix the 'root' of the bone structure in translation and rotation. A maximum 0.5 mm displacement load, equal to about 2 N was applied i.e. Abaqus steadily increase the force until the surface of the fingertip achieves a displacement of 0.5 mm. The displacement-force curve of the centre of the contact was extracted. The total contact area results under the set of loading forces from the experiment are shown in Table 4.3. The von Mises stress distribution is shown in Fig. 4.20. The displacement and contact area were used in the subsequent modelling analysis. As shown in Fig. 4.21, the displacement-normal force curve follows a nonlinear relationship, and the contact area is not linearly proportional to the normal force because of the cover and filler layers the artificial fingertip being of different properties. Note that the plots involving contact area look jagged because the number of elements at the contact point in the 2D simulation is limited in number (see the deformed flat bottom of Fig. 4.20).

Fig. 4.22 plots the relationship between contact radius and normal force
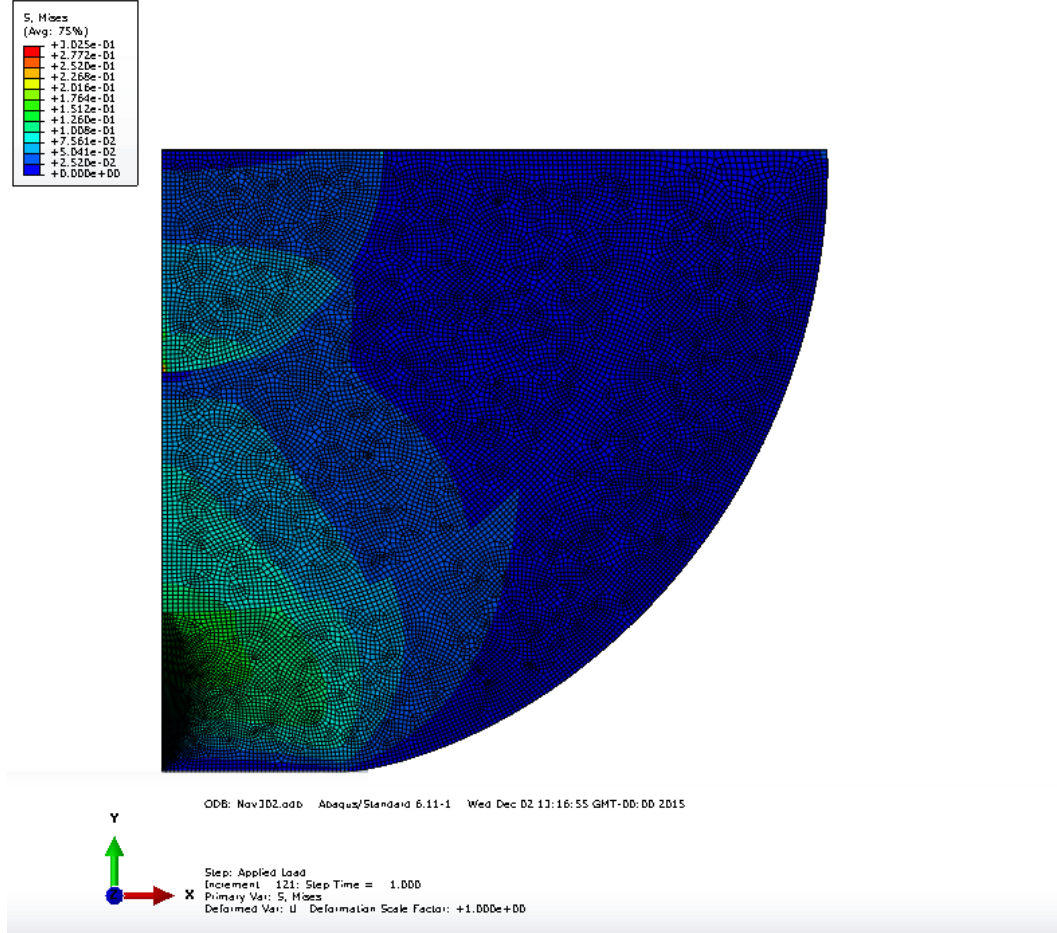
Figure 4.20: Analysis of the contact mechanism using the Abaqus software

Table 4.5: Contact radii under different normal forces (FEM Simulation)

Weight (g)	Contact force (N)	Contact radius (mm)
20	0.392	1.198
25	0.49	1.292
50	0.98	1.619
80	1.568	1.899
100	1.96	2.039
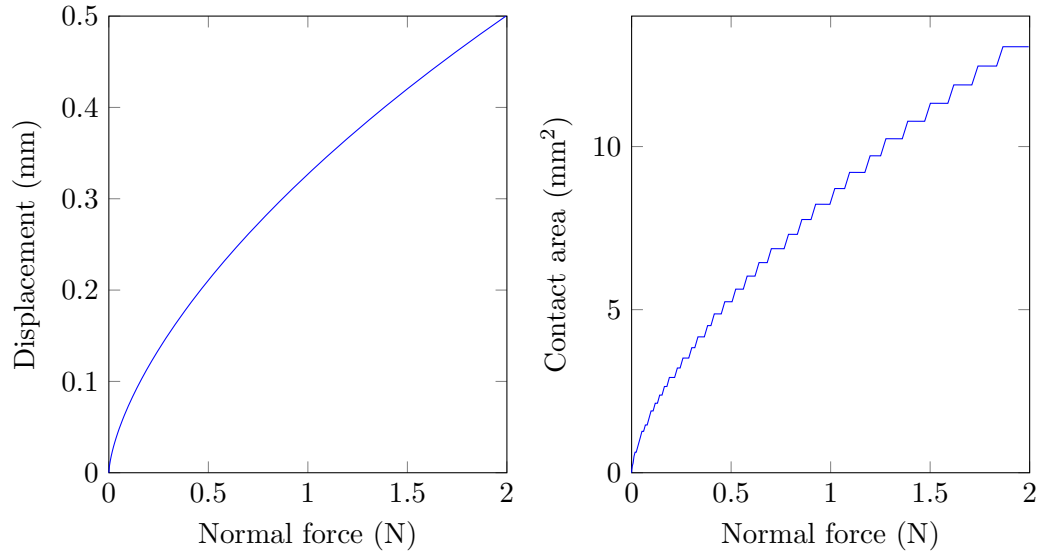
(a) The displacement—normal force curve

(b) The contact area—normal force curve
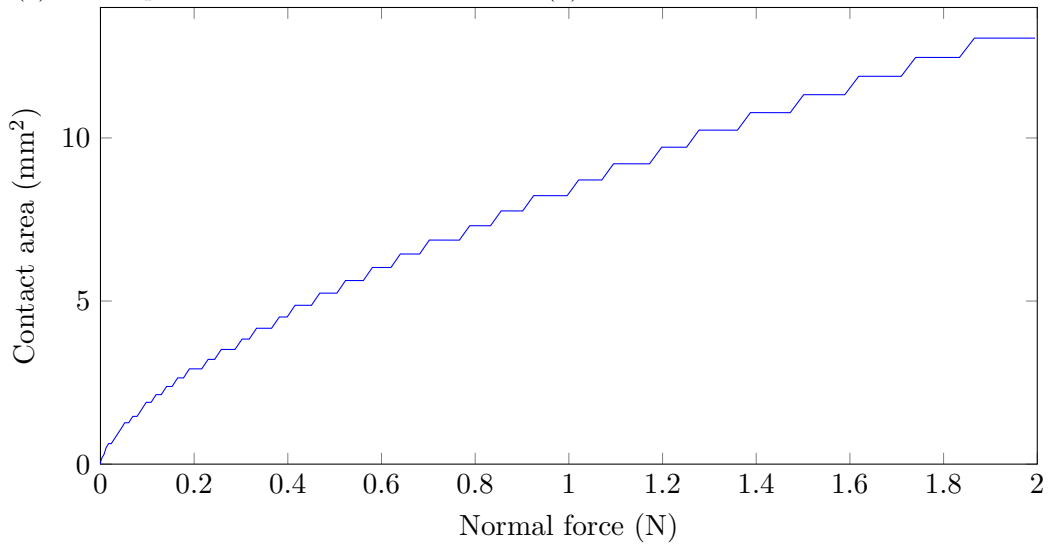
(c) The contact area—normal force curve

Figure 4.21: The FEM displacement-loading analysis on the artificial finger
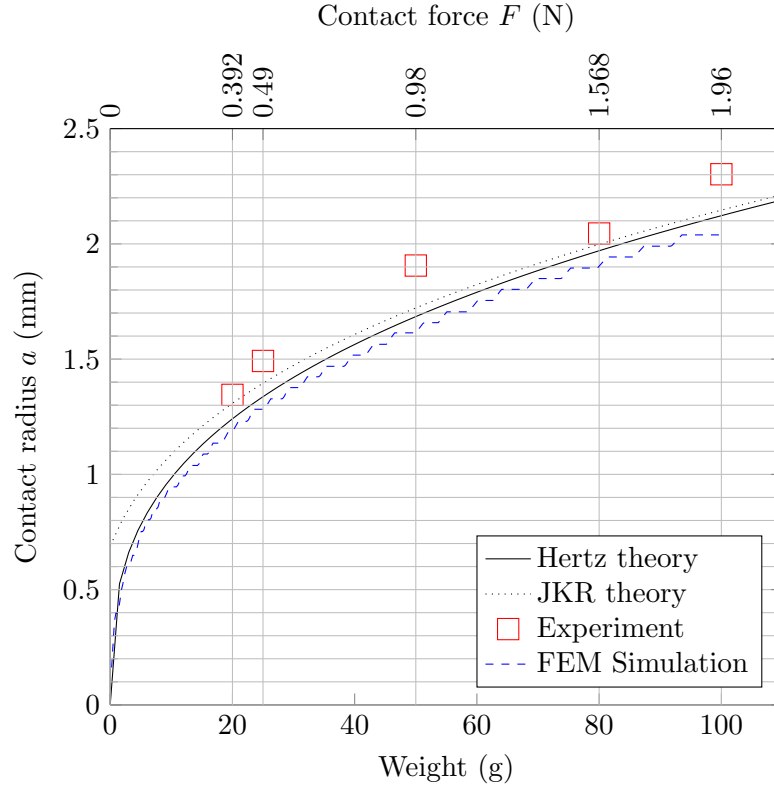
Figure 4.22: Comparison between theory, simulation and experiment results of the relationship between contact radius and normal force

found using the Hertz model, the JKR model and FEM compared with experiment results in Table 4.3. The Young's modulus value used for all three approaches was 0.945 MPa, from Table 4.1. There is a very good agreement between the approaches. The JKR contact model is slightly more accurate. However, the averaged root mean squared errors between the Hertz contact theory and the JKR contact theory is only 0.0748 mm; the coefficient of determination is $r^2 = 0.9954$. Because of this, contact of an artificial finger with a smooth surface can be modelled well with the Hertz contact theory.

The FEM and theoretical models do not take into account the presence of fingerprint ridges; the higher than expected contact radii with the experiment result seen in Fig. 4.22; one hypothesis is that the ridges increases the apparent contact area (which is being measured), due to a larger real contact area is required to maintain the same pressure for a given normal force.

97

4.6 Conclusion

Several contact theories are detailed in this chapter with equations linking friction forces, normal forces and the contact area. Micro- and nanoidentation techniques were introduced, with the different indenter tips compared.

This chapter introduced a simple measurement mechanism to measure the contact area between the artificial fingertip and the surfaces under various loading forces, using a Bruker microscope with a Through Transmissive Media (TTM) module on a pivoted glass plate. In addition, finite element modelling was applied to simulate the contact behaviour between the artificial fingertip and different surfaces. By choosing a range of hard and textured aluminium and ground steel surfaces used previously to limit deformation of the material, the FEM simulation, the theoretical model, and the experiment results are shown to have good agreement with each other—the JKR theory fitted the experiment better while the FEM simulation followed the Hertz theory better. The FEM and theoretical models do not take into account the presence of fingerprint ridges; it may be that the ridges increases the apparent contact area due to a larger real contact area is required to maintain the same pressure for a given normal force.

Overall, the contact radius was shown to be proportional to the loading force raised to the power of $1/3$. The results also show that the contact of the artificial finger with a smooth surface is approximated well by the Hertz contact theory for loads up to $2\,\mathrm{N}$.

Friction and Young's Modulus Measurement of Thermoplastic Materials

Thermoplastic elastomer (TPE) and copolymer of elastomer are commonly used in manufacturing of car interiors to give surfaces a less harsh and more pleasing feel. Materials in car interior should reflect customers' touch-feel personal taste and comfortability especially for luxury cars. Before investigating how the thermoplastic metals will affect the touch feel perception, it is important to know their physical characteristics. This chapter focuses on the measurement of the physical characteristics of selected TPE samples, such as surface topography, surface mechanical characterizations including elastic modulus and nano-hardness, and the friction characteristics. A series of coated and patterned surfaces were selected in this chapter for the objective, whose surface parameters were orthogonally independent designed. The details of measurements were explained in this chapter . For the coated samples, the thickness of the coating will affect the mechanical characteristics of the samples. Hence, the thickness of the coatings were measured first and then the hardness measurement of the samples was carried out with different penetration depth during nano-indentation. For the patterned samples, their mechanical properties are affected by the different patterns. Nano-indentation measurement were carried out in order to understand the effect of the patterns. For friction characterisation, all the friction coefficients were measured by the new friction test apparatus introduced in Chapter 3. All of the thermoplastic plates were tested under different contact forces ($0.35\,\mathrm{mm\,s^{-1}}$, $0.5\,\mathrm{mm\,s^{-1}}$ and $0.75\,\mathrm{mm\,s^{-1}}$) and stroking speeds ($2\,\mathrm{mm\,s^{-1}}$, $5\,\mathrm{mm\,s^{-1}}$

and $8\,\mathrm{mm\,s^{-1}}$).

5.1 Introduction

Surface affective engineering focuses on design factors in enhancing the touch-feel quality of surface materials or textures. As an cost-effective routine, paint finishes and embossment of soft polymer such as thermoplastic elastomer (TPE) and copolymer of elastomer are commonly used in manufacturing car interiors to give the surfaces a less harsh and more pleasing feel. They have been used for non-load bearing parts and interiors such as battery frames and bumpers in mass-produced cars, and for more complex applications such as monocoques [146]. Over-moulding of TPE are also widely applied in manufacturing control knobs and switches to achieve so-called 'soft-touch' feel [84].

The use of thermoplastic elastomer (TPE) materials offers a number of key advantages, for example: 1. easy thermoplastic processing 2. short cycle times 3. low energy consumption 4. thermal stability, providing large processing window 5. multi-component processing and thus reduced assembly costs 6. combination of two materials (hard-soft composite) 7. fully recyclable, and 8. versatile dying options, including colour effects for more advanced design. Based on the advantages of TPE materials, there is essential to understand the 'touch-feel' perception of thermoplastic materials in order for better car interiors selection.

When a person touch or stroke a surface, the surface topography and softness influence the person's perception and feel. However, the sensorial 'softness' or 'soft-touch' is a combination of sensations derived from the contact interaction with object surface and a general sensing of touch movement. Inevitably, such interaction objectively associates with both skin features and a range of surface properties such as topography, hardness and friction resistance. For surface topography, it can be measured as S_a, S_q, S_m and so on. The physical softness of a material is often measured as compressibility, hardness and elastic modulus. For friction resistance, the friction results can be easily influenced by the measurement condition. In this case, all of the friction coefficients are measured by the newly developed friction apparatus based on the artificial fingertip.

Five coatings (Mankiewicz Gebr. & Co. ALEXIT series) and five patterned polymer surfaces (Lyondellbasell, Basell, German) were selected for the investigation. The patterned samples were heated and embossed with N111, N127 pattern types. Water-based solvents (e.g waterborne polyurethane) were used for the coating. An ABS-based (acrylonitrile butadiene styrene) plastic substrate is used to paint the

polymer coating. All the samples are cut into pieces of size $20\,\text{mm} \times 10\,\text{mm}$. These thermoplastic samples had different coatings, different surface patterns and different substrate materials (see Table 5.1).

To better understand the effects of the patterning, five additional samples were created by sanding the original five patterned samples. The sanded/smoothed variants are henceforth labelled with suffix 's' for sanded. All of the physical measurement results are used in the subsequent correlation analysis. The logical order of this chapter is as follows: the surface topography and their Young's modulus were measured first in order for later theoretical analysis. Similar to the metal samples in Chapter 3, for comparison the friction coefficients were measured using both the artificial fingertip and in vivo with human fingertips. The human fingertip results will also be used in the later chapters (6 & 7).

Table 5.1: Description of soft-feel coated and patterned TPE and copolymer samples

	Name	Pattern	Material Code	Description
Soft-feel coatings	s44	Coating	Comfortlack 341-44	Water based paint
	s58	Coating	Laser-coating 342-58	Water based paint with laser treatment
	s83	Coating	Decorlack 342-83	Water based paint
	s97	Coating	Soft-coating 341-97	Water based paint
	s97R	Coating	Soft-coating 361WSL	Water based, matt, soft
Soft-touch polymer composites	1N111[*]	N111[†]	P1: Softtell TKG 300N	25% glass fibre reinforced thermoplastic polyolefin compound
	4N111[*]	N111[†]	P4: Softtell TKS 209N	Unfilled TPO compound
	5N111[*]	N111[†]	P5: Hostacom HC ERC 342	10%mineral filled polypropylene copolymer
	4N127[*]	N127[‡]	P4: Softtell TKS 209N	Unfilled TPO compound
	5N127[*]	N127[‡]	P5: Hostacom HC ERC 342	10% mineral filled polypropylene copolymer

[†]Fine patterns; [‡]Coarse patterns; [*]Sandpaper smoothed variations

Figure 5.1: Gold sputter coating machine

5.2 Surface topography measurement of thermoplastic Materials

Surface topography of these thermoplastic samples was measured first. All samples were cut into pieces of size $20\,\mathrm{mm} \times 10\,\mathrm{mm}$. The name and description of the samples are detailed in Table 5.1. For the patterned samples, the patterns affect the surface topography measurement results and it is difficult to make sure every asperity of the surface is the same. Hence, only the central part of the surface ($3\,\mathrm{mm} \times 3\,\mathrm{mm}$) was measured by a Bruker ContourGT-K 3D optical microscope, with $3\,\mathrm{mm} \times 3\,\mathrm{mm}$ the maximum range offered by the instrument. The Taylor Hobson Form Taysurf surface profilometer was also used to measure the topography of the samples; the measurement range was $0.8\,\mathrm{mm}$ and cut-off length was $0.08\,\mathrm{mm}$.

Commonly-used topographical parameters such as S_a, S_m, S_q, S_sk and S_ku are recorded and averaged across multiple tests. Because Bruker works through light interferometry, and all the samples were black, it is necessary to coat a reflective gold layer to the thermoplastic samples to obtain results that were satisfactory. Sputtering deposition creates a very thin coating of gold and is essential for Scanning Electron Microscopy (SEM) imaging. Since with SEM one can use sputtering techniques to image down to nanometre scales, one assumes the sputtering process would not alter the micrometre scale surface topography of the samples. The sputtering machine is as shown in Fig. 5.1.

5.2.1 Coated polymer samples

As shown in Figures 5.2, 5.3, 5.4 and 5.5, the surface topography of coating samples are quite smooth compared with patterned samples. Their surface texture measured

by Bruker and observation with a SEM are shown in the following figures [32]. They have a matt-like structure with a few defects due to bubble implosions. The measurement area was also set to $3\,\mathrm{mm} \times 3\,\mathrm{mm}$. Note that the measurement from Bruker ContourGT-K is three dimensional, compared with two-dimensional measurements from the Taylor Hobson Form Talysurf. Both 2D and 3D results are recorded and they are shown in Fig. 5.11.
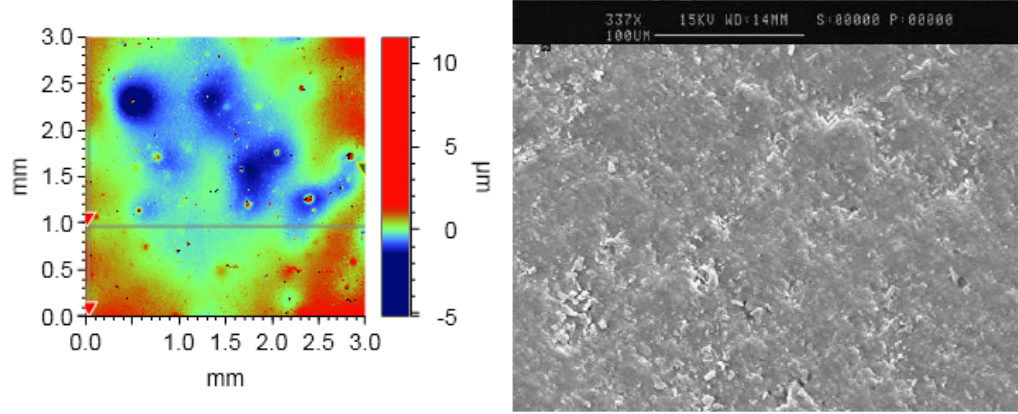
Figure 5.2: Surface topography of `s44` by Bruker ContourGT-K and its SEM photo
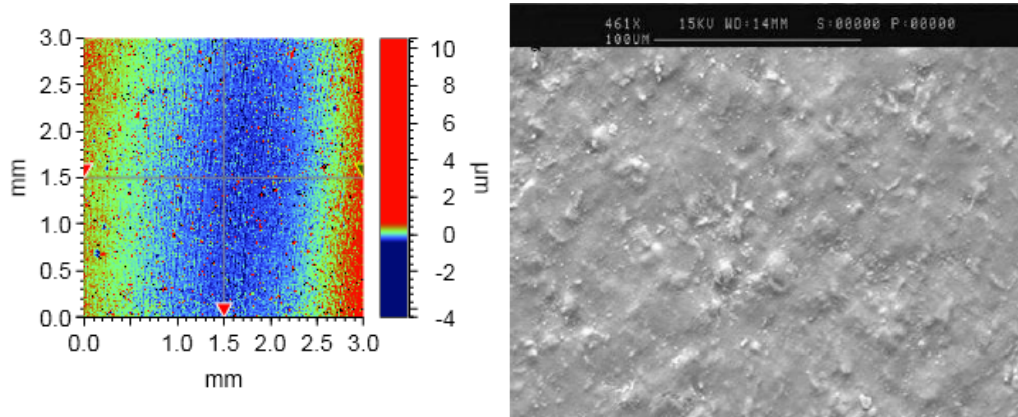
Figure 5.3: Surface topography of `s58` measured by Bruker ContourGT-K and its SEM photo

5.2.2 Patterned polymer samples

In order to observe the clear structure of patterned samples, they were scanned by a conventional Nikon Optiphot microscope [32]. The results are shown in Fig. 5.6 and Fig. 5.7. The finely patterned samples ending `N111` appear to have many irregular
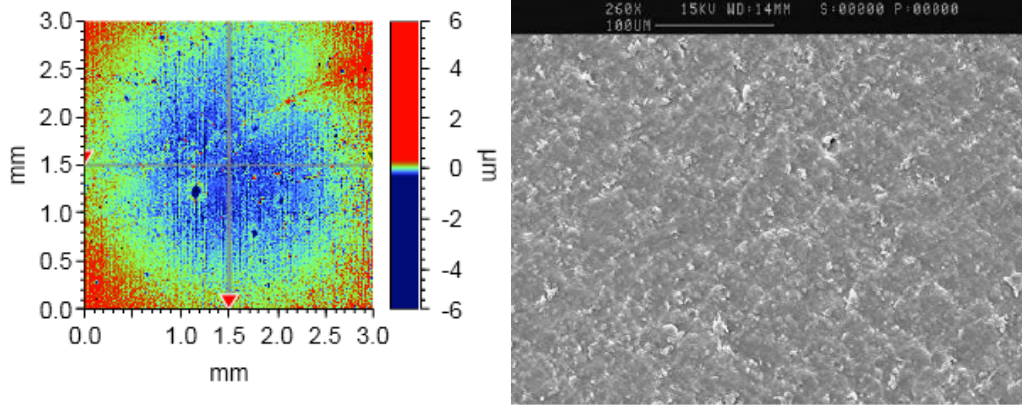
Figure 5.4: Surface topography of `s83` measured by Bruker ContourGT-K and its SEM photo
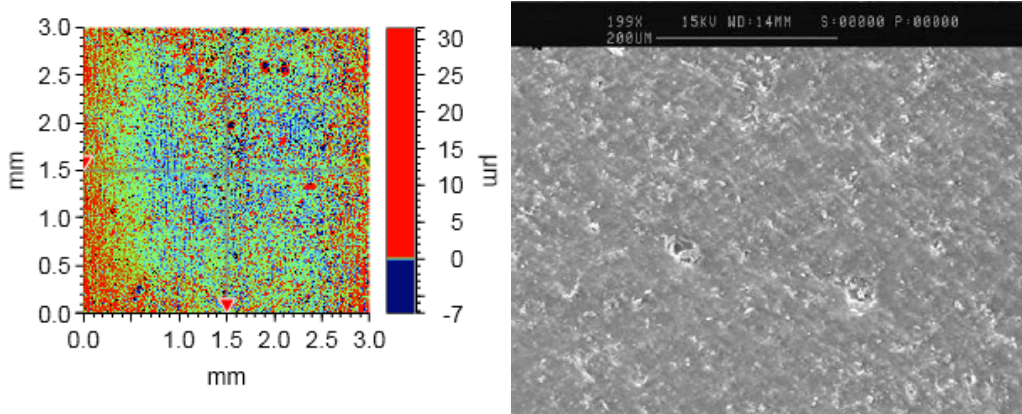
Figure 5.5: Surface topography of `s97` measured by Bruker ContourGT-K and its SEM photo

and bumpy grains. The grain sizes of `N111`'s differ slightly among the samples `1N111`, `4N111` and `5N111`. The coarse patterned samples ending `N127` appear to have arrays of many glossy spherical bumps. As a matter of appearance, `5N127` have a more glossy surface finish than `4N127`.

All the measured topography parameters of patterned samples are displayed in Table 5.2. Fig. 5.8 and Fig. 5.9 showed different surface topography of -`N127` and -`N111` patterns, within which different colour represents different height of the surface asperity of the material. The spacing of `N127` is comparatively larger than `N111`'s although they have similar roughness. The figures of other patterned samples texture are shown in Appendix A.4. Fig. 5.8 and Fig. 5.10 showed the samples of `4N127` before and after sanding with sandpaper. The most obvious difference is the decrease of surface roughness after processing. Other differences will be discussed

later.

(a) `1N111`

(b) `4N111`

(c) `5N111`
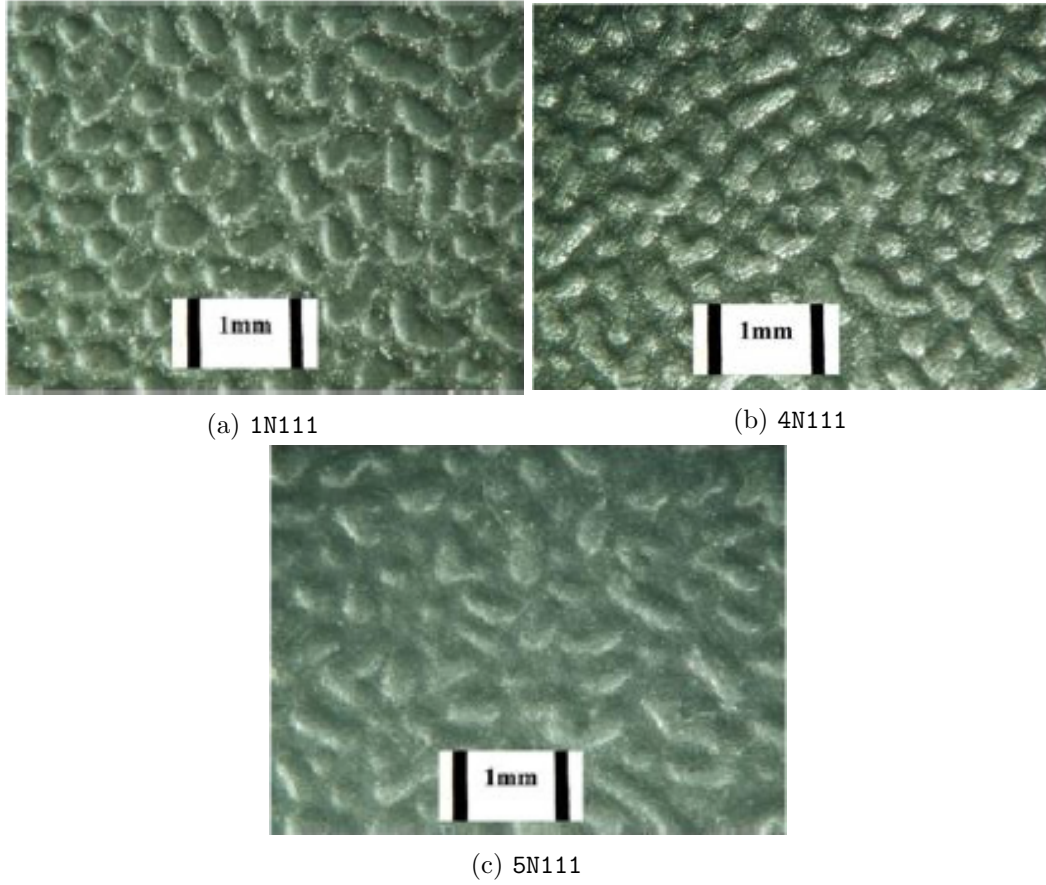
Figure 5.6: Observations of Fine polymer patterned surface morphology by microscope at same illumination condition

In order to better understand the differences between the 2D and 3D surface topography measurements, the 2D surface topography measurements of coating and thermoplastic patterned samples are also shown in Fig. 5.11 and Fig. 5.12. For the Form Talysurf 2D measurements, the measurement range was 0.8 mm and cut-off length was 0.08 mm. The blue bars are the measurement results by Bruker ContourGT-K, while the red bars are the measurement results by Taylor Hobson Form Talysurf. In Fig. 5.13, the blue bars are the normal (non-sanded) TPE samples data, and the red bars are the sanded TPE samples data. The results showed that compared with the hard materials such as steel, aluminium that are characterised in Chapter 3, the roughness values estimated by Bruker are larger than those from Form Talysurf. However, for the coated thermoplastic samples, the Bruker measurements are smaller. One reason for the disagreement is that the 2D line measurement

105

(a) 4N127   (b) 5N127
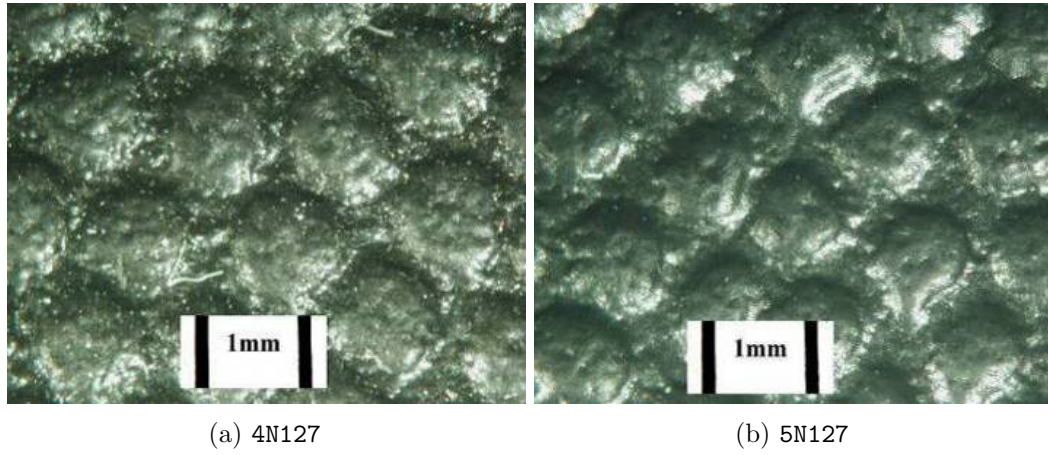
Figure 5.7: Observations of coarse polymer patterned surface morphology by microscope at same illumination condition
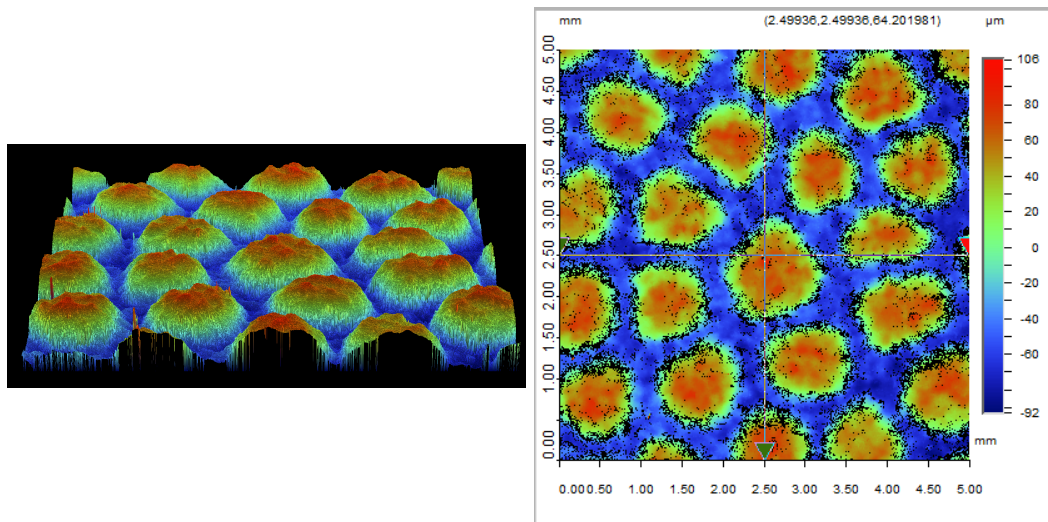
Figure 5.8: Surface texture of 4N127 under Bruker
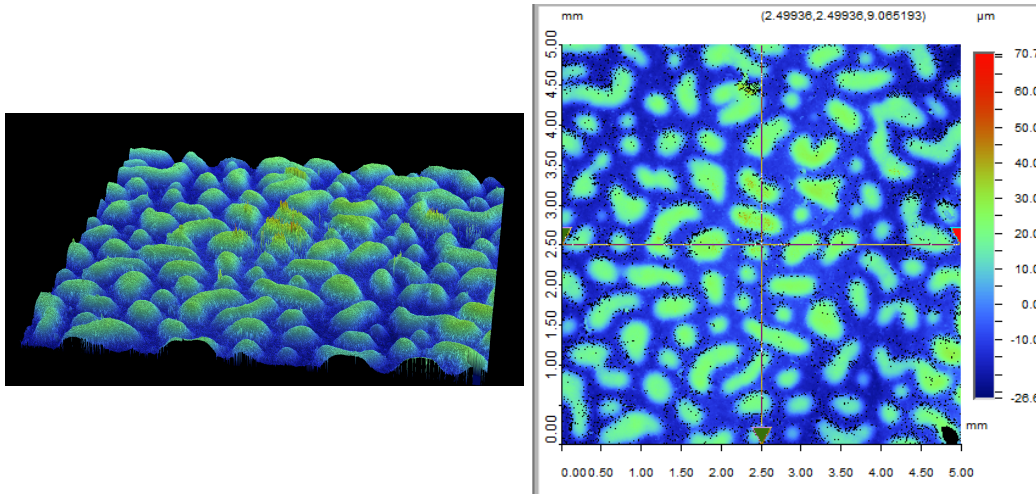
Figure 5.9: Surface texture of `4N111` under Bruker
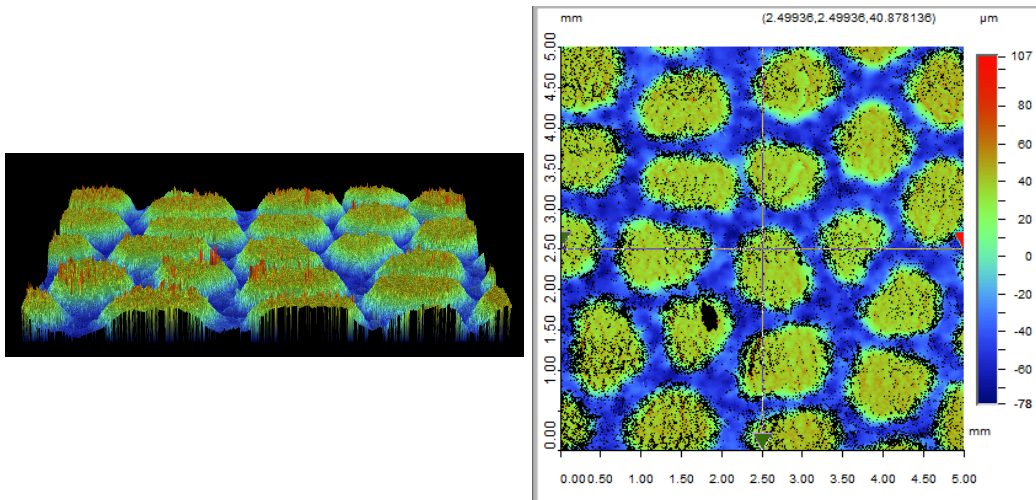
Figure 5.10: Surface texture of smoother `4N127` under Bruker

performed by Form Talysurf was not representative of the topography across a wider area. In addition, deformation may occur on the soft material during the Form Talysurf measurement due to the contact nature as opposed to the non-contact nature of the Bruker optical microscope. Based on these two reasons, the surface topography results from Bruker would be used, as they are expected to be more representative and accurate.

(a) R_a (b) R_q
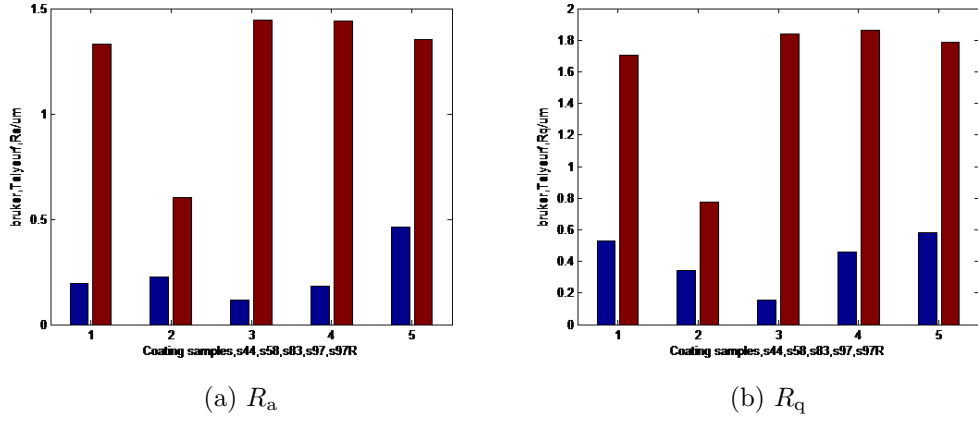
Figure 5.11: Roughness measurements of coated TPE samples comparison using ContourGT-K (blue) and Form Talysurf (red)

(a) R_a (b) R_q
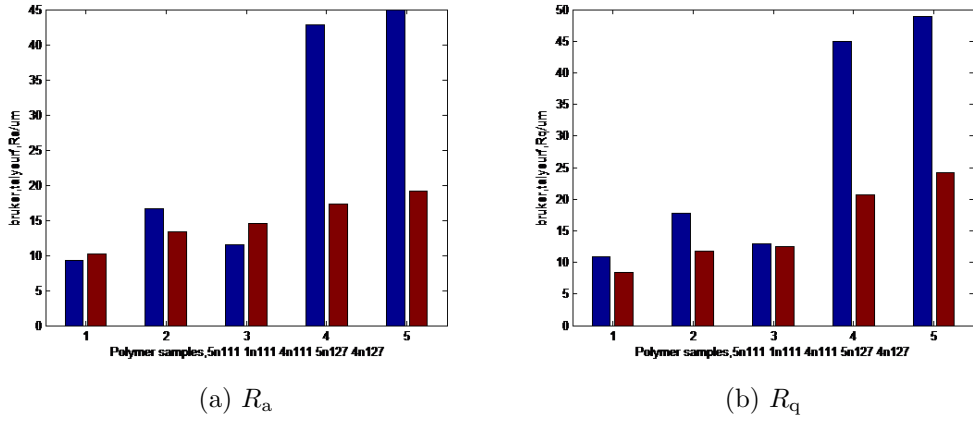
Figure 5.12: Roughness measurements of patterned TPE samples using ContourGT-K (blue) and Form Talysurf (red)

5.2.3 Summary

Based on the above analysis, the measurement results of all thermoplastic samples are summarised in Table. 5.2. All of the surface topography measurement results are applied in subsequent correlation analysis between human touch-feel and sample physical characteristics in Chapter 7.

5.3 Nano-indentation of the Thermoplastic Materials

Previously, the surface mechanical characteristics of the polymer samples have been measured by the tribological probe microscope (TPM) [17–19]. It measures the

Table 5.2: Surface topography parameters of polymer coated and patterned samples

Samples	S_a(μm)	S_{ku}(μm)	S_p(μm)	S_q(μm)	S_{sk}	S_v(μm)	S_z(μm)	S_{dq} (deg)	R_{da}(μm)	E(MPa)	H(MPa)	S_m(μm)
4N127	44.96	1.43	105.56	48.84	−0.09	−92.29	197.85	36.47	13.57	0.06	3.23	649.85
4N127s	37.32	1.36	106.83	39.67	−0.20	−78.40	185.23	45.18	15.42	0.06	3.23	649.85
4N111	11.53	1.78	70.69	12.98	0.28	−26.63	97.32	30.82	10.98	0.07	4.95	576.99
4N111s	13.23	1.73	46.48	14.73	0.45	−24.01	70.49	32.83	11.73	0.07	4.95	576.99
1N111	16.64	1.37	52.97	17.79	0.22	−40.66	92.99	33.20	11.03	0.47	22.35	508.53
1N111s	14.41	1.49	75.38	15.73	−0.04	−77.06	152.45	41.08	13.46	0.47	22.35	508.53
5N127	42.88	1.29	71.18	44.91	−0.28	−82.18	153.36	38.18	10.80	0.90	34.62	1495
5N127s	44.58	1.29	78.62	48.88	−0.26	−85.12	163.74	38.43	13.26	0.90	34.62	1495
5N111	9.31	2.39	38.78	10.90	0.69	−41.03	79.80	17.67	8.25	0.79	34.62	606.35
5N111s	9.43	1.98	49.07	10.78	0.52	−53.71	102.77	26.86	10.02	0.79	34.62	606.35
s44	0.19	144.75	31.95	0.53	8.95	−13.02	44.97	8.96	2.27	1.94	130.30	71.70
s58	0.23	68.51	10.56	0.34	4.82	−4.45	15.02	5.69	1.83	1.84	116.92	57.70
s83	0.12	33.99	5.86	0.16	1.01	−5.58	11.44	2.87	1.16	2.18	139.04	72.97
s97	0.18	261.05	31.50	0.46	11.02	−7.38	38.88	9.49	2.47	0.94	34.27	68.33
s97R	0.46	6.37	12.08	0.58	0.21	−4.70	16.77	3.36	0.87	1.95	119.12	59.60

(a) R_a

(b) R_q

Figure 5.13: Roughness measurements of normal patterned (blue) and sanded (red) TPE samples comparison measured by ContourGT-K

surface height first in the normal scanning mode and then switches to the ramping mode to increase the contact force to a pre-set value and decrease it again, while the deformation/penetration is measured. However, the TPE is limited to scanning a small area of $100\,\mu m \times 100\,\mu m$. Also, it is limited to measuring surfaces with a roughness less than $15\,\mu m$ due to the probe working range ($< 15\,\mu m$) in the z-direction. It is recognised that surface strength (hardness and modulus) varies depending on the indentation depth and load, thus the test should be made at critical load when the value of the hardness and modulus are relatively stable. Considering the scale of the micro-features in the polymer patterns, nano-indentation test was applied here to characterise their surface nano-hardness and elastic modulus. Nanoindentation is capable of measuring local properties of both the hardness and stiffness of materials, and are capable of determining properties of thin coatings or films.

5.3.1 Nano-indentation of coating polymer samples

The coating samples include two layers: coating and substrate. The details of each layer are described as above in Table 5.1 and the majority of the substrate were made from polyurethane materials. The nanoindentation results depend on which layer was pressed; if the penetration depth is deeper than the coating layer, the mechanical property inferred will be of the substrate, otherwise, the measurement would be of the coating layer. Because of this, the first important task is to determine the thickness of the coating layer for these TPE samples.

All of the five coated samples were moulded in resin and their cross-sections were polished after 24 hours of drying. Then, the cross-section of the coating was

observed under a Nikon Optiphot microscope as shown in Fig. 5.14. It is shown that for s97R and s83, the thickness of their coating layers was 65 µm and 67.5 µm. s44's coating was 48.75 µm, s58's coating was 20 µm and s97 coating was 67.5 µm. Here, the cross-section of s97R and s83 are given in the figure, while the cross-sectional photographs of the remaining samples are shown in the Appendix A.4. Because the maximum load for nano-indenter setting applied in this thesis was 500 mN, the coating thickness is much larger than the penetration depth occurred during contact. Hence, the whole contact mechanism is influenced more by the coating layer rather than at the substrate. As such, from the modelling perspective, the contact problem can be simplified to a contact between the coating layer and the artificial fingertip.

(a) s97R	(b) s83
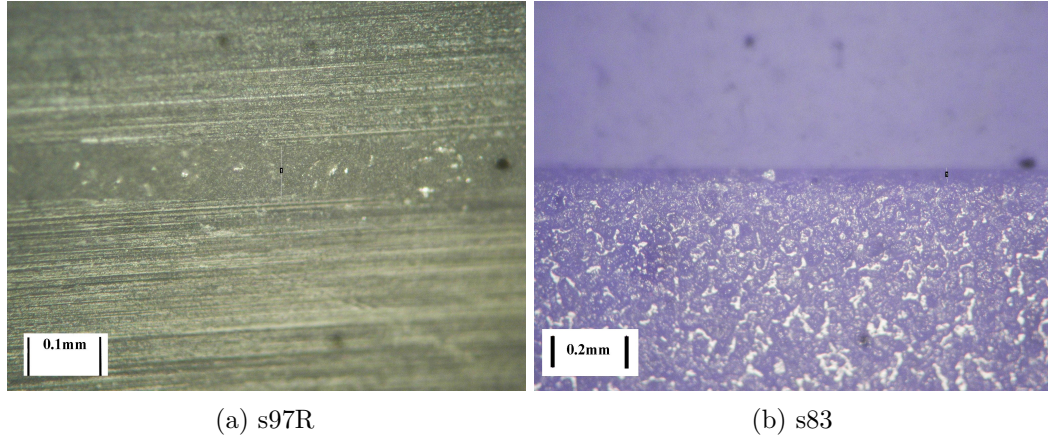
Figure 5.14: The cross-section (moulded in resin) taken by microscope

Nano-indentation with different penetration depth

In order to better observe the change of hardness and Young's modulus of the samples due to the applied loads, different loading forces from 30 mN to 500 mN were applied during the measurement. Four different spots on the surface were measured at each measurement, and every test was repeated 3 times. Every applied load was held for 5 seconds in order to avoid the creep effect. All nano-indentation images when the maximum load was 500 mN are shown in Figures 5.15, 5.16, 5.17 and 5.18. The indenter applied in these experiment s was a Berkovich tip [142]. The image also showed the indentation shape of every sample amplified by 20 times.

However, for the NHT nano-indenters, the measured surface mechanical properties (hardness and Young's modulus) vary depending on the indentation depth and load due to the indentation size effect [139, 140]. Both the measured hardness and modulus are seen to decrease with the TPE samples, converging to a constant

value when the load is high enough. Thus, the test should be made at a critical load when the value of the hardness and modulus are relatively stable.

As shown in Fig. 5.20, the maximum penetration depth was smaller than $20\,\mu m$; this was limited by the maximum load of $500\,mN$. It proves that all the contact occur in the coating layer and not in the substrate. As shown by the nanoindentation results, coating samples have much higher Young's modulus and hardness values. s83 is the hardest sample while s97 is the softest one. Although they share same substrate material, different coating mechanisms lead to different mechanical properties. Both the Young's modulus and the hardness of the coating samples follows the order of s97 < s58 < s44 < s97R < s83.
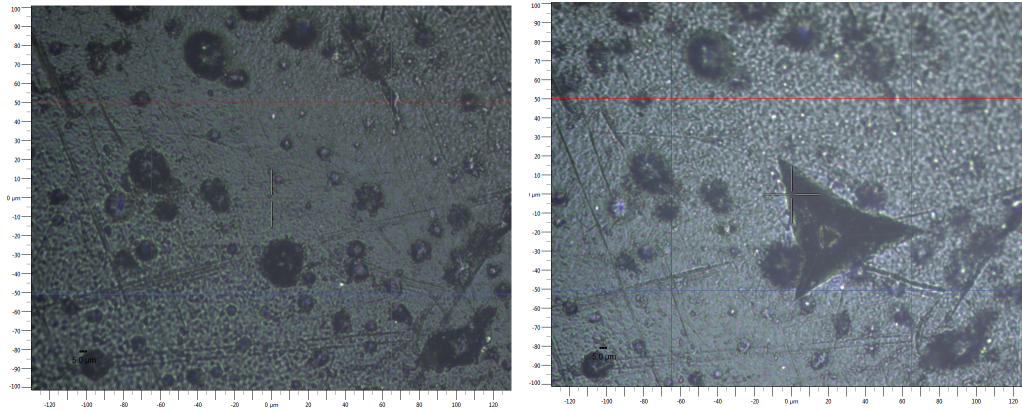
Figure 5.15: Before and after the nano-indentation of s44
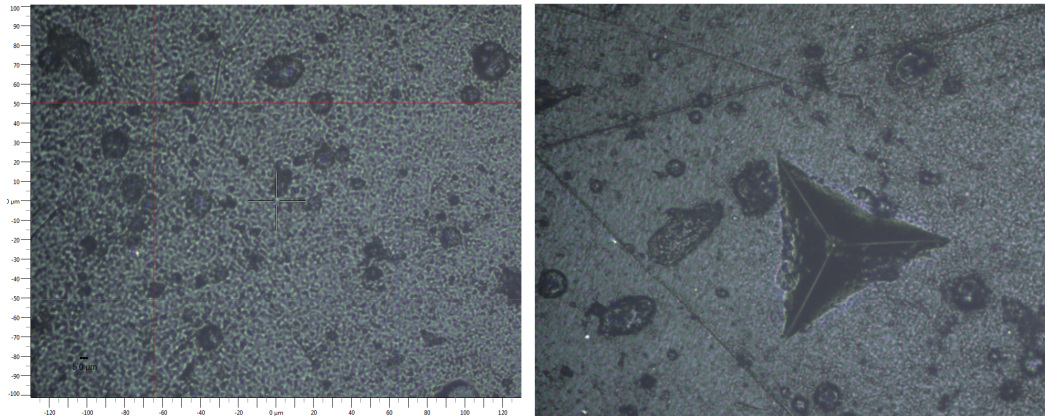
Figure 5.16: Before and after the nano-indentation of s58

112
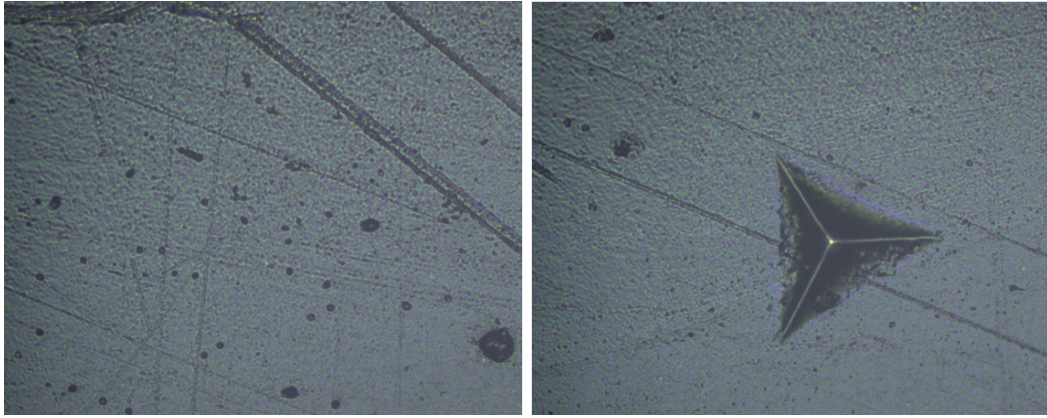
Figure 5.17: Before and after the nano-indentation of `s83`
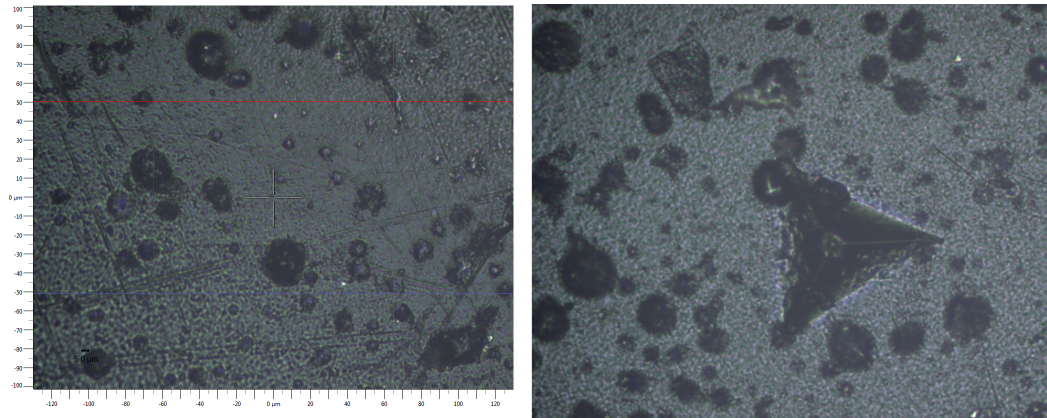
Figure 5.18: Before and after the nano-indentation of `s97`
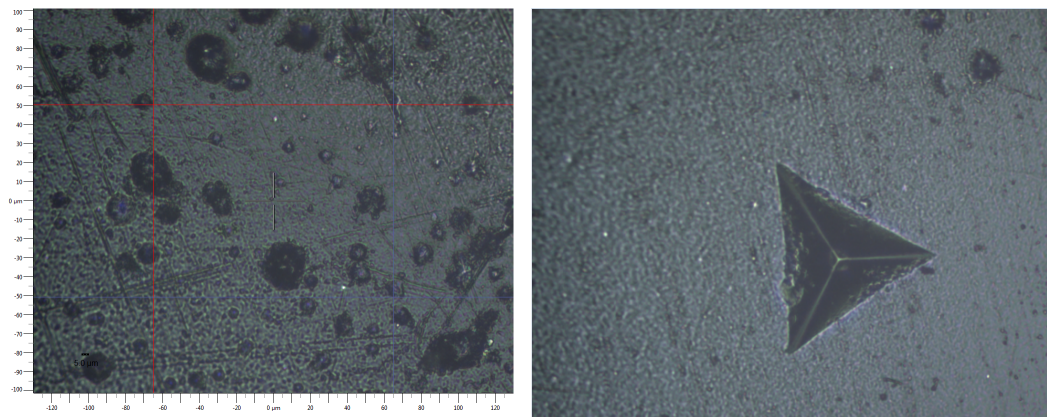
Figure 5.19: Before and after the nano-indentation of `s97R`
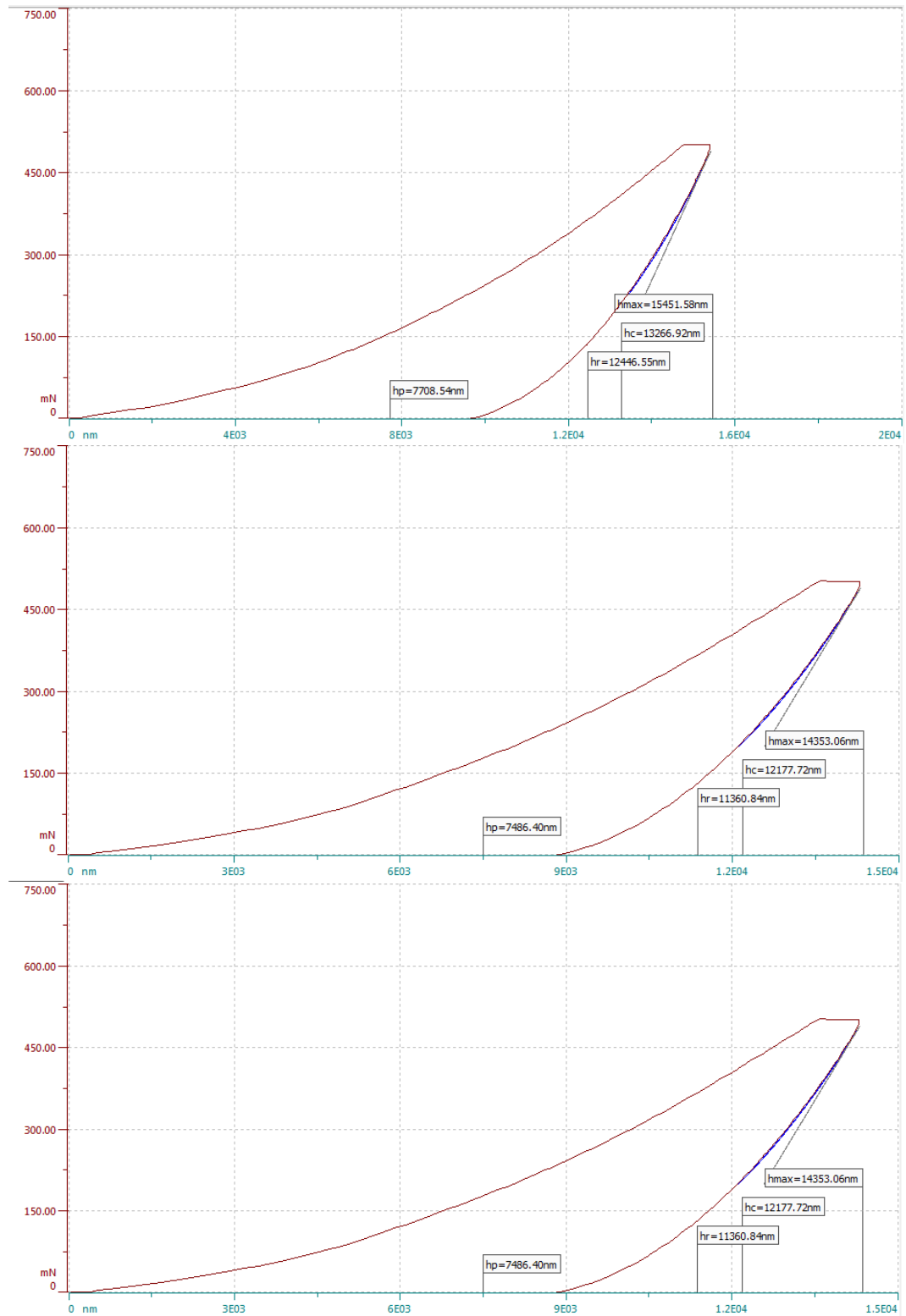
Figure 5.20: The nano-indentation results of `s58`, `s83` and `s97` when the maximum load was $500\,\mathrm{mN}$

5.3.2 Nano-indentation of patterned polymer samples

As for the patterned samples, their hardness and modulus become relatively stable when the maximum load is larger than 50 mN; this is due to the indentation size effect discussed in the previous section. To reduce the influence of indentation size effect further, four relative stable reading at different loads ranging from 50 mN to 500 mN were averaged. In addition, to reduce local effects, the indentations were performed at four different matrix locations on each sample. The total averaged values of these hardness and moduli were recorded in the following database.

The results are shown in Fig. 5.21. The sanded patterned samples practically have the same measured nano-hardness and stiffness. For the other patterned samples, 5N127 has noticeably higher stiffness than that of 5N111 but they have similar nano-hardness. The nano-hardness (and stiffness to a lesser extent) of 4N111 is somewhat higher than that of 4N127. Even though the substrate material is the same, the material might have been sensitive to the surface pattern embossment process, e.g. it may not be thermally stable in the heat press process. The results show that the coated samples with the exception of s97 are comparably harder and stiffer than the patterned polymer samples.
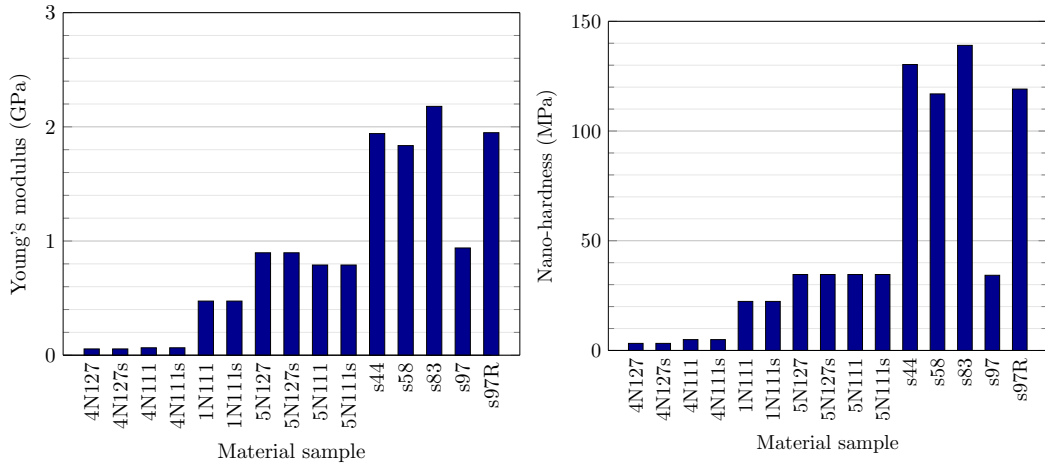
Figure 5.21: Mechanical properties of the TPE samples

5.3.3 Comparison with TPM measurements

The TPM is capable of multi-functional mapping of surface topography, nano-hardness and elastic modulus in an area of $10 \, \mu m \times 10 \, \mu m$. However, it is limited to measuring surface roughness of less than $15 \, \mu m$ due to the probe working range in z direction [32]. Thus, the mapping functions are only applicable for the coated

115

rather the patterned samples. The NHT nano-indenter does not have this limitation. However, for the NHT is susceptible to the indentation size effect discussed in Section 5.3.1. From experience when the applied load is larger than 100 mN, the measurement stabilises. Here, a comparison between two measurement methods was made to form better understanding of the results shown in Fig. 5.22.
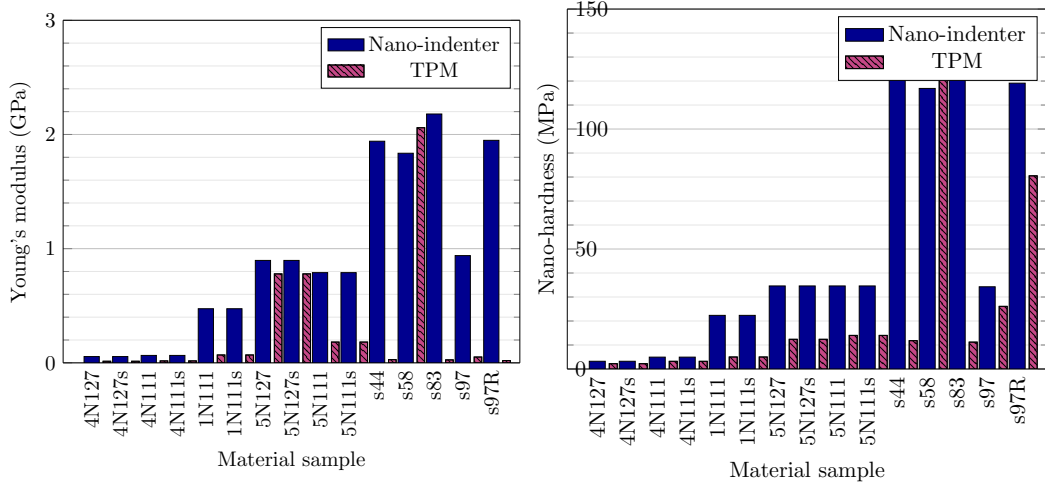
Figure 5.22: Comparison with TPM measurement

The difference between two methods is smaller for the patterned samples compared with coated samples, and when measuring hardness instead of stiffness. The maximum load applied in the NHT nanoindenter was 500 mN, therefore the deformation may be different because of the difference in the maximum load.

5.4 Friction measurement of thermoplastic materials

Compared with the metal samples, the thermoplastic samples were rougher and softer. In this section, all the coating and patterned samples were measured at the same working conditions as metal samples and each measurement was repeated 3 times. The contact forces tried were 0.35 N, 0.5 N and 0.75 N and the stroking speeds tried were $2 \, \mathrm{mm \, s^{-1}}$, $5 \, \mathrm{mm \, s^{-1}}$ and $8 \, \mathrm{mm \, s^{-1}}$. For the human finger measurements, 6 people with different age and different gender were asked to test the thermoplastic patterned samples, and one subject tested the coated samples. The comparison analysis will be shown in a later section.
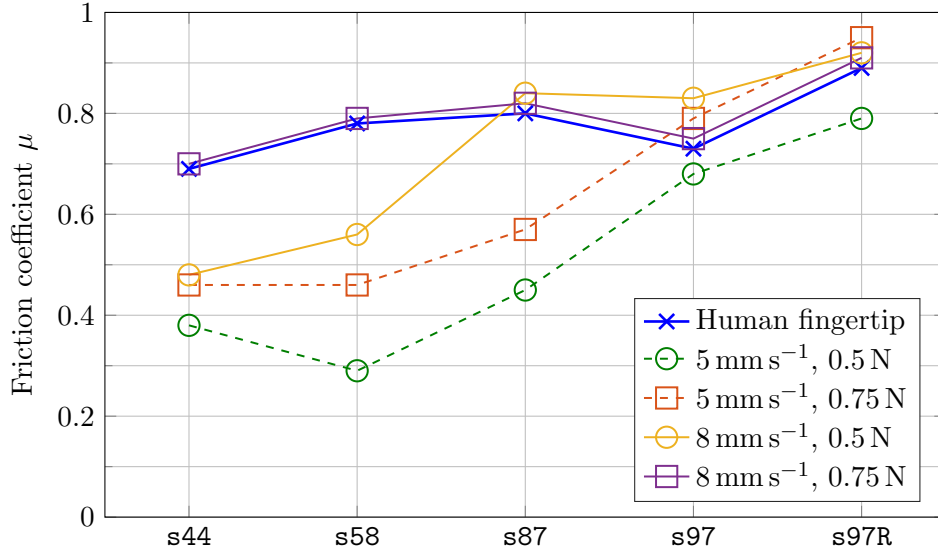
Figure 5.23: Polymer coating friction measurement under different conditions

5.4.1 Friction measurement of coated polymer samples

The friction measurement results for the coated samples are shown in Fig. 5.23. The blue line with crosses are the human finger friction coefficients, which contains data from one subject only for the coated samples. The other lines mark the measurement results carried by the artificial fingertip. The artificial fingertip measurement results are the closest to those of the human finger friction results when the contact force was $0.75\,\text{N}$ and the stroking speed was $8\,\text{mm}\,\text{s}^{-1}$. For s44, s58 and s83, the remaining measurement conditions are a little far from the human finger measurement results. However, for s97 and s97R, all of the four measurement results are close to the human finger measurement. But the human finger friction measurement was just carried out by 1 person, so the results are not very reliable.

Comparing the 5 coated samples, s97R owns the highest friction coefficient, and s44, s58, s83 follows the order of s44 < s58 < s83. However for s97,it is not very clear it is higher or lower than other samples. For s44, s58, s83 thermoplastic samples, their coating material are quite similar,and they have higher Young's modulus and hardness compared with s97 and s97R based on the nano-indentation measurement results. Their surface topography are similar to each other. Their friction coefficient are very close but s97R is higher than s97.

Depending on the human skin factors and materials tribological properties, the artificial fingertip offers an alternative for friction measurement.

5.4.2 Friction measurement of patterned polymer samples

The role that pattern type and sanding plays in the comparison of artificial fingertip friction coefficients was examined.

For human fingertip friction measurement, 6 people with different age and gender were asked to measure their friction coefficients [32]. The contact force applied was averaged at 0.5 N. For the artificial fingertip friction measurement, the normal load was set in a range of 0.35 N, 0.5 N and 0.75 N, and the linear stage sliding speed was set in a range of $2\,\mathrm{mm\,s^{-1}}$, $5\,\mathrm{mm\,s^{-1}}$ and $8\,\mathrm{mm\,s^{-1}}$. In the case of 'soft-touch' polymer, where larger friction fluctuation is expected, the output friction coefficient through human fingertip and artificial fingertip was defined in a time-averaged sense. In addition, the five patterned thermoplastic samples that were sanded by sandpaper were tested as well. The analysis is as follows.

Comparison between the human fingertip and artificial fingertip measurement
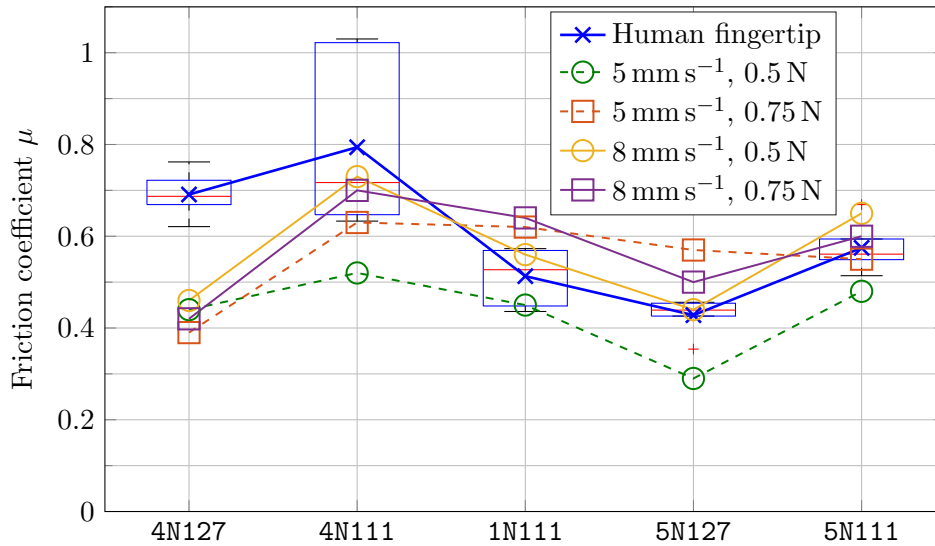
Figure 5.24: Friction coefficient measurements comparing human fingertip and artificial fingertips applied on patterned TPE samples at various stroking speed and loading forces. Boxplot applicable to human fingertip measurements of 6 adult subjects — dotted whiskers: data range, blue boxes: 25% – 75% quartiles, horizontal red lines: median, blue crosses: mean

The friction measurement result is shown in Fig. 5.24. The box plot summarises the human fingertip friction coefficient measured by 6 people. The blue lines with crosses mark the arithmetic average of the human fingertip friction coefficient.

Other lines show the friction measurement results of the artificial fingertip with different working conditions. The figure showed that the artificial fingertip friction measurement result is closest to human fingertip friction results when the stroking speed is $8\,\mathrm{mm\,s^{-1}}$ and the contact force is $0.5\,\mathrm{N}$. The results at $8\,\mathrm{mm\,s^{-1}}$ are closer to human fingertip friction measurement results compared with $5\,\mathrm{mm\,s^{-1}}$ results, mirroring observations with metallic samples in Chapter3. The same argument that the stroking speed of a human finger is faster applies [99].

The correlation coefficients between human fingertip friction coefficient and artificial fingertip friction under different working conditions are given in Table 5.3. When the sliding speed of the linear stage is slower, higher correlations ($r^2 = 0.80 \sim 0.98$) were observed between artificial fingertip friction measurements and those obtained by a human fingertip. Paradoxically, the correlation factors are lower($r^2 = 0.0545 \sim 0.67$) at higher speeds. Note that r^2 is known to be a problematic measure when there are outliers and when the relationship is nonlinear. Referring to the root mean squared errors (RMSE) quoted in Tables 5.4 to 5.6, one can see that the higher sliding speed have less error against human fingertip results. While the results with TPE samples are not as good as those of the metallic samples in Chapter 3, the friction properties of multilayer artificial fingertip is closer to a real fingertip compared to the pure material roller rig [32].

Table 5.3: Correlation between artificial finger and human finger in friction measurement

Friction Measurement conditions		
Sliding speed	Loading force	r^2
$2\,\mathrm{mm\,s^{-1}}$	$0.50\,\mathrm{N}$	0.9524
$2\,\mathrm{mm\,s^{-1}}$	$0.35\,\mathrm{N}$	0.9210
$2\,\mathrm{mm\,s^{-1}}$	$0.75\,\mathrm{N}$	0.6982
$5\,\mathrm{mm\,s^{-1}}$	$0.50\,\mathrm{N}$	0.8003
$5\,\mathrm{mm\,s^{-1}}$	$0.35\,\mathrm{N}$	0.6334
$5\,\mathrm{mm\,s^{-1}}$	$0.75\,\mathrm{N}$	0.1792
$8\,\mathrm{mm\,s^{-1}}$	$0.50\,\mathrm{N}$	0.5431
$8\,\mathrm{mm\,s^{-1}}$	$0.35\,\mathrm{N}$	0.0545
$8\,\mathrm{mm\,s^{-1}}$	$0.75\,\mathrm{N}$	0.7667

Analysis of the artificial fingertip friction results

The detailed friction measurement results of patterned thermoplastic samples are shown in the following figures. In the case of contact between the artificial finger and the soft polymer patterns, the results measured largely depend on surface strength since the deformation is large enough to flatten the local asperity. The dry sliding friction mainly depends on the surface strength of the candidate samples. The samples made of the material P4 still have the largest $\mu_{\text{artificial}}$ overall as comparing Figures 5.25 to Figures 5.26 and Fig. 5.27. However, samples made of P1 and P5 have similar dry frictional behaviour as shown by the `1N111` and `5N111` friction results.

(a) `4N127`

(b) `4N111`
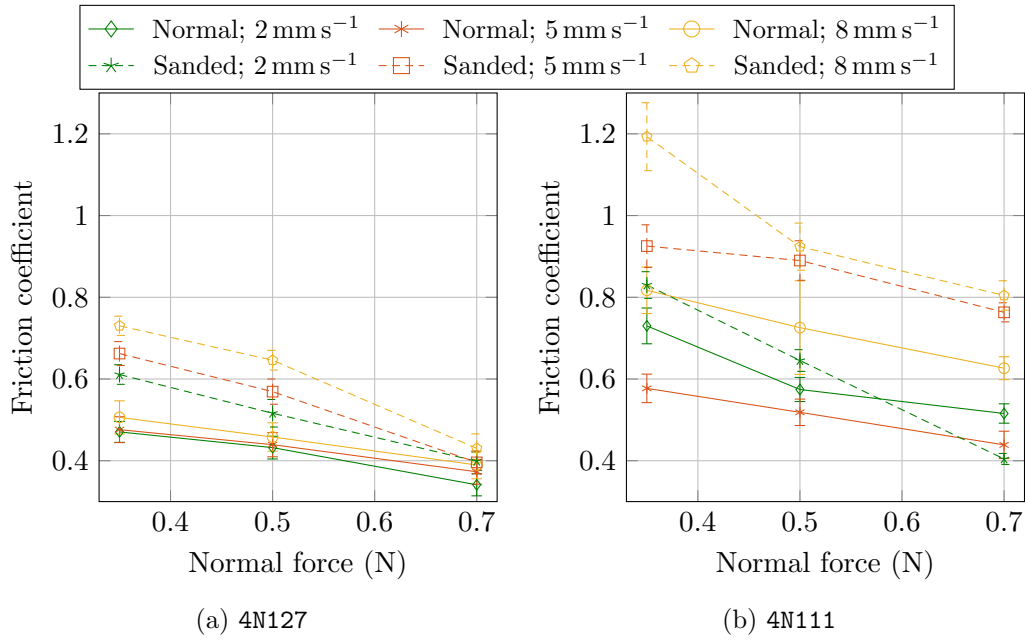
Figure 5.25: Comparison between P4 material patterned samples and sanded samples

Compared with the rougher `N127` patterns, the smoother `N111` patterns have higher friction coefficient (when they are made with the same material). With the increase of linear stage sliding speeds, higher friction coeffients were observed. For instance, a rougher surface pattern tends to help in reducing friction coefficient. This may be explained by the contact area being smaller when the surface is rougher and spacing is larger, which leads to a lower friction resistance. This general trend was also observed with the metal samples in Section 3.4.3. The detailed analysis on the relationship between friction and surface topography will be discussed in later section.

In addition, sanded samples have higher friction coefficients than the normal samples. That is because the surface roughness decreases when sandpaper was used

(a) `5N127`

(b) `5N111`
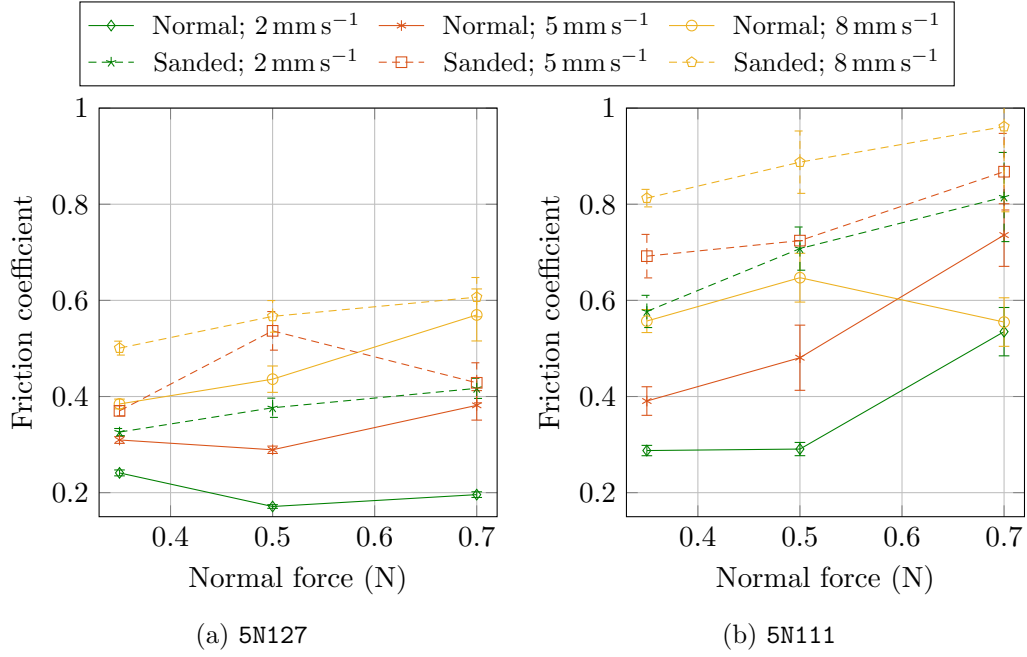
Figure 5.26: Comparison between P5 material patterned samples and sanded samples
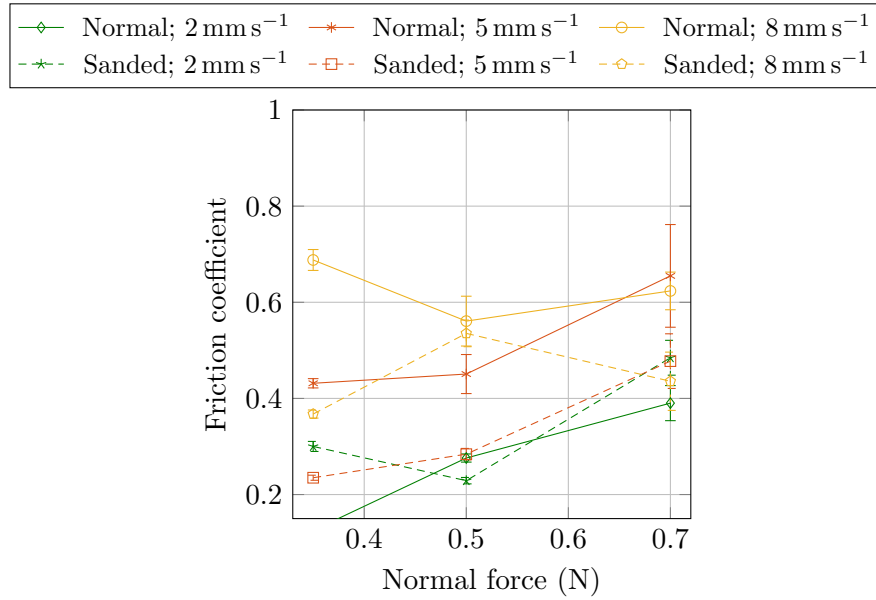
Figure 5.27: Comparison between `1N111` patterned samples and sanded samples

to sand the surface patterns. According to Chapter 4, the contact area increases as a result and the friction coefficient will, therefore, be higher. One can also see from the figures that as the stroking speed increases, the friction coefficient measured is higher. The relationship between the surfaces roughness R_q and the adhesive component of friction force will be discussed in Section 6.3. The friction coefficients and normal forces seem to be proportional to each other, but not to a power of $-1/3$ as the case with hard materials. According to Tang et al. [45], the normal displacement increases linearly with the normal force. The difference in relative hardness of two surfaces will lead to ploughing of the artificial fingertip surface. A greater friction force is required to maintain that motion.

According to Tabor's theory [118], the friction or lateral force depends on the product of the real contact area and shear strength of interface. Meanwhile, the real contact area is related to the deformation and the surface topography. Therefore, a variation of design in surface topography or mechanical properties could result in notably different tribological behaviour. Indeed, it is necessary to understand which factor dominates the mechanism of friction here. In general, samples made of material P4 have a higher friction resistance than P5 and P1. It also worth pointing out that material P4 is less stiff than the other material as shown in Table 5.21 by Young's moduli. Also, the Friction coefficient of P4 decreased with the increase of the normal forces, while P1 and P5 show the opposite trend. The material P1 and P5 showed similar friction behaviour in the comparison between `1N111` and `5N111` ($t = 0.994, p = 0.367$).One hypothesis is that for softer material, the deformation between the contacted bodies can not be ignored, and there is adhesion between the P4 material and the rubber artificial fingertip. It leads to a bigger contact area (see the JKR model in Section 4.2.3) which may be the reason of the higher friction coefficients.

5.5 Conclusion

The friction aspect of touch-feel perception is investigated for a series of thermoplastic elastomer (TPE) samples in this chapter. Thermoplastic samples are commonly used in car interiors. For these materials, different surface roughness, coatings, surface patterns and experiment conditions are shown to influence friction results. It is essential to understand their properties and their correlation with touch-feel perception, which include friction as well. Surface topographical parameters such as roughness and mechanical parameters such as hardness were measured.

Table 5.4: Friction measurement results of thermoplastic samples at $2\,\mathrm{mm\,s^{-1}}$ sliding speed (artificial finger only)

No.	In-vivo	0.5 N	0.35 N	0.75 N
5N111	1.23	0.29	0.29	0.53
5N111$_\mathtt{smooth}$	1.30	0.71	0.58	0.82
1N111	1.37	0.28	0.13	0.39
1N111$_\mathrm{smooth}$	1.50	0.23	0.30	0.48
4N111	1.94	0.57	0.73	0.52
4N111$_\mathrm{smooth}$	2.50	0.65	0.83	0.40
5N127	0.99	0.17	0.24	0.20
5N127$_\mathrm{smooth}$	1.04	0.38	0.33	0.42
4N127	1.78	0.47	0.43	0.34
4N127$_\mathrm{smooth}$	2.00	0.52	0.61	0.40
	RMSE	3.79	3.95	7.04

Table 5.5: Friction measurement results of thermoplastic samples at $5\,\mathrm{mm\,s^{-1}}$ sliding speed (artificial finger only)

No.	In-vivo	0.5 N	0.35 N	0.75 N
5N111	1.23	0.48	0.39	0.74
5N111$_\mathtt{smooth}$	1.30	0.72	0.69	0.87
1N111	1.37	0.45	0.43	0.65
1N111$_\mathrm{smooth}$	1.50	0.28	0.24	0.48
4N111	1.94	0.52	0.44	0.58
4N111$_\mathrm{smooth}$	2.50	0.89	0.92	0.76
5N127	0.99	0.29	0.31	0.43
5N127$_\mathrm{smooth}$	1.04	0.54	0.37	0.37
4N127	1.78	0.44	0.48	0.40
4N127$_\mathrm{smooth}$	2.00	0.57	0.66	0.40
	RMSE	3.52	3.30	3.82

Table 5.6: Friction measurement results of thermoplastic samples at $8\,\mathrm{mm\,s^{-1}}$ sliding speed (artificial finger only)

No.	In-vivo	0.5 N	0.35 N	0.75 N
5N111	1.23	0.65	0.58	0.55
5N111$_{\mathrm{smooth}}$	1.30	0.89	0.81	0.96
1N111	1.37	0.56	0.69	0.62
1N111$_{\mathrm{smooth}}$	1.50	0.54	0.37	0.44
4N111	1.94	0.73	0.82	0.63
4N111$_{\mathrm{smooth}}$	2.50	1.2	1.27	1.44
5N127	0.99	0.44	0.38	0.57
5N127$_{\mathrm{smooth}}$	1.04	0.57	0.50	0.61
4N127	1.78	0.46	0.51	0.39
4N127$_{\mathrm{smooth}}$	2.00	0.65	0.73	0.43
	RMSE	3.05	2.04	2.25

Nano-indentation experiment was performed to measure nano-hardness and the stiffness of the TPE samples. These were shown to be significantly different from the micro-indentation. The correlation was better with nano-hardness than Young's modulus, and with patterned samples than the coated samples. The difference in applied load may have contributed to the differences. Both the nano-hardness and Young's modulus measurement values was seen to decrease with increasing penetration depth; this is the indentation size effect seen in other literature [139, 140]. Overall the patterned samples were rougher than the coated samples while the coated surfaces were harder than the patterned samples.

On the friction characterisation, it was found that rougher surfaces were perceived to have lower friction coefficients. Higher sliding speeds generally result in higher measured friction coefficients and also lead to lower error against in vivo results. Friction coefficient for material P4 decreased with the increase of the normal forces, while materials P1 and P5 shows the opposite trend. Adhesion forces might have contributed to the phenomenon with P4.

Sanding the patterned samples to smooth them result in an insignificant change in nano-hardness and Young's modulus measurements; however, it resulted in visibly higher measured friction coefficient for all the patterned samples except sample 1N111.

Overall, the correlation between the in vivo friction measurements and those by the artificial finger is lower than the metal samples. The 'softer' TPE samples may have more complex interactions between the surfaces due to higher levels of deformation, and adhesive friction mechanism may be non-negligible.

Relationship between Friction and Surface Parameters

Iɴ ergonomics, components or materials that are more touch-desirable can be made if the relationship between human touch-feel perception and the physical properties of the contact surfaces can be understood. Commercially, products are increasingly focused on ergonomics and there is increasing demand for surface materials with desirable touch-feel properties[20]. In Chen et al. [8], correlation and regression analyses were carried out on materials used in confectionery packaging to identify the relationships between the people's touch-feel responses and the physical measurements of thirty-seven tactile textures; the results shown that touch perception is often associated with more than one physical property. These parameters are then correlated against subjective touch-feel perception on two of the fundamental (see [21]) psychophysical semantic touch-feel descriptors: 'rough/smooth' and 'slippery/sticky'.

Stroking the surface an object to experience its friction is one of the most direct way to elicit a touch-feel perception, therefore it is desirable to be able to understand the relationship between the skin-against-material friction coefficient and the tribological/mechanical parameters. These parameters include surface topography parameters (see Section 1.1) and surface mechanical properties such as the Young's modulus E and hardness H. According to the validation experiments performed in Chapter 3, the custom-built artificial finger can replicate the frictional properties of a human finger. In this chapter, both in-vivo and artificial finger friction coefficient results were used to investigate the relationships. Firstly, the Spearman's correlation analysis was performed; its objective is to give a general idea of the correlation between the friction coefficient results and the tribological/mechanical

parameters. Secondly, the relationships between the friction coefficients and the tribological parameters S_q, S_m, S_{ku}, S_{sk}, R_{dq} and the Young's modules E were deduced according to the Hertz and the Greenwood-Willam contact theories. Finally, simulation and experiment results were used to validate the theoretical relationships.

6.1 Spearman's Rank correlation analysis

The Pearson's product moment correlation coefficient (PPMCC or Pearson's r) is often used to statistically assess the level of linear correlations between two sets of variables. A value of +1 indicates total positive correlation; 0 indicates no correlation and -1 indicates total negative correlation. Numerically it is the covariance of two variables normalised by the product of their standard deviations. When the underlying data is discrete (not continuous), or if they have non-linear associations, or the presence of outliers is giving a distorted picture of the association between the two variables, the non-parametric Spearman's rank correlation (also called Spearman's rho) should be used. Numerically the Spearman's rank correlation is the Pearson's product moment correlation of the rankings of the two set of variables. It is often used in hypothesis testing to see if there is statistically significant association or correlation between the two variables. Hypothesis tests were conducted in this task to identify statistical significant correlation between the friction coefficient measurements and the tribological/mechanical parameters.

The material samples mentioned in Chapters 3 and 5 were divided to two different groups: metal and polymer. The metal group includes the milled aluminium samples from Chapter 3 labelled `AM1`–`AM6`, the turned aluminium samples labelled `AT1`–`AT6`, and the grinded steel samples `S1`–`S5`. The polymer group includes all the thermoplastic elastomer (TPE) samples, which comprises of 5 types of coated samples plus 10 types of patterned samples (see Table 5.1). Firstly, all the physical parameters data were converted into rankings. Secondly, Spearman's rank correlation coefficients between these physical parameters and the 1) human fingertip friction results, 2) artificial fingertip friction results were calculated. Thirdly, two-tailed hypothesis tests on the strength of the correlation were performed by calculating the corresponding Student's t values, which is then converted into p-values using statistical tables. Values of p below 0.05 was taken as statistically significant correlations.

6.1.1 Correlation analysis for the metal samples

For the artificial finger, results from experiments performed with normal forces of $0.5\,\mathrm{N}$ and $0.75\,\mathrm{N}$, and stroking speeds of $5\,\mathrm{mm\,s^{-1}}$ and $8\,\mathrm{mm\,s^{-1}}$ are also available.
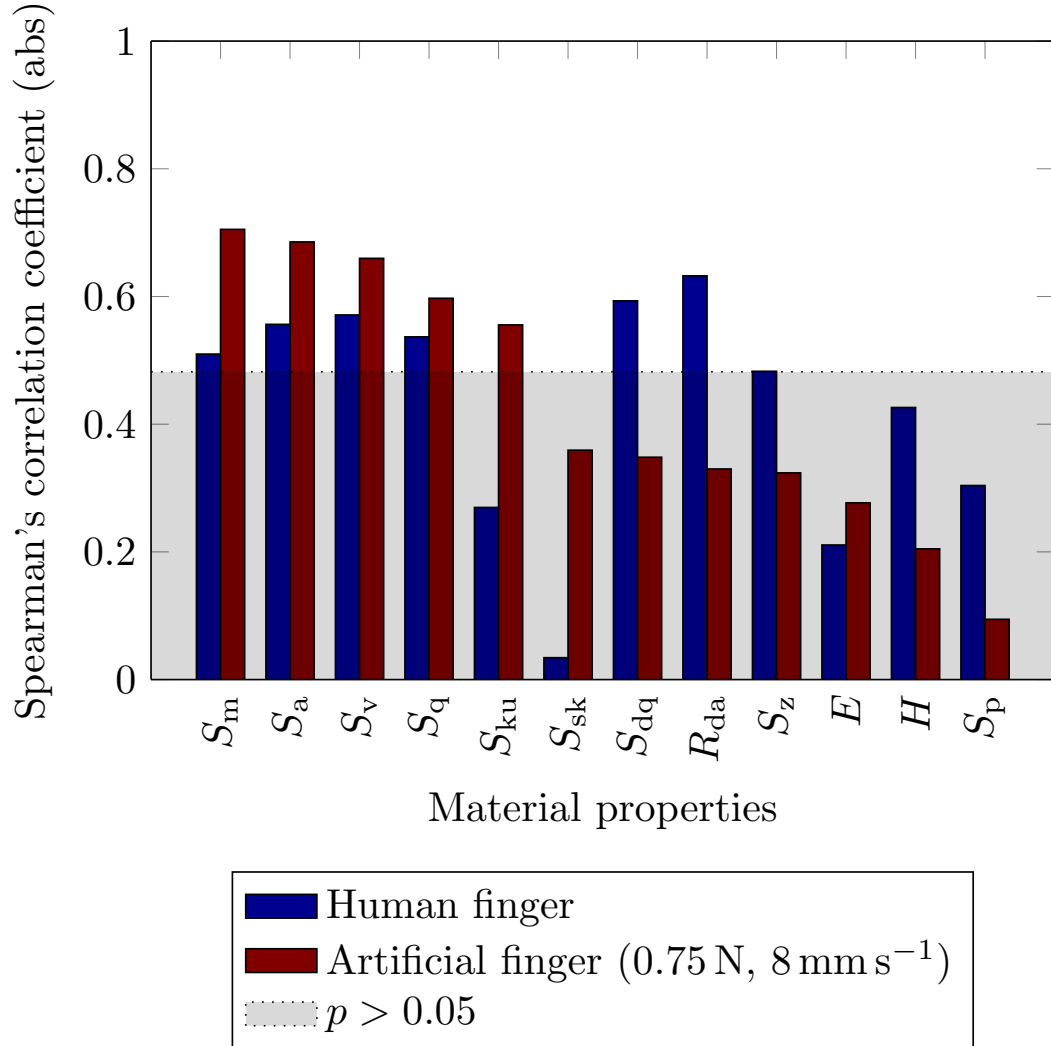
Figure 6.1: Spearman's correlations (absolute) between material properties and friction coefficients measured by human and artificial finger for metal samples

It was found that the combination of $0.75\,\mathrm{N}$ and $8\,\mathrm{mm\,s^{-1}}$ (amongst the 4 sets tried) results in highest overall correlations with the mechanical and topographical parameters. Hence, this set of results are used for comparison with the human finger correlations in Fig. 6.1.

Since one is not interested in the direction of correlation at the moment, the *absolute* values of the Spearman's correlation for the metal samples are plotted. Blue bars represent the correlation against human finger in-vivo friction coefficient measurements, while the maroon bars represent the artificial finger friction results. Correlation values above the dotted line have p values less than 0.05 and are therefore statistically significant.

The pattern of Spearman's ranking correlation coefficients is somewhat different between the in-vivo human finger results and those of the artificial finger. However, considering the statistically significant correlations between the in-vivo results, 4 out of 6 of which are also statistically significant for the artificial finger.

The artificial finger and human finger have statistically significant correlations with 4 of the S-parameters. In addition, the human finger is correlated with R_{da} and S_{dq} which are respectively the arithmetic mean slope and the root mean square slope. This is interesting as it means the human finger friction is influenced by the slope of the hills and valleys, but to a lesser extent for the artificial finger. On the other hand, the artificial finger is somewhat sensitive to the kurtosis parameter S_{ku} but not so much for the human finger.

6.1.2 Correlation analysis for the polymer samples

Results of the Spearman's rank correlation analysis for the thermoplastic materials are shown in Fig. 6.2. In contrast to the metal samples, all material properties have statistically significant correlation with both the human and the artificial finger friction coefficients, indicating complex interactions between the parameters and friction. Mechanical properties such as E and H show the highest correlation coefficient—0.92 and 0.84 respectively for human finger. Correlation with E and H is lower at 0.69 and 0.66 for artificial finger. This is in contrast with the case with metals where E and H were uncorrelated with friction. The contact mechanism with TPE is different compared to metal, with the softer plastic contact giving rise to adhesive forces and higher deformations. S_{dq} and R_{da} characterise the slope of the surface topography, which also shows the high correlation with the friction coefficients $(0.7 \sim 0.85)$. The topographical parameters of S_{a}, S_{q}, S_{z}, S_{m} and S_{v} provide roughness, spatial and hybrid topographical information for the 3D surface, which are all somewhat related. Their correlations are in the range of $0.52 \sim 0.68$

for. Lastly, S_{sk} is a measure of the asymmetry of the amplitude density curve and S_{ku} are measures of the peakiness of the amplitude density curve. Their influence $(0.4 \sim 0.7)$ was mainly due to the contact area change during the sliding friction.
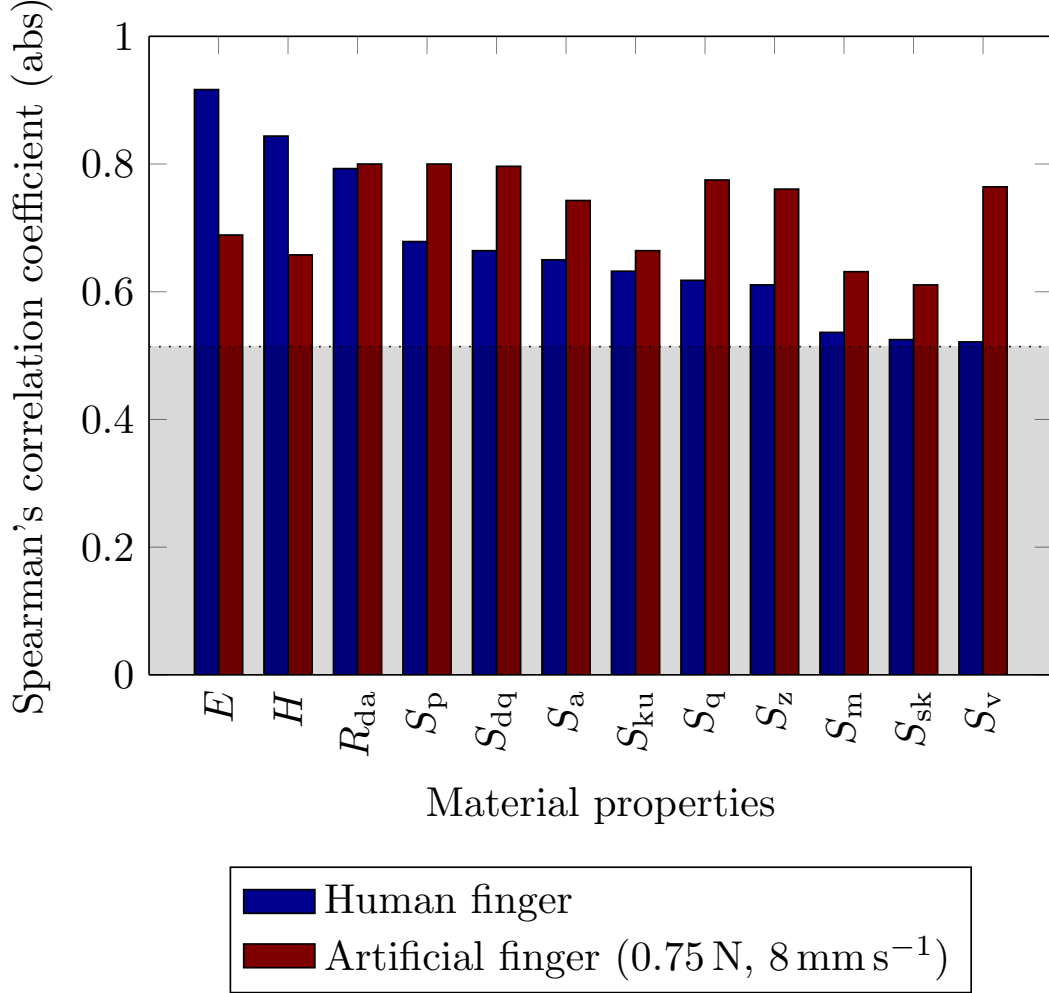
Figure 6.2: Spearman's correlations between material properties and friction coefficients measured by human and artificial finger

The Spearman's correlation analysis showed that there are statistically significant correlations between friction coefficients and specific surface physical parameters. However, theoretical analysis should be performed to investigate the underlying mechanism and look for any cause-and-effects. First, the relationships between surface friction coefficients and R_q, S_m are deduced and validated by the metal and thermoplastic samples measurement results; Secondly, the relationships between surface friction coefficients and the surface mechanical properties such as E are investigated; Thirdly, S_{sk} and S_{ku} are studied and correlated to surface friction

measurement; Finally, the relationships between surface friction coefficients and surface slope parameter R_{da} and S_{dq} are described.

Chapter 4 has shown that the Hertz contact theory is suitable for modelling the contact mechanism. However, for a rough surface with random roughness, the Greenwood-Williamson (GW) model (see Section 4.2.4) should be applied instead. On the other hand, GW modelling is based on an assumption that the height distribution of the asperity summits should follow a Gaussian distribution. Hence, the surface height distribution should be investigated to check if it follows a Gaussian distribution.

6.2 Surface height distributions

All the test surfaces had their surface topography imaged first with a Bruker ContourGT-K optical microscope. These are then analysed using MATLAB to compute their surface height distribution and Q-Q plots are plotted. Q-Q plots are used to evaluate whether a given dataset follows a known theoretical distribution—in this case, the standard Gaussian distribution was used as the reference. The surface height distributions and the corresponding Q-Q plots are shown in Figures 6.3, 6.4, 6.5 and 6.6—one sample for each of the milled aluminium, turned aluminium, steel and TPE samples, in that order. `AM1` has a heavy tail towards the low heights. Since GW model is concerned with summit height distribution being Gaussian, the heavy tail is of no concern. `s58` is the least Gaussian-like, with lighter tails at both ends. For this sample only, GW may be unsuitable. Otherwise, the Greenwood-Williamson model was used to model the contact mechanism. The surface height distributions of other surfaces are shown in the Appendix A.5.

6.3 The relationships between the friction coefficient, S_{q} and S_{m}

S_{a}, S_{q}, S_{z}, S_{m} and S_{v} are tribological parameters commonly used to quantify the surface roughness [25]. They are various statistical measures or summaries of the surface height profile of a given material. Previous literature showed an inverse linear relation between the adhesion of two surfaces and the surface roughness, such that $F_{\mathrm{adh}} \propto R_{\mathrm{q}}^{-1}$ [110]. Greenwood and Williamson [147] modelled rough surfaces as a collection of spherically tipped asperities, all with equal radius and a Gaussian asperity height distribution. This enables the use of Hertz theory on rough surfaces [104]. For many engineering surfaces, the product of the density of asperities η, their

(a) Surface height distribution

(b) Q-Q plot for testing normality

Figure 6.3: The surface height distribution of milled aluminium sample AM1

(a) Surface height distribution

(b) Q-Q plot for testing normality
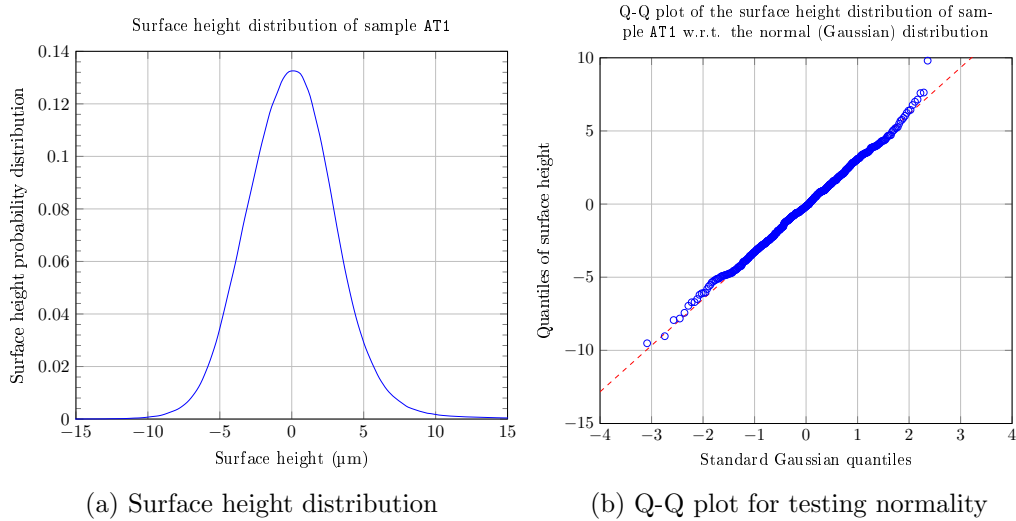
Figure 6.4: The surface height distribution of turned aluminium sample AT1

131

(a) Surface height distribution

(b) Q-Q plot for testing normality

Figure 6.5: The surface height distribution of grinded steel sample S3

(a) Surface height distribution

(b) Q-Q plot for testing normality
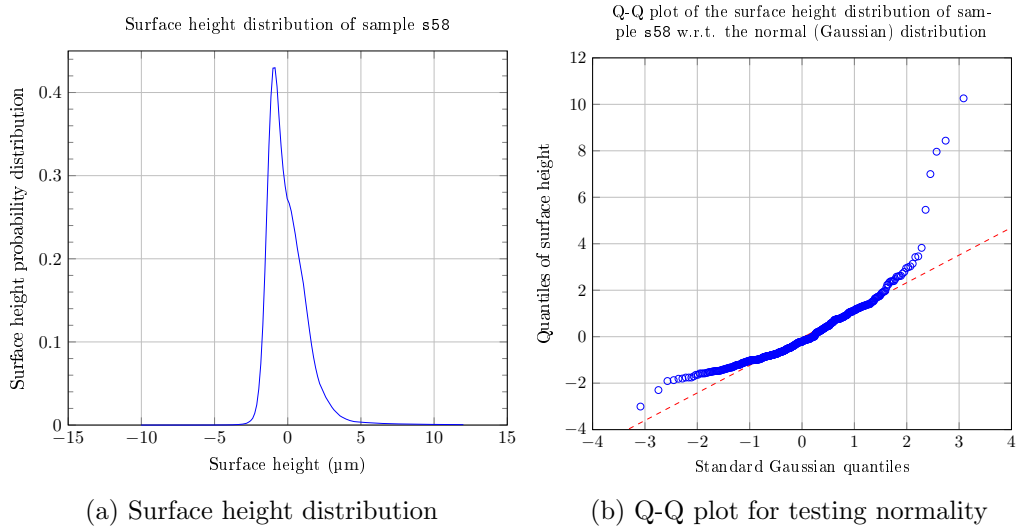
Figure 6.6: The surface height distribution of coated TPE sample s58

132

radius of curvature β and the standard deviation of the asperity height distribution σ is constant [148]. In symbols:

$$\eta \cdot \beta \cdot \sigma = C \tag{6.1}$$

where C is a constant, η is a spatial or lateral parameter, i.e. describing surface micro-geometry in the xy-plane, whilst σ only describes the z-direction. Therefore, these two parameters are orthogonal and as a first approximation, σ does not vary much with changing roughness [149]. By 'translating' the Greenwood-Williamson parameters $\beta \triangleq R$ and $\sigma \approx R_q$, it can be deducted that the curvature radius R and R_q are inversely proportional [9].

6.3.1 Theoretical deduction of the relationships

The surface heights of many samples used in this thesis roughly follows a Gaussian distribution. Because the metals samples are designed to have regular roughness S_a and S_q, they can be seen as regular patterned samples. For this type of surfaces, one can follow the analysis given by Masen [9]. With help of the GW theory, a detailed explanation was given as follows.
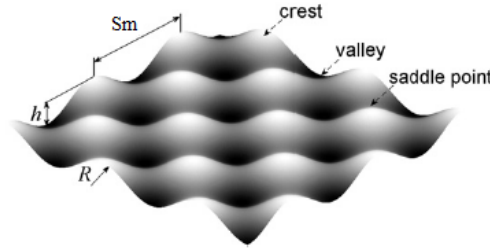
©2011 Elsevier, reprinted with permission from Masen [9]

Figure 6.7: Definition of Spacing of surfaces

The coefficient of friction is composed of a deformation and an adhesion component, while the deformation friction can be ignored as the contact materials are both elastic,

$$\mu \approx \mu_{adh}. \tag{6.2}$$

Since the surface features are arranged in a regular pattern having a pillar spacing S_m, the number of surface features N in contact with the skin can be approximated from the contact area A_0 using

$$A_0 = N S_m^2. \tag{6.3}$$

The total normal load F_n is the combined the normal loads of N surface features $F_\mathrm{n,i}$:

$$F_\mathrm{n} = N F_\mathrm{n,i} \tag{6.4}$$

assuming that the individual surface features of the textures are perfectly spherical and assuming elastic behaviour of the skin.

The Hertz theory of elastic bodies relates the circular contact area of a sphere with a plane (or more generally, between two spheres) to the elastic deformation properties of the materials. The theory neglects surface interactions.

Reproducing Eq. (4.4) from Chapter 4,

$$a_0 = \left(\frac{3F_\mathrm{n,i}R}{4E^*} \right)^{1/3}. \tag{6.5}$$

The contact area $A_0 = N\pi a^2$. Substituting (6.5) one obtains:

$$A_0 = N\pi \left(\frac{3F_\mathrm{n,i}R}{4E^*} \right)^{2/3}. \tag{6.6}$$

Assuming the pattern is regular (repeating), Eq.(6.6) also can be expressed as $A_0 = N S_\mathrm{m}^2$ [9].

The coefficient of friction is then:

$$\begin{aligned}
F_\mathrm{adh} = \tau_0 \cdot A_0 &= \tau_0 \pi N \left(\frac{3F_\mathrm{n,i}R}{4E^*} \right)^{2/3} \\
&= \tau_0 \pi \left(\frac{3F_\mathrm{n,i}R}{4E^*} \right)^{2/3} \cdot N \\
&= \tau_0 \pi \left(\frac{3RF_\mathrm{n}}{4E^*N} \right)^{2/3} \cdot N \\
&= \tau_0 \pi \left(\frac{3RF_\mathrm{n}}{4E^*} \right)^{2/3} \cdot N^{1/3}
\end{aligned}$$

Using $N = \frac{A_0}{S_\mathrm{m}^2}$

$$F_\mathrm{adh} = \tau_0 \pi \left(\frac{3RF_\mathrm{n}}{4E^*} \right)^{2/3} \cdot \left(\frac{A_0}{S_\mathrm{m}^2} \right)^{1/3}. \tag{6.7}$$

$$\mu_{adh} = \frac{F_{adh}}{F_n}$$

$$= \tau_0 \pi \left(\frac{3R}{4E^*}\right)^{2/3} \cdot \left(\frac{1}{F_n}\right)^{1/3} \cdot \left(\frac{A_0}{S_m^2}\right)^{1/3}$$

$$= \tau_0 \pi \left(\frac{3}{4E^*}\right)^{2/3} \cdot \left(\frac{R}{S_m}\right)^{2/3} \cdot \left(\frac{A_0}{F_n}\right)^{1/3} \tag{6.8}$$

$$\mu_{adh} \propto \tau_0 E^{*(-2/3)} \cdot \left(\frac{R}{S_m}\right)^{2/3} \cdot \left(\frac{A_0}{F_n}\right)^{1/3} \tag{6.9}$$

As before, following Eq. (6.1), $R \propto R_q^{-1}$, hence,

$$\mu_{adh} \propto \tau_0 E^{*(-2/3)} \cdot \left(\frac{1}{R_q S_m}\right)^{2/3} \cdot \left(\frac{A_0}{F_n}\right)^{1/3}$$

$$\propto (R_q S_m)^{-2/3}. \tag{6.10}$$

As shown in Eq. (6.10), μ_{adh} is proportional to $F_n^{-1/3}$, the normal force. μ_{adh} is also proportional to $E^{*(-2/3)}$, and to $R_q S_m^{-2/3}$. This result ignores the effect of deformation.

6.3.2 Correlation of theory and experiment for aluminium and steel samples

Frictions results from the aluminium and steel samples were first used to validate the theory derived above. Here we look at results from the human finger (in-vivo measurements) and friction results from the artificial finger when the normal forces were $0.5\,\text{N}$ and $0.75\,\text{N}$ with corresponding linear stage sliding speeds of $5\,\text{mm}\,\text{s}^{-1}$ and $8\,\text{mm}\,\text{s}^{-1}$.

Table 6.1: Coefficient of determination (r^2) for the relationship curve fitting

Materials	$\mu_{\text{in-vivo}}$	$5\,\text{mm}\,\text{s}^{-1}$		$8\,\text{mm}\,\text{s}^{-1}$	
		$\mu_{F=0.5\,N}$	$\mu_{F=0.75\,N}$	$\mu_{F=0.5\,N}$	$\mu_{F=0.75\,N}$
Surface ground steel	0.0777	0.8050	0.8507	0.8964	0.8777
Milled aluminium	0.8679	0.3563	0.4386	0.8845	0.8999
Turned aluminium	0.8194	0.6094	0.5463	0.5285	0.9113

Considering the relationship predicted by the theoretical analysis in Eq. (6.10), a log-log plot of friction μ against the product of $R_q S_m$ should result in a straight line with a slope of $-2/3$. In Figures. 6.8 and 6.9 one can see that the data roughly follows a straight line relationship. The data were regressed (curve fit) to the form

(a) $5\,\mathrm{mm\,s^{-1}}$ (b) $8\,\mathrm{mm\,s^{-1}}$
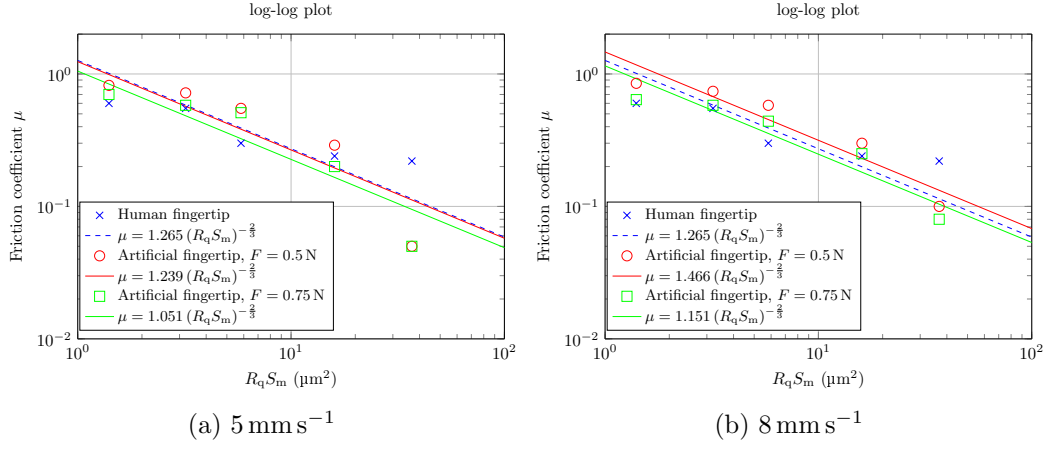
Figure 6.8: Steel Samples

(a) $5\,\mathrm{mm\,s^{-1}}$ (b) $8\,\mathrm{mm\,s^{-1}}$
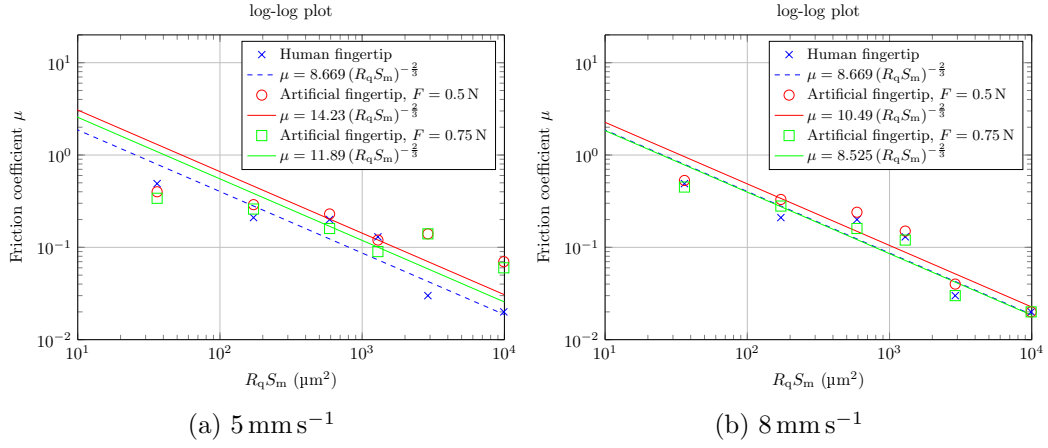
Figure 6.9: Milled aluminium Samples

(a) $5\,\mathrm{mm\,s^{-1}}$ (b) $8\,\mathrm{mm\,s^{-1}}$
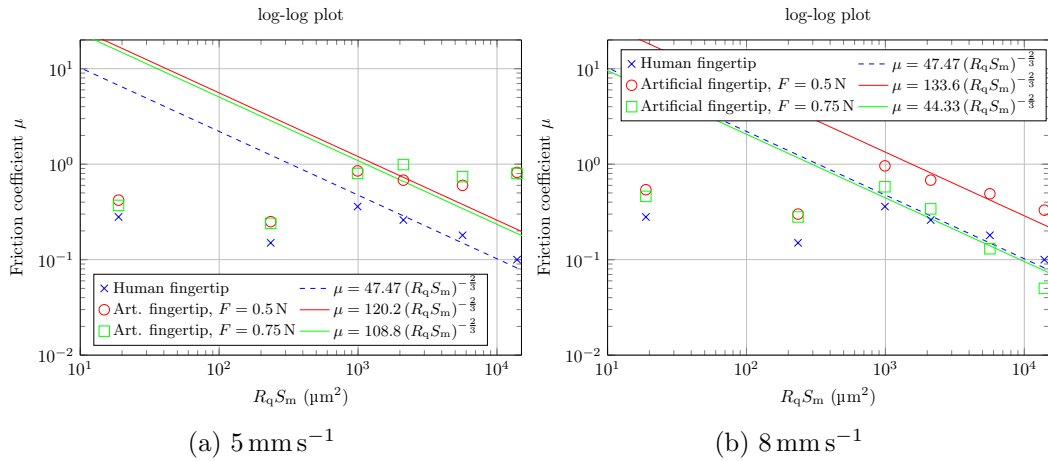
Figure 6.10: Turned aluminium Samples

136

of $a\left(R_m S_q\right)^{-2/3}$, such that the value of a resulting in the least squared errors was found and shown on the legends of the figures. For experiment results with the $8\,\mathrm{mm\,s^{-1}}$ sliding speed setting, the theoretical relation fit the data relatively well on the log-log scale (the least square fitting and the associated statistics on Table 6.1 was based on the log-log space). Overall, the fit with $5\,\mathrm{mm\,s^{-1}}$ setting appears to be worse especially for the aluminium samples. Indeed in previous chapters, it was found that the higher $8\,\mathrm{mm\,s^{-1}}$ setting for the artificial finger sliding speed results in better correlation with in-vivo human finger results.

Table 6.1 showed the coefficient of determination (r^2) between the theoretical relationship and the data. It is shown that a high r^2 ($0.8 \sim 0.9$) is obtained for steel and milled aluminium samples. For turned aluminium, the fit was unacceptable (worse than a horizontal null line) if the outliers of `AT1` and `AT2` were included. Discounting them in the fit improved the correlation to as high as 0.91. The results support the fact the theoretical relationship give a satisfactory description of reality and the friction measurement is accurate for metals.

The results have implications for industrial application—if the friction coefficients a surface preferred by customers is known, the relative surface topography parameters such as R_q, S_m can be used to tune the friction characteristics according to Eq. (6.10).

6.3.3 Correlation of theory and experiment for thermoplastic Samples

Compared with metal samples, thermoplastic materials are much softer, with a higher risk of large deformation occurring, potentially violating the assumptions of Hertz and GW contact models. The five patterned samples (`1N111`–`5N127` plus their five sandpapered counterparts in Table 5.1) have their the R_q and S_m values measured using the Bruker optical microscope and their friction coefficients measured using human and artificial fingers. Similar to Figures. 6.8 and 6.9, the results from the TPE samples are plot in log-log axes and shown in Fig. 6.11.

It can be seen from the figure that the picture is more complicated; the theoretical slope of $-\frac{2}{3}$ is only observed to fit a few data points (e.g. the rightmost 4 points of artificial finger). The true slope seems to be shallower. There is insufficient data to conclusively say whether the theoretical relationship still holds or otherwise. More data from the lower end of $R_q S_m$ is needed to investigate this further. The large variance of the friction result among the samples with similar $R_q S_m$ either indicate that $R_q S_m$ has no correlation with friction for these polymer samples, or it indicates a presence of complex phenomena. Since the samples are comparably softer than metal samples, it is possible that there were large deformations during contact. The

(a) $5\,\mathrm{mm\,s}^{-1}$ (b) $8\,\mathrm{mm\,s}^{-1}$
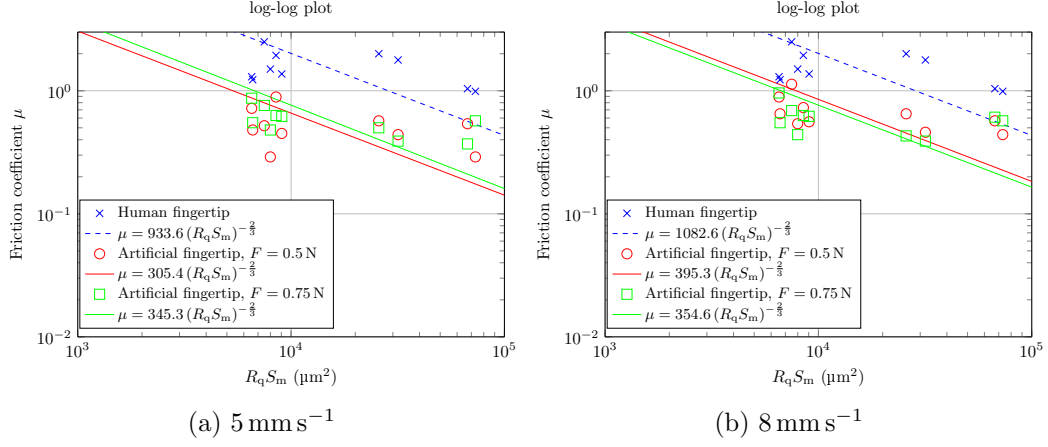
Figure 6.11: Thermoplastic patterned samples

contact area might have been larger due to adhesion. In addition, the assumption that $A = N S_m{}^2$ is not strictly correct because the surfaces of thermoplastic materials do not have regular patterns.

(a) $5\,\mathrm{mm\,s}^{-1}$ (b) $8\,\mathrm{mm\,s}^{-1}$
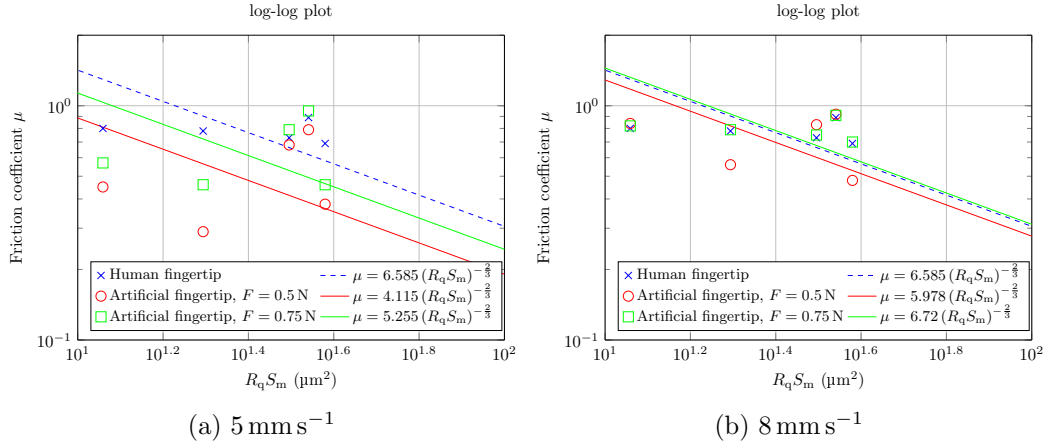
Figure 6.12: Thermoplastic coating samples

Results on the coated samples (`s44`–`s97R` in Table 5.1) are shown in Fig. 6.12. Like the case with patterned samples, the data seems to have a slope shallower than the theoretical relationship, but there are insufficient samples to draw any concrete conclusions. There are several reasons for possible deviations from theory; like the patterned samples, the coated samples do not have regular patterns on the surface, and the assumption that $A = N S_m{}^2$ used to derive Eq. (6.10) is only an approximation. The contact for the coated samples is also more complex because the substrate still has an effect on the deformation during friction measurement even

138

though the friction mechanism only occurs on the coating.

6.4 The influence of Young's modulus to contact area and friction coefficient analysis

According to Eq.(6.10), the Young's modulus also has an influence on the contact area. When the Young's modulus is smaller, the real contact area increases. As a result, the perceived friction also increases. Although it is generally accepted that the Young's modulus affects the friction coefficient, it still worth investigating the real contact area. Here the ratio of the nominal contact area to the real contact area was calculated using the Greenwood-William simulation program developed in [150, 151]. The MATLAB implementation is shown in Appendix A.8.

6.4.1 Simulation of the Greenwood-Williamson Model

The GW model can be used to analyse the real contact area of various surfaces of different characteristics. While the Hertz contact theory allows one to estimate how many peaks and valleys are included in the contact area, the GW model can calculate the real contact area as a ratio of the nominal contact area in every peaks and valleys. However, the GW model is limited to several assumptions: 1) The rough surface is covered with a number of asperities, which, at least near their summit, are spherical; 2) All the asperity summits have a constant radius on each surface; 3) The asperity heights vary randomly; Height profiles of many engineering surfaces obey Gaussian distribution.

The GW model is normally applied to model contact between randomly rough surfaces and the Hertz contact theory is applied to contact between each asperity. It results in the real contact area that is dependent (slightly) non-linearly on the load even for a very small load. In this case, a more general and accurate contact mechanics theory which can be applied to many different length scales is needed.

Aramaki, Cheng and Chung [151] used a quadratic function to approximate an asperity with width L and height ζ, in the form of

$$z = -\frac{4\zeta}{L^2}x^2 + \frac{4\zeta}{L}x. \tag{6.11}$$

The Greenwood-William simulation MATLAB program mentioned before [150, 151] uses this approximation to fit the roughness of the surface.

Software simulations were performed to analyse the real and nominal contact area for the metal and thermoplastic samples. As shown in Fig. 6.13b for the sample
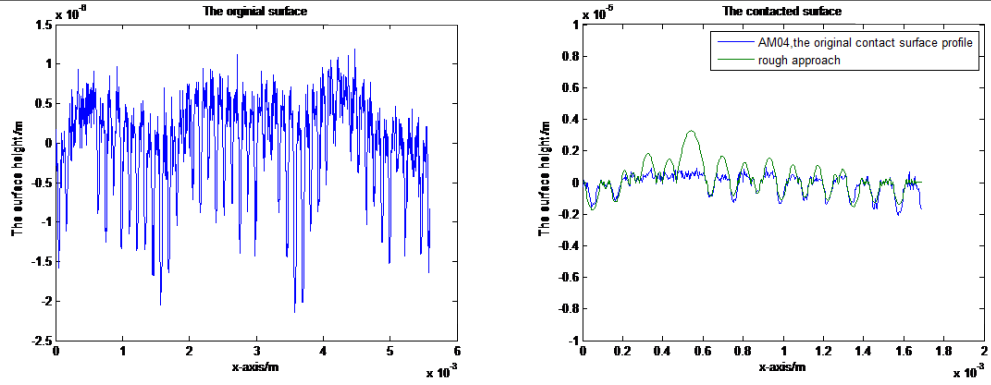
(a) The original surface roughness of AM1

(b) Contact surface profile before and after approach when normal force was 0.98 N
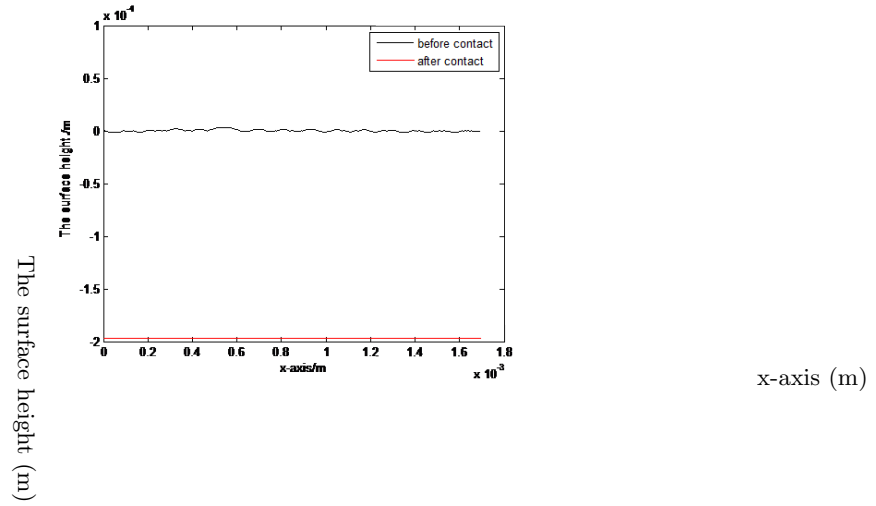
(c) The surfaces separation before and after the deformation

Figure 6.13: AM1 rough approach and its contact results

AM1 (see Table 3.3), the surface approximation by the Aramaki formulation captures most of the surface roughness details, although there is an error of 0.2 μm in some peaks of the surfaces. After the surface approximation, the GW contact model was used to analyse the contact mechanism of every peak and valley when the surface height was higher than the separation distance between the two contact surfaces. The contact force was set to 0.98 N, and the radius of artificial fingertip was set to 7.5 mm. Fig. 6.13c showed the deformation between the contact of artificial fingertip and the AM04 sample. The contact radius was calculated as 1.7 mm and the real contact area was calculated as 99.72% of the nominal contact area.

Comparing Fig. 6.13b to Fig. 6.14 for AM6, the contact surface profile changed
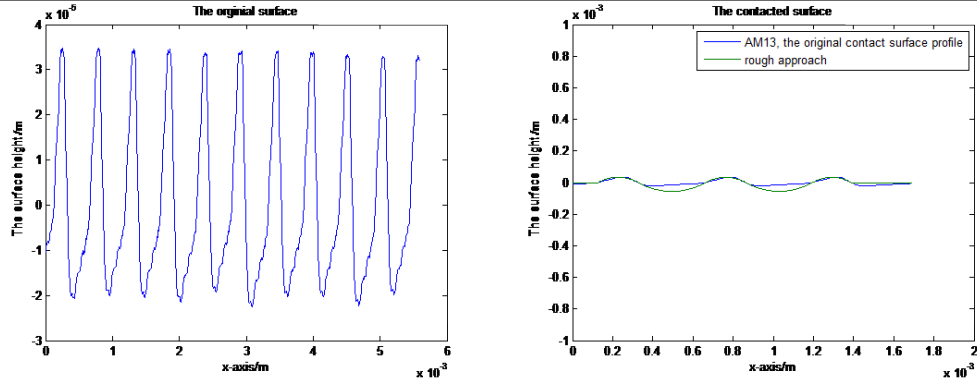
(a) The original surface roughness of `AM6`

(b) Contact surface profile before and after approach when normal force was $0.98\,\text{N}$
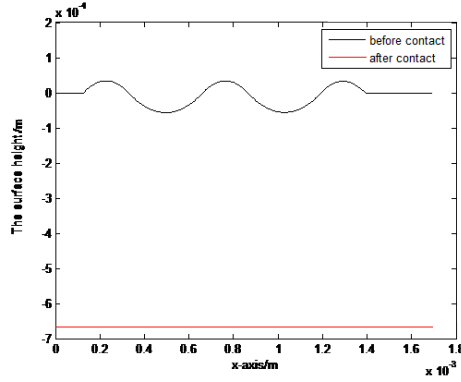
(c) The surfaces separation before and after the deformation

Figure 6.14: `AM6` rough approach and its contact results

when the surface roughness changed. However, the real contact to nominal contact area ratio remains the same at 99.72%. However, aluminium is not a very good material for this kind of modelling because it is too hard relative to the artificial fingertip, meaning that nearly all of the deformation occurs on the artificial fingertip rather than on the contact surface. This is why there was no observable change in the contact area between the aluminium (and steel) samples.

In Chapter 4, the contact areas were investigated using an optical contact area measurement mechanism consisting of a glass plate in lieu of a material sample. The MATLAB program introduced in this section also validates the results from Chapter 4. The GW model is suitable for modelling the contact mechanism for the samples investigated.

141

6.4.2 The correlation analysis results

Table 6.2: Contact area simulation of various materials with different Young's moduli

Sample	Young's modulus (MPa)	Contact radius (µm)	% of real contact
Steel	220.000	1695	99.55%
Aluminium	70.000	1695	99.55%
5N127	779.5	1696	99.60%
5N111	182.5	1698	99.65%
1N111	69.5	1703	99.70%
4N127	17.5	1728	99.72%
4N111	14.25	1735	99.78%
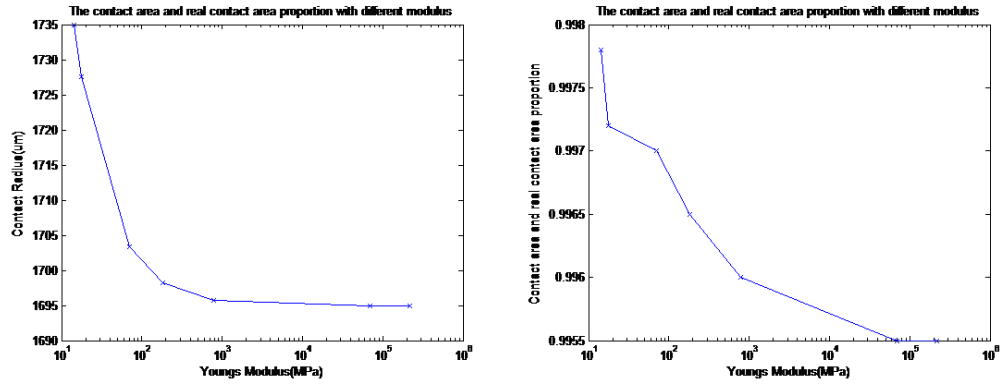
(a) Contact radii of different surfaces with different Young's moduli (b) The ratio of real to nominal contact area

Figure 6.15: Contact area results when the normal force was 0.98 N

Contact area analysis results of all samples are tabulated in Table 6.2 and plotted in Fig. 6.15. The change of contact radius is small across the materials. The normal force in all contact was set to 0.98 N. The contact area increases when the material Young's modulus increases, i.e. when the material is less stiff, or colloquially, softer. The proportion of the real contact area also increases when the material is less stiff. The ratio shows that there was nearly full contact between the two bodies across different roughness. According to the Eq. (6.10), dry sliding friction also becomes higher when the material is less stiff. The friction results are already presented in Chapters 3 to 5—the friction coefficients of TPE materials were much bigger than the steel and aluminium samples in the same measurement conditions.

6.5 The relationship analysis between friction, S_{sk} and S_{ku}

For description of surface topography, the roughness parameters S_a and S_q do not capture all the information. Very different surface profiles can show similar or identical values of standard roughness parameters. The opposite is also possible, very similar surfaces may end up having very different roughness parameters. S_a describes the overall height variations, without any details on waviness and it is not sensitive to small changes in profile height. Compared with S_a, S_q is more sensitive to the variance of height, while it does not pick up detailed information on the surface roughness.

Skewness and kurtosis are the third and fourth moment of the density function, which are used to characterise asymmetry and the flatness of the surface distribution. For engineer surfaces that have non-Gaussian surface topography, S_{sk} gives the skewness on the distribution and is sensitive to occasional deep valleys or high peaks. Zero skewness by definition appears in symmetrical height distributions, while positive skewness describes surfaces with high peaks or filled valleys, and negative skewness describe surfaces with deep scratches or lack of peaks. S_{ku} is defined as kurtosis which describes the sharpness of the probability density distribution of the height profile. S_{ku} is less than 3 when surfaces have relatively few high peaks and low valleys, while S_{ku} is more than 3 when the surfaces have relatively high number of high peaks and low valleys [67, 78].

Negative skewness   Kurtosis lower than 3

Positive skewness   Kurtosis higher than 3
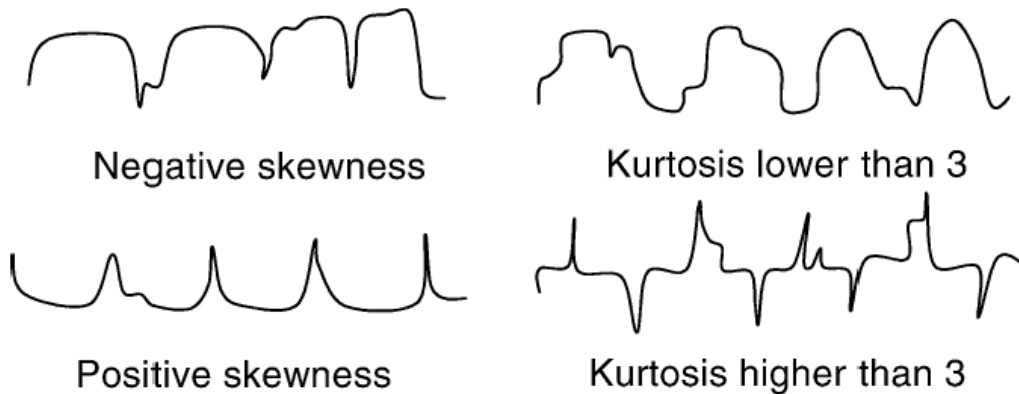
©2012 SAGE Publications, reprinted from Sedlaček, Podgornik and J.Vižintin [67]

Figure 6.16: Surfaces with various skewness and kurtosis values

The nth moment of the surface roughness function can be described as follows.

The probability density function P_h defines the probability of locating a point at a height h. Denote $\bar{h}$ to be the mean height (the first moment of height). This is not to be confused with S_a, which is the L^1-norm of height, i.e. the averaged absolute height values about the mean. S_a is the first moment only if the heights are strictly positive. S_q is the second moment of height. Fig. 6.16 shows the effect of S_{sk} and S_{ku} on the surface roughness [73].

$$h_n = \int_{-\infty}^{\infty} (h - \bar{h})^n P_h \, dh \tag{6.12}$$

$$R_{sk} = \frac{1}{\sigma^3} \int_{-\infty}^{\infty} (h - \bar{h})^n P_h \, dh \tag{6.13}$$

$$R_{ku} = \frac{1}{\sigma^4} \int_{-\infty}^{\infty} (h - \bar{h})^n P_h \, dh \tag{6.14}$$

where σ is the S_q of the surface and the standard deviation of P_h. For a Gaussian distribution, the skewness is zero and the kurtosis is 3. Sedlaček, Podgornik and J.Vižintin [67] reported that for dry sliding, positive S_{sk} values lead to a greater real contact area and a large number of peaks in the contact, as well as the tangential and adhesion forces compared to a Gaussian distributed surface. It means that negative R_{sk} lead to lower friction. Negative S_{sk} values describe surfaces with deep scratches or a lack of peaks; the real contact area decreases in this case[152]. For S_{ku} greater than 3, surfaces is filled with high peaks and low valleys. The real contact area will decrease due to partial contacts. The influence of S_{sk} and S_{ku} on dry sliding friction can be used as a guideline for designing surface topography with reduced friction.

Compared to the Gaussian distribution($S_{ku} = 3, S_{sk} = 0$),surfaces with a high S_{ku} and a positive S_{sk} should result in a lower static friction coefficient during dry contact [74]. When S_{ku} increases from 2 to 10, the static friction decreases by a factor of about 6 [75], mainly due to an increased contact area [76]. Under dry sliding higher values of parameter S_{ku} and more negative values of S_{sk} led to lower friction, indicating that deep valleys act as wear particle traps [152].

6.5.1 The theoretical analysis

According to the GW contact model described in Section 4.2.4, if the surface height distribution is known, the real contact area between surfaces can be calculated using the equations given. The probability density function (pdf) of the surface height defines the probability of locating a point at a height h and is denoted by P_h. The probability density function can be used to calculate the higher order moments of

the height distribution, using

$$m_{\text{n}} = \int_{-\infty}^{\infty} (h - \bar{h})^n P_{\text{h}} \, \mathrm{d}h \tag{6.15}$$

where $\bar{h}$ is the mean height of h, which is generally removed during data processing and therefore is usually zero. As such, the first moment is zero. The second moment m_2 is the variance σ^2, which is the square of the standard deviation when $\bar{h} = 0$. The third moment m_3 is the skewness, which shows degree of symmetry of the surface profiles. If the mean is on the left side of the distribution mode, the skewness will be negative with a relatively large numbers of peaks than valleys at a certain height. The skewness of Gaussian distribution surfaces is 0. The fourth moments $m4$ represents the peakedness(degree of pointedness or bluntness) of the distribution. A surface with low kurtosis has a relatively larger number of peaks than valleys at a certain height. The influence of S_{sk} and S_{ku} to surface height probability as shown in Figures 6.17 and 6.18 [73].
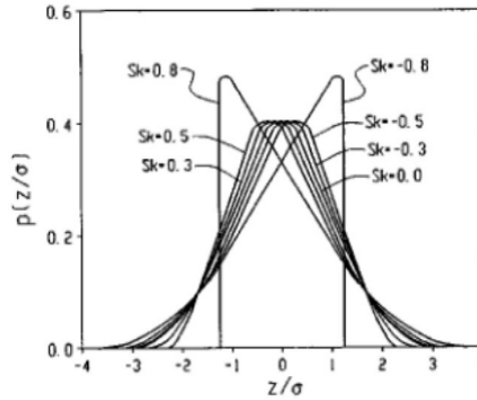
Figure 6.17: The influence of skewness to surface height probability distribution [73]

As the skewness and kurtosis are the third and fourth moments of the probability density function, the curve fitting parameters can be determined in terms of the skewness and the kurtosis. Once the probability density function is determined, a contact model can be developed using the GW modelling approach [147]. Based on the classical theory of friction[153], the kinetic friction is proportional to the real area of contact which is higher for smoother surfaces [147].

The Pearson system of frequency curves, based on the methods of moments, provides a family of curves which can be used to generate an equation for a distribution for which the first four moments are known [154], i.e. the probability density function can be generated for a distribution having a known mean, standard deviation, skewness and kurtosis.
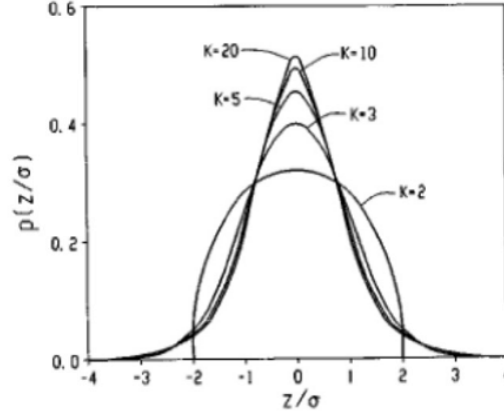
Figure 6.18: The influence of kurtosis to surface height probability distribution [73]

In Pearson's curve fitting, κ is defined as the type of the height probability distribution in Eq. (6.16). Different values of κ determine different equations obtained for the probability density functions. The value of κ ranges from ∞ to $-\infty$, and depending on the range it calculated, the appropriate equation of the density function is obtained. The list of the different types of curves and the range of κ for which they are applicable is shown [155]. There are three main types of Pearson curves which cover the majority of the cases. These are types I, IV and VI. The parameters for the different types of density functions depend solely on the skewness and kurtosis [75].

$$\kappa = \frac{S_{\text{sk}}{}^2(S_{\text{ku}} + 3)^2}{4(2S_{\text{ku}} - 3S_{\text{sk}}^2 - 6)(4S_{\text{ku}} - 3S_{\text{sk}}{}^2)} \tag{6.16}$$

The value of κ determines the type of the curve. There are three main types of Pearson curves which cover the majority of the cases. According to the contact model described in Section 4.2.5, the probability distribution of the surface height can be determined. The parameters in the curves for the non-Gaussian probability density functions are functions of the standard deviation, skewness and the kurtosis. Once the non-Gaussian probability density functions are obtained in this manner, the calculated results can be substituted into the Greenwood-Williamson model.

Based on the classic GW contact model, the normalised contact area, normalised number of contacts and the normalised contact force can be calculated. The following figures show the simulated contact area and the friction results in [73] on one material. In order to better understand how S_{sk} and S_{ku} affect the contact and the friction, simulation based on our samples was performed compared with the friction coefficient experiment results.

6.5.2 The real contact area analysis

According to the above theoretical analysis, if we know the surface height data such as surface mean height ($\bar{h}$), the standard deviation (S_{q}), the third moment (S_{sk}) and the fourth moment (S_{ku}), the surface probability distribution can be constructed. The more moments are known, the more precisely the shape of the distribution will fit the real sample.

In this thesis, all surface height data are measured accurately (see Chapter 3). Based on Kotwala and Bhushan [122], the probability density distribution of height profile of the measured surfaces can be derived using the MATLAB statistics toolbox.

The influence of S_{sk} and S_{ku} can be simulated using the GW model described before. The milled aluminium sample `AM1` was chosen and either one of the parameters S_{sk} and S_{ku} was set to be constant while the other was varied. The analysis results are shown in Fig. 6.19. When $S_{\mathrm{sk}} = 0$, the nominal real contact area decreases with the increase of S_{ku}. And when $S_{\mathrm{ku}} = 3$, the nominal real contact area decreases with the increase of S_{sk}. However, the results is only valid when the other surface topography parameters remains the same. The influence of surface topography on the surface friction will mostly likely depend on other parameters such as S_{q} and S_{m}.

(a) Influence of S_{ku} when $S_{\mathrm{sk}} = 0$ (b) Influence of S_{sk} when $S_{\mathrm{ku}} = 3$
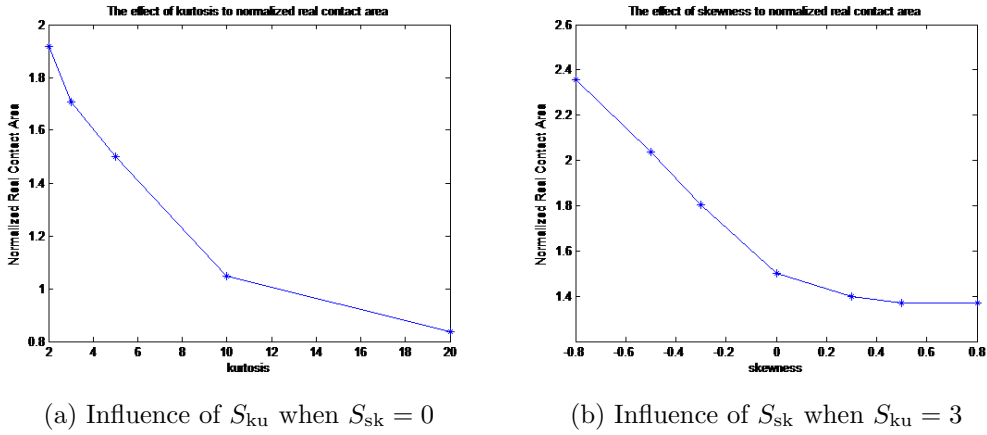
Figure 6.19: Influence of S_{k} and S_{ku} on the normalised real contact area

6.6 The relationship between surface friction and the surface slope ($R_{\mathbf{da}}$, $S_{\mathbf{dq}}$)

The averaged slope of the surface profile, R_{da} and S_{dq}, were shown to correlate with surface friction. It is defined as the mean absolute profile slope over the assessment length. This parameter can be calculated by calculating all the slopes between each

two successive points of the surface profile, then calculating the average of such slopes. The mathematical expression for calculation the mean slope parameters is given by [156]:

$$S_{dq} = \frac{1}{L} \int_0^L |\frac{dy}{dx}| \, dx \qquad (6.17)$$

and numerically evaluated as

$$S_{dq} = \frac{1}{n-1} \sum_{i=1}^{n-1} \frac{\delta yi}{\delta xi}. \qquad (6.18)$$

When the slope of the harder asperities increases, the stresses required to overcome these asperities also increase during sliding. This situation induces a higher level of shear stresses in the pin and thus result in a higher coefficient of friction [157].

Yandell [158] indicated that approximately 80% of the hysteretic energy dissipated occurs in the volumes represented by the hatching observed in Fig. 6.20. It is concluded that the coefficient of hysteretic friction of the two textural components can be predicted reasonably well by the average slope of their contacted surfaces in the direction of sliding. Yandell [158] also theorised that the load dependence of rubber μ values obtained from dry testing of smooth surfaces where adhesion is usually considered predominating could be attributed to a hysteric mechanism involving the micro-roughness of a smooth, paired material.

When the mean surface slope increases, the real contact area decreases, and the friction coefficient decreases as well. When the same material has the same roughness parameters such as S_q, higher surface slopes will have fewer asperity at the sampling length. It means that the real contact decreases at the sampling length, and the friction coefficient decreases as a result. In order to validate the analysis, the metal samples and the thermoplastic samples are applied to analyse the relationship between friction and surface mean slope.

The relationship between the mean slope R_{da} and μ of metal samples are shown in Figures 6.21 and 6.22. Following from the theoretical analysis, the friction coefficient decreases when the mean slope increases. The results support this view, especially on the steel and milled aluminium samples. However, this is based on the assumption that the samples are the same material. When looking across samples of different materials, the μ are not necessarily correlated to R_{da}.

As shown in Fig. 6.23, the thermoplastic patterned and coated samples don not obey this rule because the substrate was made of different materials, with different Young's modulus and hardness. The contact mechanism between the two bodies are
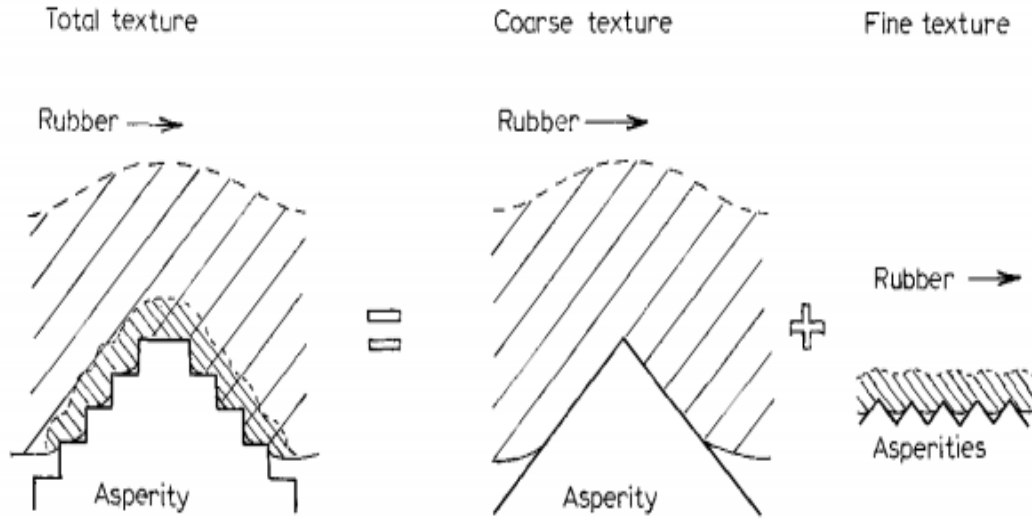
Figure 6.20: Analysis of surface texture as two components. Hatched areas represent volumes of rubber in which about 80 percent of hysteretic energy is dissipated
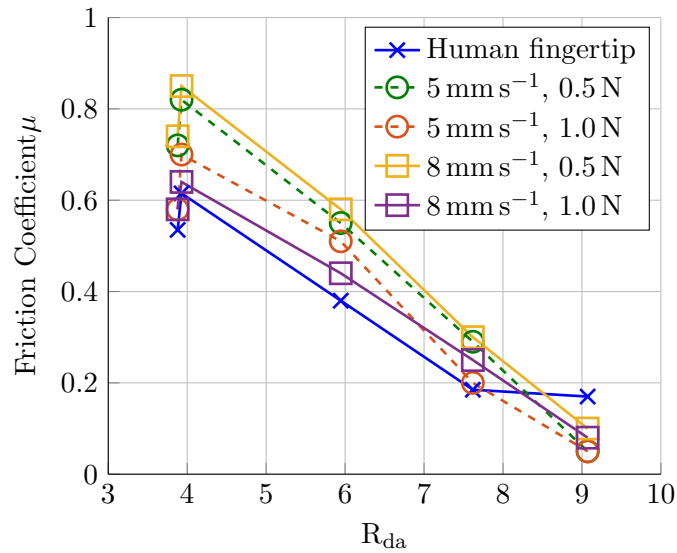
Figure 6.21: The relationships between R_{da} and friction coefficient for the steel samples

(a) Milled aluminium

(b) Turned aluminium
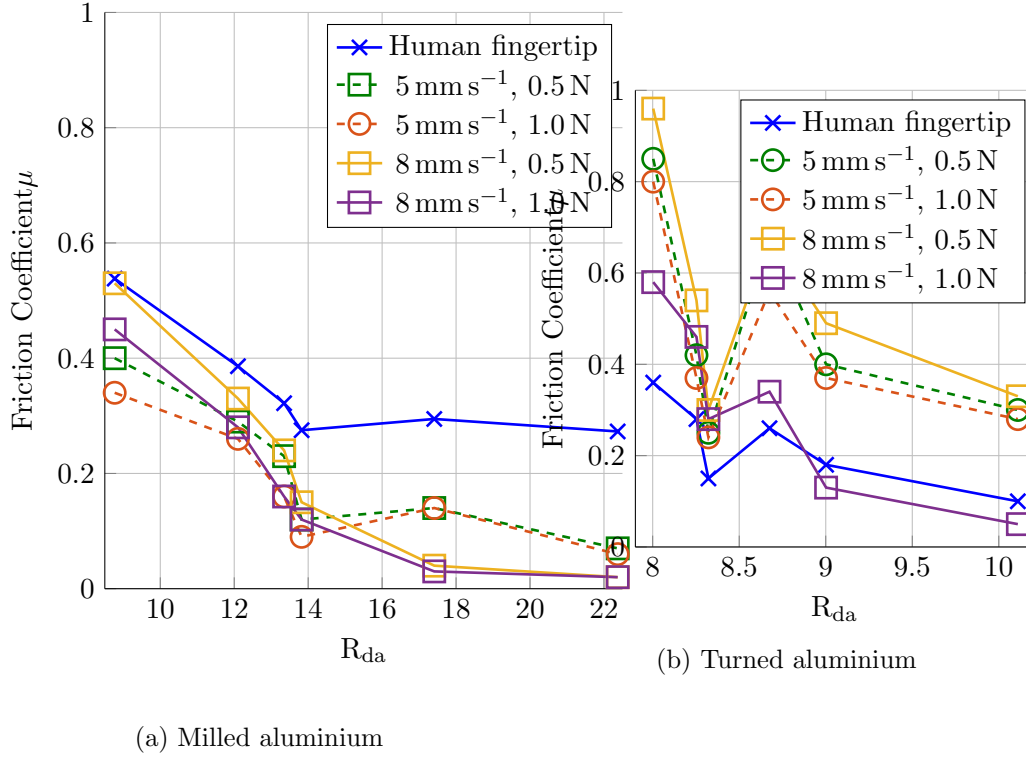
Figure 6.22: The relationships between R_{da} and friction coefficient for the aluminium samples

different, and the relationship is not clear anymore.

6.7   Conclusion

This chapter studied the relationship between surface friction coefficients and surface properties parameters, both theoretically and experimentally. Firstly, a correlation analysis has been carried out using Spearman's rank correlation method. For metal samples, a subset of surface topography parameters such as S_{a}, S_{ku}, S_{q}, S_{v}, S_{z} and S_{m} appear to have varying influence on the friction coefficient. For thermoplastic samples, which are softer, every surface parameter including the mechanical parameters of E and H appears to influence the surface friction.

Theoretical analyses has been carried out to offer insights into the relationships systematically by grouping related parameters First, the relationships between surface friction coefficients and R_{q}, S_{m} were deduced using Greenwood-Williamson theory, and comparisons were made with the metal and thermoplastic samples measurement results; Secondly, the relationships between surface friction coefficients and the

(b) Coated
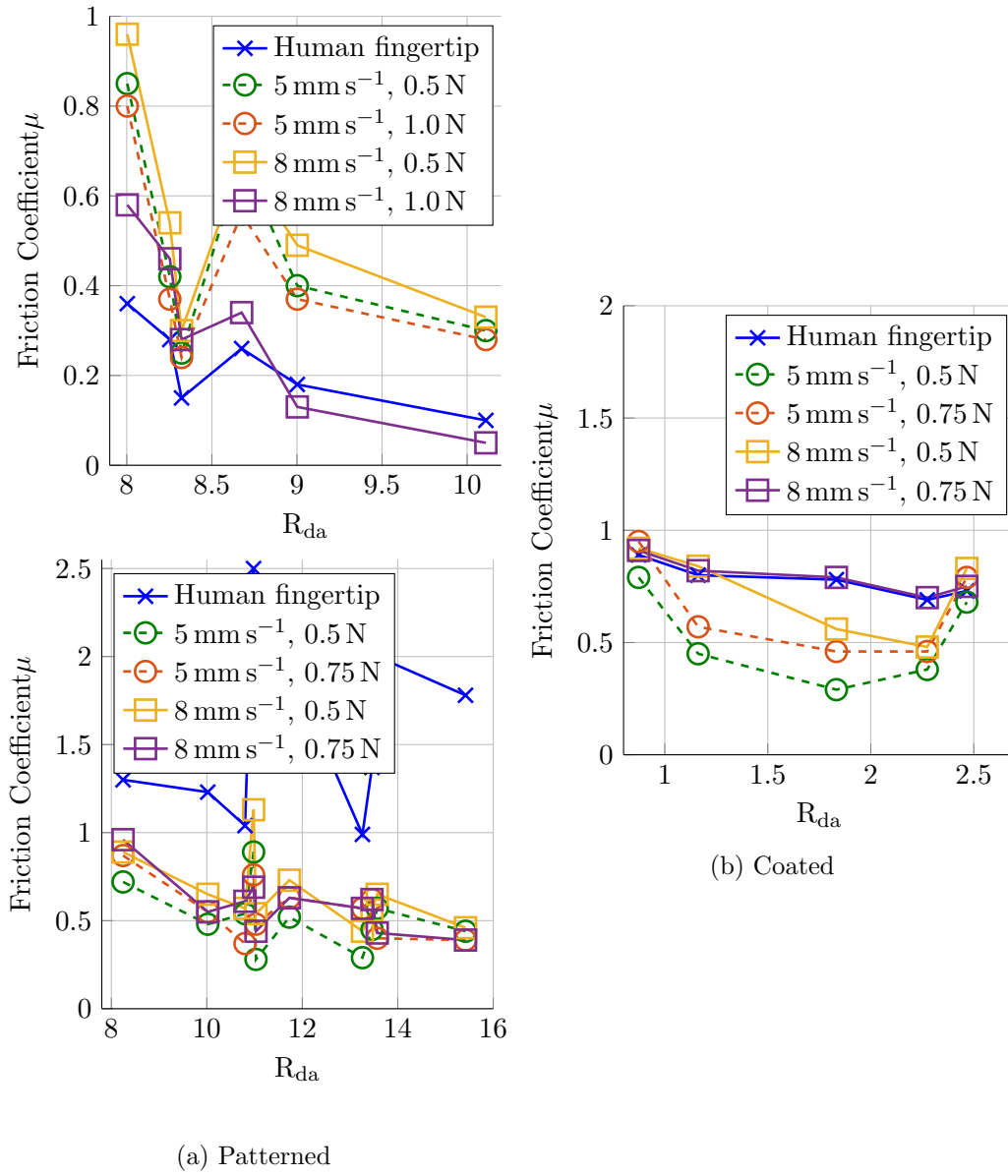
(a) Patterned

Figure 6.23: The relationships between R_{da} and friction coefficient for the thermoplastic patterned and coated samples

surface mechanical properties such as E are investigated; Thirdly, S_{sk} and S_{ku} are studied and correlated to surface friction measurement; Finally, the relationships between surface friction coefficients and surface slope parameter R_{da} and S_{dq} are described.

GW model predicts the dependence of friction on the product of $R_q S_m$ raised to the power of $-2/3$. Correlation and curve fitting shows the model prediction is acceptable for metal but much less so for the thermoplastic samples. Compared with metal samples, thermoplastic materials are much less stiff and softer, with a higher risk of large deformation occurring, potentially violating the assumptions of Hertz and GW contact models. For example, the contact area might have been larger due to adhesion. In addition, the assumption in GW theory that $A = N S_m{}^2$ is not strictly correct because the surfaces of thermoplastic materials do not have regular patterns.

Simulation was performed to analyse the real and nominal contact area for the metal and thermoplastic samples. The MATLAB program introduced also validates the results from Chapter 4. There was no observable change in the contact area between the aluminium (and steel) samples due to their hardness being much greater than that of the artificial finger, and the majority of the deformation occurs on the artificial fingertip.

The theory also predicts a decrease of the friction coefficient when the mean slope (R_{da}) increases. The results support this view, especially on the steel and milled aluminium samples. The relationship only holds true across the same material. This is why the prediction does not hold true for TPE results, whereas the material varies between the samples.

As the friction coefficient is system dependent, a more comprehensive look at different materials and surface patterns is required.

Modelling Touch-feel Perception

Touch-feel perception of products has become a dominant factor in winning or losing customers in many industries from automotive, consumer electronics, to packaging of luxury products such as perfumes and cosmetic boxes [15, 85, 87]. The pursuit for higher perceived product quality has led to growing R&D globally in quantifying and modelling touch-feel perception over the past decade [14, 159]. If the relationship between the qualitative touch-feel perception and the quantitative surface physical properties can be established, material and surface texture design can be guided to meet the customer demands [7].

Following surface characterisation in previous chapters, the touch-feel perception ranking experiments in terms of 5 pairs of psychophysical adjectives/descriptors [160] had been introduced in this chapter. The significance of every surface parameters on the touch-feel perception was analysed using Spearman's rank correlation coefficient initially. Then, the more sophisticated rank-ordered logit (ROL) models were deployed to look for multinomial associations [161, 162]. ROL is one of the standard tools specifically designed to model rank data [163]. ROL model uses latent (unobserved) segments to endogenously identify the unobserved ranking capabilities of respondents. In addition to being able to test statistical significance of the relationships like the Spearman's rank correlation analysis, the ROL model outputs a linear logistic regression model of the relationship between the surface parameters to a latent preference factor, which may then be used to establish the probability of observing a specific rank through logistic link functions.

7.1 Introduction

Affective engineering is the study of the interactions between the customer and the product at the emotional level. It is also known as 'Kansei engineering'—the development of products and services by translating the customer's psychological feelings and needs into the domain of product design [164]. In the research stage, different material surfaces are produced, then categorised by subjectively feeling and describing them semantically using various adjectives. Multivariate analysis methods are then applied to investigate the relationship between the adjectives and the surface physical properties. Generally, touch-feel is concerned with four psychophysical descriptor pairs: 'smooth/rough', 'slippery/sticky', 'warm/cold' and 'soft/hard' [159, 160, 165]. These four pairs are underpinned by different mechanisms. For example, soft/hard feel is dominated by material hardness followed by friction resistance [85], and warm/cold is attributed to the heat transfer property between textures and finger skin [165]. A fifth subjective 'like/dislike' descriptor pair was also investigated for completeness, but it is unlikely to have causal or mechanistic relationships.

Previous research in quantifying perception of touch-feeling had been conducted within our research group, on car interior components using the custom-built tribological probe microscope (TPM) [17–19]. The results show the strongest correlations between the perceived feeling and the measured surface roughness, followed by hardness, and the weakest—but still modest—with the friction coefficient. On the other hand, no concrete evidence supported touch-feel associations with friction for moist/dry or slippery/sticky descriptors.

Researchers often rely on surveys to determine the individual preferences, and sometimes the respondent is asked to rank a set of presented choices in order of preference or against a set of criteria. Rank-ordered logistic regression (ROL) is one of the standard tools specifically designed to model rank data [163]. ROL models were introduced by [166], and is also known as the Placket–Luce model [167] or the exploded logit model [168]. The method using maximum likelihood estimator can be applied to both complete and incomplete ranking data, and to data with tied ranks [161]. It has been applied in many aspects such as voter preferences, ageing studies marketing and transportations.

In this chapter, 54 subjects were asked to rank the thermoplastic elastomer (TPE) samples in terms of the aforementioned 5 pairs psychophysical adjectives/-descriptors. Then ROL modelling analysis was carried out using the Stata software. Compared with the other correlation methods, the results not only give the signific-

ance of the correlation between human touch-feel perception descriptors and surface physical parameters, but it also give the regression coefficients on the parameters as a linear latent factor model.

7.2 Touch-feel perception ranking measurement

In this thesis, part of the touch-feel perception ranking data came from [32] with permission of the author. The tactile evaluation process is divided into two parts according to their materials: metal samples and TPE samples. Before the evaluation session, its purpose and the procedure were explained to the participants. The TPE samples include five coated samples and five patterned samples characterised in Chapter 5.

The metal samples include six milled aluminium samples, six turned aluminium samples and five surface ground steel samples; all of which were characterised in Chapter 3. For the metal samples only, the subjective evaluation session was conducted by Yue [32] from whom the data were borrowed. Six people of different age and gender (students, technicians, and academic staff recruited from the University of Warwick) formed the participant group. Each participant was asked first to rank the material specimens in terms of 'smooth/rough', and then similarly for 'slippery/sticky'. The session lasted approximately 20 minutes for each participant. Since only two descriptor pairs were tested and the number of participants was low, only Spearman's rank correlation analysis was performed for these data.

For the TPE samples, the five coated and five patterned samples (excluding the sandpapered variants, see Table 5.1) were evaluated together by 54 subjects, recruited from the University of Warwick comprising of students and members of staff. The participants include 28 females (aged 26–50 years, mean = 34.6) and 26 males (aged 26–60 years, mean = 36.8). In the evaluation process, all the participants did not previously participate in any tactile evaluation or sensory experiments and were not aware of the purpose of the experiment. Each evaluation took about 20 minutes. The participants were asked to rank the feelings on the samples in terms of the five descriptor pairs: rough/smooth, soft/hard, sticky/slippery, cold/warm and like/dislike. These are the four fundamental touch-feel psychophysical descriptor pairs [159, 160, 165], but with an additional subjective general preference term 'like/dislike' added.

7.3 Literature review on correlation methods

With the data for touch-feel perception, surface physical characteristics and friction data available, the next step is to perform correlation analysis between them. There are many correlation methods from the simplest regression models to the complex statistical models. Here, the advantage and disadvantage of several typical correlation methods are illustrated as follows.

7.3.1 Linear regression and partial correlation

Partial correlation is the marginal contribution of a single predictor to reduce the unexplained variation in the outcome of linear regression [169]. Partial correlation indicates the explanatory value attributable to a single predictor after taking into account all of other predictors. In linear regression, it is explained in terms of the reduction of the sum of the squared errors attributable to an individual predictor. Due to the nature of the ranking data, the partial correlation method is only feasible if the averaged ranks are used, in which case it cannot provide information on the significance of correlations between the various physical characteristics. A partial correlation statistic for logistic regression has been proposed [170], based on Wald chi-square statistic for individual coefficients and the likelihood of an intercept-only model. While this statistic has the same range as partial correlation in linear regression and there are some similarities in interpretation. However, the Wald chi-square statistic may be a poor estimator in small-to-medium size samples [171]. In order to illustrate the weakness mentioned, the analysis results from previous work are shown in Fig. 7.1.

As shown in Fig. 7.1, the correlation between different average perceived ranking and relative surface physical parameters are expressed. The results can prove that perceived roughness was highly correlated with S_m, the perceived softness was correlated with H/E, and the human in vivo friction coefficients are highly correlated with the 'cool/warm' rankings and the 'slippery/sticky' rankings. However, there are several problems with this method. Firstly, much of the inter-subject information may be lost by using the averaged perceived ranking. Secondly, the model ignores any covariance between different physical parameters by looking at the correlation one variable at a time. For example, the perceived rough/smooth ranking may be a combination of many parameters such as the hardness and the friction of the surfaces. Lastly, the method can not solve the small-to-medium size data. Most importantly, this method cannot assess the correlation significance, unless the Spearman's rank correlation analysis is also performed.

156
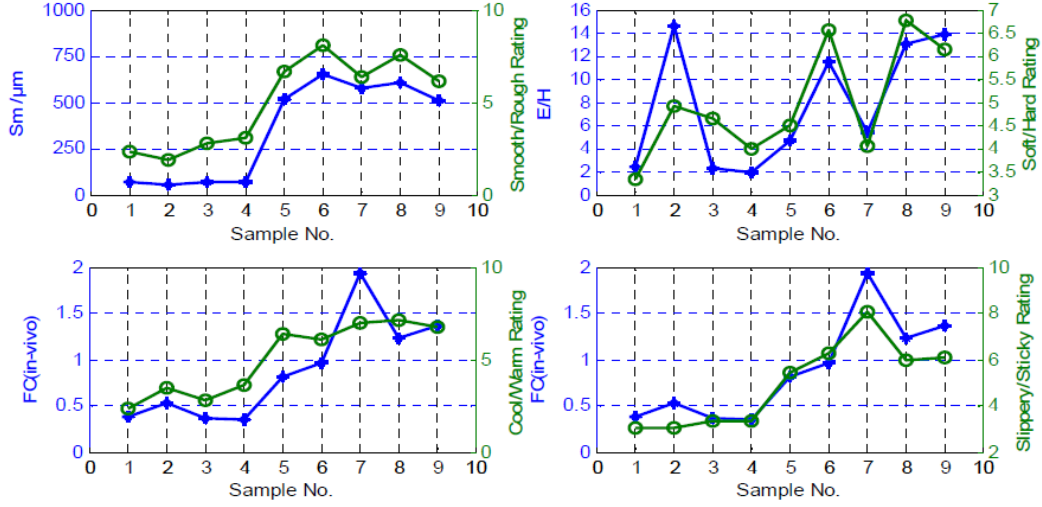
Figure 7.1: Comparison of the tactile sensorial rankings and sensitive physical parameters Yue [32]

7.3.2 Kendall's W test, Wilcoxon signed-rank test and Spearman's rank correlation analysis

Before establishing the relationship between touch-feel perception and surface physical parameters, an effective evaluation to differentiate the difference among the samples was carried out in [32]. The ranking data were analysed using non-parametric statistics. Kendall's W test [172] is conventionally employed to test the samples and study the concordance or effectiveness of the evaluation.

The Kendall's W value (also known as Kendall's coefficient of concordance) is defined as

$$W = \frac{12S}{k^2(n^3 - N)} \tag{7.1}$$

where S is defined as

$$S = \sum_{i=1}^{N}(R_i - \overline{R})^2 = \sum_{i=1}^{N} R_i{}^2 - \frac{(\sum_{i=1}^{N} R_i)^2}{N} \tag{7.2}$$

where R_i is the rank sum of the sample i evaluated by all the subjects and N is the total number of the samples. The Kendall's W value ranges from 0 to 1, where zero represents the evaluation is not effective, and one means there is a great concordance among the subjects. An asymptotic chi-square value can be calculated to assess the correlation significance based on Kendall's W. If the asymptotic Chi-square value calculated from Kendall's W is greater than the critical chi-square value at a targeted

confidence level [173], e.g. 0.05, such that

$$\chi_{\mathrm{r}}^2 = k(N-1)W > \chi_{0.05/2}{}^2 \times (N-1), \tag{7.3}$$

then significant differences exist among the samples in the candidate evaluation mode. It also means at least one sample is effectively perceived to be different. The advantage of this method is the ease of computation and is able to quantify the correlation significance with a p-value. However, the results only indicate the evidence that there is some correlation between the rankings, not the magnitude of the influence. Although p-value decreases as the magnitude of an influence increases, the magnitude is not quantifiable nor interpretable, especially with categorical ranking data.

In addition, Wilcoxon signed-rank test was applied to further explore the pairwise difference among the samples. In the Wilcoxon test, the pairwise difference in ranking is associated with a positive or negative sign. The output contains two parameters: one is the normalised z-value (standard score) calculated from the rank sum of the less frequent sign, the other is the p-value (2-tailed) for examining the confidence level at the significant difference among the samples. In our case, by comparing the samples in pairs, their tactile evaluation difference could be statistically confirmed. However, the results still can not give a clear, interpretable relationship between the perceived touch-feel perception and surface physical parameters.

For the tactile evaluation data, the evaluation process can be treated as a case of k people evaluating N samples in m terms of tactile senses (described by sensorial/affective adjectives). So the evaluation rankings are assembled to a $N \times m \times k$ data array. In previous work [32], each type of touch-feel perception ranking was reduced to averaged ranking data for each sample and perceptual items. Spearman's rank correlation analysis was then performed on the combined matrix. Correlation between each pair of the measured surface properties and the evaluated items was then calculated. The correlation between the physical parameters and the tactile perceptions was marked significant when the correlation coefficient $|r_{\mathrm{s}}| > 0.5$ and p-value < 0.05. Comparisons of the correlation coefficient r_{s} could assist in selecting the most effective physical factors. However, similar to the other methods, the magnitude of the correlation is not directly interpretable and cannot be used to write an analytical relationship that links the ranking to a specific variable.

7.3.3 Factor Analysis and PCA

Factor analysis is a statistical process in which the values of observed data are expressed as functions of a number of possible causes in order to find which are the

most important. It is to determine the variability among the observed, correlated variables in terms of a potentially lower number of unobserved variables called latent factors. Factor analysis originated in psychometrics and is used in behavioural science, social science, marketing product management, operations research. The aim of this method is to reduce the dimensionality of data while maximising the information preserved, collapsing from large numbers of observed variables to a smaller number of underlying latent variables.

The most common form of factor analysis, PCA (principal component analysis), seeks a linear combination of variables such that the maximum variance is extracted from the observed variables. PCA is available from the SPSS software [172]. It involves the calculation of the eigenvalue decomposition of a data covariance matrix, usually after mean centring the data for each factor. PCA results in a reduction of interdependent variables, typically to two or three independent variables called principal components, from which a majority of the data variance can be explained. PCA has been applied in the study of semantic components of affective words and seeking explanation of relations between affective and sensorial words [8]. Although the results have shown that the tactile perception is correlated with the surface physical characteristics, the relationship cannot be interpreted or quantified physically.
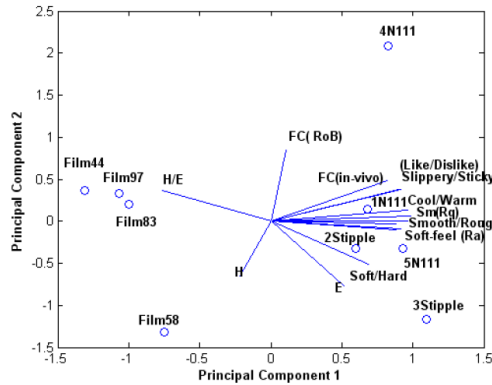
Figure 7.2: Biplot of the loadings of characteristic variables and the scores of the samples (Yue [32])

Two factors (PC1 and PC2) were extracted using SPSS software in Yue [32]. PC1 accounted for 63% of variance and PC2 for 19%, totalling 82%. PC1 is physically dominated by roughness and in-vivo friction, while PC2 largely depends on the compliance and dry sliding friction. The factor scores were shown in Fig. 7.2. In this case, 'smooth/rough', 'cool/warm' and 'soft-feel' are highly independent and they contributed to the major psychophysical loadings on PC1 at the psychophysical

level. It means these perception modes are physically determined by the surface topography and compliance index (H/E). For PC2, the result indicated the perceived softness is linked with dry sliding friction or surface strength. However, the problem with this method is that we can not define what the physical meaning of the two factors is, even though there exists a clear correlation between the surface physical parameters and human touch-feel perception.

7.3.4 Summary

Based on the discussions, each method has its pros and cons but the common problem amongst them is the lack of ability to interpret and formulate a model capable of prediction from the correlation observed. To this end, a method called rank ordered logit (ROL) modelling is introduced. Not only does the significance of the correlations is available, the model directly fits a linear regression model from the surface tribological/mechanical parameters to the touch-feel ranking data through continuous latent factors. The model can then generate probabilistic predictions of rank data by linking the latent factors with the probability distribution through logistic link functions.

7.4 Rank ordered logit modelling Analysis

A ROL model uses latent segments to endogenously identify the ranking capabilities of individuals. Each segment corresponds to a different assumption on the ranking capability. Using simulations and empirical applications [163], it resulted in a clear efficiency gain over a multinomial logit model in case some individuals are unable to rank. In addition, the rank ordered logit modelling does not suffer from biases due to ranking inabilities of some of the respondents. Generally we can suppose that the objective is to learn the (determinants of) preferences of individuals over a discrete set of items. Preferences can be recovered from historical data but if some items are not available yet, a survey is usually the option. Denote the number of ranking choices (items) by J. As described in [174], the individuals preferences are represented using the random utility framework. The random utilities for individual i are a set of latent variables $U_{i1},...,U_{iJ}$, defined as

$$U_{ij} = V_{ij} + \varepsilon_{ij} \tag{7.4}$$

where $i = 1, ..., N$ indexes individuals and $j = 1, ..., J$ indexes the items. The utility consists of two parts: V_{ij} is the deterministic component of the utility, which is determined by the characteristics of the observed individuals; and ε_{ij} is the random

component of the utility of the alternative choice j for individual i. Generally, the deterministic part of the utility is modelled as

$$V_{ij} = x_i' \beta_j \qquad (7.5)$$

where x_i is an m-dimensional vector with characteristics of individual i and β_j is an m-dimensional parameter vector specific to alternative j. Traditionally, respondents are asked to choose their most preferred option out of the complete set of J alternatives. Let $y_{ij} = 1$ denote the respondent i most prefers alternative j. The information $y_{ij} = 1$ implies that for this respondent the utility of alternative j is larger than all other alternatives, that is,

$$U_{ij} \geq max\{U_{i1}, ..., U_{iJ}\} \qquad (7.6)$$

The probability depends on the distribution of ε_{ij}. If we assume that ε_{ij} has an independent type-I extreme value distribution, which leads to the well-known expression for the probability that item j is the most preferred by individual i. The equation is the setup of a multinomial logit (MNL) model:

$$Pr[y_{ij} = 1; \beta] = Pr[U_{ij} \geq max\{U_{i1}, ..., U_{iJ}\}] = \frac{exp(V_{ij})}{\sum_{l=1}^{J} exp(V_{il})} \qquad (7.7)$$

where $\beta = \{\beta_1, ..., \beta_J\}$ and β_J is set to zero for identification.

Generally, the information of the most preferred item is enough to estimate the model parameters. However, more information of every respondent will be obtained if the ranking of alternatives is known. In this case, the response of respondent i by the vector is defined as $y_i = (y_{i1}, ..., y_{iJ})'$, which denotes the rank that individual i gives to item j. For example, $y_{ij} = 2$ means the respondent ranked the alternative j to be the second most preferred option. For notational convenience, the item number $r_{ij} = (r_{i1}, ..., r_{iJ})'$ was defined as the item number that received rank j by individual i. The relation between them can be described as follows:

$$y_{ik} = j \Leftrightarrow r_{ij} = k \qquad (7.8)$$

for $j, k = 1, ..., J$. By combining the above equations, a complete ordering ranking of the underlying utilities r_i can be described as

$$U_{ir_{i1}} > U_{ir_{i2}} > ... > U_{ir_{iJ}} \qquad (7.9)$$

Under the assumption of Eq. (7.4) and the assumption of the extreme value distribution, the rank-ordered logit (ROL) model can be obtained following Beggs, Cardell and Hausman [166] and Chapman and Staelin [175]. The probability of deserving a

particular ranking r_i equals

$$Pr[r_i; \beta] = Pr[U_{\text{ir}_{i1}} > U_{\text{ir}_{i2}} > ... > U_{\text{ir}_{iJ}}] = prod_{j=1}^{J-1} \frac{exp(V_{\text{ir}_{ij}})}{\sum_{l=1}^{J} exp(V_{\text{ir}_{il}})} \qquad (7.10)$$

The ROL model can be seen as a series of MNL models described above: an MNL for the most preferred item; another MNL for the second-ranked item to be preferred over all items except the one with rank 1 and so on. Finally, the probability of a full ranking is made up of the product of these separate MNL probabilities. The product contains only $J - 1$ probabilities, because ranking the least preferred item (the last item) is done with probability 1.

7.5 Analysis of the touch-feel perception data

The rank-ordered logit model was applied to analyse how decision makers combine attributes of alternatives into overall evaluations of the attractiveness of these alternatives. All of the data analysis are performed using the Stata software, which fits the rank-ordered logistic regression model with maximum likelihood methods [162].

Unlike the metal data which involved only 6 participants, there are data for 14 subjects with the TPE samples to fit a meaningful ROL model. The raw data are shown in Appendix A.6. In this case, the correlation analysis between every touch-feel perception descriptor and every single surface parameter were performed. Not only the p-values were computed, the linear correlation coefficients and their associated 95% confidence intervals are also available.

Firstly, the correlation analysis between each touch-feel perception descriptor and every surface physical parameter was carried out by the Stata software, the raw outputs are given in Appendix A.7. The program outputs the slope or the linear factor of proportionality between the input tribological/mechanical/friction parameters with the latent touch-feel factor. The associated p-values for the slopes are also available. To avoid co-linearity among the parameters, the surface parameters were divided as three groups according to difference properties: surface topography parameters, surface mechanical parameters and surface friction parameters. One parameter was selected from each group according to the smallest p-value. Then, the linear correlation equation is calculated between each touch-feel perception descriptor and the three parameters in order to give the most effective information for human touch-feel perception study. For all of the touch-feel perception, ranking data is from 0-9 while 0 is corresponds to the material rated as having its attribute most closely

associated with the first word of the descriptor pair, e.g. 'smooth'. Similarly, a rank of 9 means the second word is the best matching label.

7.5.1 Smooth/rough

Table 7.1: Surface topographical, mechanical, and friction parameters with statistically significant correlation with 'smooth/rough' ranking data

		Corr. coef.	Std.	p-value	95% C.I.	
Roughness	S_{a}	0.17	0.02	<0.001	0.13	0.21
	S_{p}	0.04	0.004	<0.001	0.03	0.05
	S_{q}	0.17	0.02	<0.001	0.13	0.22
	S_{sk}	−0.07	0.01	<0.001	−0.11	−0.04
	S_{v}	−0.09	0.01	<0.001	−0.11	−0.07
	S_{z}	0.03	0.003	<0.001	0.02	0.04
	S_{m}	0.005	0.000	<0.001	0.004	0.007
	S_{dq}	0.09	0.01	<0.001	0.07	0.12
	R_{da}	0.35	0.04	<0.001	0.27	0.43
Mech.	E	−1.03	0.13	<0.001	−1.29	−0.78
	H	−0.012	0.001	<0.001	−0.015	−0.009
Fric.	$\mu_{\mathrm{in\text{-}vivo}}$	1.6	0.2	<0.001	1.1	2.0
	$\mu_{\mathrm{artificial}}$ $0.5\,\mathrm{N};\,5\,\mathrm{mm\,s^{-1}})$	1.8	0.5	<0.001	0.8	2.8
	$\mu_{\mathrm{artificial}}$ $(0.75\,\mathrm{N};\,8\,\mathrm{mm\,s^{-1}})$	−11.2	1.1	<0.001	−13.6	−8.9

For Smooth/Rough ranking looking at Table 7.1, most of the surface physical parameters show high correlation with the ranking results ($p < 0.05$) except the artificial finger friction results ($0.5\,\mathrm{N}; 8\,\mathrm{mm\,s^{-1}}$), where $p > 0.28$. For S_{a}, S_{p}, S_{q} ,S_{z} ,S_{dq} ,R_{da} and S_{m}, human in vivo friction and the two artificial fingertip friction results, the ranking data is proportional to each surface physical parameter. In contrast, S_{sk}, S_{ku}, S_{v}, E, H and the artificial fingertip friction ($0.75\,\mathrm{N}; 8\,\mathrm{mm\,s^{-1}}$) showed inverse relationship with the smooth/rough latent factor.

The direction of proportionality for artificial finger for the $0.5\,\mathrm{N}$ case disagrees with the $0.75\,\mathrm{N}$ case. Indeed, it can be seen in the following section that the $0.5\,\mathrm{N}$ case agrees with the in-vivo results but the $0.75\,\mathrm{N}$ case shows usually the opposite. Because of this discrepancy, the human friction results are assumed to be representative of the friction measurement.

To show an example of the correlation between touch-feel perception of 'smooth/rough' ranking with the engineering parameters, S_{z} and S_{q} are plotted against the averaged ranking value for the different material samples in Fig. 7.3. The lines connecting across the sample are there to better highlight the correlations
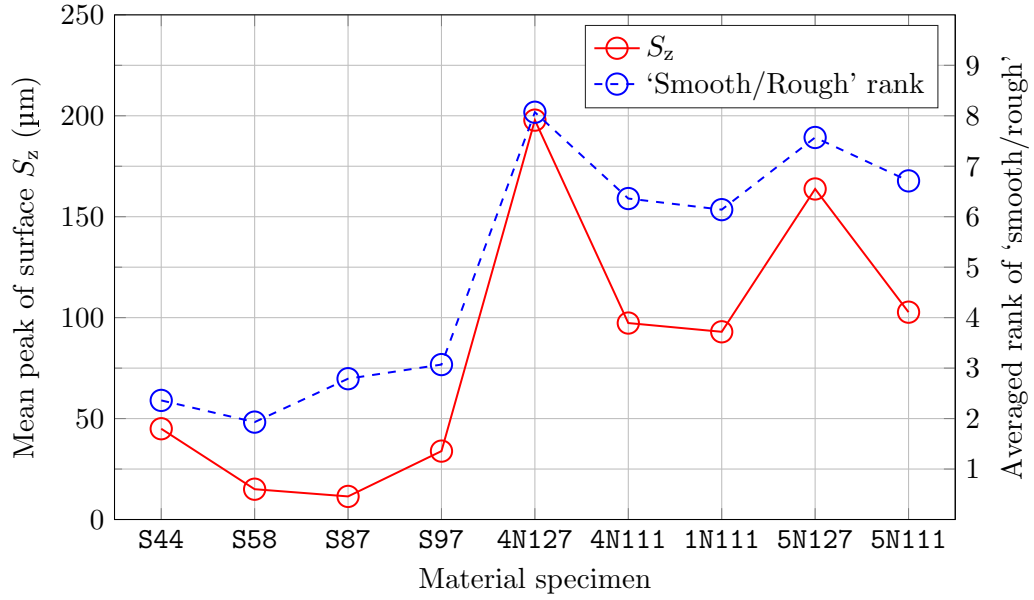
(a) S_z
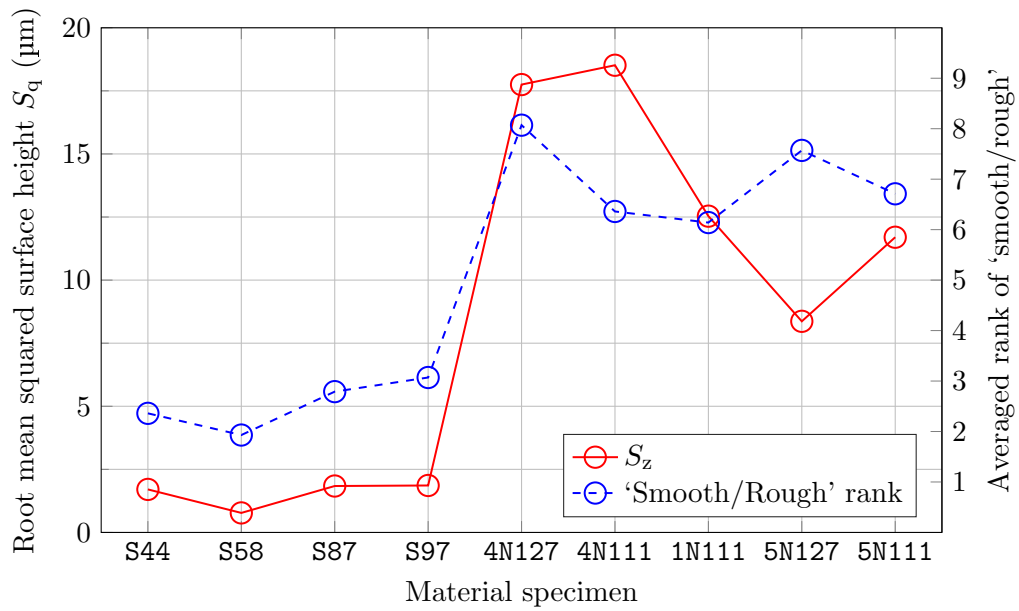
(b) S_q

Figure 7.3: Visualising the correlation between touch-feel perception of 'smooth/rough' ranking with surface roughness parameters S_z and S_q

between the average ranking and the parameters, rather than indicating any relations between the samples. The lines show an inverse trend with the ranking values (higher ranking values = perceived to be rougher), i.e. samples with higher roughness parameters were perceived to be rougher subjectively, which is to be expected. On can also see the trends for S_z and S_q are both similar, meaning these parameters encode similar information and has similar influence on touch-feel, and this co-linearity has to be eliminated when fitting a multinomial ROL model, as done below.

Table 7.2: The combined parameters correlation with 'smooth/rough' Ranking

Parameters	Corr. coef.	Std.	p-value	95% C.I.	
S_p	0.028	0.007	0.000	0.014	0.042
E	-0.059	0.209	0.775	-0.471	0.351
$\mu_{\text{in-vivo}}$	1.179	0.362	0.001	0.469	1.889

The further step is to combine the influences of all the physical parameters through multinomial regression, rather than looking at them independently. S_p, E and human finger friction ($\mu_{\text{in-vivo}}$) were chosen arbitrarily, each from the parameter group of surface topography property, surface mechanical property and surface friction characteristic respectively. The result is shown in table 7.2. It can be seen that E cease to be statistically significant as opposed to the case when the parameters are modelled one by one. The latent factor of 'smooth/rough' can then be modelled as $0.0284736 \times S_p + 1.179652 \times \mu_{\text{in-vivo}}$.

7.5.2 Soft/hard

For soft/hard descriptor pair, the analysis results are quite different from Smooth/Rough ranking. E and H displayed high correlation with the soft/hard ranking data as expected with $p \leq 0.001$ and $p \leq 0.021$, respectively. E and H are positively proportional to the latent factor—this means that when the test samples have lower E and H values, people associate the samples to be softer and the resulting ranking is numerically lower. For the influence of surface roughness parameters, there are high correlation between S_p, S_z, S_{dq}, R_{da} and the soft/hard ranking results. These parameters are inversely proportional to the soft/hard latent factor. For friction characteristics, human fingertip friction showed the highest correlation with $p < 0.001$, which has an inverse correlation with the ranking results. According to the contact area calculation of Eq. (4.8), the contact area decreases when the hardness of the surface increases. The friction coefficient decreases with a decrease of the contact

Table 7.3: Surface topographical, mechanical, and friction parameters with statistically significant correlation with 'soft/hard' ranking data

		Corr. coef.	Std.	p-value	95% C.I.	
Roughness	S_p	−0.017	0.003	<0.001	−0.025	−0.010
	S_q	−0.015	0.008	0.044	−0.030	−0.0004
	S_z	−0.007	0.002	0.001	−0.012	−0.003
	S_dq	−0.027	0.009	0.002	−0.044	−0.010
	R_da	−0.073	0.024	0.003	−0.122	−0.024
Mech.	E	0.39	0.11	0.001	0.16	0.62
	H	0.003	0.001	0.021	0.002	0.006
Fric.	$\mu_\mathrm{in\text{-}vivo}$	−0.9	0.2	<0.001	−1.3	−0.4
	$\mu_\mathrm{artificial}$ $(0.5\,\mathrm{N};\ 5\,\mathrm{mm\,s^{-1}})$	−1.229	0.583	0.035	−2.372	−0.087
	$\mu_\mathrm{artificial}$ $(0.75\,\mathrm{N};\ 8\,\mathrm{mm\,s^{-1}})$	2.4	0.903	0.006	0.6	4.2

area, and hence the in vivo friction is inversely related to the soft/hard factor. The correlation results support the theory.

7.5.3   Cool/warm

Cool/warm not only depends on the heat conductivity and diffusivity of the test samples, but also depends on the ambient temperatures.

From Table 7.4, S_dq, R_da, E, H, and human friction showed the highest correlation with $p < 0.001$. S_dq and R_da describe the average slope of the asperities of the surfaces and they are proportional to the cool/warm ranking results. The reason for this maybe when the average slope of the surface is higher, more friction/adhesion induced heating when people stroke the samples. This also explains why the human friction is also proportional to the ranking data. For surface hardness, lower values of E, H lead to higher friction and more energy is loss during stroking, hence they are inversely proportional to the ranking.

For other surface parameters, S_a, S_p, S_q, S_sk, S_v, S_z and the artificial fingertip friction also correlated with the cool/warm ranking with p-value < 0.05. S_sk, S_v and the artificial fingertip friction is inversely proportional to the ranking data while others are proportional to the ranking.

To show an example of the correlation between touch-feel perception of 'cool/warm' ranking with the engineering parameters, R_da is plotted against the averaged ranking value for the different material samples in Fig. 7.4. The result

Table 7.4: Surface topographical, mechanical, and friction parameters with statistically significant correlation with ·cool/warm' ranking

		Corr. coef.	Std.	p-value	95% C.I.	
Rough	S_{a}	0.019	0.008	0.018	0.0033	0.0035
	S_{p}	0.011	0.003	0.002	0.0040	0.018
	S_{q}	0.019	0.008	0.0013	0.0039	0.033
	S_{sk}	-0.046	0.018	0.010	-0.081	-0.011
	S_{v}	-0.012	0.04	0.007	-0.020	-0.003
	S_{z}	0.006	0.002	0.002	0.002	0.011
	S_{m}	0.001	0.000	<0.001	0.0005	0.0015
	S_{dq}	0.039	0.008	<0.001	0.021	0.056
	R_{da}	0.14	0.02	<0.001	0.09	0.19
Mech.	E	-0.6	0.1	<0.001	-0.8	-0.4
	H	-0.008	0.001	<0.001	-0.011	-0.005
Fric.	$\mu_{\mathrm{in\text{-}vivo}}$	1.1	0.2	<0.001	0.7	1.6
	$\mu_{\mathrm{artificial}}$ ($0.5\,\mathrm{N}$; $5\,\mathrm{mm\,s^{-1}}$)	1.122	0.545	0.039	0.053	2.192
	$\mu_{\mathrm{artificial}}$ ($0.75\,\mathrm{N}$; $5\,\mathrm{mm\,s^{-1}}$)	1.249	0.565	0.027	0.142	2.356
	$\mu_{\mathrm{artificial}}$ ($0.75\,\mathrm{N}$; $8\,\mathrm{mm\,s^{-1}}$)	-2.8	0.864	0.001	-4.5	-1.1
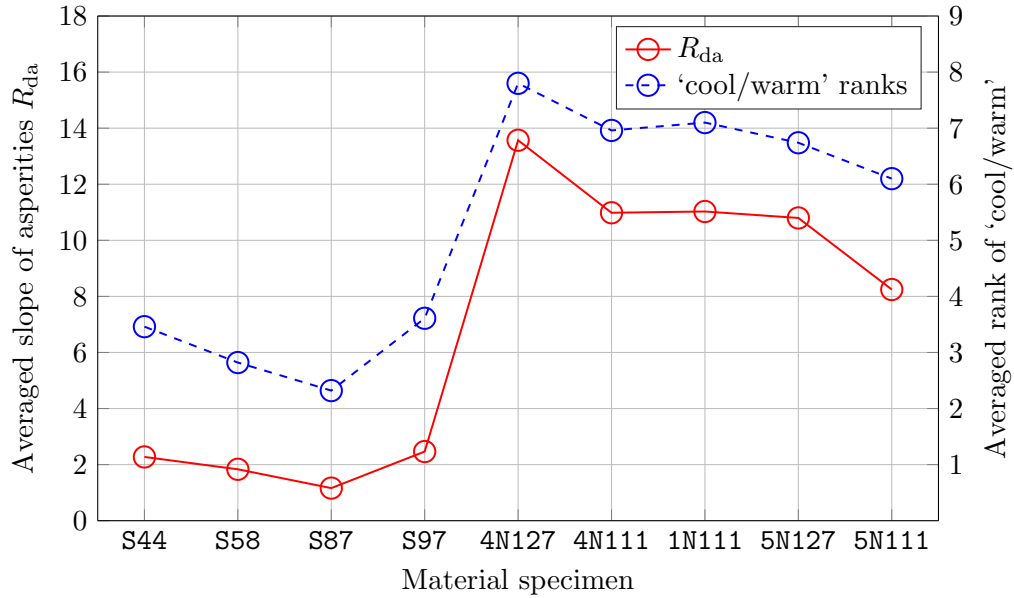
Figure 7.4: Visualising the correlation between touch-feel perception of 'cool/warm' ranking with surface parameter R_{da}

shows an positive trend with the ranking values, i.e. samples with higher R_{da} were perceived to be warmer.

The multivariate correlation is shown in Table 7.5. Sm, E and human finger friction were selected to represent their respective group. The results show that E and human finger friction have higher influence than S_{m} according to the p-values. The latent factor for 'cool/warm' can be modelled as $-0.3816585 \times E + 0.7120606 \times \mu_{\text{in-vivo}}$.

Table 7.5: The combined parameters correlation with 'cool/warm' Ranking

Parameters	Corr. coef.	Std.	p-value	95% C.I.	
S_{m}	0.0002	0.000	0.444	-0.0001	0.000 94
E	-0.381	0.165	0.021	-0.706	-0.056
$\mu_{\text{in-vivo}}$	0.712	0.324	0.028	0.075	1.348

7.5.4 Slippery/sticky

Table 7.6: Surface topographical, mechanical, and friction parameters with statistically significant correlation with ·slippery/sticky' Ranking

		Corr. coef.	Std.	p-value	95% C.I.	
Rough	S_{a}	0.019	0.008	0.025	0.002	0.035
	S_{p}	0.015	0.003	<0.001	0.007	0.022
	S_{q}	0.018	0.007	0.019	0.003	0.034
	S_{v}	-0.010	0.004	0.017	-0.019	-0.002
	S_{z}	0.007	0.002	0.001	0.003	0.012
	S_{dq}	0.027	0.009	0.002	0.010	0.044
	S_{m}	0.0009	0.000	<0.001	0.0004	0.001
	R_{da}	0.09	0.02	<0.001	0.04	0.15
Mech.	E	-0.45	0.127	<0.001	-0.70	-0.20
	H	-0.006	0.001	<0.001	-0.009	-0.003
Fric.	$\mu_{\text{in-vivo}}$	1.2	0.2505	<0.001	0.7	1.7
	$\mu_{\text{artificial}}$ 0.5 N; 5 mm s^{-1})s	1.364	0.528	0.010	0.327	2.400
	$\mu_{\text{artificial}}$ (0.75 N; 8 mm s^{-1})	-2.479	0.910	0.006	-4.264	-0.694

From Table 7.6, surface topography parameters S_{p}, R_{da}, S_{m}, surface mechanical property parameters E, H, and human friction coefficients showed the highest correlation with $p < 0.001$. S_{p},R_{da},S_{m} and human friction are proportional to the slippery/sticky ranking. When the perceived friction is higher, many people may associate it as sticky. In contrast, E and H are inversely proportional to the
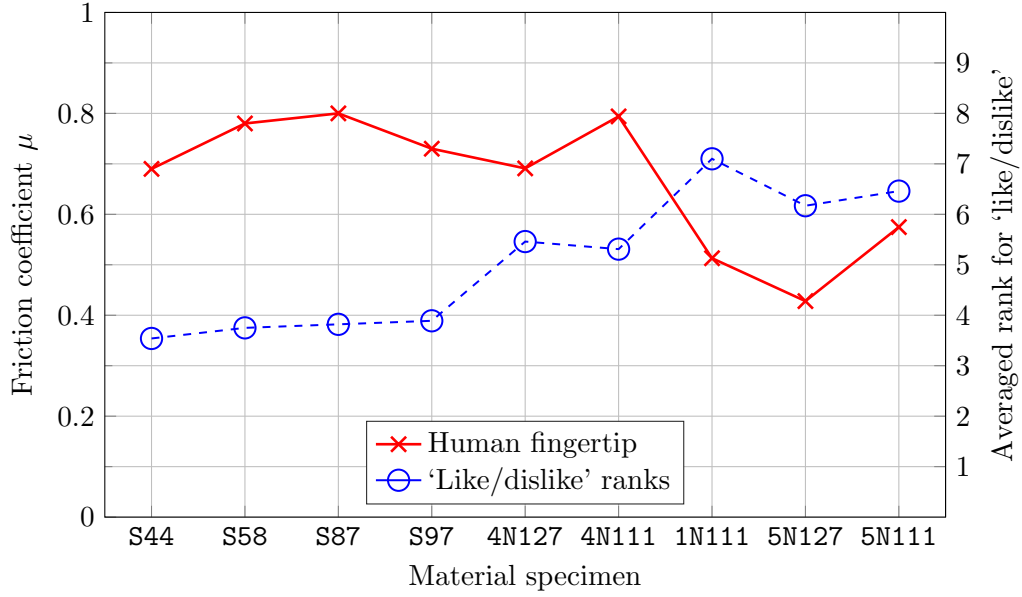
Figure 7.5: Visualising the correlation between touch-feel perception of 'like/dislike' ranking with in vivo friction coefficient $\mu_{\text{in-vivo}}$

slippery/sticky ranking according to the results. This may have been mediated by the influence of E and H on the perceived friction.

In addition, S_{a}, S_{q}, S_{v}, S_{z}, S_{dq} and the artificial fingertip friction coefficients also showed statistically significant correlation with the ranking data. They are all proportional to the ranking except S_{v} and the artificial fingertip friction with normal force of $0.75\,\text{N}$ and sliding speed$=8\,\text{mm}\,\text{s}^{-1}$.

With respect to multivariate model, as shown in the table 7.7, the importance of human finger friction is stronger than S_{m} and E. The result suggests that 'slippery-sticky' can be described mainly as a function of human fingertip.

Table 7.7: The combined parameters correlation with 'slippery/sticky' Ranking

Parameters	Corr. coef.	Std.	p-value	95% C.I.	
S_{m}	0.0003	0.000	0.382	-0.0003	0.0009
E	-0.149	0.170	0.381	-0.483	0.184
$\mu_{\text{in-vivo}}$	0.859	0.348	0.014	0.176	1.542

7.5.5   Like/dislike

To show an example of the correlation between touch-feel perception of 'cool/warm' ranking with the engineering parameters, R_{da} is plotted against the averaged ranking

value for the different material samples in Fig. 7.4. The result shows an positive trend with the ranking values, i.e. samples with higher R_{da} were perceived to be warmer.

Like/dislike perception is perhaps the most subjective descriptor pair. Observing the results in Appendix A.7, the human in vivo friction coefficient is the only parameter correlated with the like/dislike ranking results. The in vivo friction is also plotted against the averaged ranking in Fig. 7.5 for different samples. The human friction coefficients are inversely proportional to the rank values, which means that the subjects preferred samples with higher friction. The lack of correlations may be due to the fact that the descriptor requires very subjective judgements that are not influenced by the parameters investigated.

Table 7.8: The highest correlated parameters with 'like/dislike' Ranking

Parameters	Corr. coef.	Std.	p-value	95% C.I.	
$\mu_{\text{in-vivo}}$	-0.773	0.241	0.001	-1.246	-0.301

7.6 Conclusions

In previous chapters, the database of surface physical properties including surface topography parameters, surface mechanical properties and surface friction coefficients have been established for a variety of metal and thermoplastic elastomer samples. The relationship between surface friction coefficients and other physical parameters has been investigated in Chapter 6. One of the objectives of the thesis is to identify how the human touch-feel perception relates to the surface tribological/mechanical parameters. To this end, this chapter compared several correlation methods suitable for ranking data incorporated results from previous work [32].

Although several correlation methods can be applied, many of them are limited by statistical power and inability to interpret the results and generate a model that is capable of prediction. To remedy this, rank ordered logit modelling method was introduced to model the human touch-feel perception and the surface physical parameters of metal and thermoplastic materials.

A majority of the surface physical parameters showed correlation with the 'smooth/rough' ranking. For S_a, S_p, S_q, S_z, S_{dq}, r_{da}, S_m, human friction and artificial fingertip friction ($0.5\,\text{N};5\,\text{mm}\,\text{s}^{-1}$ and $0.75\,\text{N};5\,\text{mm}\,\text{s}^{-1}$), the ranking data is proportional to each surface physical parameter while S_{sk}, S_{ku}, S_v, E, H and the artificial fingertip friction ($0.75\,\text{N};8\,\text{mm}\,\text{s}^{-1}$) form inversely proportional relationship

with the ranking. The latent factor can be modelled as $0.0284736 \times S_{\mathrm{p}} + 1.179652 \times \mu_{\text{in-vivo}}$.

For 'soft/hard' ranking, E and H showed high correlation with the ranking data and they are proportional to the ranking results. It supports the fact that the rank ordered logit modelling is applicable and that the correlation analysis is correct. Most of the surface topography parameters are inversely proportional to the ranking. The human friction and the artificial finger friction showed inversely linear correlation with the ranking analysis.

For 'cool/warm' ranking, the surface topography parameters and human friction coefficients display a positive correlation with the ranking, while other parameters are inversely proportional to the ranking data. However, the results still need to be investigated because the 'cool/warm' ranking should, in theory, be related to the thermal conductance.

The 'slippery/sticky' rankings show similar results, with a higher friction positively associated with the rank data. However, for 'Like/dislike' ranking, only the human friction correlated with the ranking data. It is possible that the descriptor is too subjective to be influenced by the parameters.

Conclusion

This chapter summarises the key research contributions and crucial findings of this thesis.

8.1 Conclusion

This thesis concerns the following scientific fields: surface topography metrology, micro- and nano-indentation, skin tribology, tribological instrument design using computer-aided design; contact mechanism theory, finite element modelling, affective engineering and modelling of touch-feel perception tactile.

8.1.1 The friction test apparatus with an artificial fingertip for touch-feel studies

Touch-feel perception plays an important role in product design from automotive interiors, consumer electronics to product packaging. Tribological studies have been conducted in literature to try to link the touch-feel perception to surface tribological parameters. Chapters 1 and 2 reviews the topics of tribology and touch-feel perception in existing literature. Touch-feel perception is subjective and depends on many test condition and factors, therefore an instrument that is able to predict or quantify touch-feel perception in a more automated, repeatable, faster manner can potentially enable faster turn-around and cost savings in product design and affective engineering. Because experiencing friction is the most direct mechanism for touch-feel perception, the design of a new friction measurement apparatus is the first step in developing an artificial touch-feel perceiving device.

Another way assist product development for affective engineering is to study the correlation between the surface tribological/mechanical properties of a material and the touch-feel perception. Any relationship that links a specific engineering parameter or intrinsic property of the material to touch-feel perception helps material scientists and designers to optimise a product for higher perceived touch-feel and enhance the desirability and perceived quality of the end product.

To this end, the friction apparatus introduced in Chapter 3 is one of the focus of the work presented. Human fingertip conditions such as age and wetness influence the friction coefficient measurements. Different normal forces and sliding speeds also influence the results. These lead to large variations between subjects. To make the experiments more repeatable, controllable and robust against environmental factors, an artificial fingertip was developed to replace in-vivo friction measurements with human fingers. In order to minimise the differences between the results obtained in-vivo and that using an artificial finger, the artificial finger is anthropomorphic—it has a bio-inspired multilayered structure consisting of the cover, filler and bone layers using materials that have similar mechanical properties to the epidermis, sub-skin and bone of a human finger. The dimension of the fingertip is also similar to that of a human index fingertip. The surface of the artificial fingertip was also imprinted with a real human fingerprint, which was found to be beneficial (Section 3.2.2).

In the human friction measurement, the stiffness of the fingertip plays a key according to the Hertz contact theory. Hence, the bulk Young's modulus of the artificial fingertip was simulated in finite element modelling and experimentally measured using micro- and nano-indentation (Section 4.3). The results confirmed that the artificial fingertip has properties similar to that of a human fingertip.

In addition, the artificial fingertip was designed to work in conjunction with the friction test rig. The rig contains a sample holder platform with adjustable height, dampers for stabilisation, spring for load force adjustment and most importantly, a linear stage. the objective of the linear stage is to mimic the reciprocating movement of a human fingertip when a person strokes the material surfaces. The mechanical drawings of the apparatus are available and shown in Section 3.2.

Twelve aluminium and five steel samples were used to test the accuracy of the friction measurement apparatus. By comparing with the in-vivo human fingertip friction results and previous work [4, 32], it was shown that the new design is excellent for emulating human finger at friction sensing and has outperformed older hardware designs.

8.1.2 The theoretical modelling for the contact between the artificial fingertip and the surfaces

The friction measurement results showed the artificial fingertip can represent the human fingertip for friction properties determination. In order to better understand the contact mechanism, the contact area was investigated to help validate and choose a suitable theoretical contact model. A custom-built instrument was developed that allows a variable loading force to be applied when a glass plate is pressed against the artificial finger (Section 4.4). The transparent nature of the glass allows an optical microscope to study the contact area. Because all the test materials were much stiffer than the artificial fingertip, a glass plate was suitably representative as the contact bodies. Based on the summarised theories and contact area measurement results, the contact mechanism follows the Hertz contact theory.

8.1.3 The thermoplastic materials properties identification

Thermoplastic elastomers (TPE) are commonly used in automotive car interiors to give the car interior surfaces a less harsh and more pleasing feel [2]. One of the objectives of this thesis is to generate a guideline for car interiors designers and material scientists to enhance the touch-feel aspect. To do so the properties of thermoplastic samples should be investigated. Naturally, the surface topography, material mechanical properties and their friction properties will affect the touch-feel perception. To investigate this, four coated and five patterned TPE samples were chosen to be characterised using different measurement instruments. Compared to the metal samples, it is more difficult to measure the mechanical and friction properties of the TPE samples. This is because their coatings and patterns influence the measurement results even though the substrate material may be the same. The coated samples were mould in resin first to observe their coating thickness. By calculating the deformation depth occurs during friction, its mechanical properties such as the Young's modulus and hardness were established based on the coating rather than the substrate. The mechanical properties were measured using the NHT nano-indenter. For friction measurement, different normal forces and different stroking speeds were applied to the samples. Compared to the metal samples, the different patterns, coatings and the softness of the TPE samples mean that the results were harder to interpret.

The relationship between surface friction coefficients and the contact forces and the relationship between surface friction coefficients and the linear stage sliding speeds were analysed. It is concluded that as the contact forces increase, the friction

coefficients decrease; and with higher sliding speeds (which simulates the human finger speed of stroking), the friction coefficients were higher.

8.1.4 Correlation analysis for touch-feel perception

With the availability of the surface friction measurement results and their surface tribological/mechanical parameters, the next step is to correlate them with the touch feel perception and this is discussed in Chapter 6. Firstly, because the friction is the most direct feedback when a person feels a material surface, it is essential to correlate the friction coefficients with other physical parameters. Spearman's rank correlation analysis was first applied to investigate their correlation. The results showed for metal samples, all the surface topography parameters play a role in the friction coefficient determination except the surface mean slope parameters S_{dq} and R_{da}. For the TPE samples, all the parameters appear to have statistically significant influences on the surface friction.

In addition, theoretical analysis predicted a power-law relationship between friction coefficient and the product $R_q \cdot S_m$. The log-log plot results of metal and thermoplastic samples confirmed the prediction that the friction coefficient is approximately proportional to $(R_q \cdot S_m)^{2/3}$. The relationship between friction coefficients and surface Young's modulus was easily obtained from the Hertz contact theory and the Greenwood-Williamson (GW) extension (Section 4.2.4). By simulating the GW model, the real contact area results showed with the increase of Young's modulus, the real contact area will decrease. However, for the surface mean slope S_{dq} and R_a, there is not a strict relationship between friction and them.

Lastly, the touch-feel perception was assessed by asking participants to rank the material samples in a range of psychophysical measures. In Chapter 7, correlations between samples physical property parameters and touch feel perception ranking data were investigated. For metal samples, surface topography parameters such as S_a, S_p, S_q and S_m appear to be highly correlated with human touch-feel perception (> 0.8). In addition, the friction measurement also shows a high Spearman's correlation coefficient (0.95).

For thermoplastic samples, the results are more complicated. However, the Spearman's correlation analysis gave a guideline for touch feel perception studies.

8.2 Research limitations

Limited by time and funding, this research has several limitations detailed as follows, suggestions on improvement and further work are also given.

8.2.1 Limitations of instrumentation

As described in Chapter 3, a new friction measurement apparatus based on an artificial fingertip has been introduced. The artificial fingertip can represent the human fingertip in friction properties to some degree. However, the thermal properties of human fingertip were not considered in this thesis. In addition, while dimensions were similar, the shape of the artificial fingertip was not the same as a human fingertip. Meanwhile, the friction measurement apparatus was sensitive to the working environment. The signal-to-noise ratio limits the accuracy. These limits its application as a benchmark test for dry sliding friction. A more accurate design to compensate the effects and to increase the bandwidth of friction sensor is desirable.

Another limitation for this work is the thermal properties measurements of the samples. Although the thermal measurement was developed in previous work, the more accurate physical parameters such as thermal conductivity and thermal diffusivity need to be measured more accurately. Better test samples can be specifically designed to better validate the relationship equation introduced in Chapter 6. The samples could be tuned with specific surface topography parameters, e.g. R_q, S_m. In addition, test samples with less stiffness should be designed to validate the relationship equation between friction coefficients and the Young's modulus. In the current results, as the artificial fingertip was too soft, and full contact almost always occurs during the contact.

8.2.2 Case study limitations

Fifty-four subjects have been asked to rank the thermal-plastic samples by using 5 different descriptors. The ranking statistical analysis has given a guideline for industries on how to design a material for better touch-feel. The intent of case study research is one of analytic rather than statistical generalisation [176]. Therefore, a larger sample of participants should be recruited to enhance the statistical power of the relationships and to confirm the findings. Although this research contains both analytic and statistical generalisation, the quality of the case study research is best justified on its analytical results. Further work such as investigating age and gender influences is also potentially very interesting for the industry.

Furthermore, research into improving the semantic descriptors to best quantify human touch-feel perception may be beneficial. In this thesis, just 5 descriptors were selected according to previous literature. When people choose one product, they may have preconceptions or personal preferences that are not readily captured by

the descriptors investigated. In recent literature, Rasch models have been applied to develop a scale to measure tactile interaction linked with physical properties [177].

References

[1] Skedung, L., Arvidsson, M., Chung, J. Y., Stafford, C. M., Berglund, B. and Rutland, M. W. 'Feeling small: exploring the tactile perception limits'. In: *Nature* 2617 (2013).

[2] Liu, X., Chan, M. K., Hennessey, B., Rübenach, T. and Alay, G. 'Quantifying touch-feel perception on automotive interiors by a multi-fuction tribological probe microscope'. In: *Journal of physics: conference series*. Vol. 13. 2005, pp. 357–361.

[3] Adams, M. J., Johnson, S. A., Lefèvre, P., Lévesque, V., Hayward, V., André, T. and Thonnard, J.-L. 'Finger pad friction and its role in grip and touch'. In: *Journal of The Royal Society Interface* 10.80 (2012).

[4] Liu, X., Yue, Z., Cai, Z., Chetwynd, D. G. and Smith, S. T. 'Quantifying touch-feel perception:tribological aspects'. In: *Measurement Science and Technology* 19 (2008), pp. 1–9.

[5] Shao, F., Childs, T. H. C. and Henson, B. 'Developing an artificial fingertip with human friction properties'. In: *Tribology International* 42.11-12 (2009), pp. 1575–1581.

[6] Shao, F., Chen, X. J. and Barnes C. J.and Henson, B. 'A novel tactile sensation measurement system for qualifying touch perception'. In: *Proc. Inst. Mech. Eng. H J. Eng. Med.* 224.1 (2010), pp. 97–105.

[7] Chen, X., Shao, F., Barnes, C. J., Childs, T. H. C. and Henson, B. 'Exploring relationships between touch perception and surface physical properties'. In: *International Journal of Design* 3.2 (2009), pp. 67–76.

[8] Chen, X., Barnes, C. J., Childs, T. H. C. and Shao, F. 'Materials' tactile testing and characterization for consumer products' affective packaging design'. In: *Materials and Design* 30 (2009), pp. 4299–4310.

[9]   Masen, M. A. 'A systems based experimental approach to tactile friction'. In: *Journal of the Mechanical Behavior of Biomedical Materials* 4.8 (2011), pp. 1620–1626.

[10]   van Kuilenburg, J., Masen, M. A., Groenendijk, M. N. W., Bana, V. and van der Heide, E. 'An experimental study on the relation between surface texture and tactile friction'. In: *Tribology International* 48 (2012), pp. 15–21.

[11]   Skedung, L., Danerlöv, K., Olofsson, U., Johannesson, C. M., Aikala, M., Kettle, J., Arvidsson, M., Berglund, B. and Rutland, M. W. 'Tactile perception: finger friction, surface roughness and perceived coarseness'. In: *Tribology International* 44 (2011), pp. 505–512.

[12]   Derler, S., Schrade, G. and Gerhardt, L. 'Tribology of human skin and mechanical skin equivalents in contact with textiles'. In: *Wear* 263.7–12 (2007), pp. 1112–1116.

[13]   Childs, T. H. C. and Benson, B. 'Human tactile perception of screen-painted surfaces: self-report and contact mechanics experiments'. In: *Proc. Inst. Mech. Eng. J J. Eng. Tribol.* 221 (2007), pp. 427–441.

[14]   Barnes, C. J., Childs, T. H. C., Henson, B. and Southee, C. H. 'Surface finish and touch—a case study in a new human factors tribology'. In: *Wear* 257 (2004), pp. 740–750.

[15]   Terlizzi, J. J. and Minoo, J. 'Multi-touch display screen with localized tactile feedback'. 20090167704. 2009.

[16]   Meyer, D. J., Wiertlewski, M., Peshkin, M. A. and Colgate, J. E. 'Dynamics of ultrasonic and electrostatic friction modulation for rendering texture on haptic surfaces'. In: *2014 IEEE haptics symp.* 2014, pp. 63–67.

[17]   Liu, X., Bell, T., Chetwynd, D. G. and Y., L. X. 'Characterisation of engineered surface by a novel four-in-one tribological probe microscope'. In: *Wear* 255 (2003), pp. 385–394.

[18]   Liu, X. and Gao, F. 'A novel multi-function tribological probe microscope for mapping surface properties'. In: *Measurement Science and Technology* 15 (2004), pp. 91–102.

[19]   Liu, X. and Piotter, V. 'Mapping micro-mechanical properties of carbon filled polymer composites by tpm'. In: *Precision Engineering* 31 (2007), pp. 162–168.

[20]   Bhise, V. D. *Ergonomics in the automotive design process.* CRC Press, 2011.

References

[21] Nagano, H., Okamoto, S. and Yamada, Y. 'Semantically layered structure of tactile textures'. In: *Haptics: neuroscience, devices, modeling, and applications*. Vol. 8618. LNCS. 2014, pp. 3–9.

[22] Challener, C. *Formulating soft-touch coatings: a balancing act*. CoatingsTech. 2016. URL: http://www.paint.org/article/formulating-soft-touch-coatings-balancing-act/ (visited on 26/01/2017).

[23] Hollins, M., Bensmaia, S., Karlof, K. and Young, F. 'Individual differences in perceptual space for tactile textures: evidence from multidimensional scaling.' In: *Perception & Psychophysics* 62.8 (2000), pp. 1534–1544.

[24] Cohen, D. K., Smith, S., Novak, E. L. and Masters, A. T. *Quantitatively measuring surface texture and shaft lead of dynamic sealing systems*. AN549. Bruker Corporation. 2011.

[25] International Standards Organization. *Geometrical product specifications (GPS) — Surface texture: Areal — Part 2: Terms, definitions and surface texture parameters*. Geneva, Switzerland, 2012.

[26] Sharpe, J., Ahlgren, U., Perry, P., Hill, B., Ross, A., Hecksher-Sørensen, J., Baldock, R. and Davidson, D. 'Optical projection tomography as a tool for 3D microscopy and gene expression studies'. In: *Science* 296.5567 (2002), pp. 541–545.

[27] Nonenmacher, M. and Wickramasinghe, H. K. 'Scanning probe microscopy of thermal conductivity and subsurface properties'. In: *Applied Physics Letters* 61.2 (1992), pp. 168–170.

[28] Greenwood, J. A. and Tripp, J. H. 'The elastic contact of rough spheres'. In: *Journal of Applied Mechanics* 34.1 (1967), p. 153.

[29] Peressadko, A. G., Hosoda, N. and Persson, B. N. J. 'Influence of surface roughness on adhesion between elastic bodies'. In: *Physical Review Letters* 95.12 (2005), p. 124303.

[30] van Kuilenburg, J., Masen, M. A., Bana, V., Groenendijk, M. and van der Heide, E. 'Towards the development of product surfaces with enhanced tactile properties'. In: *Proceedings of the 14th nordic symposium on tribology*. Ed. by Marklund, P., Almqvist, A. and Kassfeldt, E. Storforsen, Sweden: Luleå Tekniska Universitet, 2010.

[31] Johansson, R. S. and Flanagan, J. R. 'Coding and use of tactile signals from the fingertips in object manipulation tasks'. In: *Nature Reviews Neuroscience* 10 (2009), pp. 345–359. DOI: 10.1038/nrn2621.

[32] Yue, Z. 'Systematic study of touch-feel perception: surface affective engineering aspects'. Doctoral dissertation. Coventry: School of Engineering, Univ. of Warwick, 2010.

[33] Stone, H. and Sidel, J. L. *Sensory evaluation practices*. 3rd ed. Cambridge, US-MA: Academic Press, 2004.

[34] Kandel, E. R., Schwartz, J. H. and Jessell, T. M. *Principles of neural science*. McGraw-Hill Medical, 2000.

[35] Kringelback, M. L. 'The human orbitofrontal cortex: linking reward to hedonic experience'. In: *Nature Reviews. Neuroscience* 6 (2005), pp. 691–702.

[36] Hutchings, I. M. *Tribology:friction and wear of engineering materials*. CRC Press, 1992.

[37] Derler, S., Gerhardt, L., Lenz, A., Bertaux, E. and Hadad, M. 'Friction of human skin against smooth and rough glass as a function of the contact pressure'. In: *Tribology International* 42 (2009), pp. 1565–1574.

[38] Tomlinson, S. E., Lewis, R. and Carre, M. J. 'The effect of normal force and roughness on friction in human finger contact'. In: *Wear* 267 (2009), pp. 1311–1318.

[39] Skedung, L., Danerlöv, K., Olofsson, U., Aikala, M., Niemi, K., Kettle, J. and Rutland, M. W. 'Finger friction measurement on coated and uncoated printing papers'. In: *Tribology Letters* 37 (2010), pp. 389–399.

[40] Maeno, T., Kobayashi, K. and Yamazaki, N. 'Relationship between the structure of human finger tissue and the location of tactile receptors'. In: *JSME International Journal Series C* 41 (1998), pp. 94–100.

[41] Gitis, N. and Sivamani, R. 'Tribometrology of skin'. In: *Tribology and Lubrication Technology* (2005).

[42] Wiertlewski, M. 'Reproduction of tactual textures: transduceers mechanics, and signal encoding'. Doctoral dissertation. University Pierreet Marie Curie, 2011.

[43] Egawa, M., Oguri, M., Hirao, T., Takahashi, M. and Miyakawa, M. 'The evaluation of skin friction using a frictional feel analyzer'. In: *Skin Reserach and Technology* 8.1 (2002), pp. 41–51.

[44] Koudine, A. A., H., B. M. A. P., Aubert, L. and L., L. J. 'Frictional properties of skin: proposal of a new approach'. In: *International Journal of Cosmetic Science* 22 (2000), pp. 11–20.

References

[45] Tang, W., Ge, S.-r., Zhu, H., Cao, X.-c. and Li, N. 'The influence of normal load and sliding speed on frictional properties of skin'. In: *Journal of Bionic Engineering* 5 (2008), pp. 33–38.

[46] Gerhardt, L. .-., Strässe, V., Lenz, A., Spencer, N. D. and Derler, S. 'Influence of epidermal hydration on the friction of human skin against textiles'. In: *Journal of the Royal Society, Interface* 5 (2008), pp. 1317–1328.

[47] Cottenden, A. M., Wong, W. K., Cottenden, D. J. and Farbrot, A. 'Development and validation of a new method for measuring friction between skin and nonwoven materials'. In: *Proc. Inst. Mech. Eng. H* 222.5 (2008), pp. 791–803.

[48] Li, W., Qu, S. X. and Zhou, Z. R. 'Reciprocating sliding behavior of human skin in vivo at lower number of cycles'. In: *Tribology Letters* 23.2 (2006).

[49] Wu, J. Z., Dong, R. G., Rakheja, S., Schopper, A. W. and Smutz, W. P. 'A structural fingertip model for simulating of the biomechanics of tactile sensation'. In: *Medical Engineering and Physics* 26 (2004), pp. 165–175.

[50] Pailler-Mattei, C., Pavan, S., Vargiolu, R., Pirot, F., Falson, F. and Zahouani, H. 'Contribution of stratum corneum in determining biotribological properties of the human skin'. In: *Wear* 263.7–12 (2007), pp. 1038–1043.

[51] Hanafusa, H. and Asada, H. 'Stable prehension of objects by the robot hand with elastic fingers'. In: *Transactions of the Society of Instrument and Control Engineers* 13 (1977), pp. 370–377.

[52] Cutkosky, M. R., Jourdain, J. and Wright, P. 'Skin materials for robotic fingers'. In: *Proc. ieee international conference on robotics and automation.* Vol. 4. 1987, pp. 1649–1654.

[53] Shimoga, K. B. and Goldenberg, A. A. 'Soft materials for robotic fingers'. In: *Robotics and automation.* IEEE international conference on robotics and automation, 1992.

[54] Murakami, K. and Hasegawa, T. 'Novel fingertip equipped with soft skin and hard nail for dexterous multi-fingered robotic manipulation'. In: *International conference on robotics & automation.* 2003.

[55] Han, H. and Kawamura, S. 'Analysis of stiffness of human fingertip and comparison with artificial fingers'. In: *Proc. ieee int. conf. systems, man, and cybernetics.* Vol. 2. Tokyo: IEEE, 1999, pp. 800–805.

[56] Han, H., Shimada, A. and Kawamura, S. 'Analysis of friction on human fingers and design of artificial fingers'. In: *Proc. IEEE international conference on robotics and automation.* Vol. 4. Minneapolis, Minnesota, 1996, pp. 3061–3064.

[57] Wettels, N., Santos, V. J., Johansson, R. S. and Loeb, G. E. 'Biomimetic tactile sensor array'. In: *Advanced Robotics* 22 (2008), pp. 829–849.

[58] Wettels, N., Fishel, J. A. and Loeb, G. E. 'Multimodal tactile sensor'. In: *The human hand as an inspiration for robot hand development.* Ed. by Balasubramanian, R. and Santos, V. J. Cham, Switzerland: Springer International Publishing, 2014, pp. 405–429. ISBN: 978-3-319-03017-3.

[59] Shao, F., Childs, T. H. C., Barnes, C. J. and Henson, B. 'Finite element simulations of static and sliding contact between a human fingertip and textured surfaces'. In: *Tribology International* 43.12 (2010), pp. 2308–2316.

[60] Inoue, T. and Hirai, S. 'Elastic model of deformable fingertip for soft-fingered manipulation'. In: *IEEE Transaction on Robotics* 22.6 (2006), pp. 1273–1279.

[61] Gee, M. G., Tomlins, P., Calver, A., Darling, R. H. and Rides, M. 'A new friction measurement system for the frictional component of touch'. In: *Wear* 259 (2005), pp. 1437–1442.

[62] Wolfram, L. J. 'Friction of skin'. In: *Cosmet. Chem* 34 (1983), pp. 465–476.

[63] Johnson, S. A., Gorman, D. M., Adams, M. J. and Briscoe, B. J. 'The friction and lubrication of human stratum corneum.' In: *Thin films in tribology* (1993), pp. 663–672.

[64] Adams, M. J., Briscoe, B. J. and Johnson, S. A. 'Friction and lubrication of human skin'. In: *Tribology Letters* 26.3 (2007), pp. 239–253.

[65] Lederman, S. J., Howe, R. D., Klatzky, R. L. and Hamilton, C. 'Force variability during surface contact with bare finger or rigid probe'. In: *12th symposium on haptic interfaces for virtual environment and teleoperator systems - ieee virtual reality 2004.* 2004, pp. 154–160.

[66] Pasumarty, S. M., Johnson, S. A., Watson, S. A. and Adams, M. J. 'Friction of the human finger pad: influence of moisture, occlusion and velocity'. In: *Tribology Letters* 44 (2011), pp. 117–137.

[67] Sedlaček, M., Podgornik, B. and J.Vižintin. 'Planning surface texturing for reduced friction in lubricated sliding using surface roughness parameter skewness and kurtosis'. In: *Journal of engineering tribology* 226.8 (2012), pp. 661–667.

[68] Sivamani, R. K., Goodman, J., Gitis Norm, V. and Maibach, H. I. 'Coefficient of friction: tribological studies in man — an overview'. In: *Skin Research and Technology* 9 (2003), pp. 227–234.

[69]   Menezesa, P. L., Kishorea and Kailasb, S. V. 'Effect of surface roughness parameters and surface texture on friction and transfer layer formation in tin–steel tribo-system'. In: *Journal of Materials Processing Technology* 208.1–3 (2008), pp. 372–282.

[70]   Torrance, A. 'Using profilometry for the quantitative assessment of tribological function: PC-based software for friction and wear prediction'. In: *Wear* (1995), pp. 397–404.

[71]   Briggs, G. A. D. and Briscoe, B. J. 'Effect of surface roughness on rolling friction and adhesion between elastic solids'. In: *Nature* 260 (1976), pp. 313–315.

[72]   Tambe, N. S. and Bhushan, B. 'Scale dependence of micro/nano-friction and adhesion of MEMS/NEMS materials, coatings and lubricants'. In: *Nanotechnology* 15.11 (2004).

[73]   Bhushan, B. 'Surface having optimized skewness and kurtosis pparameter for reduced static and kinetic friction'. English. 6007896 (Columbus, Ohio). 1995.

[74]   Michalski, J. and Pawlus, P. 'Description of honed cylinders surface topography'. In: *International Journal of Machine Tools and Manufacture* 34 (1994), pp. 199–210.

[75]   Tayebi, N. and Polycarpou, A. A. 'Modelling the effect of skewness and kurtosis on the static friction coefficient of rough surfaces.' In: *Tribology International* 37 (2004), pp. 491–505.

[76]   Jeng, Y. 'Impact of plateaued surfaces on tribological performance'. In: *STLE Tribology transactions* 39.1 (1996), pp. 354–361.

[77]   Liu, X. and Chetwynd D. G.and Gardner, J. W. 'Surface characterisation of electroactive thin polymetric film bearings'. In: *International Journal of Machine tools and Manufacture* 38.5-6 (1998), pp. 669–675.

[78]   Sedlaček, M., Podgornik, B. and Vižintin, J. 'Correlation between standard roughness parameter skewness and kurtosis and tribological behavior of contact surfaces'. In: *Tribology International* 48 (2012), pp. 102–112.

[79]   Katz, D. *The world of touch.* English. Ed. and trans. by Krueger, L. E. Hove, U.K.: Psychology Press, 1982.

[80]   Schiff, W. and Foulke, E. *Tactual perception: a sourcebook.* Cambridge University Press, 1982.

[81]   Coles, T. R., Meglan, D. and John, N. W. 'The role of haptics in medical training simulators: a survey of the state of the art'. In: *IEEE Transactions on Haptics* 4.1 (2011).

[82]   Smith, D. R., Andrews, D. M. and Wawrow, P. T. 'Development and evaluation of the automative seating discomfort questionnaire (ASDQ)'. In: *International Journal of Industrial Ergonomics* 36.2 (2006), pp. 141–149.

[83]   Hacaambwa, T. M. and Giacomin, J. 'Subjective response to seated fore-and-aft direction whole-body vibration'. In: *International Journal of industrial Ergonomics* 37.1 (2007), pp. 61–72.

[84]   Hennessey, B. J. 'The subjective tactile perception of passenger vehicle interior ssurface and their objective physical measurement'. Master's thesis. University of Surrey, 2006.

[85]   Kawazu, K., Kai, M., Kioike, K., Imada, M. and Yasuda, K. 'Study of favourable paint—quantifying the sense of touch for painted panels'. In: *SAE International Journal of Materials and Manufacturing* 109 (2000), pp. 782–787.

[86]   Elkharraz, G., Thumfart, S., Akay, D., Eitzinger, C. and Henson, B. 'Texture features corresponding to human touch feeling'. In: *Proceeding icip'09 proceedings of the 16th ieee international conference on image processing*. 2009, pp. 1333–1336.

[87]   Barns, C., Childs, T., Henson, B. and Lillford, S. 'Kansei engineering toolkit for the packaging industry'. In: *The TQM Journal* 20.4 (2008), pp. 372–388.

[88]   Shimoga, K. B. and Goldenberg, A. A. 'Grasp admittance center: a concept and its implications'. In: *Proc. IEEE int. conf. robot.* Vol. 1. IEEE, 1991, pp. 293–298.

[89]   Phillips, J. R., Johansson, R. S. and Johnson, K. O. 'Responses of human mechanoreceptive afferents to embossed dot arrays scanned across fingerpad skin'. In: *The Journal of Neuroscience* 12.3 (1992), pp. 827–839.

[90]   Dandekar, K., Raju, B. I. and Srinivasan, M. A. '3-D finite-element models of human and monkey fingertips to investigate the mechanics of tactile sense'. In: *Journal of Biomechanical Engineering* 125 (2003), pp. 682–691.

[91]   Peña, A., Arronte, M., Posada, E. D., Ponce, L. and Flores, T. 'Non-invasive optical method for epidermal thickness estimation'. In: *OnLine Journal of Biological Sciences* 14.2 (2014), pp. 163–166. DOI: 10.3844/ojbsci.2014.163.166.

References

[92]   Physik Instrument. *M-272 ceramic linear drive for automation*. 2011. URL: http://www.pi-china.cn/products/FILES/M272_EN.pdf.

[93]   Smith, S. T. and Chetwynd, D. G. 'Foundations of ultra-precision mechanism design'. In: vol. 2. Developments in Nanotechnology. Boca Raton, US-FL: CRC Press, 1994. Chap. 4, pp. 88–92.

[94]   Paros, J. and Weisbord, L. 'How to design flexure hinges'. In: *Machine Design* 37 (1965), pp. 151–156.

[95]   Wang, T., Qiu, J. and Liu, X. 'Definition measurement unit with flexure hinges for a wind tunnel balance'. In: *Proc. 2010 ieee international conference on information and automation (icia)*. Harbin, China, 2010.

[96]   Xie, Z. 'Derivation of the precise calculation formula of compliance and optimal design of circular flexure'. In: *2011 international conference on electric information and control engineering (iceice)*. Wuhan, China: IEEE, 2011, pp. 3102–3105.

[97]   Yong, Y. K., Lu, T.-F. and Handley, D. C. 'Review of circular flexure hinge design equations and derivation of empirical formulations'. In: *Precision Engineering* 32 (2008), pp. 63–70.

[98]   Tian, Y., Shirinzadeh, B. and Zhang, D. 'Stiffness estimation of the flexure-based five-bar micro-manipulator'. In: *Proc. 10th intl.conf. on control, automation, robotics and vision (icarcv)*. Hanoi, Vietnam, 2008, pp. 599–604.

[99]   Tanaka, Y., Bergmann Tiest, W. M., Kappers, A. M. L. and Sano, A. 'Contact force and scanning velocity during active roughness perception'. In: *PLOS ONE* 9.3 (2014), e93363. ISSN: 1932-6203. URL: http://www.ncbi.nlm.nih.gov/pmc/articles/PMC3968175/.

[100] Greenwood, J. 'Adhesion of elastic spheres'. In: *Proc. R. Soc. A* 453 (1997), pp. 1277–1297.

[101] Naylor, P. F. D. 'The skin surface and friction'. In: *British Journal of Dermatology* 67 (1955), pp. 239–246.

[102] El-Shimi, A. F. 'In vivo skin friction measurements'. In: *Journal of the Society of Cosmetic Chemists* 28 (1977), pp. 37–51.

[103] Sivamani, R. K., Goodman, J., Gitis, N. V. and Maibach, H. I. 'Friction coefficient of skin in real-time'. In: *Skin Research and Technology* 9 (2003), pp. 235–239.

[104] Johnson, K. L. *Contact mechanics*. Cambridge, U.K.: Cambridge University Press, 1987.

[105]   Persson, B. N. J. 'Contact mechanics for randomly rough surfaces'. In: *Surface Science Reports* 61 (2006), pp. 201–207.

[106]   Persson, B. N. J., Butcer, F. and Chiaia, B. 'Elastic contact between randomly rough surfaces: comparison of theory with numerical results'. In: *Physical Review B* 65 (2002).

[107]   Persson, B. 'Theory of rubber friction and contact mechanics'. In: *Journal f chemical physics* 115.8 (2001).

[108]   Palasantzas, G. 'Influence of self-affine roughness on the adhesive friction coefficient of a rubber body sliding on a solid substrate'. In: *Surface Science* 565.2–3 (2004), pp. 191–196.

[109]   Scaraggi, M. and Persson, B. N. J. 'Friction and universal contact area law for randomly rough viscoelastic contacts'. In: *Journal of Physics: Condensed Matter* 27.10 (2015), p. 105102.

[110]   Fuller, K. N. G. and Tabor, D. 'The effect of surface roughness on the adhesion of solids'. In: *Proc. R. Soc. A* 345.1642 (1975), pp. 327–342.

[111]   Williams, J. *Engineering tribology*. Cambridge University Press, 2005.

[112]   Ciavarella, M., Delfine, V. and Demelio, G. 'A "re-vitalized" Greenwood and Williamson model of elastic contact between fractal surfaces'. In: *Journal of the Mechanics and Physics of Solids* 54 (2006), pp. 2569–2591.

[113]   Hertz, H. 'Ueber die berührung fester elastischer körper'. In: *Journal fur die Reine und Angewandte Mathematik* 92 (1882), pp. 156–171.

[114]   Bush, A. W., Gibson, R. D. and Keogh, G. P. 'The limit of elastic deformation in the contact of rough surfaces'. In: *Mechanics Research Communications* 3 (1976), pp. 169–174.

[115]   Greenwood, J. A., Johnson, K. L. and Matsubara, E. 'A surface roughness parameter in Hertz contact'. In: *Wear* 100.1-3 (1984), pp. 47–57.

[116]   Johnson, K. L., Kendall, K. and Roberts, A. D. 'Surface energy and the contact of elastic solids'. In: *Proc. R. Soc. A* 324.1558 (1971), pp. 301–313.

[117]   Fischer-Cripps, A. C. *Nanoindentation*. Springer, 2011.

[118]   Tabor, D. 'Surface forces and surface interactions'. In: *Journal of Colloid and Interface Science* 58 (1977), pp. 2–13.

[119]   Mikic, B. B. and Roca, R. T. 'A solution to the contact of two rough spherical surfaces'. In: *Journal of Applied Mechanics* 41 (1974), pp. 801–803.

References

[120] Greenwood, J. A. 'A simplified elliptic model of rough surface contact'. In: *Wear* 261 (2006), pp. 191–200.

[121] Giuseppe. 'A slightly corrected Greenwood and William model predicts asymptotic linearity between contact area and load'. In: *Journal of the Mechanics and Physics of Solids* 57 (2009), pp. 1093–1102.

[122] Kotwala, C. A. and Bhushan, B. 'Contact analysis of non-Gaussian surfaces for minimum static and kinetic friction and wear'. In: *Tribology Transactions* 39.4 (1996).

[123] Persson, B. N. J. 'Elastoplastic contact between randomly rough surfaces'. In: *Physical Review Letters* 87 (11 2001), p. 116101. DOI: 10.1103/PhysRevLett.87.116101.

[124] Persson, B. N. J., Carbone, G., Samoilov, V. N., Sivebaek, I. M., Tartaglino, U., Volokitin, A. I. and Yang, C. 'Contact mechanics, friction and adhesion with application to quasicrystals'. In: *Fundamentals of friction and wear on the nanoscale*. Ed. by Gnecco, E. and Meyer, E. Cham, Switzerland: Springer International Publishing, 2015. Chap. 13, pp. 249–287. DOI: 10.1007/978-3-319-10560-4_13.

[125] Yang, C. and Persson, B. N. J. 'Contact mechanics: contact area and interfacial separation from small contact to full contact'. In: *Journal of Physics: Condensed Matter* 20 (2008).

[126] Manners, W. and Greenwood, J. A. 'Some observations on persson's diffusion theory of elastic contact'. In: *Wear* 261 (2006), pp. 600–610.

[127] Iivarinen, J. T., Korhonen, R. K., Julkunen, P. and Jurvelin, J. S. 'Experimental and computational analysis of soft tissue stiffness in forearm using a manual indentation device'. In: *Medical Engineering & Physics* 33.10 (2011), pp. 1245–1253. ISSN: 1350-4533.

[128] Geerligs, M., van Breemen, L., Peters, G., Ackermans, P., Baaijens, F. and Oomens, C. 'In vitro indentation to determine the mechanical properties of epidermis'. In: *Journal of Biomechanics* 44.6 (2011), pp. 1176–1181.

[129] Tobin, D. J. 'Biochemistry of human skin - our brain on the outside'. In: *Chemical Society Reviews* 35.1 (2006), pp. 52–67.

[130] Pailler-Mattei, C., Bec, S. and Zahouani, H. 'In vivo measurements of the elastic mechanical properties of human skin by indentation tests'. In: *Medical Engineering and Physics* 30.5 (2008), pp. 599–606.

[131] van Kuilenburg, J., Masen, M. A. and van der Heide, E. 'Contact modelling of human skin: what value to use for the modulus of elasticity'. In: *Journal of Engineering Tribology* 227.4 (2012), pp. 349–361.

[132] Zahouani, H., Pailler-Mattei, C., Sohm, B., Vargiolu, R., Cenizo, V. and Debret, R. 'Characterization of the mechanical properties of a dermal equivalent compared with human skin in vivo by indentation and static friction tests'. In: *Skin Research and Technology* 15.1 (2009), pp. 68–76.

[133] Yuan, Y. and Verma, R. 'Measuring microelastic properties of stratum corneum'. In: *Colloids and Surfaces, B: Biointerfaces* 48.1 (2006), pp. 6–12.

[134] Qi, H. J., Joyce, K. and Boyce, M. C. 'Durometer hardness and the stress-strain behavior of elastomeric materials'. In: *Rubber Chemistry and Technology* 76.2 (2003), pp. 419–435. DOI: 10.5254/1.3547752.

[135] Yang, Y., Bagnaninchi, P. O., Ahearne, M., Wang, R. K. and Liu, K.-K. 'A novel optical coherence tomography-based micro-indentation technique for mechanical characterization of hydrogels'. In: *Journal of the Royal Society Interface* 4.17 (2007), pp. 1169–1173.

[136] Dintwa, E., Tijskens, E. and Ramon, H. 'On the accuracy of the hertz model to describe the normal contact of soft elastic spheres'. In: *Granular Matter* 10.3 (2008), pp. 209–221.

[137] Chhetri, D. K., Zhang, Z. and Neubauer, J. 'Measurement of Young's modulus of vocal folds by indentation'. In: *Journal of Voice* 25.1 (2011), pp. 1–7.

[138] Isaac, G. H., Thompson, J., Williams, S. and Fisher, J. 'Metal-on-metal bearings surfaces: materials, manufacture, design, optimization, and alternatives'. In: *Proc. inst. mech.eng.h.* Ed. by IMechE. Vol. 220. 2. IMechE, 2006, pp. 119–133.

[139] Williams, C. C. and Wickramasinghe, H. K. 'Scanning thermal profiler'. In: *Applied Physics Letters* 49 (1986), pp. 1587–1589.

[140] Han, C., Sanei, S. H. R. and Alisafaei, F. 'On the origin of indentation size effects and depth dependent mechanical properties of elastic polymers'. In: *Journal of Polymer Engineering* 36 (2015). DOI: 10.1515/polyeng-2015-0030.

[141] Oliver, W. C. and Pharr, G. M. 'Measurement of hardness and elastic modulus by instrumented indentation: Advances in understanding and refinements to methodology'. In: *Journal of Materials Research* 19.1 (2004), pp. 3–20.

189

References

[142] Berkovich, E. S. 'Three-faceted diamond pyramid for studying microhardness by indentation'. In: *Zavodskaya Laboratoria* 13.3 (1950), pp. 345–347.

[143] Kuo, J.-C. and Huang, I.-H. 'Extraction of plastic properties of aluminum single crystal using berkovich indentation'. In: *Materials Transactions* 51.11 (2010), pp. 2104–2108.

[144] Bruker. *Through transmissive media module.* 2016. URL: https://www.bruker.com/products/surface-and-dimensional-analysis/3d-optical-microscopes/accessories/through-transmissive-media-ttm-module.html (visited on 28/09/2016).

[145] Tabor, D. and Greenwood, A. 'The friction of hard sliders on lubricated rubber: the improtance of deformation loss'. In: *Proc. Physiological Society* 71 (1957), pp. 989–1001.

[146] Nishida, S., Saito, Y., Iwasaki, K. and Aoki, S. 'Vehicle of monocoque construction formed from thermoplastic resin members'. U.S. pat. 20160137229 (Japan). 2016.

[147] Greenwood, J. A. and Williamson, J. B. P. 'Contact of nominally flat surfaces'. In: *Proc. R. Soc. A* A295 (1966), pp. 300–319.

[148] Whitehouse, D. J. and Archard, J. F. 'The properties of random surfaces of significance in their contact'. In: *Proc. R. Soc. A* 316.1524 (1970), pp. 97–121.

[149] de Rooij, M. B. 'Tribological aspects of unlubricated deepdrawing processes'. Doctoral dissertation. Enschede, Netherlands: Univ. of Twente, 1998.

[150] Sérgio, M. O. T. 'Analysis of surface roughness and models of mechanical contacts'. Doctoral dissertation. Pisa, Italy: Facoltà di Ingegneria, Università di Pisa, 2004.

[151] Aramaki, H., Cheng, H. S. and Chung, Y. 'The contact between rough surfaces with longitudinal texture—part I: average contact pressure and real contact area'. In: *Journal of Tribology* 115 (1993), pp. 419–424.

[152] Sedlaček, M., Vilhena, L. M. S., Podgornik, B. and Vižintin, J. 'Surface topography modelling for reduced friction'. In: *Journal of Mechanical Engineering* 57.9 (2011), pp. 674–680.

[153] Bowden, F. P. and Tabor, D. *The friction and lubrication of solids.* Oxford University Press, 1950.

[154] Johnson, N. J. 'Systems of frequency curves generated by methods of translation'. In: *Biometrika Trust* 36.1/2 (1949), pp. 149–176.

[155] Elderton, W. P. and Johnson, N. L. *Systems of frequency curves.* Ed. by D.Rasch. Vol. 12. 190-191 3. Cambridge Univerisity Press, 1969.

[156] Parthasarathi, N. L., Borah, U. and Albert, S. K. 'Correlation between coefficient of friction and surface roughness in dry sliding wear of AISI type 316 L (N) stainless steel at elevated temperatures'. In: *Computer Modelling and New Technologies* 17.1 (2013), pp. 51–63.

[157] Smith, R. H. *Analyzing friction in the design of rubber products and their paired surfaces.* CRC Press, 2008.

[158] Yandell, W. O. 'A new theory of hysteretic sliding friction'. In: *Wear* 17.4 (1971), pp. 229–244.

[159] Krueger, L. E. *Tactual perception in historical perspective: David Katz's world of touch.* Cambridge University Press, 1982. Chap. 1.

[160] Heller, M. A. and Schiff, W. *The psychology of touch.* Mahwah, US-NJ: Lawrence Erlbaum Associates, 1991.

[161] Allison, P. D. and Christakis, N. A. 'Logit model for sets of ranked items'. In: *Sociological Methodology* 24 (1994), pp. 199–228.

[162] Long, J. S. and Freese, J. 'Rank-ordered logit model'. In: *Review of regression models for categorical dependent variables using stata.* 3rd ed. 2014. Chap. 8.12.5.

[163] Fok, D., Paap, R. and van Dijk, B. 'A rank-ordered logit model with unobserved heterogeneity in ranking capabilities'. In: *Journal of Applied Econometrics* 27 (5 2012), pp. 831–846.

[164] Nagamachi, M. 'Kansei engineering as a powerful consumer-oriented technology for product development'. In: *Applied Ergonomics* 33 (3 2002), pp. 284–294.

[165] Okamoto, S., Nagano, H. and Yamada, Y. 'Psychophysical dimensions of tactile perception of textures'. In: *IEEE Transactions on Haptics* 6.1 (2013), pp. 81–93.

[166] Beggs, S., Cardell, S. and Hausman, J. 'Assessing the potential demand for electrical cars'. In: *Journal of Econometrics* 16 (1981), pp. 1–19.

[167] Marden, J. I. *Analyzing and modeling rank data.* Monographs on Statistics & Applied Probability. London: Chapman & Hall, 1996.

[168] Girish N. Punj, R. S. 'The choice process for graduate business schools'. In: *Journal of Marketing Research* 15.4 (1978), pp. 588–598.

References

[169]   Neter, J., Wasserman, W. and Kutner, M. H. *Applied linear statisitical models*. 3rd ed. Boston MA:Irwin, 1990.

[170]   Bhatti, I. P., Lohano, H. D., Pirzado, Z. A. and Jafri, I. A. 'A logistic regression analysis of the ischemic heart disease risk'. In: *Journal of Applied Sciences* 6.4 (2006), pp. 785–788.

[171]   Agresti, A. *Categorical data analysis*. 2nd ed. Hoboken, US-NJ: Wiley, 2002.

[172]   Brace, N., Snelgar, R. and Kemp, R. *SPSS for psychologists*. 5th ed. Palgrave Macmillan, 2012. ISBN: 9780230362727.

[173]   Kitada, R., Hashimoto, T., Kochiyama, T., Kito, T., Okada, T., Matsumura, M., Lederman, S. J. and Sadato, N. 'Tactile estimation of the roughness of gratings yields a graded response in the human brain: an fMRI study'. In: *Neuroimage* 25.1 (2005), pp. 90–100.

[174]   Manski, C. 'The structure of random utility models'. In: *Theory and Decision* 8 (1977), pp. 228–254.

[175]   Chapman, R. and Staelin, R. 'Exploiting rank ordered choice set data within the staochastic utility model'. In: *Journal of Marketing Research* 19 (1982), pp. 288–301.

[176]   Rindova, V. 'Editor's comments: publishing theory when you are new to the game.' In: *Academy of Management Review* 33.2 (2008), pp. 300–303.

[177]   Camargo, F. R., Kawamo, K., Motohata, K., Hayashi, K., Henson, B. and Kawai, T. 'Applying the rasch model to measure kansei responses to fabric seats'. In: *International conference on kansei engineering and emotion research*. (11th–13th June 2014). Linköping, 2014.

Appendices

A.1   Design of the friction measurement apparatus

DETAIL A
SCALE 2 : 5

Artificial finger

Height adjustable stand

Adjustable spring

A

Capacitive sensor

Sample under test

Sample holder

Flexure stand

Flexure

Load cell

Linear stage

Sample under test

Flexure

	NAME	SIGNATURE	DATE				TITLE:
DRAWN	Hui Niu		19/01/2016				

TITLE:
Artificial finger friction measurement apparatus

MATERIAL:

DWG NO.

A4

WEIGHT:

SCALE:1:5

SHEET 1 OF 1

DETAIL A
SCALE 1 : 1

35
50
40
R5
10
11
Ø 5
10
Ø 8
6
40
11
R5
5
36
72
25

A

	NAME	SIGNATURE	DATE			TITLE:
DRAWN	Hui Niu		19/01/2016			
CHK'D						
APPV'D						
MFG						
Q.A						

UNLESS OTHERWISE SPECIFIED:
DIMENSIONS ARE IN MILLIMETERS
SURFACE FINISH:
TOLERANCES:
  LINEAR:
  ANGULAR:

FINISH:

DEBURR AND
BREAK SHARP
EDGES

REVISION 1

TITLE:
Flexure

MATERIAL:

DWG NO.

A4

WEIGHT:

SCALE:1:2

SHEET 1 OF 1

According to the detailed design shown in chapter 3, all of the schematic diagrams are shown as follows by using SolidWorks computer aided design (CAD) software.

The flexure part is shown as follows:
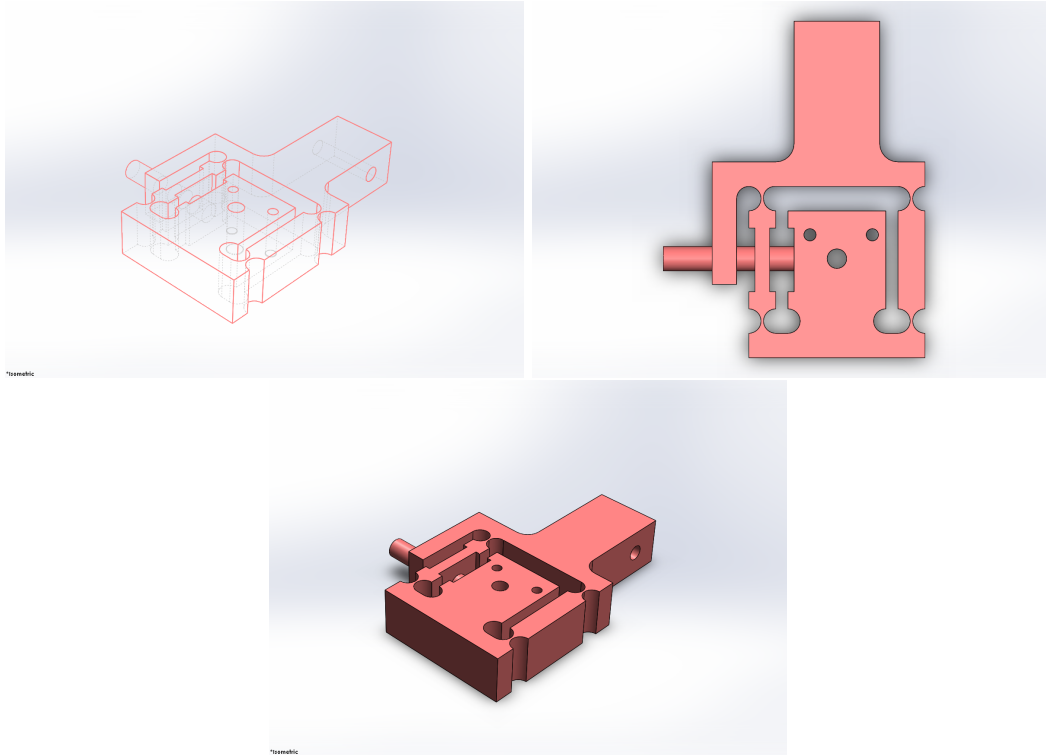
Figure A.1: The structure of flexure

The whole design is shown as follows:
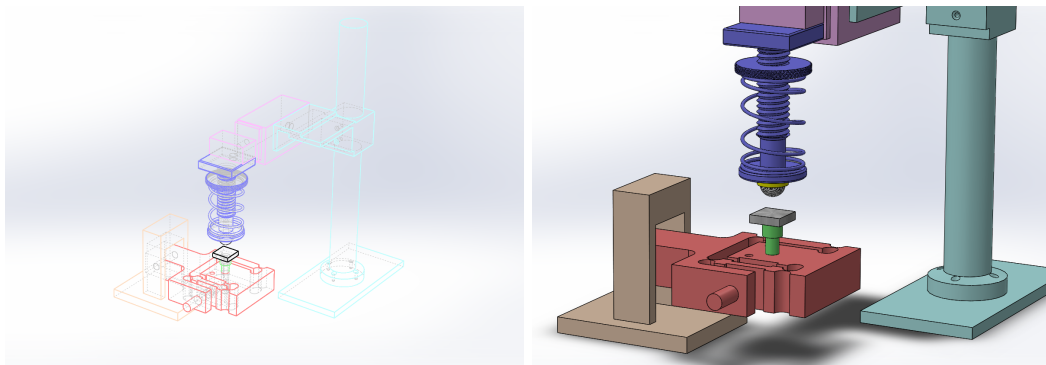
Figure A.2: The whole structure of the friction apparatus (1)
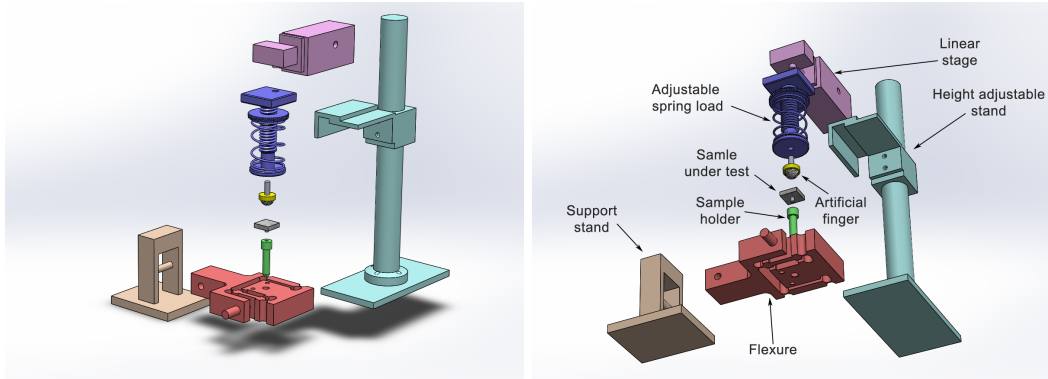
Figure A.3: The whole structure of the friction apparatus (2)
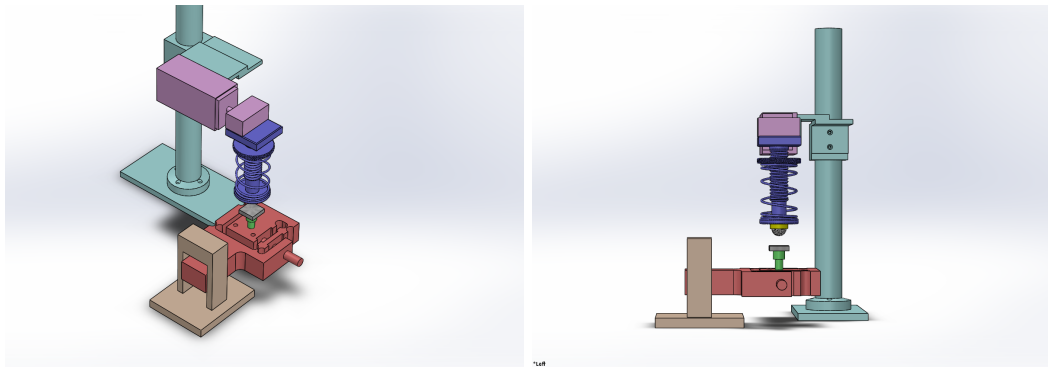
Figure A.4: The whole structure of the friction apparatus (3)
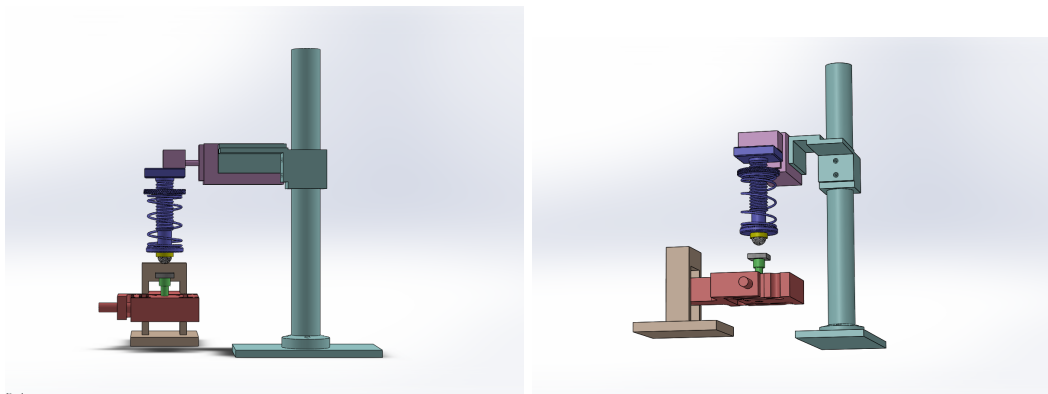
Figure A.5: The whole structure of the friction apparatus (4)

A.2 Stiffness estimation of the flexure in the friction apparatus

A.2.1 Theoretical calculation

The flexure was made of aluminium (Young's modulus = 70 GPa). The flexure works on the basic mechanical principle that a force applied to an elastic element produces a measurable deflection. The results obtained a linear output relationship between the applied force and the measured deflection and to make the instrument insensitive to forces which are not applied directly along the sensing elements. For a given size and stiffness, the displacements are smooth and continuous. The force for a given deflection is dependent upon the elastic modulus of the flexure [93].

(a) dry condition
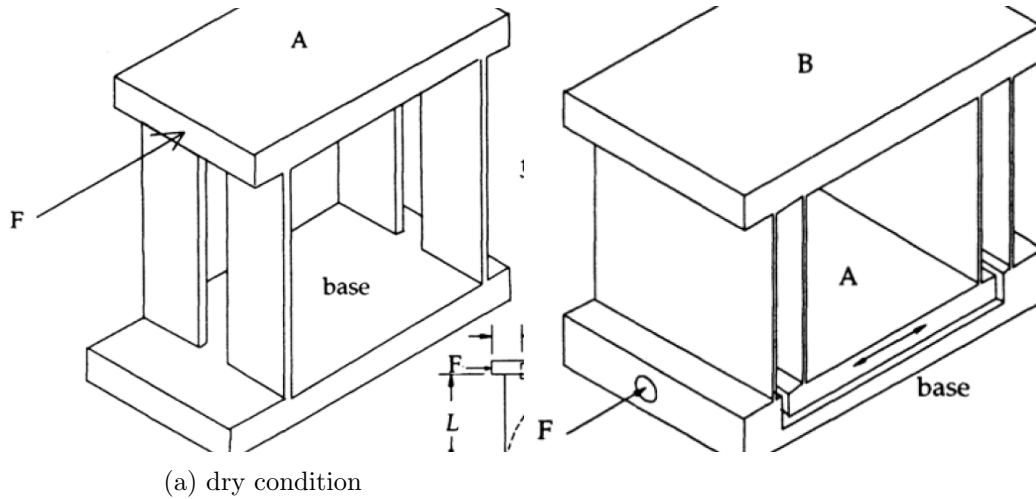
Figure A.6: Flexure system

A small controlled displacement is achieved by applying a force to an elastic mechanism of known stiffness. The simple cantilever is rarely usable because an actuate locus is traced out by any point on the beam. To design a mechanism for linear or angular motion we use other geometries that exploit symmetry and superposition. The resistance to torsional deflection is commonly improved by attaching two (or more) of these flexures together to form the simple linear spring mechanism. Consequently, any change in height of platform A relative to its support B will be compensated by an equal and oppsite change in height if B relative to the base.

Consideration of the deflected shape of the leaf springs reveals that most of the bending occurs near the roots, with the middle sections remaining relatively straight.

Thus, for only a small increase in drive direction stiffness, the buckling strength of the springs can be improved and errors due to their imperfections simultaneously reduced by clamping thick reinforcing plates to the central section of the springs[93].

In the application where limited rotation is required, such hinges hold many advantages over classical rotation joints, including no friction, no clearance, high resolution, lightweight and compact.
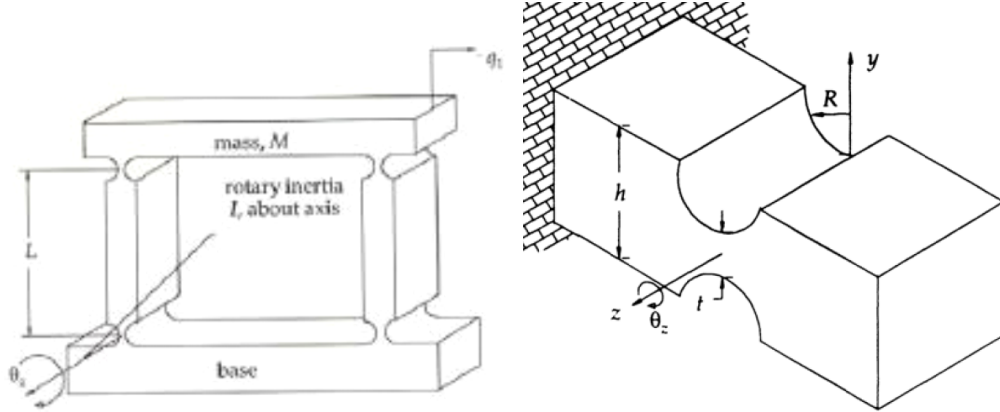
Figure A.7: The instrument
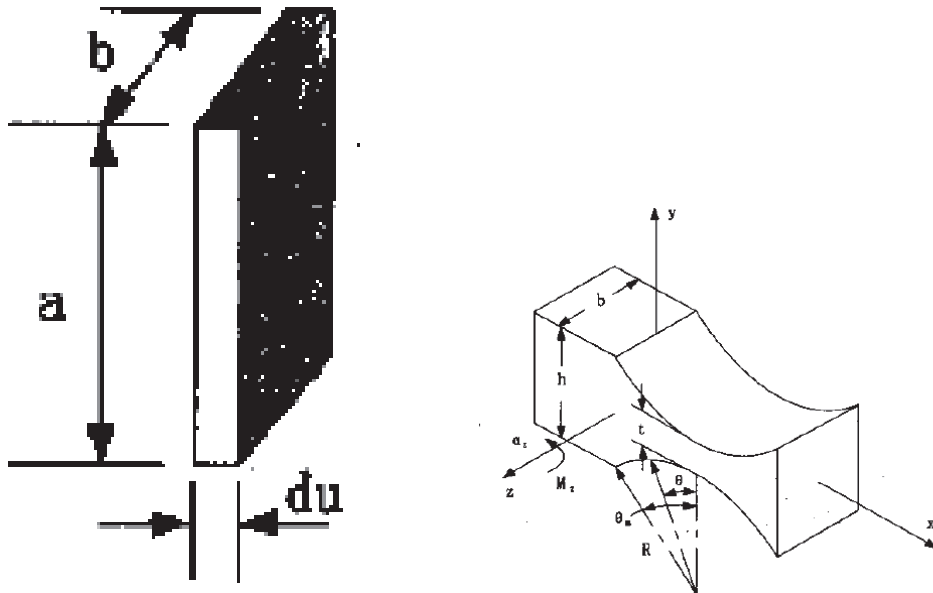
Figure A.8: Notch hinge

Compliance is the most important parameter for flexure hinge design. It can

be calculated based on the bending theory of Euler-Bernoulli beam:

$$a = t + 2R - 2R\cos\theta \tag{A.2.1}$$

$$\mathrm{d}u = \mathrm{d}(R\sin\theta) = R\cos\theta\,\mathrm{d}\theta \tag{A.2.2}$$

$$\mathrm{d}\alpha_z = \frac{M_z}{EI_z}\mathrm{d}u = \frac{12M_z}{EbR^2}\frac{\cos\theta}{(\frac{t}{R}+2-2\cos\theta)^3}\mathrm{d}\theta \tag{A.2.3}$$

$$\frac{\alpha_z}{M_z} = \frac{12}{EbR^2}\int_{-\theta_m}^{\theta_m}\frac{\cos\theta}{(\frac{t}{R}+2-2\cos\theta)^3}\mathrm{d}\theta \tag{A.2.4}$$

which can be simplified as follows [94]:

$$\theta_z = \frac{9\pi R^{1/2}M}{2Ebt^{5/2}} \tag{A.2.5}$$

The accuracy of the spring flexure is primarily dependent upon the accuracy of the centre of the holes, with the materials removed from the rest of the body being of little influence. A simple linear spring has four notches and each notch acts as a rotary bearing. For small deflections and assuming that the ratio $h/(2R+t)$ is near unity—that is the notches are nearly semicircular—If a driven force F is applied in the line of the mid-point of the legs, the moment at each hinge is simply $FL/4$, and the displacement can be obtained as

$$\lambda = \frac{F}{q} \simeq \frac{8Ebt^{5/2}}{9\pi L^2 R^{1/2}}. \tag{A.2.6}$$

Alternatively, for $t < R < 5t$, an approximation derived empirically from finite element studies [93] is given by

$$\theta_z = \frac{2KRM}{EI} = \frac{24KRM}{Ebt^3} \tag{A.2.7}$$

Where K is a correlation factor for the notch curvature modelled and $K = 0.565\frac{t}{R} + 0.166$. K_t is the stress concentration factor caused by the circular notch hinge. A stress concentration (often called stress raisers or stress risers) is a location in an object where stress is concentrated. An object is strongest when force is evenly distributed over its cross-sectional area. Usually, α is the ratio of the maximum stress σ_{max} to the average stress σ on the same cross-section, where $\alpha = \frac{\sigma_{max}}{\sigma}$, it is larger than 1.

As for the flexure used in this thesis, the dimensions are $t = 1\,\mathrm{mm}, R = 5\,\mathrm{mm}, b = 25\,\mathrm{mm}, h = 11\,\mathrm{mm}, L = 50\,\mathrm{mm}$. The maximum deflection of a notch hinge mechanism is normally governed by the peak stress in the thinnest section of the hinges. This peak stress or maximum allowable stress is typically 0.1 to 0.3 of the effective yield stress for metal springs. Here we choose $\sigma_{max} = 0.1\mathrm{MPa}$ and

l5cm

Table A.1: Flexure stiffness measurement

Weight (g)	Load (N)	Deflection (mm)
0	0	0
20	0.196	1.250
30	0.294	2.188
40	0.392	3.126
60	0.588	4.064

$\sigma_{\mathrm{r}} = 0.1 * 20 = 2\mathrm{MPa}$. The parameters for the flexure used in this thesis are:

$$K_{\mathrm{t}} = \frac{2.7t + 5.4R}{8R + E} + 0.325 = \frac{2.7 \cdot 0.001 + 5.4 \cdot 0.005}{8 \cdot 0.005 + 0.001} + 0.325 = 1.049 \quad \text{(A.2.8)}$$

$$M_{\mathrm{max}} = \frac{bt^2}{6K_{\mathrm{t}}} \cdot \sigma_{\mathrm{max}} = \frac{0.025 \cdot 0.001^2}{6 \cdot 1.049} \cdot 2 \cdot 10^6 = 7.9 \times 10^{-3} \mathrm{N\,m} \quad \text{(A.2.9)}$$

$$\theta_{\mathrm{max}} = \frac{9\pi R^{1/2} M}{2Ebt^{5/2}} = \frac{9 \cdot 3.14 \cdot \sqrt{(0.005)} \cdot 7.9 \cdot 10^{-3}}{2 \cdot 70 \cdot 10^9 \cdot 0.025 \cdot 0.001^{5/2}} = 1.43 \times 10^{-3} \quad \text{(A.2.10)}$$

$$\lambda = \frac{F}{q} \simeq \frac{8Ebt^{5/2}}{9\pi L^2 R^{1/2}} = \frac{8 \cdot 70 \times 10^9 \cdot 0.025 \cdot 0.0015^{5/2}}{9 \cdot 3.14 \cdot 0.052^2 \cdot 0.005^{1/2}} = 81.57 \,\mathrm{kN\,m^{-1}} \quad \text{(A.2.11)}$$

$$F_{\mathrm{max}} = \lambda \cdot q_{\mathrm{max}} = 81.57 \times 10^3 \cdot 74 \times 10^{-6} = 6.12 \,\mathrm{N} \quad \text{(A.2.12)}$$

Hence, according to the calculations, the maximum load we can apply to the instrument is $6.12 \,\mathrm{N}$.

A.2.2 Experimental calculation

To calibrate the flexure mechanism for friction measurement, the flexure was mounted vertically and precision weights were placed on the top of the flexure. Its displacement was measured by a Taylor Hobson *Form Talysurf* surface profilometer. The results are shown in Table A.1. By computing the slope of the data through linear regression, the stiffness of the flexure was estimated to be $33.5 \,\mathrm{kN\,m^{-1}}$.

A.3 Contact area measurement experiments

This section shows images of contact area measurement experiment using Bruker optical microscope. The black area represents a contact in all figures below except Fig. A.9.
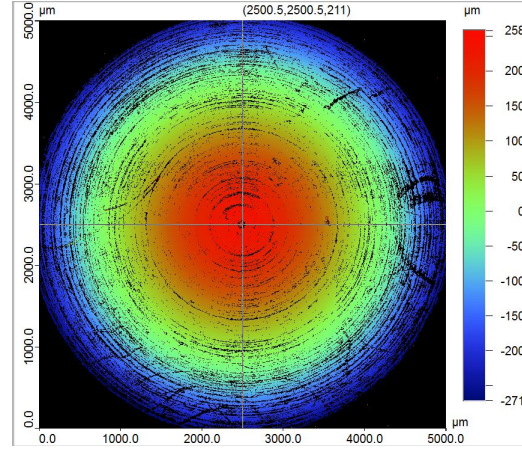
Figure A.9: The artificial fingertip without the glass plate

(a) Contact area estimation

(b) Contours
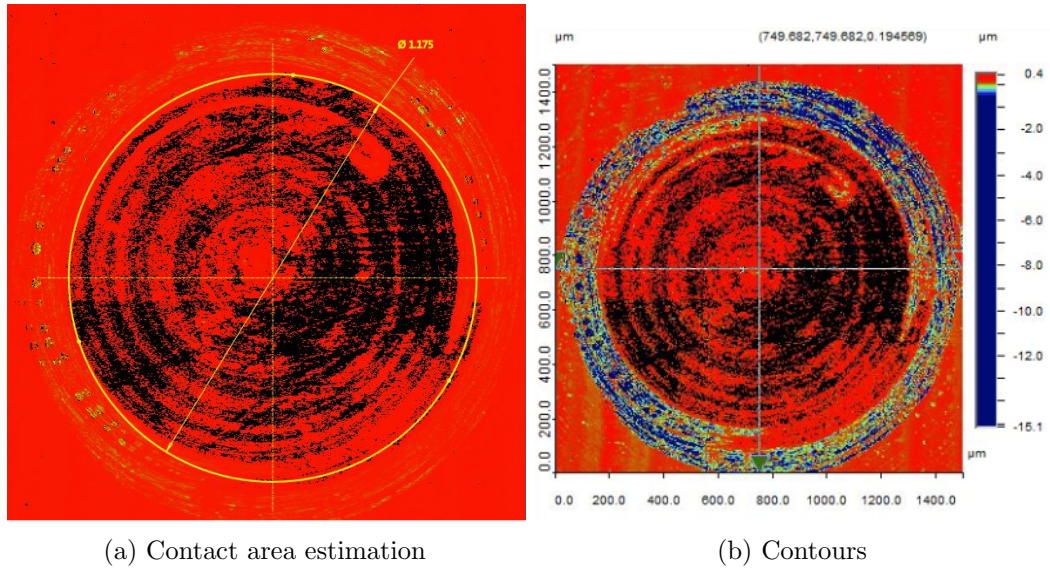
Figure A.10: Contact area measurement with glass plate resting on the fingertip (no added weights)
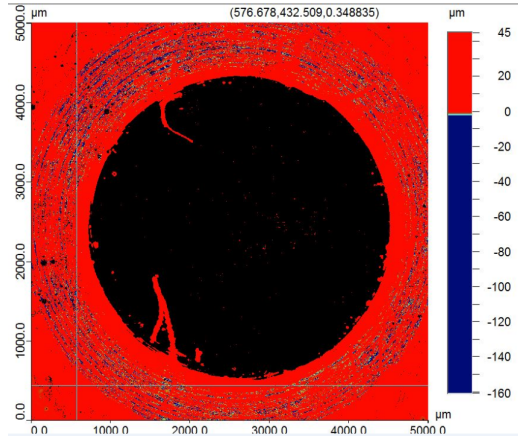
Figure A.11: The contact area with 50 g weight
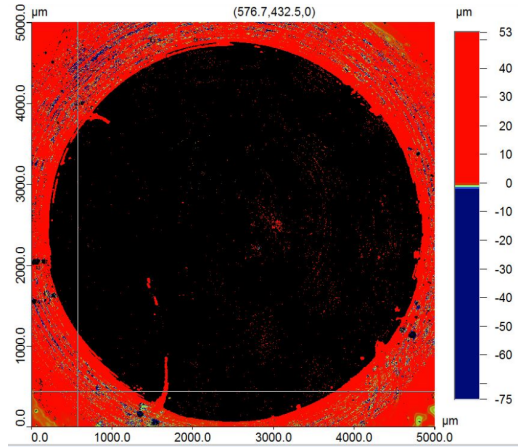
Figure A.12: The contact area with 100 g weight
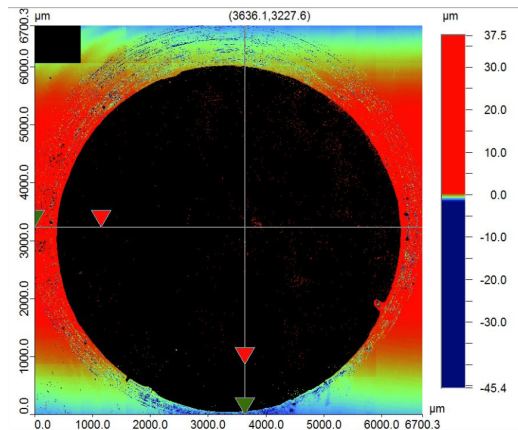
Figure A.13: The contact area with 200 g weight

Figure A.14: The contact area with 300 g weight

A.4 Surface topography measured by Bruker

The surface topography textures of the various metal and thermoplastic samples were measured by a Bruker microscope, the results are shown in this section.

A.4.1 Metal Samples

Aluminium samples

(a) 2D   (b) 3D
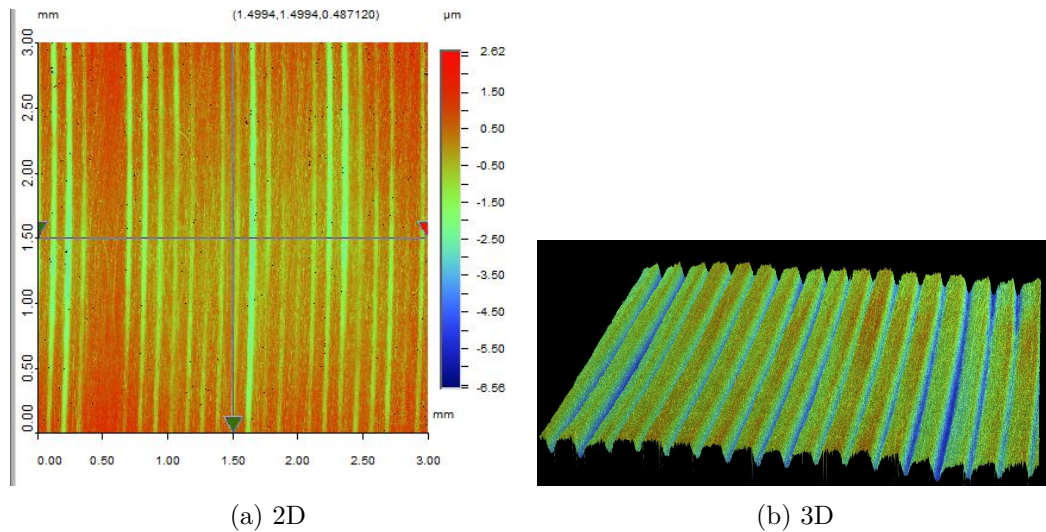
Figure A.15: The surface texture of `AM1`

(a) 2D

(b) 3D
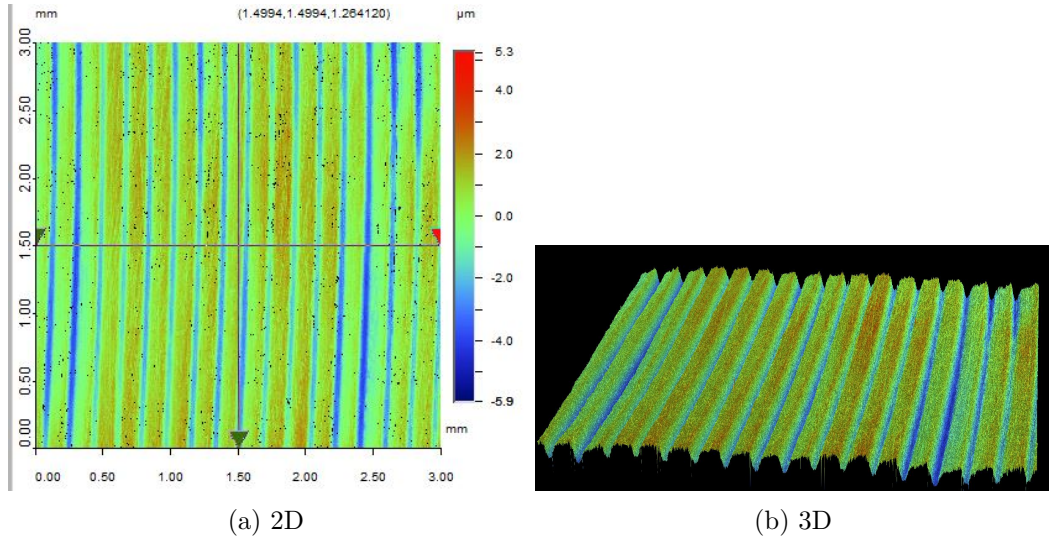
Figure A.16: The surface texture of AM2

(a) 2D

(b) 3D
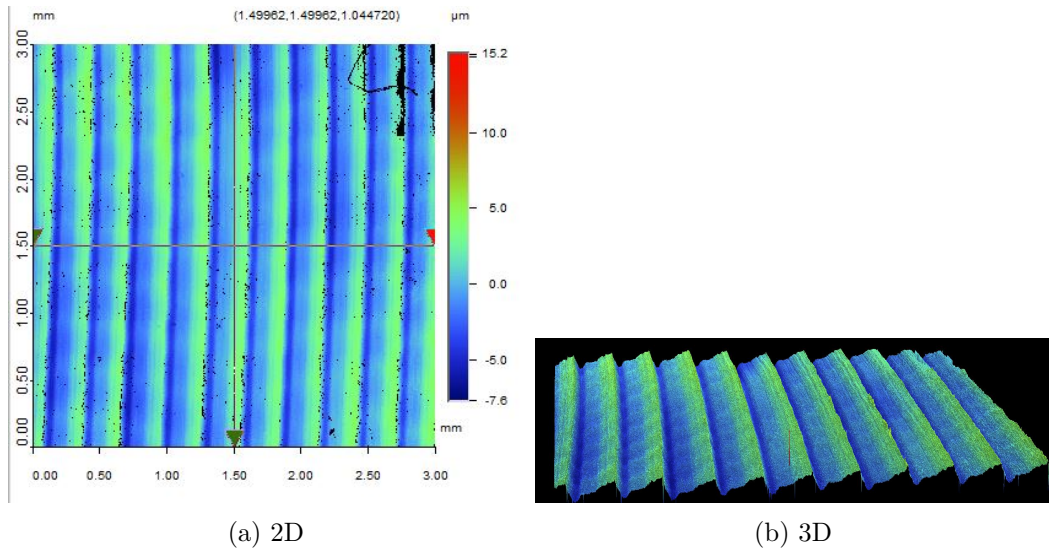
Figure A.17: The surface texture of AM3

(a) 2D

(b) 3D
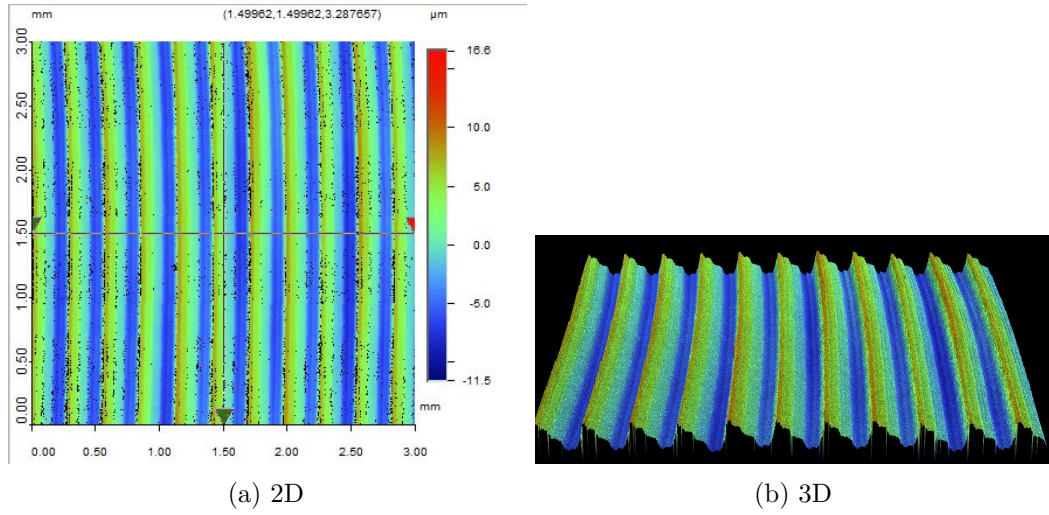
Figure A.18: The surface texture of `AM4`

(a) 2D

(b) 3D
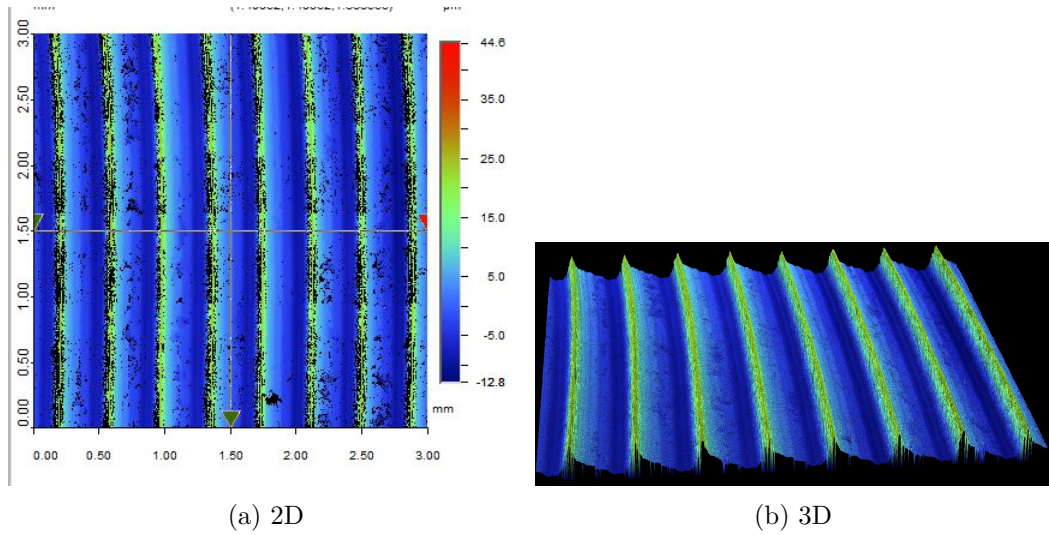
Figure A.19: The surface texture of `AM5`

206

(a) 2D

(b) 3D
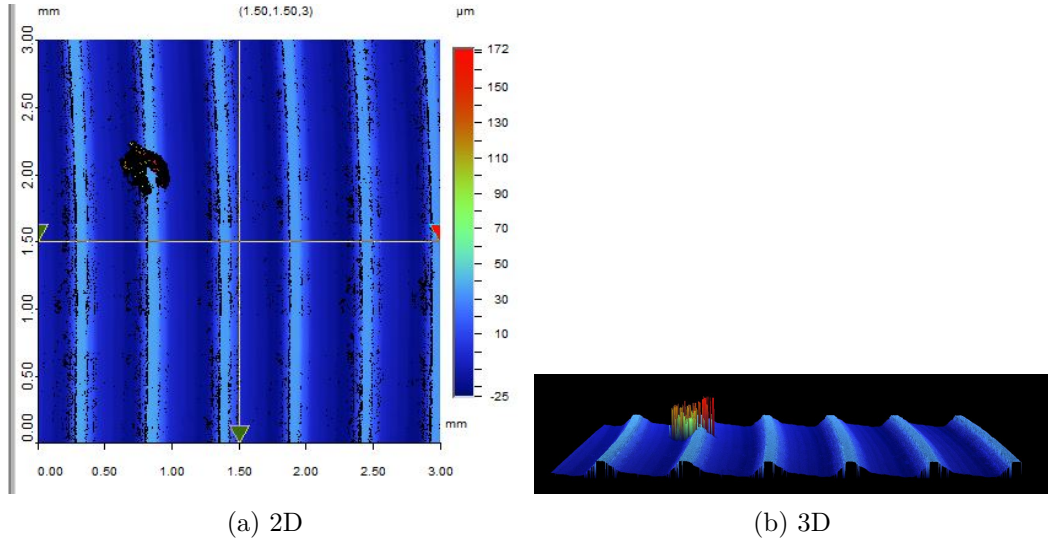
Figure A.20: The surface texture of `AM6`

(a) 2D

(b) 3D
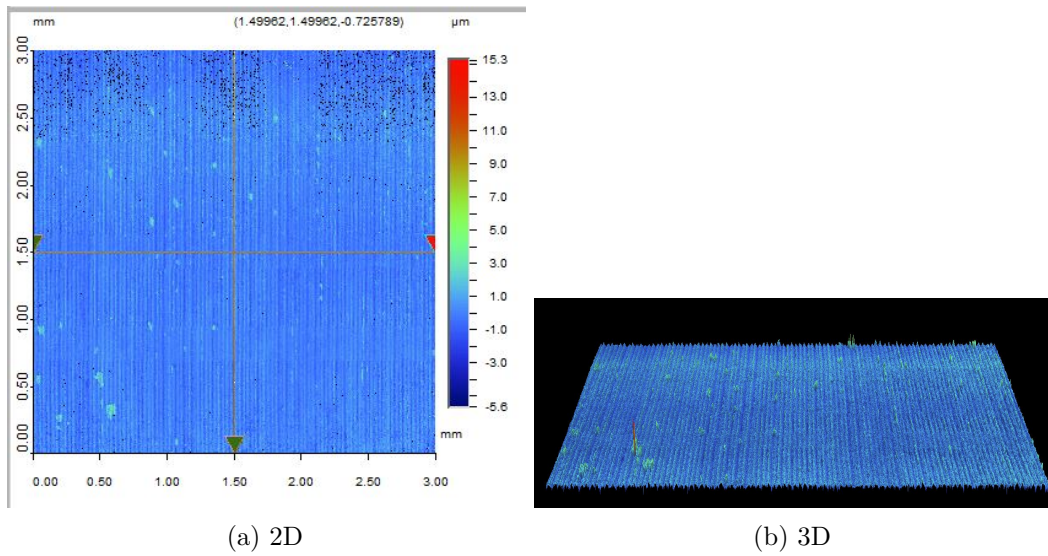
Figure A.21: The surface texture of `AT1`

(a) 2D   (b) 3D

Figure A.22: The surface texture of AT2

(a) 2D   (b) 3D
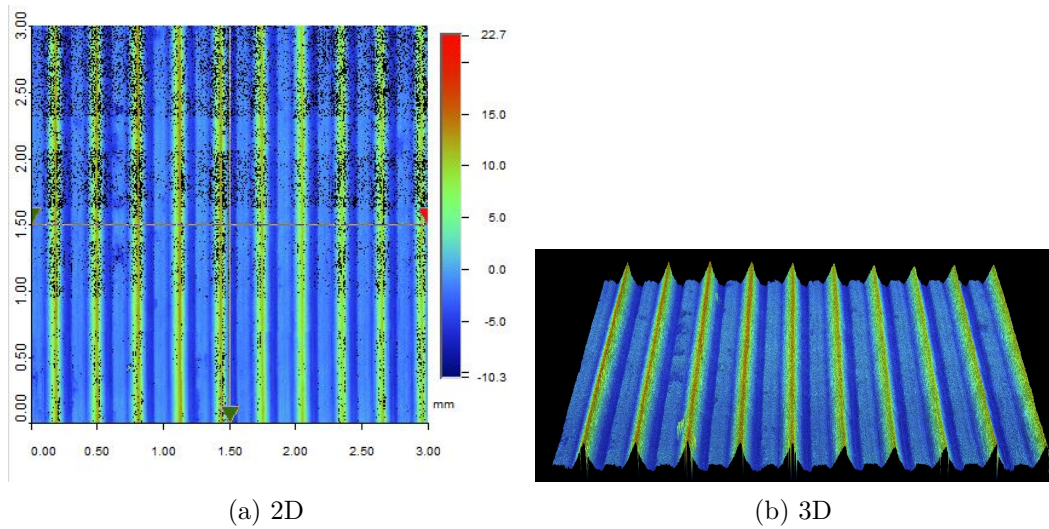
Figure A.23: The surface texture of AT3

(a) 2D

(b) 3D
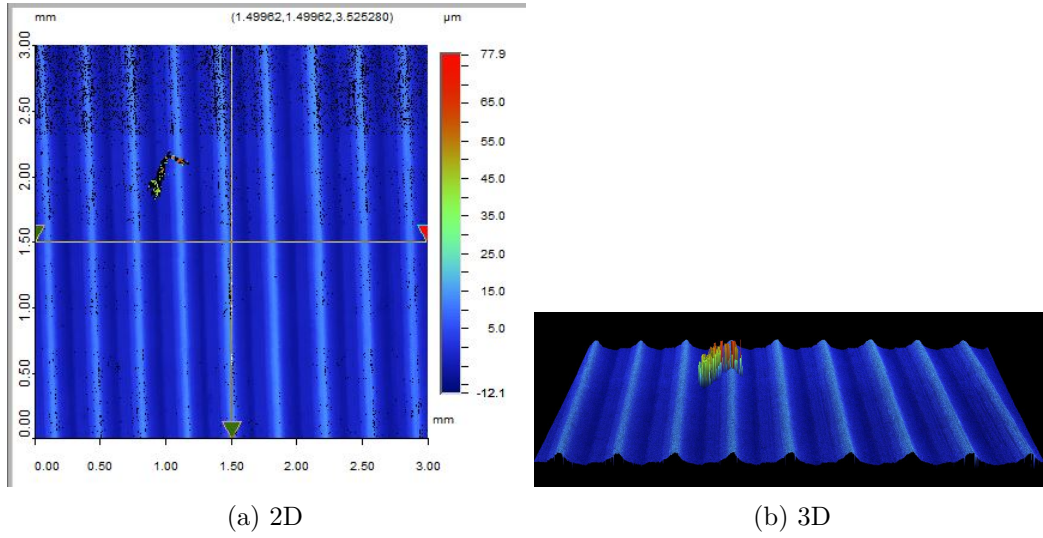
Figure A.24: The surface texture of `AT4`

(a) 2D

(b) 3D
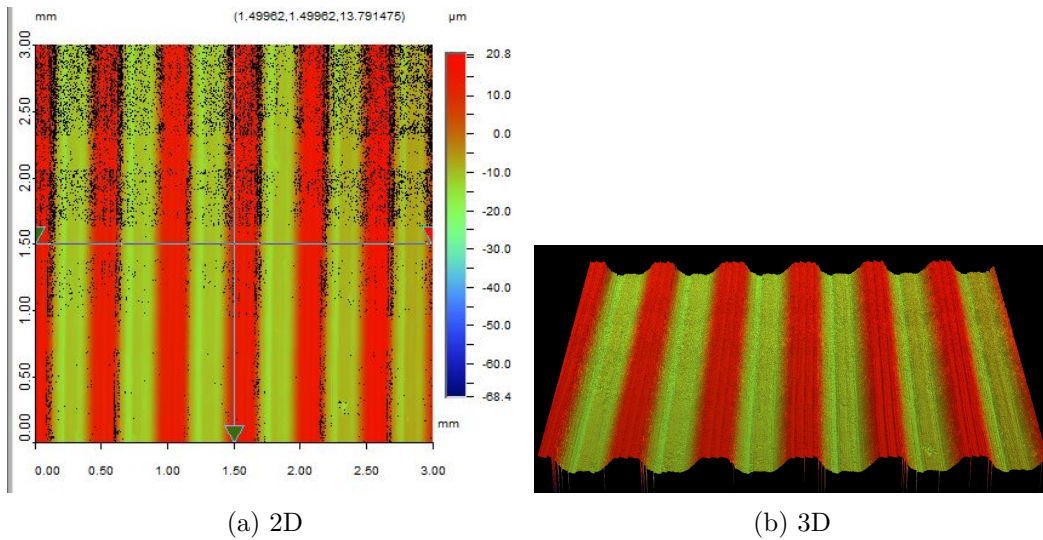
Figure A.25: The surface texture of `AT5`

209

(a) 2D

(b) 3D
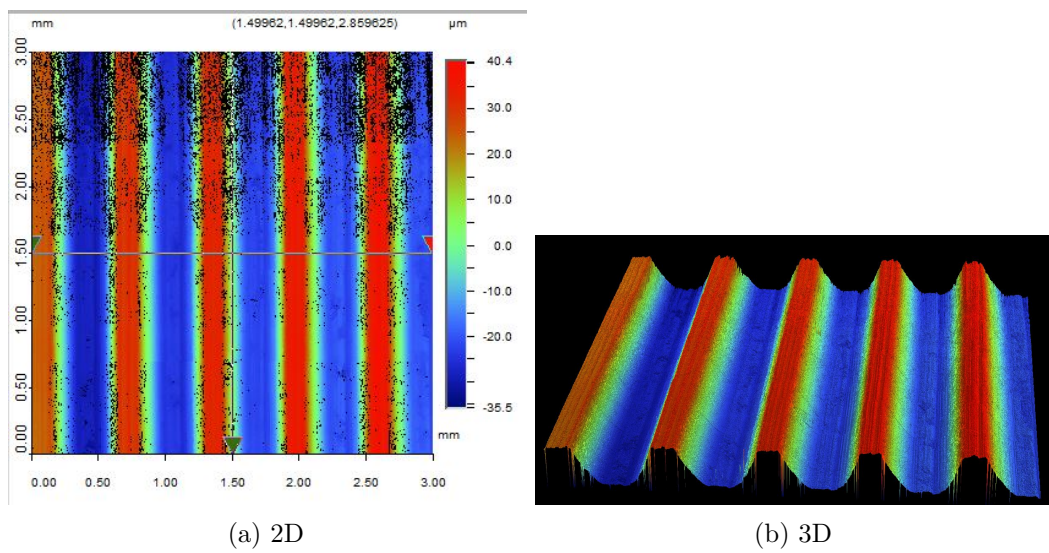
Figure A.26: The surface texture of `AT6`

Steel samples

(a) 2D   (b) 3D
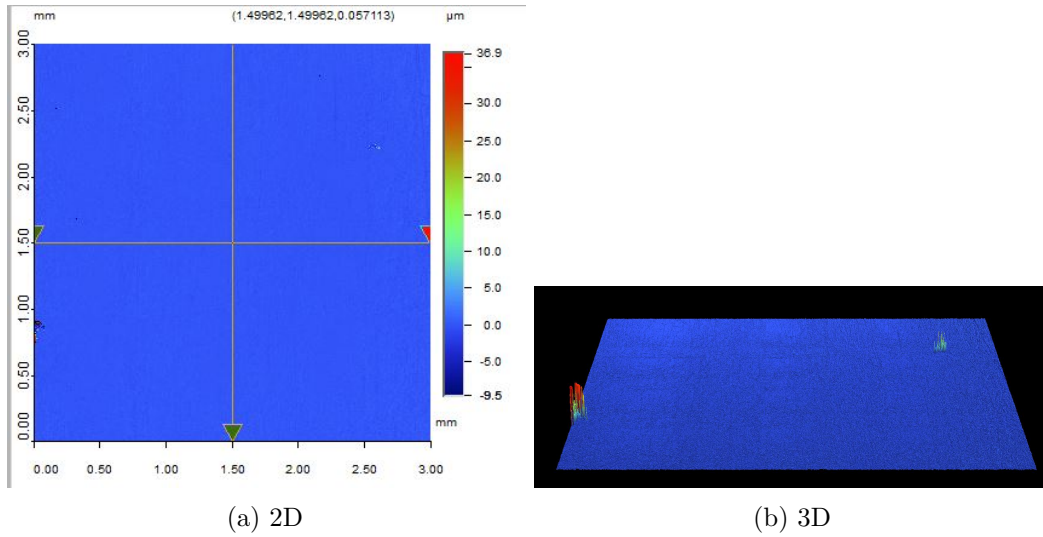
Figure A.27: The surface texture of S1

(a) 2D   (b) 3D
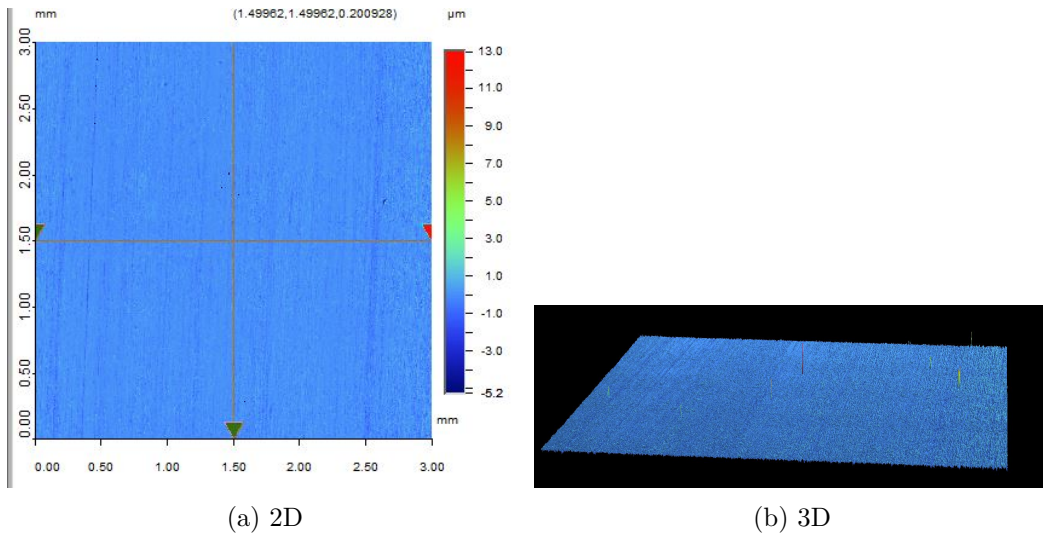
Figure A.28: The surface texture of S2

A.4.2   Thermoplastic Samples

The surface topography textures of the various thermoplastic samples are as follows.

211

(a) 2D

(b) 3D
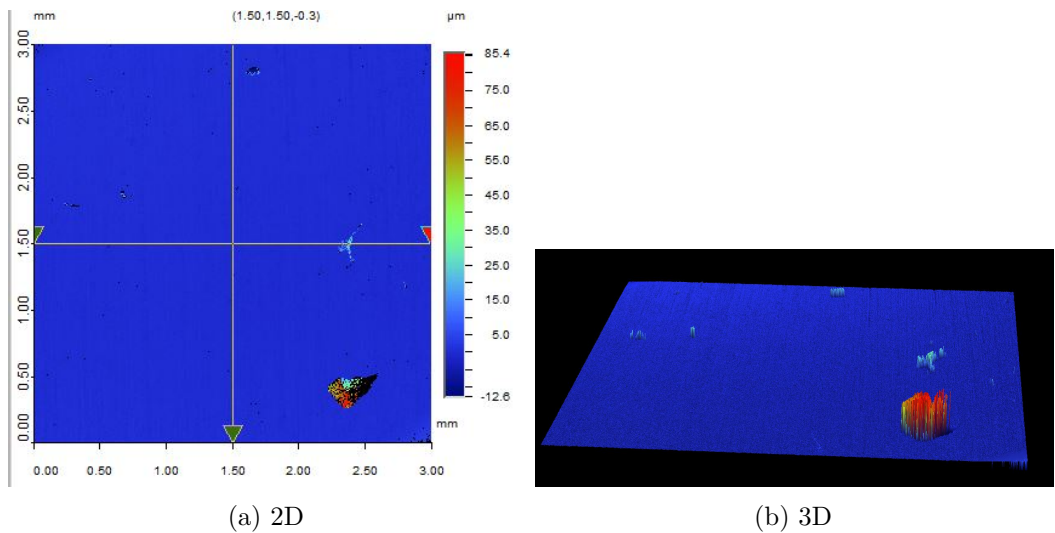
Figure A.29: The surface texture of S3

(a) 2D

(b) 3D
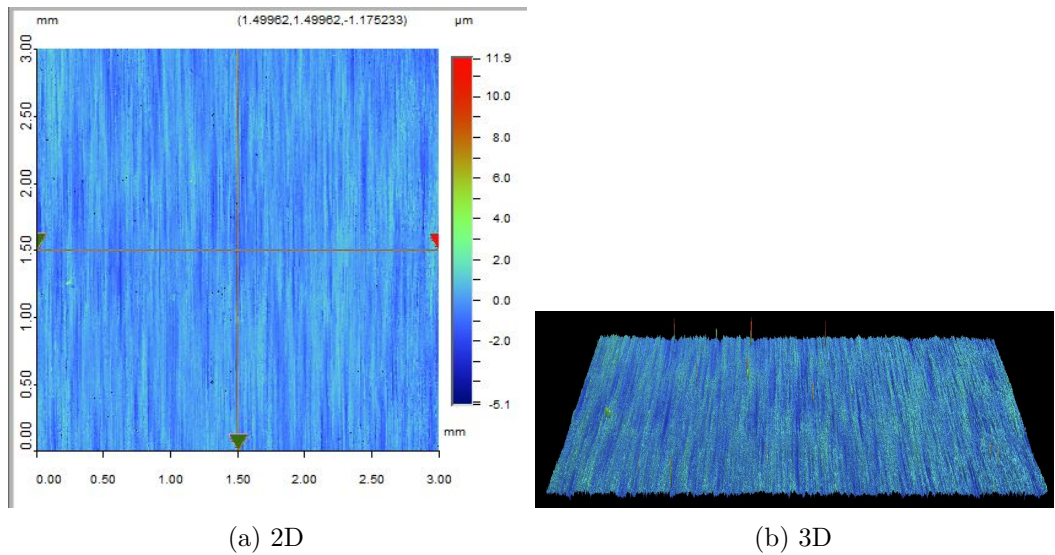
Figure A.30: The surface texture of S4

(a) 2D

(b) 3D
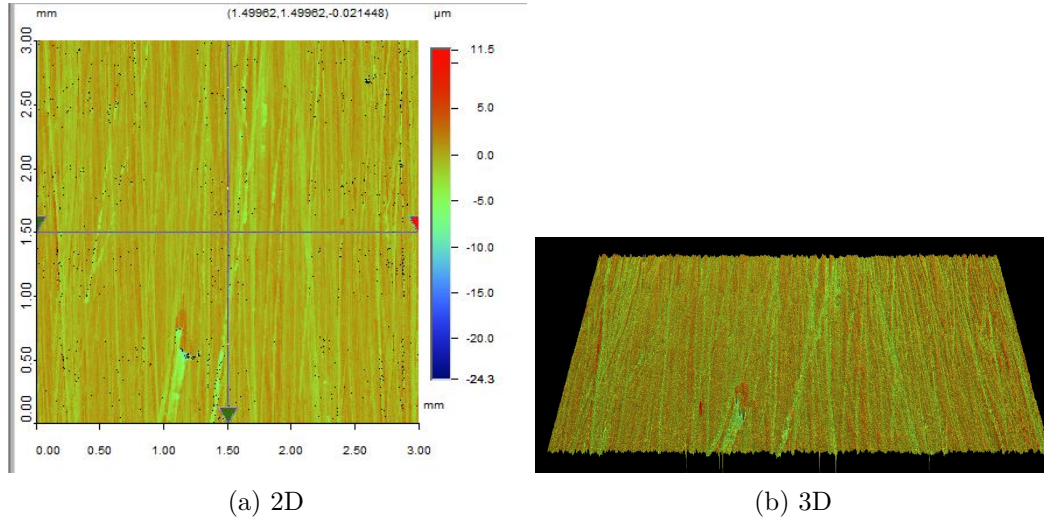
Figure A.31: The surface texture of S5

(a) 2D

(b) 3D
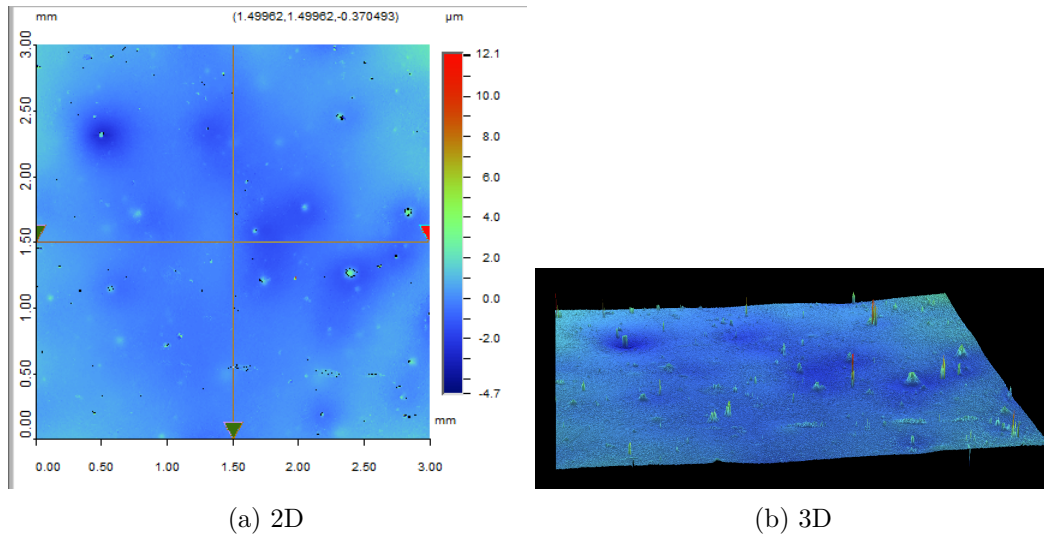
Figure A.32: The surface texture of s44

(a) 2D

(b) 3D

Figure A.33: The surface texture of s58

(a) 2D

(b) 3D
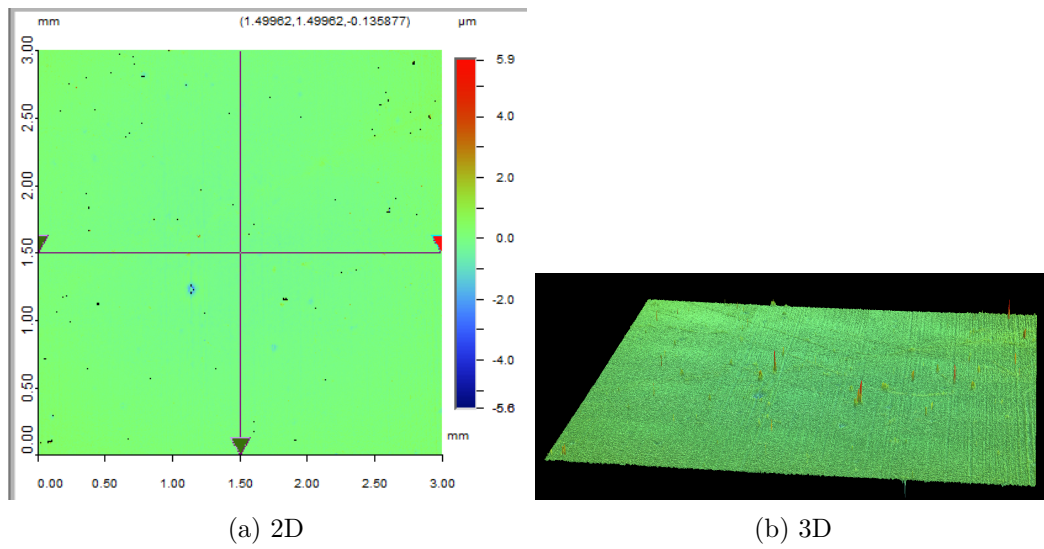
Figure A.34: The surface texture of s83

(a) 2D

(b) 3D

Figure A.35: The surface texture of `s97`

Coated samples

Patterned Samples

(a) 2D

(b) 3D
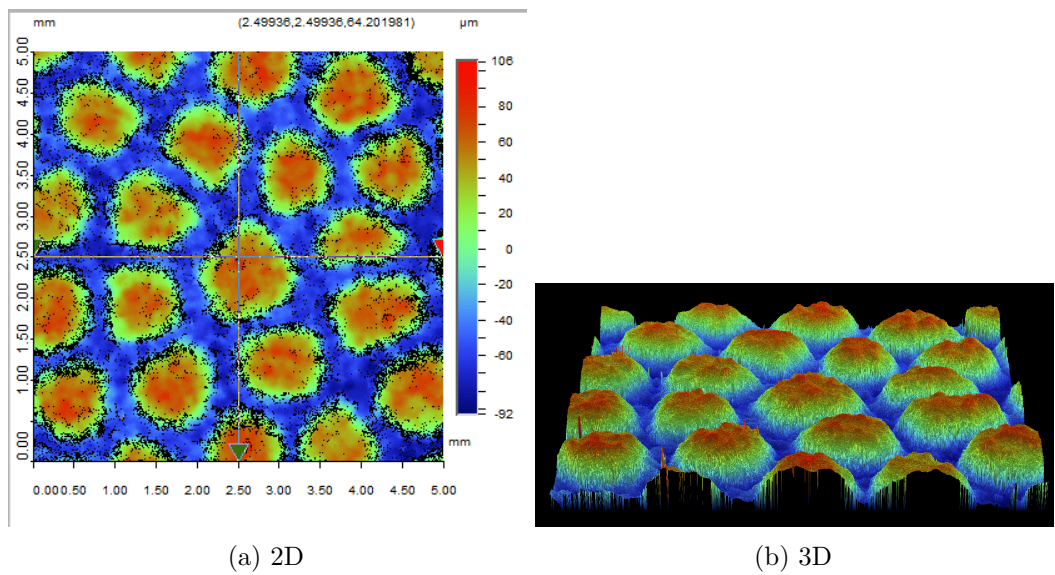
Figure A.36: The surface texture of `4N127`

A.5 The height distribution of different surfaces

215

(a) 2D

(b) 3D
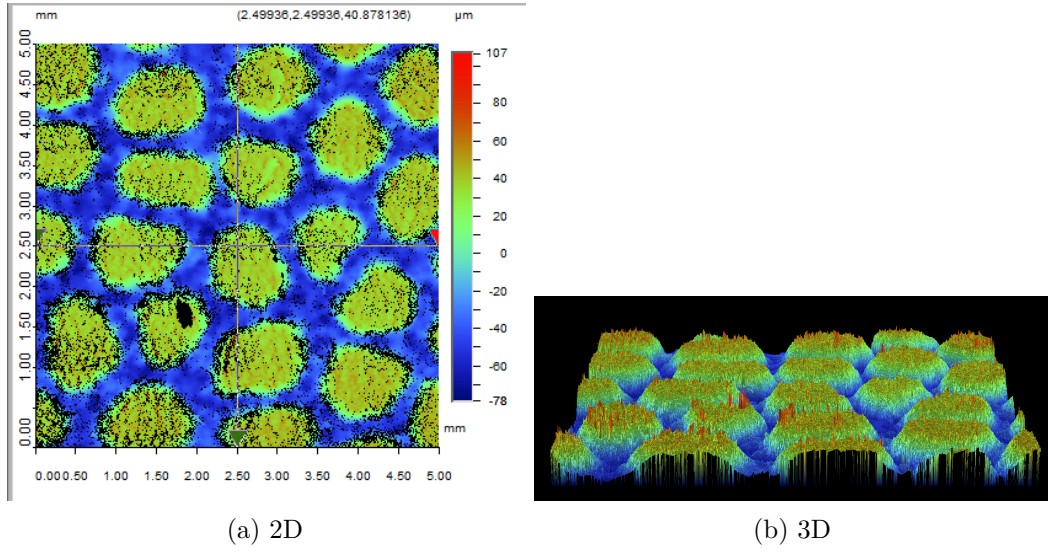
Figure A.37: The surface texture of sanded `4N127`

(a) 2D

(b) 3D
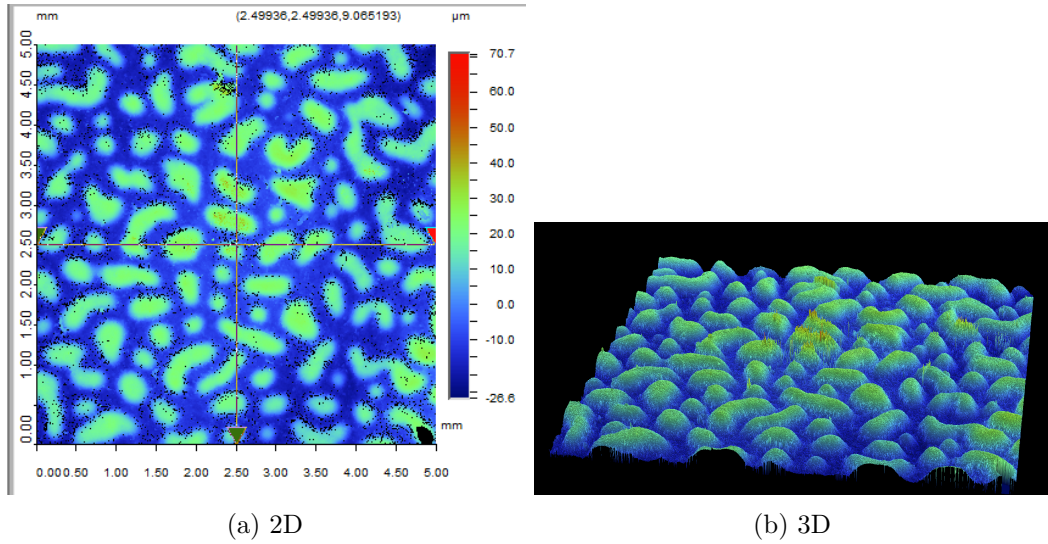
Figure A.38: The surface texture of `4N111`

(a) 2D

(b) 3D
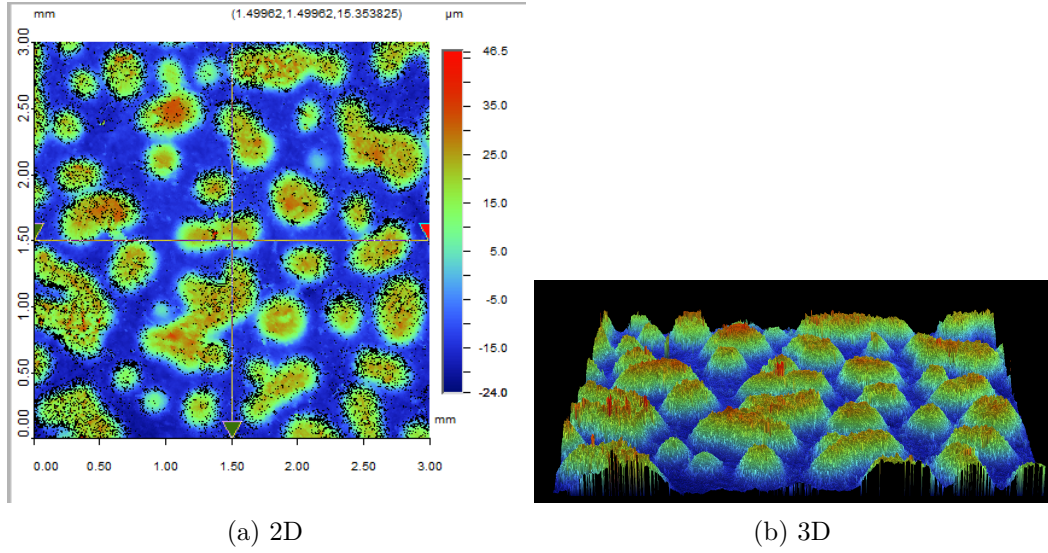
Figure A.39: The surface texture of sanded 4N111

(a) 2D

(b) 3D
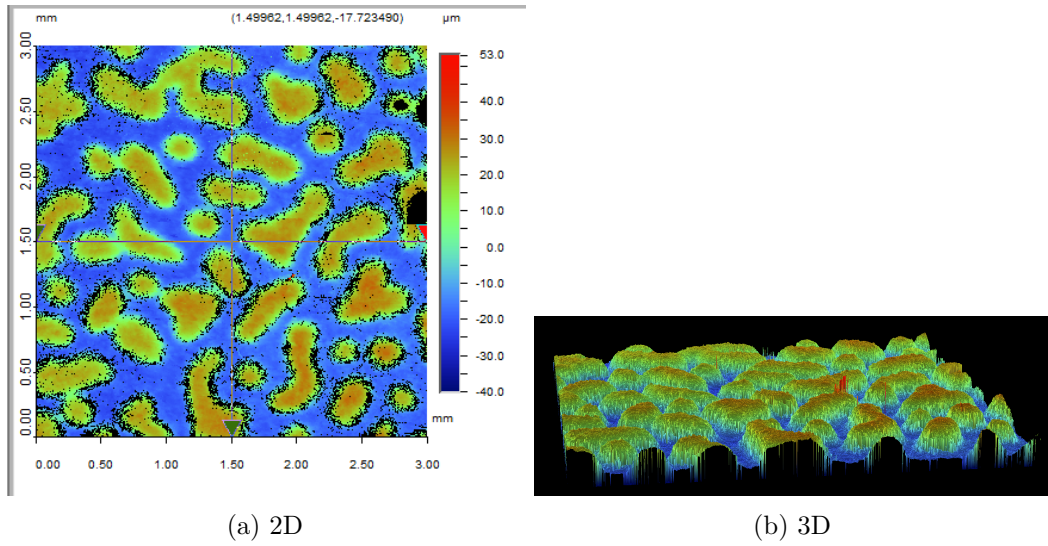
Figure A.40: The surface texture of 1N111

217

(a) 2D (b) 3D
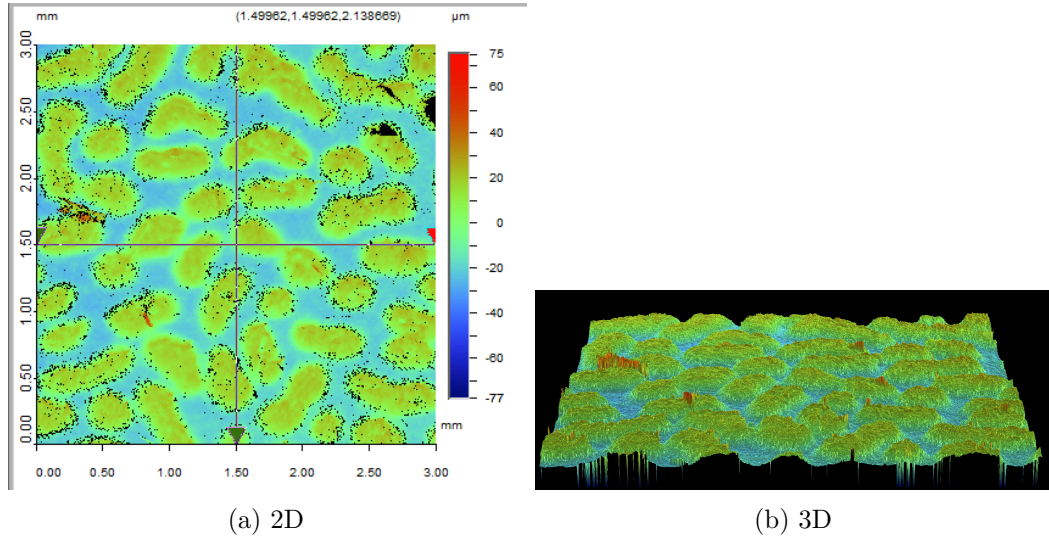
Figure A.41: The surface texture of sanded `1N111`

(a) 2D (b) 3D
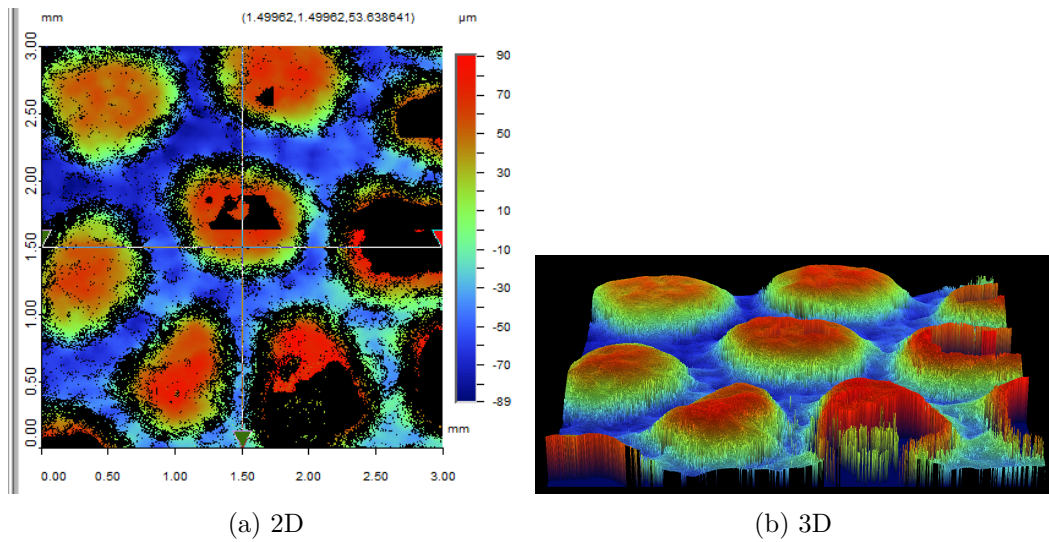
Figure A.42: The surface texture of `5N127`

218

(a) 2D

(b) 3D
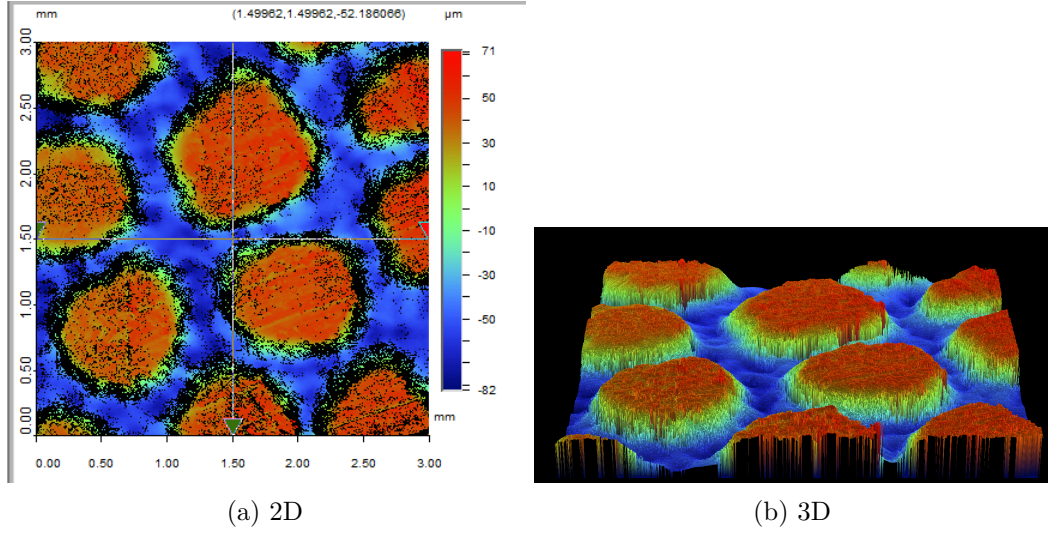
Figure A.43: The surface texture of sanded `5N127`

(a) 2D

(b) 3D
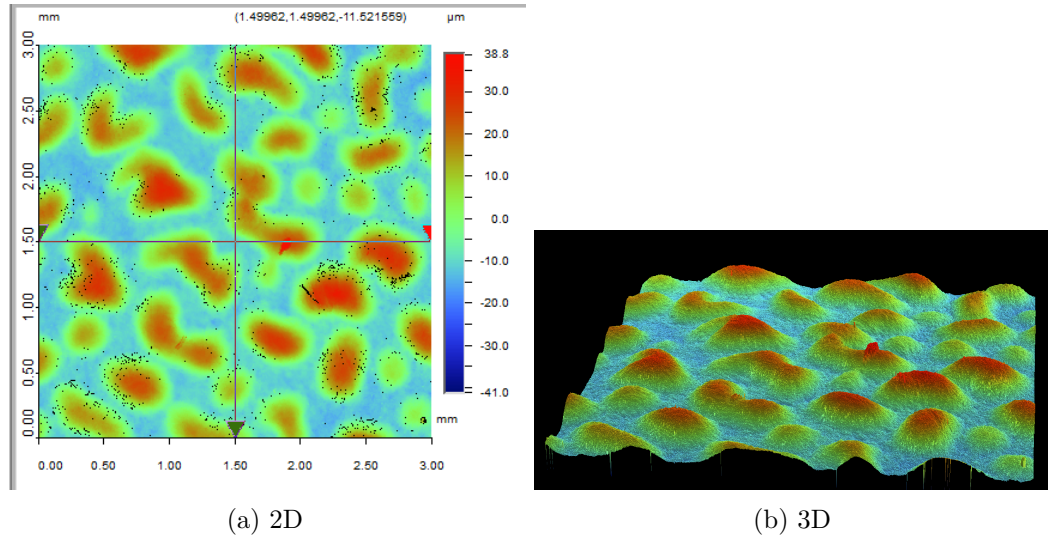
Figure A.44: The surface texture of `5N111`

(a) 2D

(b) 3D
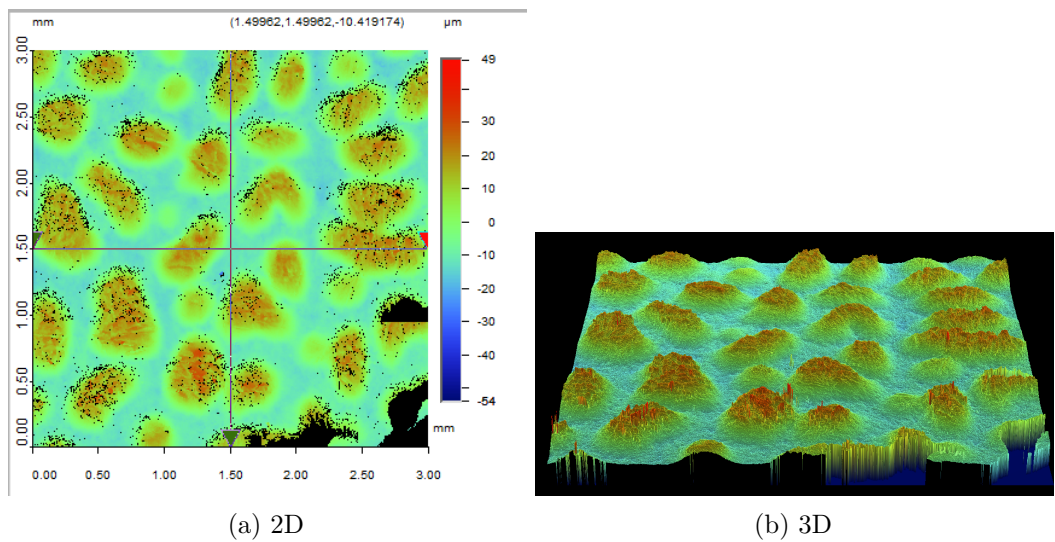
Figure A.45: The surface texture of sanded `5N111`

(a) AM1

(b) AM2

(c) AM3

(d) AM4

(e) AM5

(f) AM6

Figure A.46: The surface height distributions of the milled aluminium samples

(a) t0.4

(b) t1

(c) t33

(d) t46

(e) t79

Figure A.47: The surface height distributions of the turned aluminium samples

(a) S1

(b) S2

(c) S3

(d) S4

(e) S5

Figure A.48: The surface height distributions of the grinded steel samples

(a) `s44`

(b) `s58`

(c) `s83`

(d) `s97`

(e) `S97R`

Figure A.49: The surface height distributions of coated polymer samples

A.6 Touch-feel ranking raw data

This section lists the raw ranking data for the subjective touch-feel perception of 14 subjects. A lower ranking means the subject preferred the first word of

the psychophysical descriptor. This table include additional material samples 2S (2Stipple) and 3S (3Stipple) from Yue [32].

Table A.2: Smooth/rough touch-feel perception raw ranking data on TPE samples

Participant	s44	s58	s83	s97	3S	3S	4N111	5N111	1N111
1	4	3	2	1	7	9	5	8	6
2	3	1	2	4	6	9	5	8	7
3	3	1	4	2	5	8	7	9	6
4	3	4	1	2	7	9	8	5	6
5	4	2	1	3	8	7	5	9	6
6	2	1	4	5	6	7	3	8	9
7	3	1	2	4	7	8	6	9	5
8	2	1	3	4	5	7	9	6	8
9	2	1	3	4	5	7	9	8	6
10	2	1	4	3	8	9	6	7	5
11	1	4	2	3	6	7	9	8	5
12	1	2	4	3	9	8	7	6	5
13	1	2	3	4	7	9	5	8	6
14	2	3	4	1	8	9	5	7	6

Table A.3: Soft/hard touch-feel perception raw ranking data on TPE samples

Participant	s44	s58	s83	s97	3S	3S	4N111	5N111	1N111
1	2	4	3	1	7	9	5	8	6
2	6	9	5	3	4	8	1	7	2
3	2	6	5	1	4	7	8	9	3
4	4	5	3	6	2	8	1	7	9
5	2	7	8	9	1	5	4	3	6
6	1	2	3	4	5	7	9	8	6
7	4	1	3	2	6	7	5	8	9
8	2	3	1	4	7	6	5	9	8
9	2	5	4	1	6	8	3	7	9
10	1	6	6	6	6	6	6	6	2
11	9	7	8	6	5	3	1	2	4
12	3	5	6	7	2	8	1	9	4
13	1	2	4	3	6	5	7	8	9
14	8	7	6	3	2	5	1	4	9

Table A.4: Cool/warm touch-feel perception raw ranking data on TPE samples

Participant	s44	s58	s83	s97	3S	3S	4N111	5N111	1N111
1	2	4	3	1	7	9	8	6	5
2	1	3	4	5	7	2	8	6	9
3	7	8	5	9	3	4	1	6	2
4	2	4	1	3	8	6	5	7	9
5	1	2	4	3	6	5	9	7	8
6	2	3	1	4	5	8	9	7	6
7	1	3	2	4	6	5	7	9	8
8	3	4	2	1	6	8	7	9	5
9	-	-	-	-	-	-	-	-	-
10	1	3	2	4	7	7	7	7	7
11	1	2	4	3	5	6	9	8	7
12	1	3	2	4	6	5	8	7	9
13	3	1	6	5	8	4	2	9	7
14	5	6	1	2	7	8	9	3	4

Table A.5: Slippery/sticky touch-feel perception raw ranking data on TPE samples

Participant	s44	s58	s83	s97	3S	3S	4N111	5N111	1N111
1	3	2	4	1	7	6	9	8	5
2	2	1	4	8	5	6	9	3	7
3	2	7	4	1	5	8	9	6	3
4	4	3	1	2	7	8	9	6	5
5	8	7	9	-	1	2	-	3	4
6	2	3	1	4	7	8	9	6	5
7	1	4	2	3	5	6	9	8	7
8	2	4	3	1	5	7	8	9	6
9	2	1	3	5	7	4	9	8	6
10	4	1	3	2	6	7	9	5	8
11	1	3	2	4	5	8	9	7	6
12	2	1	3	4	7	8	9	5	6
13	3	1	2	5	4	6	9	7	8
14	8	6	7	2	5	4	1	3	9

Table A.6: Like/dislike touch-feel perception raw ranking data on TPE samples

Participant	s44	s58	s83	s97	3S	3S	4N111	5N111	1N111
1	5	4	6	1	8	9	2	3	7
2	8	2	7	4	3	1	9	5	6
3	2	4	3	1	8	7	9	5	6
4	2	3	4	1	6	5	9	8	7
5	9	8	7	6	1	2	3	4	5
6	3	2	1	5	6	7	9	8	4
7	1	4	2	3	6	5	9	8	7
8	5	8	7	9	6	2	4	1	3
9	-	-	-	-	-	-	-	-	-
10	1	3	4	2	7	7	7	7	7
11	1	3	2	4	5	6	9	8	7
12	2	1	3	4	5	6	7	9	8
13	2	1	4	3	5	6	9	8	7
14	6	7	1	9	2	3	5	8	4

A.7   Rank ordered logit model outputs

This section contains the raw output from Stata software.

A.7.1 Smooth/rough

```
      rank |     Coef.   Std. Err.      z    P>|z|     [95% Conf. Interval]
-------------+----------------------------------------------------------------
        sa |   .1768571   .0210967     8.38   0.000     .1355083    .2182059


-------------------------------------------------------------------------------
      rank |     Coef.   Std. Err.      z    P>|z|     [95% Conf. Interval]
-------------+----------------------------------------------------------------
  skunounit | -.0025742   .0008692    -2.96   0.003    -.0042777   -.0008707
-------------------------------------------------------------------------------


      rank |     Coef.   Std. Err.      z    P>|z|     [95% Conf. Interval]
-------------+----------------------------------------------------------------
        sp |   .0421991   .0046873     9.00   0.000     .0330122     .051386


      rank |     Coef.   Std. Err.      z    P>|z|     [95% Conf. Interval]
-------------+----------------------------------------------------------------
        sq |   .1748451    .020858     8.38   0.000     .1339642     .215726


      rank |     Coef.   Std. Err.      z    P>|z|     [95% Conf. Interval]
-------------+----------------------------------------------------------------
  ssknounit |  -.077455   .0183808    -4.21   0.000    -.1134807   -.0414293


      rank |     Coef.   Std. Err.      z    P>|z|     [95% Conf. Interval]
-------------+----------------------------------------------------------------
        sv | -.0928602     .01019    -9.11   0.000    -.1128322   -.0728882
-------------------------------------------------------------------------------


      rank |     Coef.   Std. Err.      z    P>|z|     [95% Conf. Interval]
-------------+----------------------------------------------------------------
        sz |   .0346574   .0035288     9.82   0.000     .0277411    .0415737


      rank |     Coef.   Std. Err.      z    P>|z|     [95% Conf. Interval]
-------------+----------------------------------------------------------------
     sdqdeg |   .0985392   .0111322     8.85   0.000     .0767206    .1203579


      rank |     Coef.   Std. Err.      z    P>|z|     [95% Conf. Interval]
-------------+----------------------------------------------------------------
       rda |   .3574194   .0420403     8.50   0.000     .2750218    .4398169


-------------------------------------------------------------------------------
      rank |     Coef.   Std. Err.      z    P>|z|     [95% Conf. Interval]
-------------+----------------------------------------------------------------
      egpa |  -1.036071   .1300179    -7.97   0.000    -1.290902    -.781241
-------------------------------------------------------------------------------


      rank |     Coef.   Std. Err.      z    P>|z|     [95% Conf. Interval]
-------------+----------------------------------------------------------------
      hmpa | -.0123763   .0015743    -7.86   0.000    -.0154619   -.0092907
-------------------------------------------------------------------------------


      rank |     Coef.   Std. Err.      z    P>|z|     [95% Conf. Interval]
-------------+----------------------------------------------------------------
      smum |   .0059777   .0006757     8.85   0.000     .0046533    .0073022
```

229

A.7. Rank ordered logit model outputs

```
         rank |    Coef.   Std. Err.     z    P>|z|    [95% Conf. Interval]
--------------+----------------------------------------------------------------
humanfingertip |  1.617537   .2140939    7.56   0.000    1.197921    2.037154


         rank |    Coef.   Std. Err.     z    P>|z|    [95% Conf. Interval]
--------------+----------------------------------------------------------------
      f05n5mms |  1.886903   .5087345    3.71   0.000    .8898017    2.884004


         rank |    Coef.   Std. Err.     z    P>|z|    [95% Conf. Interval]
--------------+----------------------------------------------------------------
     f075n5mms |  1.614054   .5474985    2.95   0.003    .5409764    2.687131
--------------------------------------------------------------------------------



--------------------------------------------------------------------------------
         rank |    Coef.   Std. Err.     z    P>|z|    [95% Conf. Interval]
--------------+----------------------------------------------------------------
      f05n8mms |  .4936133   .4587409    1.08   0.282   -.4055024    1.392729
--------------------------------------------------------------------------------
         rank |    Coef.   Std. Err.     z    P>|z|    [95% Conf. Interval]
--------------+----------------------------------------------------------------
     f075n8mms | -11.28523   1.197521   -9.42   0.000   -13.63232   -8.938128
--------------------------------------------------------------------------------
```

A.7.2 Soft/hard

```
   Soft-Hard

  rank |     Coef.   Std. Err.      z    P>|z|     [95% Conf. Interval]
-------------+----------------------------------------------------------------
        sa |  -.0157454   .0081792    -1.93   0.054    -.0317763    .0002854


-------------+----------------------------------------------------------------
      rank |     Coef.   Std. Err.      z    P>|z|     [95% Conf. Interval]
-------------+----------------------------------------------------------------
  skunounit |  -.0006424   .0008328    -0.77   0.440    -.0022748    .0009899
-------------+----------------------------------------------------------------


-------------+----------------------------------------------------------------
      rank |     Coef.   Std. Err.      z    P>|z|     [95% Conf. Interval]
-------------+----------------------------------------------------------------
        sp |  -.0179318   .0039028    -4.59   0.000    -.0255811   -.0102825


      rank |     Coef.   Std. Err.      z    P>|z|     [95% Conf. Interval]
-------------+----------------------------------------------------------------
        sq |  -.0155276   .0077085    -2.01   0.044    -.0306359   -.0004193


      rank |     Coef.   Std. Err.      z    P>|z|     [95% Conf. Interval]
-------------+----------------------------------------------------------------
  ssknounit |  -.0104221    .018052    -0.58   0.564    -.0458034    .0249593


      rank |     Coef.   Std. Err.      z    P>|z|     [95% Conf. Interval]
-------------+----------------------------------------------------------------
        sv |   .0070789   .0042153     1.68   0.093     -.001183    .0153408


      rank |     Coef.   Std. Err.      z    P>|z|     [95% Conf. Interval]
-------------+----------------------------------------------------------------
        sz |  -.0077923    .002247    -3.47   0.001    -.0121963   -.0033883


-------------+----------------------------------------------------------------
      rank |     Coef.   Std. Err.      z    P>|z|     [95% Conf. Interval]
-------------+----------------------------------------------------------------
       Sdq |  -.0269975   .0087813    -3.07   0.002    -.0442085   -.0097865


      rank |     Coef.   Std. Err.      z    P>|z|     [95% Conf. Interval]
-------------+----------------------------------------------------------------
       rda |  -.0729725   .0248448    -2.94   0.003    -.1216675   -.0242776


-------------+----------------------------------------------------------------
      rank |     Coef.   Std. Err.      z    P>|z|     [95% Conf. Interval]
-------------+----------------------------------------------------------------
      egpa |   .3907037   .1168124     3.34   0.001     .1617556    .6196518


      rank |     Coef.   Std. Err.      z    P>|z|     [95% Conf. Interval]
-------------+----------------------------------------------------------------
      hmpa |   .0034152   .0014752     2.32   0.021     .0005239    .0063066


-------------+----------------------------------------------------------------
      rank |     Coef.   Std. Err.      z    P>|z|     [95% Conf. Interval]
```

A.7. Rank ordered logit model outputs

```
-------------+------------------------------------------------------------
       smum |  -.0000869   .0002965    -0.29   0.769    -.000668    .0004942
-------------+------------------------------------------------------------
```

```
------------------------------------------------------------------------------
        rank |     Coef.   Std. Err.      z    P>|z|    [95% Conf. Interval]
--------------+---------------------------------------------------------------
humanfingertip |  -.9117715   .2425994    -3.76   0.000    -1.387258    -.4362854
```

```
------------------------------------------------------------------------------
        rank |     Coef.   Std. Err.      z    P>|z|    [95% Conf. Interval]
-------------+----------------------------------------------------------------
     f05n5mms |  -1.229405   .5831025    -2.11   0.035    -2.372265    -.0865448
------------------------------------------------------------------------------
```

```
        rank |     Coef.   Std. Err.      z    P>|z|    [95% Conf. Interval]
-------------+----------------------------------------------------------------
    f075n5mms |  -.4293775   .5651098    -0.76   0.447    -1.536972    .6782174
```

```
        rank |     Coef.   Std. Err.      z    P>|z|    [95% Conf. Interval]
-------------+----------------------------------------------------------------
     f05n8mms |  -.1393298   .4681834    -0.30   0.766    -1.056952    .7782927
```

```
------------------------------------------------------------------------------
        rank |     Coef.   Std. Err.      z    P>|z|    [95% Conf. Interval]
-------------+----------------------------------------------------------------
    f075n8mms |   2.461545   .9034179     2.72   0.006     .6908782    4.232211
```

A.7.3   Cool/warm

Cool/warm

rank	Coef.	Std. Err.	z	P>|z|	[95% Conf. Interval]	
sa	.0193054	.0081463	2.37	0.018	.003339	.0352718

rank	Coef.	Std. Err.	z	P>|z|	[95% Conf. Interval]	
skunounit	-.0017034	.0008734	-1.95	0.051	-.0034152	8.52e-06

rank	Coef.	Std. Err.	z	P>|z|	[95% Conf. Interval]	
sp	.0112156	.0036578	3.07	0.002	.0040464	.0183847

rank	Coef.	Std. Err.	z	P>|z|	[95% Conf. Interval]	
sq	.0189439	.0076633	2.47	0.013	.0039241	.0339638

rank	Coef.	Std. Err.	z	P>|z|	[95% Conf. Interval]	
ssknounit	-.0463632	.0181054	-2.56	0.010	-.0818491	-.0108773

rank	Coef.	Std. Err.	z	P>|z|	[95% Conf. Interval]	
sv	-.0116984	.0043305	-2.70	0.007	-.0201859	-.0032108

rank	Coef.	Std. Err.	z	P>|z|	[95% Conf. Interval]	
sz	.0064677	.0021084	3.07	0.002	.0023353	.0106001

rank	Coef.	Std. Err.	z	P>|z|	[95% Conf. Interval]	
sdqdeg	.0392902	.0088375	4.45	0.000	.0219691	.0566113

rank	Coef.	Std. Err.	z	P>|z|	[95% Conf. Interval]	
rda	.1425981	.0268104	5.32	0.000	.0900507	.1951455

rank	Coef.	Std. Err.	z	P>|z|	[95% Conf. Interval]	
egpa	-.6547415	.1227156	-5.34	0.000	-.8952596	-.4142233

rank	Coef.	Std. Err.	z	P>|z|	[95% Conf. Interval]	
hmpa	-.0085575	.0015322	-5.59	0.000	-.0115605	-.0055544

233

A.7. Rank ordered logit model outputs

```
        rank |     Coef.   Std. Err.      z     P>|z|    [95% Conf. Interval]
-------------+----------------------------------------------------------------
        smum |   .0010795   .0002468     4.37   0.000     .0005957    .0015633


        rank |     Coef.   Std. Err.      z     P>|z|    [95% Conf. Interval]
-------------+----------------------------------------------------------------
humanfingertip |  1.183851   .2241171     5.28   0.000     .7445897    1.623113


-----------------------------------------------------------------------------
        rank |     Coef.   Std. Err.      z     P>|z|    [95% Conf. Interval]
-------------+----------------------------------------------------------------
     f05n5mms |  1.122841   .5453434     2.06   0.039     .0539872    2.191694
-----------------------------------------------------------------------------


        rank |     Coef.   Std. Err.      z     P>|z|    [95% Conf. Interval]
-------------+----------------------------------------------------------------
    f075n5mms |  1.248937   .5646989     2.21   0.027     .1421472    2.355726
        rank |     Coef.   Std. Err.      z     P>|z|    [95% Conf. Interval]
-------------+----------------------------------------------------------------
     f05n8mms |  .5878243   .4583948     1.28   0.200    -.3106129    1.486262


        rank |     Coef.   Std. Err.      z     P>|z|    [95% Conf. Interval]
-------------+----------------------------------------------------------------
    f075n8mms | -2.832103   .8644471    -3.28   0.001    -4.526388   -1.137818
```

A.7.4 Slippery/sticky

```
      rank |     Coef.   Std. Err.      z    P>|z|     [95% Conf. Interval]
-------------+----------------------------------------------------------------
        sa |   .0187009   .0083168     2.25   0.025     .0024003    .0350016


      rank |     Coef.   Std. Err.      z    P>|z|     [95% Conf. Interval]
-------------+----------------------------------------------------------------
  skunounit | -.0003995   .0008438    -0.47   0.636    -.0020534    .0012543


      rank |     Coef.   Std. Err.      z    P>|z|     [95% Conf. Interval]
-------------+----------------------------------------------------------------
        sp |   .0149081   .0039646     3.76   0.000     .0071376    .0226786


-------------------------------------------------------------------------------
      rank |     Coef.   Std. Err.      z    P>|z|     [95% Conf. Interval]
-------------+----------------------------------------------------------------
        sq |   .0184435   .0078594     2.35   0.019     .0030392    .0338477
-------------------------------------------------------------------------------


-------------------------------------------------------------------------------
      rank |     Coef.   Std. Err.      z    P>|z|     [95% Conf. Interval]
-------------+----------------------------------------------------------------
  ssknounit | -.0225969   .0184969    -1.22   0.222    -.0588503    .0136564


      rank |     Coef.   Std. Err.      z    P>|z|     [95% Conf. Interval]
-------------+----------------------------------------------------------------
        sv | -.0106285    .004462    -2.38   0.017    -.0193739    -.001883
-------------------------------------------------------------------------------
      rank |     Coef.   Std. Err.      z    P>|z|     [95% Conf. Interval]
-------------+----------------------------------------------------------------
        sz |   .0074487   .0022384     3.33   0.001     .0030615    .0118359


-------------------------------------------------------------------------------
      rank |     Coef.   Std. Err.      z    P>|z|     [95% Conf. Interval]
-------------+----------------------------------------------------------------
    sdqdeg |   .0272854   .0087163     3.13   0.002     .0102018     .044369
-------------------------------------------------------------------------------


-------------------------------------------------------------------------------
      rank |     Coef.   Std. Err.      z    P>|z|     [95% Conf. Interval]
-------------+----------------------------------------------------------------
       rda |   .0935822     .02644     3.54   0.000     .0417607    .1454037
-------------------------------------------------------------------------------


-------------------------------------------------------------------------------
      rank |     Coef.   Std. Err.      z    P>|z|     [95% Conf. Interval]
-------------+----------------------------------------------------------------
      egpa | -.4531487   .1270893    -3.57   0.000    -.7022392   -.2040583


-------------------------------------------------------------------------------
      rank |     Coef.   Std. Err.      z    P>|z|     [95% Conf. Interval]
-------------+----------------------------------------------------------------
      hmpa |  -.006399   .0015738    -4.07   0.000    -.0094836   -.0033144
-------------------------------------------------------------------------------
```

A.7. Rank ordered logit model outputs

```
------------------------------------------------------------------------------
        rank |      Coef.   Std. Err.      z    P>|z|     [95% Conf. Interval]
-------------+----------------------------------------------------------------
        smum |    .000988   .0002569     3.85   0.000     .0004845    .0014915
------------------------------------------------------------------------------
```

```
------------------------------------------------------------------------------
         rank |      Coef.   Std. Err.      z    P>|z|     [95% Conf. Interval]
--------------+---------------------------------------------------------------
humanfingertip |   1.199367   .2508925     4.78   0.000     .7076273    1.691108
------------------------------------------------------------------------------
```

```
------------------------------------------------------------------------------
        rank |      Coef.   Std. Err.      z    P>|z|     [95% Conf. Interval]
-------------+----------------------------------------------------------------
     f05n5mms |   1.363528   .5286251     2.58   0.010     .3274413    2.399614
------------------------------------------------------------------------------
```

```
------------------------------------------------------------------------------
        rank |      Coef.   Std. Err.      z    P>|z|     [95% Conf. Interval]
-------------+----------------------------------------------------------------
    f075n5mms |   1.095117    .565245     1.94   0.053    -.0127426    2.202977
------------------------------------------------------------------------------
```

```
------------------------------------------------------------------------------
        rank |      Coef.   Std. Err.      z    P>|z|     [95% Conf. Interval]
-------------+----------------------------------------------------------------
     f05n8mms |   .8611865   .4706108     1.83   0.067    -.0611936    1.783567
------------------------------------------------------------------------------
```

```
------------------------------------------------------------------------------
        rank |      Coef.   Std. Err.      z    P>|z|     [95% Conf. Interval]
-------------+----------------------------------------------------------------
    f075n8mms |  -2.478857   .9105878    -2.72   0.006    -4.263576   -.6941372
------------------------------------------------------------------------------
```

A.7.5   Like/dislike

```
------------------------------------------------------------------------
      rank |      Coef.   Std. Err.      z    P>|z|     [95% Conf. Interval]
-------------+----------------------------------------------------------
        sa |  -.0032496    .008358    -0.39   0.697    -.0196309    .0131317


------------------------------------------------------------------------
      rank |      Coef.   Std. Err.      z    P>|z|     [95% Conf. Interval]
-------------+----------------------------------------------------------
 skunounit |   .0011956   .0007868     1.52   0.129    -.0003465    .0027377


------------------------------------------------------------------------
      rank |      Coef.   Std. Err.      z    P>|z|     [95% Conf. Interval]
-------------+----------------------------------------------------------
        sp |  -.0052275   .0035387    -1.48   0.140    -.0121633    .0017083
------------------------------------------------------------------------


------------------------------------------------------------------------
      rank |      Coef.   Std. Err.      z    P>|z|     [95% Conf. Interval]
-------------+----------------------------------------------------------
        sq |  -.0037138   .0078453    -0.47   0.636    -.0190903    .0116626
------------------------------------------------------------------------


------------------------------------------------------------------------
      rank |      Coef.   Std. Err.      z    P>|z|     [95% Conf. Interval]
-------------+----------------------------------------------------------
 ssknounit |   .0292743   .0174032     1.68   0.093    -.0048354    .0633839


      rank |      Coef.   Std. Err.      z    P>|z|     [95% Conf. Interval]
-------------+----------------------------------------------------------
        sv |   .0021325   .0042304     0.50   0.614    -.0061589     .010424


      rank |      Coef.   Std. Err.      z    P>|z|     [95% Conf. Interval]
-------------+----------------------------------------------------------
        sz |   -.002325   .0020882    -1.11   0.266    -.0064179    .0017678


------------------------------------------------------------------------
      rank |      Coef.   Std. Err.      z    P>|z|     [95% Conf. Interval]
-------------+----------------------------------------------------------
    sdqdeg |  -.0083244     .00813    -1.02   0.306     -.024259    .0076102
------------------------------------------------------------------------


------------------------------------------------------------------------
      rank |      Coef.   Std. Err.      z    P>|z|     [95% Conf. Interval]
-------------+----------------------------------------------------------
       rda |   -.036923    .023376    -1.58   0.114    -.0827392    .0088932
------------------------------------------------------------------------


------------------------------------------------------------------------
      rank |      Coef.   Std. Err.      z    P>|z|     [95% Conf. Interval]
-------------+----------------------------------------------------------
      egpa |   .1264147   .1133936     1.11   0.265    -.0958327    .3486621
------------------------------------------------------------------------


------------------------------------------------------------------------
```

A.7. Rank ordered logit model outputs

```
       rank |     Coef.   Std. Err.      z    P>|z|    [95% Conf. Interval]
------------+----------------------------------------------------------------
       hmpa |   .0014538   .0015248     0.95   0.340    -.0015347    .0044424
----------------------------------------------------------------------------


       rank |     Coef.   Std. Err.      z    P>|z|    [95% Conf. Interval]
------------+----------------------------------------------------------------
       smum |  -.0002614    .000323    -0.81   0.418    -.0008945    .0003716
----------------------------------------------------------------------------


           rank |     Coef.   Std. Err.      z    P>|z|    [95% Conf. Interval]
---------------+-------------------------------------------------------------
humanfingertip |  -.7736414   .2410955    -3.21   0.001     -1.24618   -.3011028
-------------------------------------------------------------------------------


       rank |     Coef.   Std. Err.      z    P>|z|    [95% Conf. Interval]
------------+----------------------------------------------------------------
    f05n5mms |  -.4828978    .585076    -0.83   0.409    -1.629626    .6638302
----------------------------------------------------------------------------


       rank |     Coef.   Std. Err.      z    P>|z|    [95% Conf. Interval]
------------+----------------------------------------------------------------
   f075n5mms |   .0992003   .5922853     0.17   0.867    -1.061658    1.260058
----------------------------------------------------------------------------


       rank |     Coef.   Std. Err.      z    P>|z|    [95% Conf. Interval]
------------+----------------------------------------------------------------
    f05n8mms |  -.5309948   .4761112    -1.12   0.265    -1.464156     .402166
----------------------------------------------------------------------------


       rank |     Coef.   Std. Err.      z    P>|z|    [95% Conf. Interval]
------------+----------------------------------------------------------------
   f075n8mms |   .9106376   .8304582     1.10   0.273    -.7170306    2.538306
----------------------------------------------------------------------------
```

A.8 MATLAB program code to simulate a Greenwood-Williamson contact model

```matlab
% model Greenwood and Williamson (GW)
%function [p_g]=greenwood
%=================================================
%====Greenwood and Williamson Model====
%=================================================
%Input data:vector data_z with the roughness points and vector
%data_x with the respective coordinates
%Output data:percentage of contact real area ,deformation, plot with the
%original profile and deformed profile
N=1*10^3;    %the sample points
rL=10;       %the length of x
h=0.1;       %height
c1=0.05;     % variance
[data_z ,data_x]=rsgene1D(N,rL ,h,c1);
figure(1)
plot(data_x ,data_z);
x=data_x ;
rug=data_z ;
%load applied
load=1.9894;%N/mm
%properties of the material
H=2785;%Mpa
E1=205000;% Mpa
E2=62750; % Mpa(%Glass)
niu1=0.29;
niu2=0.2;
Ecom=1/((1-niu1^2)/E1+(1-niu2^2)/E2); %[MPa]
%rug is the vector with one profile of the roughness topography
%the profile will be approached by polynomial functions using the
%Aramki formulation
%determination of ACF(auto correlation function)length and the coefficient
%of ACF, ACF length is the length where autocorrelation is 0.368(=1/e)
[ACF,Lags ,Bounds]=autocorr(rug ,length(x)-1);
index_ACF_0368=1;
while ACF(index_ACF_0368)>0.368
    index_ACF_0368=index_ACF_0368+1;
end
%plot(x,ACF);%plot with the function of autocorrelation
length_ACF=x(index_ACF_0368)-x(1);
alfa=1/length_ACF ;
%standard deviation ;
sigma=std(rug);
%definition of a vector L_peak(peaks),obtained considering the cross with
%the reference line ;
n=length(x);
k=1;
for i=1:n-1
    if((rug(i)<=0)&(rug(i+1)>0));
        j=i+1;
        while((rug(j)>=0)&(j+1<n))
            if rug(j+1)<0
                Lpeak(k,1)=x(i)-rug(i)*(x(i+1)-x(i))/(rug(i+1)-rug(i));
                Lpeak(k,2)=x(j)-rug(j)*(x(j+1)-x(j))/(rug(j+1)-rug(j));
                L_peak(k)=Lpeak(k,2)-Lpeak(k,1);
                k=k+1;
            end
            j=j+1;
```

```matlab
            end
59      end
end
61 %defintion of a vector L_valley(valleys),obtained considering the cross
%with the reference line;
63 k=1;
for i=1:n-1
65      if((rug(i)>=0)&(rug(i+1)<0));
            j=i+1;
67          while ((rug(j)<=0)&(j+1<n))
                    if rug(j+1)>0
69                          Lvalley(k,1)=x(i)-rug(i)*(x(i+1)-x(i))/(rug(i+1)-rug(i));
                            Lvalley(k,2)=x(j)-rug(j)*(x(j+1)-x(j))/(rug(j+1)-rug(j));
71                          L_valley(k)=Lvalley(k,2)-Lvalley(k,1);
                            k=k+1;
73                  end
                    j=j+1;
75          end
      end
77 end
%create one vector with the x positions of the all crossings with the
79 %reference line
for i=1:(length(L_peak))
81      Lp(i)=Lpeak(i,1);
        Lp(i+length(L_peak))=Lpeak(i,2);
83 end
for i=1:(length(L_valley))
85      Lv(i)=Lvalley(i,1);
        Lv(i+length(L_valley))=Lvalley(i,2);
87 end
%vector x that contain all x positions(points of rough points and the
        crossings)
89 X=[];
X=[x';Lp';Lv'];
91 X=unique(X);
X=sort(X);
93
%create one new vector RUG with the same length that X
95 RUG=[];
for i=1:length(X)
97      for j=1:length(x)
            if X(i)==x(j)
99                  RUG(i)=rug(j); %the others positions RUG=0
            end
101     end
end
103 %generation of the one profile approach by parabolas
csi_peak=L_peak*sqrt(2/pi)*alfa*sigma; %equation 8 Aramki part I
105 csi_valley=L_valley*sqrt(2/pi)*alfa*sigma;
mean_L_peak=(mean(L_peak));
107 mean_L_valley=(mean(L_valley));
mean_L=1/2*(mean(L_peak)+mean(L_valley));
109 K1_peak=8*(csi_peak)./(L_peak.^2); %equation 9-b Aramki part I
K1_valley=8*(csi_valley)./(L_valley.^2);
111 %generation of the vector with points that represent parabolas
%start the vectors with zeros and the same length that X
113 parabola=zeros(1,length(X));
parabola_peak=zeros(1,length(X));
115 parabola_valley=zeros(1,length(X));
for i=1:length(L_peak)
117     j=find(X==(Lpeak(i,1)));
        while(X(j)>=Lpeak(i,1)&X(j)<=Lpeak(i,2))
119             parabola(j)=-(4*csi_peak(i)/(L_peak(i)^2))*(X(j)-Lpeak(i,1)-L_peak(i)
                    /2)^2+csi_peak(i);
```

```matlab
                parabola_peak(j)=parabola(j);
121             j=j+1;
        end
123 end
    for i=1:length(L_valley)
125     j=find(X==(Lvalley(i,1)));
        while (X(j)>=Lvalley(i,1)&X(j)<=Lvalley(i,2))
127         parabola(j)=(4*csi_valley(i)/(L_valley(i)^2))*(X(j)-Lvalley(i,1)-
                L_valley(i)/2)^2-csi_valley(i);
            parabola_valley(j)=parabola(j);
129         j=j+1;
        end
131 end
    temp_rq=0;
133 for i=1:length(rug)
        temp_rq=temp_rq+(rug(i))^2
135 end

137 increment=0.0001; %increment of the displacement delta[micron]
    %critic interference for each peak
139 for i=1:length(L_peak)
        delta_c(i)=(pi*k*H/(2*Ecom))^2*(1/K1_peak(i)); %micron
141 end
    y=max(parabola);
143 lt=zeros(length(L_peak),1); %vector taht indicate if the deformation is
        elastic(0) pr plastic(1)
    ltemp=0;
145 f=zeros(length(L_peak),1); %load applied in each asperity
    n_steps=0;
147 while sum(f)<load
        y=y-increment;
149     n_steps=n_steps+1;
        for i=1:length(L_peak)
151         %elastic
            if lt(i,1)==0&(csi_peak(i)-y)>0
153             f(i)=(4/3)*Ecom*((1e-3/K1_peak(i))^(0.5))*((csi_peak(i)-y)*1e-3)
                    ^(3/2);
                if (csi_peak(i)-y>delta_c(i))
155                 lt(i,1)=1;
                end
157         end
            %plastic
159         if lt(i,1)==1&(csi_peak(i)-y)>0
                f(i)=2*pi*(1e-3/K1_peak(i)*csi_peak(i)-y)*1e-3*H;
161         end
        end
163 end
    %contact area
165 A_cont=0;
    for i=2:length(RUG)
167     if parabola(i)>=y
            A_cont=A_cont+(X(i)-X(i-1));
169     end
    end
171 %percentage of contact area
    A_cont_a=A_cont/X(length(X))
173 %plot deformed profile
    for i=1:length(RUG)
175     if parabola(i)>y
            parabola_de(i)=y;
177     else
            parabola_de(i)=RUG(i);
179     end
    end
```

```
181  figure(2)
     plot(X,parabola,'k');
183  hold on;
     plot(X,parabola_de,'LineWidth',1.4);
185  hold off;
     %deformation
187  deformation=max(parabola)-abs(y);
```

Listing A.1: greenwood_model.m